Molecular Simulation Study of Noble Gas + *n*-Decane Binary Mixtures at Reservoir Conditions

A Thesis
Submitted to The University of Manchester
For the Degree of
Doctor of Philosophy (PhD)
In The Faculty of Engineering and Physical Sciences

Tule Sirikitputtisak

School of Chemical Engineering and Analytical Science

2013

Contents

Word Count 36,356

List of Figures

List of Tables

Molecular Simulation Study of Noble Gas + n-Decane Binary Mixtures at Reservoir Conditions

Tule Sirikitputtisak, The University of Manchester, 10th December 2013

Submitted for the degree of Doctor of Philosophy

Abstract

Carbon capture and sequestration are considered to be a temporary fix to the climate change global crisis. Following the noble gas tracers injection field experiment at Salt Creek in the state of Wyoming, USA, these tracers may be used to characterise the reservoir as a potential geological sequestration site for carbon dioxide. This study aims to investigate various thermodynamics properties of the five noble gases (Xe, Kr, Ar, Ne, and He) in *n*-decane at reservoir conditions (340 K – 460 K and 10 MPa – 200 MPa). The study utilises the SKS force field to describe *n*-decane and both Gibbs Ensemble Monte Carlo and molecular dynamics simulations were used to investigate the solubility, diffusivity, and vapour-liquid equilibrium of the five binary mixtures.

The size of the noble gases was found to be important in these nonpolar mixtures where typical interactions are weak and short-ranged. The enthalpies of solvation were calculated and found to be directly correlated to the size of the solute where the energy required for the formation of a cavity to accommodate the solute is compensated by the nature of the intermolecular interaction between solvent and solute. The mixture of Ar + *n*-decane is of interest particularly because the ε value for Ar is very similar to that of the CH_3 group, resulting in the overall non-mononicity of several thermodynamics properties. Additionally, maxima in enthalpies of solvation were observed in Xe and Kr in *n*-decane solution at 200 MPa. While these maxima were observed in two different species at similar conditions, they are accommodated by unusually high uncertainties - further investigation is required before definitive conclusions can be drawn.

The results from the vapour-liquid equilibrium study of the five noble gas + *n*-decane binary mixtures were in good agreement with the Peng-Robinson equation of state predictions. What is more, the diffusion coefficient ratios amongst the five noble gases in *n*-decane were investigated in light of Stoke-Einstein's relation and Enskog's hard-sphere relation. Three different radii of solute-solvent interaction were investigated and the best fit was observed when $R = \sigma_{solute} + R_{gyration}^{decane}$. Additionally, the diffusion coefficients were utilised in the reservoir simulation to investigate the role of diffusion within the reservoir.

Declaration

The University of Manchester

Candidate Name: Tule Sirikitputtisak

Faculty: Engineering and Physical Sciences

Thesis Title: Molecular Simulation Study of Noble Gas + *n*-Decane Binary Mixtures at Reservoir Conditions

Declaration to be completed by the candidate:

I declare that no portion of the work referred to in the thesis has been submitted in support of an application for another degree or qualification of this or any other university or other institute of learning.

Signed:

Date: 10th December 2013

Copyright

Acknowledgements

I would like to thank my supervisors, Professor Christopher Ballentine and Professor Andrew J. Masters, for such contagiously enthusiastic and intelligible conversations with endless possibilities, and particularly for not giving up on me when I was headed for the abyss. Your exuberant encouragements never fail to inspire and are confoundingly appreciated.

I would also like to thank my colleagues in the C19/B9 postgraduate students' office. Thank you for the conversations that never fail to entertain, and the comfort of knowing there are others in the same boat. Special thanks to the Development and Promotion of Science and Technology Talents Project and the Office of Educational Affairs, Royal Thai Embassy, in Washington, D.C., and London for the full scholarship support. And not least the education support office staffs who always offer great guidance and academic support.

Colossal heartfelt thanks to my family in Canada who always supported me and my family in Thailand who have galvanised me to be who I am today. And most importantly my babies' mama, Carissa, thank you for your unwavering love and support through the thick and thin. Thank you for such ebullient encouragements and bringing out the best in me. And for the selfless sacrifices you made, I will always be indebted and grateful.

Chapter One

Introduction to Noble Gases and Hydrocarbons

One of the single largest problems to threaten the existence of humanity to date is the mismanagement of greenhouse gas emissions. These greenhouse gases can take on many forms and can be as commonly occurring as water vapour. Although anthropogenic carbon dioxide (CO_2) is not the most potent of the greenhouse gases, for what it lacks in quality it makes up in unprecedented quantity. The atmospheric concentration of CO_2, which was about 280 parts per million (ppm), broke through the daily average of 400 ppm milestone in May of 2013 - an alarming 120 ppm higher than the pre-industrial era's average (IPCC, 2007). According to the Intergovernmental Panel on Climate Change's (IPCC) report "Impacts, Adaptation and Vulnerability" released in April of 2007, many large scale global effects are likely to happen and some are already underway. Large scale deglaciation of ice sheets, causing sea level increase, implies the transfiguration of coastlines, fresh water, estuaries, and marine ecosystems (IPCC, 2007). Changes in weather patterns and level of precipitations worldwide will cause floods, droughts, as well as an unprecedented level of heat waves (IPCC, 2007). These effects may hit much closer to home than one expects as grain prices spiked and can be observed worldwide in 2008.

While technological advancement is not the ultimate answer to the consumption habit issue, as we cannot solve the problem with the same mindset that created it in the first place, many mitigation techniques have been proposed to date as a temporary solution; a tourniquet to a life threatening injury. Simply increasing efficiency in the larger point sources, such as natural gas or coal-fired power stations, may equate to less fossil fuel required for the same amount of energy produced, and therefore less emissions. Sequestration of CO_2 has also been

proposed in what can be separated into three major categories: Biological, Oceanic, and Geological sequestration (Gough et al., 2002).

Biological sequestration is the natural process of soil and vegetation absorption of CO_2 where the capacity depends on the size and type of soil and vegetation. This is an attractive option as it is relatively inexpensive and widely available throughout the world. However, it can be easily disturbed when the land usage changes, a source of a small but significant contribution to the climate change itself (IPCC, 2007). Figure 1 shows the climate system with a large number of influencing factors.

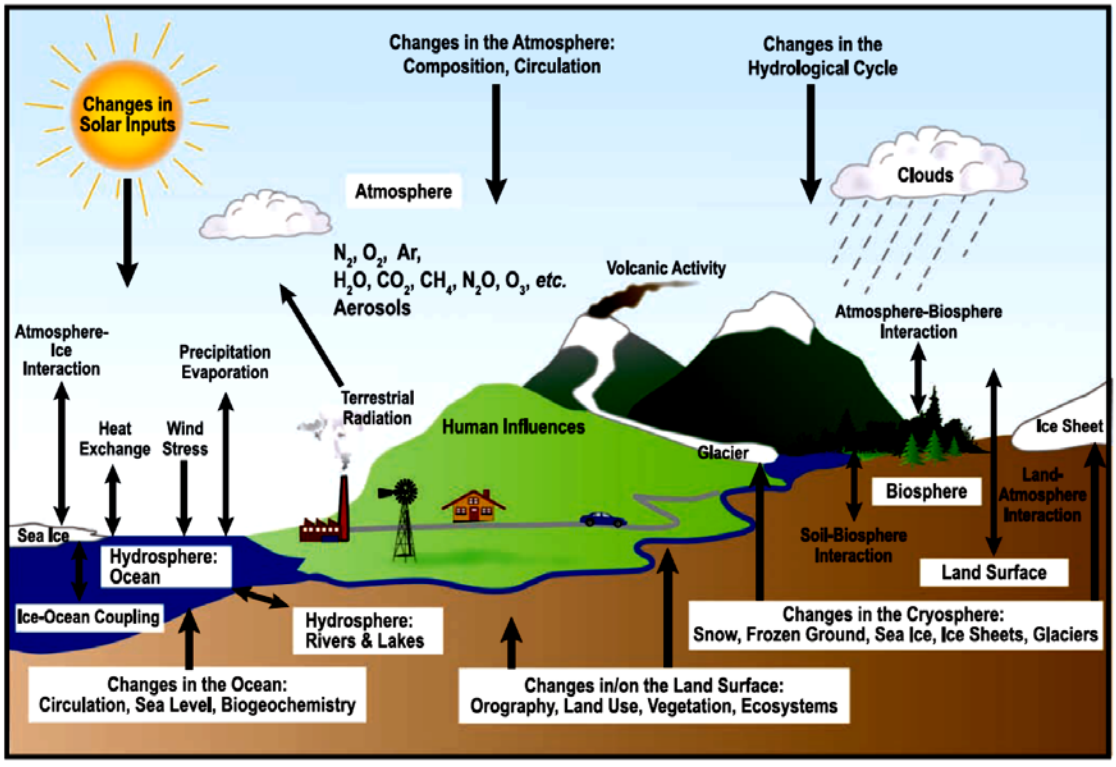

Figure 1. Climate system, their processes, and interactions adopted from (IPCC, 2007)

At first glance, oceanic CO_2 depository is also an attractive option. Marchetti (Marchetti, 1977) was among the earlier explorers of the idea. Covering the majority of the earth's surface, the deep sea offers a large capacity for CO_2 storage. At depth beyond 1,000 metres, the impermeable hydrate can help accelerate the

production of carbonic acid, subsequent reaction with limestone, and the eventual production of bicarbonate which can then be dissolved. This storage potential however lies in an obscure territory, for arguably we know less of the oceans depth than we do the extraterrestrial. The effects of salinity and acidity are not well established and have only been brought to our attentions as an effect and potential positive feedback loop of climate change itself. A vast complex ecosystem beyond our comprehension can easily be crippled, if not desolated, at a slight tip of the scale. If this were to happen, the sinking of organic decompositions can produce far more potent greenhouse gases, such as methane and nitrogen monoxide, further exacerbating the problem (Yang et al., 2008). Faced with an onset of a much larger problem, we shall leave this as a last resort.

Another mitigation technique, a geological CO_2 sequestration site in depleted gas and oil reservoirs, has also been proposed and has been gaining much interest. As early as the 1920's, excess gas was injected back into reservoirs to store for future use (Bargas et al., 1992). The rapid production responses were then observed and were later developed as an Enhanced Oil Recovery (EOR) technique. On principle of minimum miscibility pressure, the injected gas helps reduce the viscosity as well as causes oil swelling thus making it easier for extraction. Other fluids, such as water and nitrogen, were also injected to maintain reservoir pressure and sweep the field with various injection techniques. In particular, CO_2 was used as a primary solvent as it becomes supercritical when the temperature reaches 304.25K and 7.39MPa of pressure, well under most reservoirs conditions. By injecting the undesired supercritical carbon dioxide into an active or depleted oil reservoir, both the goals of sequestering CO_2 and enhancing the recovery of oil are achieved. A number of large scale geological sequestration pilots have been underway, including the governmental subsidized Sleipner project in the Norwegian North Sea where over 10 mega tonnes of CO_2 have been injected since 1996. Similar projects throughout the world have also been observed including, but not limited

to, the In Salah project in Algeria, the Ordos project in Mongolia, the Weyburn-Midale project in Saskatchewan, Canada, and the 2014 Gorgon project on the Barrow Island, Australia.

Concerns with the geological sequestration are directed toward the possible leakage and the integrity issues where the wells may not be properly sealed throughout the exploration drilling history of a given field or the faults in sealing cap rocks (Bachu, 2008; Bruant et al., 2002). In addition, the physicochemical reactions of CO_2 are not well understood within these complex crustal structures for the minimum mandatory storage period of thousands of years (Lindeberg, 2003).

To help address these problems, the use of the nonradioactive noble gases as tracer has been established (Ballentine et al., 2002). Injecting along with the supercritical carbon dioxide, the noble gas can then track the injected fluid. Noble gases have low chemical reactivity and naturally exist in low abundance within the crustal structures, making a perfect tracer.

1.1. Noble Gases and Hydrocarbons Systems

1.1.1. Noble Gases

The five nonradioactive noble gases: Helium (He), Neon (Ne), Argon (Ar), Krypton (Kr), and Xenon (Xe) are members of group VIII of the periodic table. They are inert gases which are stable and do not often react or form chemical bonds with other elements. A number of isotopes including ^{4}He, ^{40}Ar, and $^{131-136}Xe$ within the earth's crust can be created directly from the radioactive decay of Thorium, Uranium, and Potassium.

There are many applications for use of noble gases, for example, they can be used in the breathing apparatus for deep-sea diving - a subject of depression sickness and narcosis. Xe in particular is widely used to study cerebral blood flow and pulmonary diseases (Weiskopf et al., 2000). It was formally proposed in the medical community as a general anesthetic for its nontoxicity, high solubility in lipids, and nonflammability (Weiskopf et al., 2000). It is a structureless particle whose high polarizability enhances dispersion forces (Bonifácio et al., 2010).

Nobel gases' low pre-existing level in the crust is sensitive to the partitioning between fluid phases. They are significantly less soluble in water than oil, thus can be used as an indicator for the degree of flow and water-oil interaction within the reservoir (Crovetto et al., 1982; Kharaka & Specht, 1988; Pollack, 1981). This, combined with the high sensitivity of the detecting instrument available, allows a very low artificial concentration level, in the order of parts per billion, to be resolved when compared against the natural background.

1.1.2. n-Decane

n-Decane is part of the *n*-alkane homologous series, previously known as paraffin, in organic chemistry where the general formula can be written in terms of Carbon and Hydrogen as C_nH_{2n+2}. They also exhibit structural isomerism where the isomer forms may have identical formulae, but different structure. This is due to the similarity between the C-C bonds and C-H bonds and thus can be arranged differently; the variation increases with the number of carbon backbones. The *n* prefix in *n*-alkane denotes the 'normal' form and *i* for 'isomer' form. Some examples of these homologues include Methane, Ethane, Hexane, Decane, Hexadecane, Dodecane, and so on.

Table 1. Critical properties of decane and noble gases (Design Institute for Physical Properties)

IUPAC name	Molecular formula	Molecular weight	T_c (K)	P_c (Pa)	V_c (m3/kmol)	Z_c
DECANE	C10H22	142.2817	617.7	2110000	0.617	0.254
XENON	Xe	131.29	289.74	5840370	0.118	0.286
KRYPTON	Kr	83.8	209.35	5501950	0.0912	0.288
ARGON	Ar	39.948	150.86	4898000	0.07459	0.291
NEON	Ne	20.1797	44.4	2653000	0.0417	0.3
HELIUM	He	4.0026	5.2	227500	0.0573	0.302

The main components of the alkanes are made up of the methylene group, CH_2, and the methyl group, CH_3. It is these functional groups which will be used as a pseudo atom and represent the molecule in the united atom force fields which will later be discussed. The overall structure of *n*-alkanes takes the same form with single sigma bonds of approximately 109.5 degrees bond angle and alkanes are differentiated by the number of CH_2 group, which are added onto the carbon backbone. Such homologous series are extensively studied, similar to the noble gases, where simple structure and relatively chemically inert homologous series can serve as a fundamental for other compounds.

The critical properties of *n*-dencane and noble gases are listed in Table 1. The striking similarity between noble gases and *n*-alkanes can also be observed through the nearly identical spherical diameters and molecular potentials representing xenon and *n*-alkanes (Bonifácio et al., 2010).

1.2. Previous Studies

The alkane binary mixtures have been extensively studied, particularly the xenon + *n*-alkane mixtures at ambient conditions for many applications in process engineering, medical community, and gas and oil industry.

1.2.1. Solubility of Noble Gases in n-Alkanes

In 1981, Pollack experimentally measured the solubilities of ^{133}Xe in twelve *n*-alkane binary mixtures from *n*-pentane to *n*-hexadecane at 20℃ (Pollack, 1981). The results were given in terms of Ostwald solubility which is the ratio of unit volume of dissolved gas per unit volume of liquid at equilibrium, as shown in Table 2. It was found that the Ostwald solubility and the Gibbs energy decreases with increasing number of carbon atom in the *n*-alkane chain (Pollack, 1981).

Table 2. Solubility of ^{133}Xe in *n*-alkanes at 20.0°C, redrawn from (Pollack, 1981)

Solvent	Ostwald Solubility L(20.0°C)	Mole Fraction $x_2 \times 10^2$	Gibbs Energy $\Delta\mu_2^o$ (cal/mole)
n-C_5H_{12}	5.39	2.52	2145
n-C_6H_{14}	5.01±0.11	2.65	2116
n-C_7H_{16}	4.61	2.73	2097
n-C_8H_{18}	4.34±0.03	2.85	2073
n-C_9H_{20}	4.13	2.98	2047
n-$C_{10}H_{22}$	3.90±0.02	3.06	2031
n-$C_{11}H_{24}$	3.73	3.17	2010
n-$C_{12}H_{26}$	3.57	3.27	1993
n-$C_{13}H_{28}$	3.44	3.37	1975
n-$C_{14}H_{30}$	3.33	3.48	1957
n-$C_{15}H_{32}$	3.23	3.58	1940
n-$C_{16}H_{34}$	3.14	3.68	1923

Recognising that gas solubility is inversely correlated to the number of carbon atoms, Mizerovsky and Smirnova used a group of correlation for solubility of gases and thermophysical characteristics of *n*-alkanes such as isothermal compressibility coefficients, thermal expansions and the likes, as the basic building blocks. A new description of the solubility of noble gases in organic liquids was

proposed from the basis of nitrogen and noble gases in *n*-alkanes at standard pressure and temperature of 298.15K (Mizerovsky & Smirnova, 2010). Mizerovsky and Smirnova (2010) observed the independency between K_D (constant of distribution of the gas between intrinsic phase and liquid) and the size of solvent and suggested that the interaction between the diffusing gas and the *n*-alkanes does not occur throughout the chain but rather with the methyl and methylene groups. It should also be noted that K_D increases dramatically with the electronics polarizability of the gas; K_D for Xe is two order of magnitude higher than He (Mizerovsky & Smirnova, 2010). Similar to this finding, in their 1978 study of solubility of all five noble gases up to critical point of water, Potter and Clynne also noted that molecular weight of the noble gases, less He, are directly proportional to the solubility (Potter & Clynne, 1978).

In the 2007 molecular dynamics study, Makrodimitri et al. investigated the solubility of 17 different compounds in polymer Poly(dimethylsiloxane) (PDMS) including *n*-alkanes, light gas, and noble gases. The conditions varied from 300-450K and 0.1 to 40 MPa. The resulting solubility coefficients are reported in Table 3 and Figure 2.

Table 3. Infinite dilution solubility coefficients ($\frac{cm^3(STP)}{cm^3\ pol\ atm}$) of noble gases in PDMS at 0.1MPa (Makrodimitri et al., 2007).

Gas	Temperature (K)		
	300	375	450
He	0.058±0.001	0.091±0.001	0.125±0.001
Ne	0.078±0.001	0.109±0.001	0.139±0.001
Ar	0.31±0.02	0.27±0.01	0.26±0.01
Kr	0.76±0.04	0.58±0.02	0.47±0.02
Xe	2.8±0.2	1.4±0.1	0.9±0.1

Makrodimitri et al. used the TraPPE force field to represent n-alkanes and observed a systematic decrease of solubility at infinite dilution with increasing temperature for lighter gases, and vice versa for relatively heavier gases

(Makrodimitri et al., 2007). It was also indicated that solubility of gas in polymer is directly correlated to the critical temperature (T_c) of the gas solute (Makrodimitri et al., 2007).

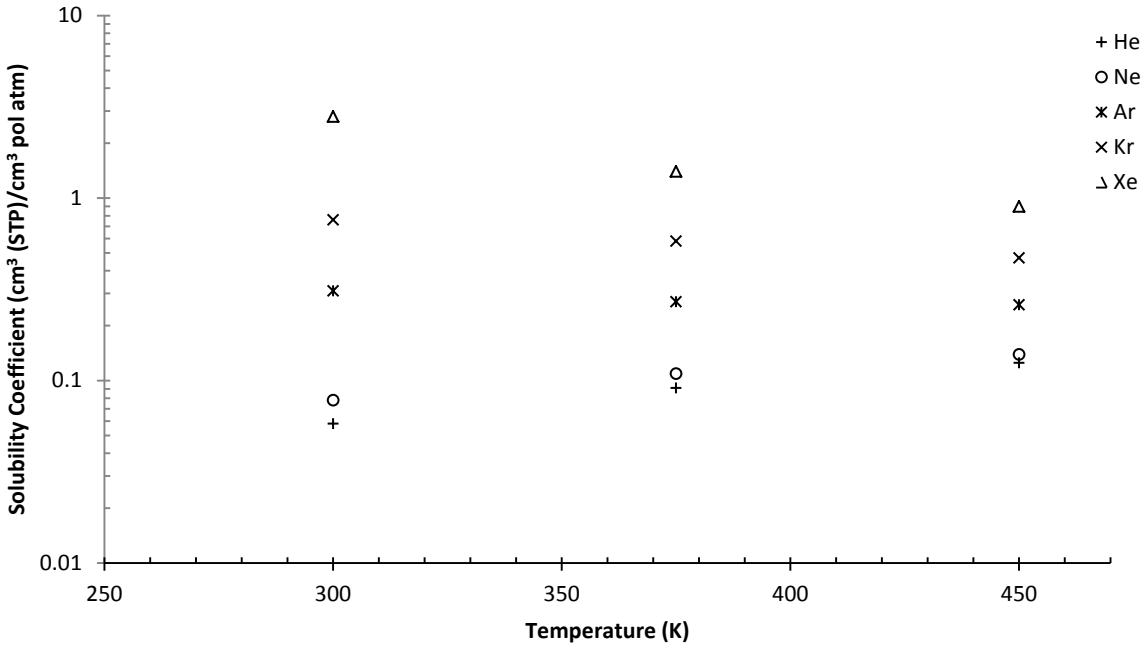

Figure 2. Infinite dilution solubility coefficients of noble gases in PDMS at 0.1MPa redrawn from (Makrodimitri et al., 2007).

In 2010, Bonifácio et al. carried out a complete theoretical, experimental, as well as simulation study, of solubility of the Xe + *n*-pentane and Xe + *n*-hexane mixtures (Bonifácio et al., 2010). The temperature ranged from 254 K to 305 K, covering the critical temperature of xenon at 289.74 K. Monte Carlo simulations with TraPPE-UA force field were used to calculate Henry's constant for both systems and compared to that from the experimental results. Additionally, SAFT-VR was used to quantitatively predict the solubilities. From their several previous works, as well as the prediction by SAFT-VR, the diameter of the sphere representing the xenon as well as its molecular potential are very similar to that of *n*-alkanes (Bonifácio et al., 2010; Dias et al., 2004; Filipe, Gomes de Azevedo, et al., 2000; Filipe, Martins, et al., 2000). And thus the xenon + *n*-alkane binary mixtures under

investigation in this study behaves very similar to that of *n*-alkane + *n*-alkane system (Bonifácio et al., 2010). Not exceeding 9%, the simulation results are quite accurate when compared to the experimental results for both binary mixtures investigated, however the deviation increases with the temperature. Henry's coefficients were observed to increase with temperature, and maximum enthalpies of solvation were observed at reduced temperature of 0.54, an equivalent of 254.5K for xenon + *n*-pentane mixture and 275K for xenon + *n*-hexane mixture.

1.2.2. Diffusion of Noble Gases in n-Alkanes

In a series of experimental tracer diffusion study of Evans et al., a wide range of binary systems were investigated to verify the validity of the Stoke-Einstein equation and rough-hard-sphere theory (Chen et al., 1981; Chen et al., 1982; Evans et al., 1981). The systems examined included Ar, Kr, and Xe and *n*-decane among many other mixtures. The Taylor Dispersion Technique was used to experimentally measure the diffusion coefficient at temperatures between 25℃ and 160℃. The measurement utilizes the linear flow of solvent where solute is later injected. The Gaussian distribution is then measured and the binary diffusion coefficient is given as

$$D = \frac{0.2310\mathrm{r}^2 t_r}{\left(w_{\frac{1}{2}}\right)^2} \qquad (1)$$

Where

t_r = residence time of the solute in the capillary tube

r = radius of the capillary tube

w = width at half-height of the eluted peak

In addition to the ambiguity in the particle radius assignment, it was pointed out that the Stoke-Einstein's equation does not hold where there is a large disparity between the size of solute and solvent, particularly where solvent is significantly larger than the solute molecules (Chen et al., 1981; Chen et al., 1982; Evans et al., 1981; Pollack et al., 1990). Such deviations are depicted by Figure 3, where $D\eta$ was plotted against an inverse of solute radius, $\frac{1}{r}$.

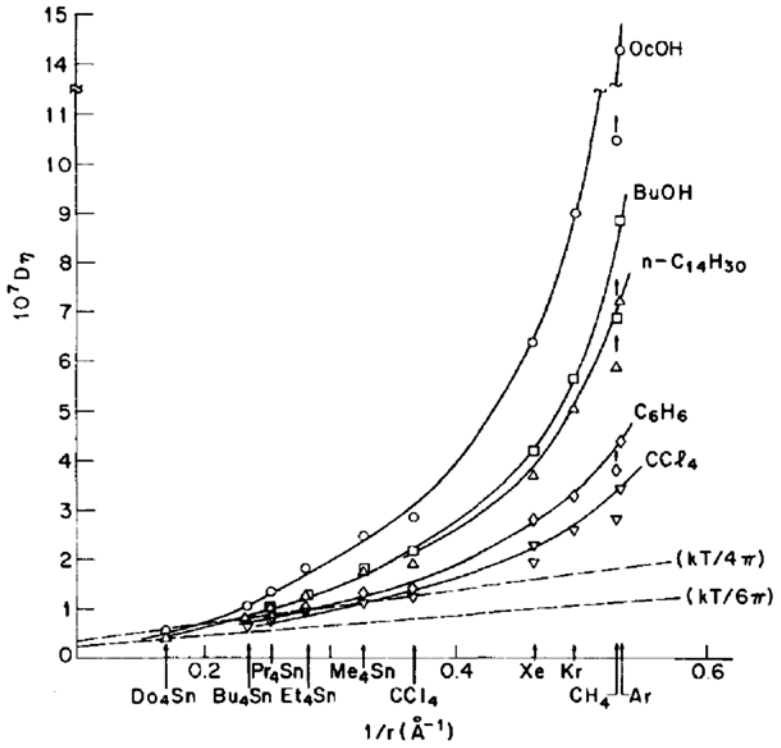

Figure 3. Stoke-Einstein relation between $D\eta$ and $\frac{1}{r}$, adopted from (Evans et al., 1981)

The fraction of 4 or 6, for the slip or stick boundary, in the Stoke-Einstein's equation evidently cannot address the slope. The rough-hard-sphere approach, an extension to the work of (Alder et al., 1974) where angular momentum transfer upon collision is taken into account, was also proposed. However, this was later proven to be inadequate, in particular, for the noble gas + *n*-decane mixture (Chen et al., 1982). The experimental measurement of the noble gas + *n*-decane mixtures

are extracted from Chen et al. (1982) and shown in Table 4. These numbers are an average of at least four measurements with standard deviation of less than 3%. This data will be used to calibrate our simulation as will be later discussed.

Table 4. Diffusion coefficient 10^{-5} cm²/sec of noble gases in *n*-decane at various temperatures as reported by (Chen et al., 1982)

Temperature (K)	Ar	Kr	Xe
298	4.87±0.007	3.51±0.006	2.86±0.003
333	7.72±0.007	5.75±0.003	4.60±0.003
373	-	-	7.13±0.005
433	19.3±0.002	14.6±0.001	12.2±0.001

It should be noted, however without theoretical basis, the diffusion correlation can be described very well by (Evans et al., 1981)

$$D\eta^p = \mathrm{AT} \tag{2}$$

Where

$p\ and\ A$ = dimensionless parameters depend mainly on the solute

The proposed $D\eta^p$ correlation was further explored by (Pollack & Enyeart, 1985; Pollack et al., 1990)

The diffusion of radioactive ^{133}Xe in twelve different *n*-alkane mixtures, from *n*-pentane to *n*-hexadecane, at 20℃ were measured in the experimental study by (Pollack & Enyeart, 1985). From the measurement, Pollack and Enyeart (1985) suggested a new modified Stokes-Einstein relation for ideal case as follows

$$D = \frac{A}{\eta^p} = \frac{C(k_B T)^{\frac{5}{6}}}{(\mathrm{mR}^2)^{\frac{1}{6}}\eta^{\frac{2}{3}}} \tag{3}$$

Where

C = dimensionless constant

p = indicator of said correlation between microscopic and macroscopic property.

The diffusion was reported in terms of viscosity, η, as follows

$$D = \frac{(1.26 \pm 0.06) \times 10^{-6}}{\eta^{0.686 \pm 0.011}} \quad (4)$$

As depicted in Table 5, the reported uncertainty is approximately 4.2% where cross-sectional area and solubilities are the key contributors. A linear trend of diffusion coefficient with respect to the number of carbon backbone was observed where the nonpolar solute and solvent interactions are most likely weak and short-ranged. Similar observation was also made when the solubility of Xe in *n*-alkane binary mixtures were measured (Pollack, 1981; Pollack & Himm, 1982). The results reported in Table 5 for Xe in *n*-decane solution are in good agreement with that of (Chen et al., 1982) at similar conditions.

Table 5. Average diffusion coefficient from 25 determinations of ^{133}Xe in *n*-alkane binary mixtures at at 20℃ with 4.2% uncertainty (Pollack & Enyeart, 1985)

Alkane	D (10^{-5}cm^2/sec)	Alkane	D (10^{-5}cm^2/sec)
***n*-C_5H_{12}**	7.96	*n*-$C_{11}H_{24}$	2.52
***n*-C_6H_{14}**	6.71	*n*-$C_{12}H_{26}$	2.29
***n*-C_7H_{16}**	5.54	*n*-$C_{13}H_{28}$	1.91
***n*-C_8H_{18}**	4.53	*n*-$C_{14}H_{30}$	1.67
***n*-C_9H_{20}**	3.75	*n*-$C_{15}H_{32}$	1.45
***n*-$C_{10}H_{22}$**	3.05	*n*-$C_{16}H_{34}$	1.27

Similar measurement was later carried out in the temperature range of 10-40℃ (Pollack et al., 1990). The results are shown in Table 6.

Table 6. Diffusion coefficient of ^{133}Xe in *n*-alkane binary mixtures at various temperatures (Pollack et al., 1990)

Alkane	D (10^{-5}cm^2/sec)			
	10.0℃	20.0℃	30.0℃	40.0℃
***n*-C_8H_{18}**	3.93	4.37	5.15	6.02
***n*-$C_{10}H_{22}$**	2.50	2.95	3.43	3.97
***n*-$C_{14}H_{30}$**	1.32	1.57	1.90	2.25

In the evaluation of the united atom force fields for alkanes in the series of equilibrium molecular dynamics studies by Dysthe et al. (2000), a number of force fields are rated according to their *simplicity*, *transferability* among the homologous series, *property independency* where good prediction of one property extend to others, and *state independency* where accuracy is independent of temperature, density, and composition (Dysthe et al., 2000). It was found that viscosities of the pure component may be overestimated up to 80% and as much as 250% overestimating the diffusion coefficient with high pressure and low temperature (Dysthe et al., 2000). Dysthe et al. (2000) also found that 2% difference in density may translate to 30% in transport coefficient predictions where transport properties are more directly related to density than to pressure. Wang and Hou (2011) also demonstrated great statistical inaccuracies among the diffusion coefficients reported, unlike other bulk properties such as density in literature, some experimental values of the same system may exhibit over 40% difference (Wang & Hou, 2011).

In addition to the study of united atom force field by Dysthe et al. (2000), Wang and Hou (2011) investigated the General AMBER force field, GAFF, and its capacity in determining diffusion coefficients of organic solutes in organic solution, organic solutes in aqueous solution, and proteins in aqueous solution through the *Einstein relation* which will be later discussed (Wang & Hou, 2011). Theoretically, the accurate diffusion coefficient can be determined as $t \to \infty$. However, neither accurate nor reproducible values can be produced for the system like benzene in ethanol or phenol in water with single long simulation (Wang & Hou, 2011). Wang and Hou (2011) recommended the use of several short molecular dynamics simulations to substantially improve the statistical accuracy of the mean square displacements, MSD.

1.2.3. Phase equilibria of Noble Gases and n-Alkanes

After an extended search, no literature on the phase equilibria investigation of noble gas and *n*-alkane were found. However, comparable studies of the systems with small alkane and longer n-alkane were investigated.

In 2006, Aparicio-Martínez and Hall investigated the global phase diagrams of various *n*-alkane + *n*-alkane binary mixtures using the perturbed-chain statistical associating fluid theory (PC-SAFT). Among other factors, the relative size, defined as the ratio of molar masses, of the components in the *n*-alkane + *n*-alkane mixtures have been identified as a determinant of the critical region in the study. In the homologous series of ethane and *n*-alkanes up to *n*-pentane, Aparicio-Martínez and Hall (2006) observed the increase of the critical loci with increasing relative sizes (Aparicio-Martínez & Hall, 2006). The methane + *n*-decane mixture is thought to be in the Type I mixture in the (Konynenburg & Scott, 1980) six classifications of phase-behavior patterns. A Type I system is where a complete liquid miscibility is observed, critical locus of lower and higher critical temperatures are continuous, and relative size difference exceeds a certain ratio (Kay, 1968; Rowlinson & Swinton, 1982). The triple point of the methane + *n*-decane mixture was also observed at higher temperature than other shorter *n*-alkanes mixtures and the separation of liquid phase was not observed. The global phase diagram of the ethane + *n*-alkane mixture is shown in Figure 4.

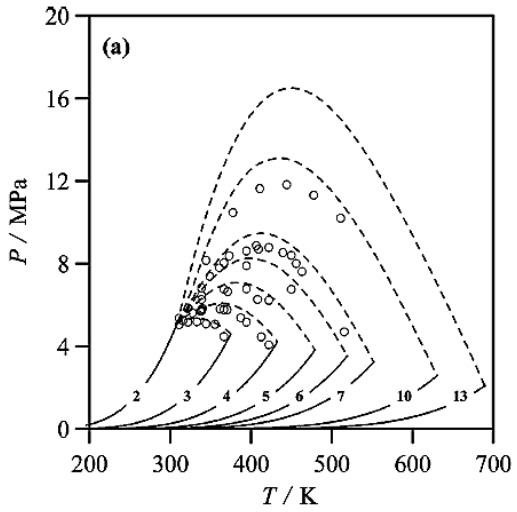

Figure 4. The global phase diagram of ethane + n-alkane mixtures with number indicating the number of carbon backbone and o indicating experimental results, adopted from (Aparicio-Martínez & Hall, 2006)

Most of the points are comparable to the experimental values where available. For example, the data of the ethane + *n*-pentane system has been taken from (Ekiner & Thodos, 1966b; Reamer et al., 1960) as depicted in Figure 5 and ethane + *n*-decane system from (Reamer et al., 1964).

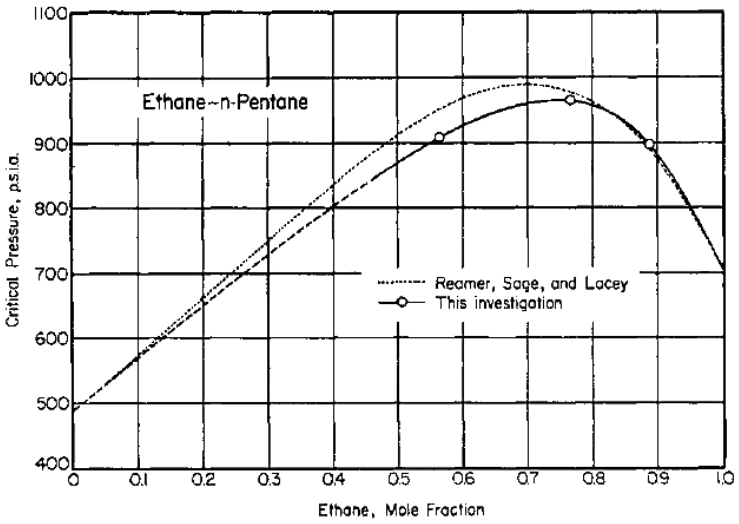

Figure 5. The critical pressure locus in terms of ethane mole fraction in ethane + *n*-pentane mixture, adopted from (Ekiner & Thodos, 1966b)

The relative size and the maximum critical loci plot is shown in Figure 6.

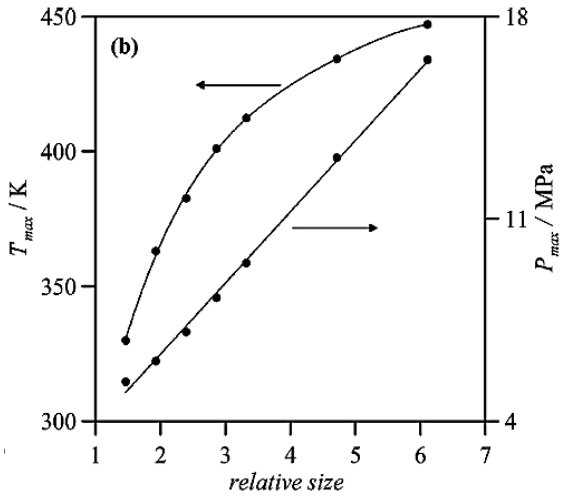

Figure 6. The relative size of the mixture components in relation to the maximum critical loci, adopted from (Aparicio-Martínez & Hall, 2006)

Partial miscibility in liquid phase was observed in the methane + *n*-hexane and can be classified as Type V where two separate lines connect the lower critical temperature to the upper critical endpoint and higher critical temperature to the lower critical end point.

Aparicio-Martínez and Hall (2006) also noted that mixture of *n*-alkane and other *n*-alkane heavier than ethane or methane for smaller N can be classified as Type I and those with larger N can be classified as Type V of the (Konynenburg & Scott, 1980) classification, where N indicates the number of carbon backbone.

What is more, in the experimental critical temperature and pressure measurements of the ethane + *n*-pentane + *n*-heptane ternary mixture by Ekiner and Thodos in 1966, while linear loci of critical temperature was noted, a maxima in critical pressure was also observed (Ekiner & Thodos, 1966a).

1.3. Field Experiment and Problems

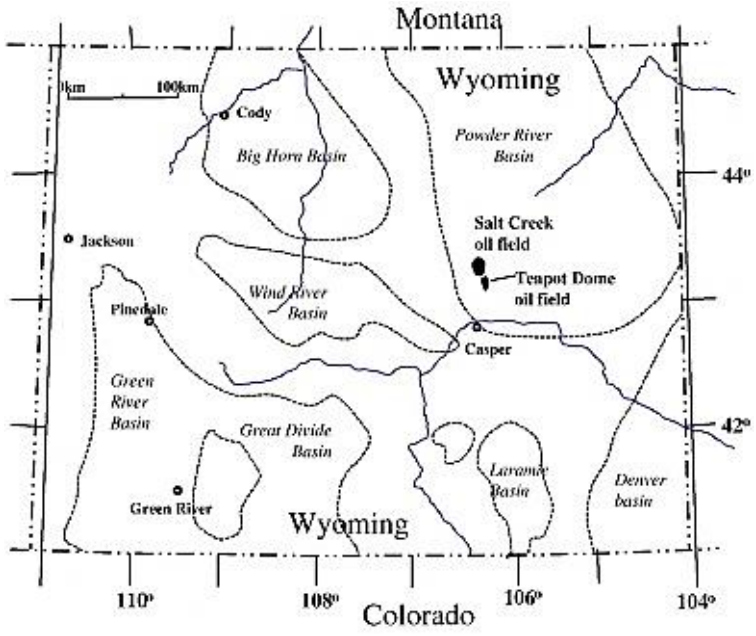

Figure 7. Location of Salt Creek oil field in the State of Wyoming, USA (Mackintosh & Ballentine, 2012)

In 2010, the Carbon Research into Underground Storage (CRIUS) group carried out a 3 months field experiment in the Salt Creek oil field, in the state of Wyoming, USA, as shown in Figure 7. As part of this project, Salt Creek was chosen as a testing site primarily for its shallowness. The depth of the wells utilized in the experiment were around 900 metres, the minimum required for a CO_2 sequestration site (Shafeen et al., 2004).

Salt Creek is situated on a 40 kilometers stretch of anticline extending north-northwest by south-southwest (Mackintosh, 2009). The drilling in the area was first carried out in 1889 and has since produced an estimated 7 billion barrels of oil and another estimated 1.8 billion barrels of recoverable oil (Wo et al., 2009). By 1925 there were over 1100 wells drilled into Second Wall Creek alone and it is expected that throughout the life time of Salt Creek, there will be over 3000 wells drilled (Estabrook & Rader, 1925).

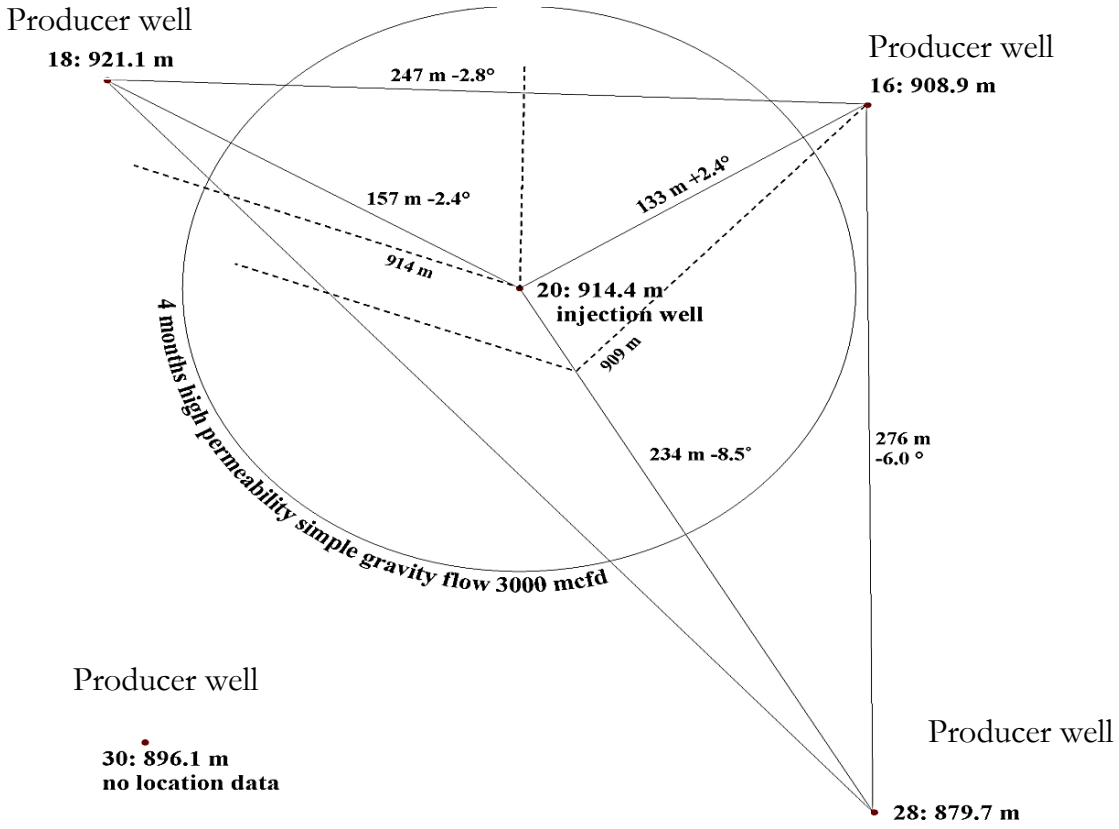

Figure 8. Injection pattern, Salt Creek, Wyoming.

The tracer injection started in early September 2011 and spanned a period of two weeks. The fluid samples were then collected daily from all four well outlets (and some surrounding wells) for the following 2 months. The author was fortunate enough to be part of the sample collection team for a rotation during the two months sampling period. The samples were then analyzed for Eh-pH and the presence of tracers utilizing mass spectrometry.

Figure 9. The author at the Salt Creek sampling site

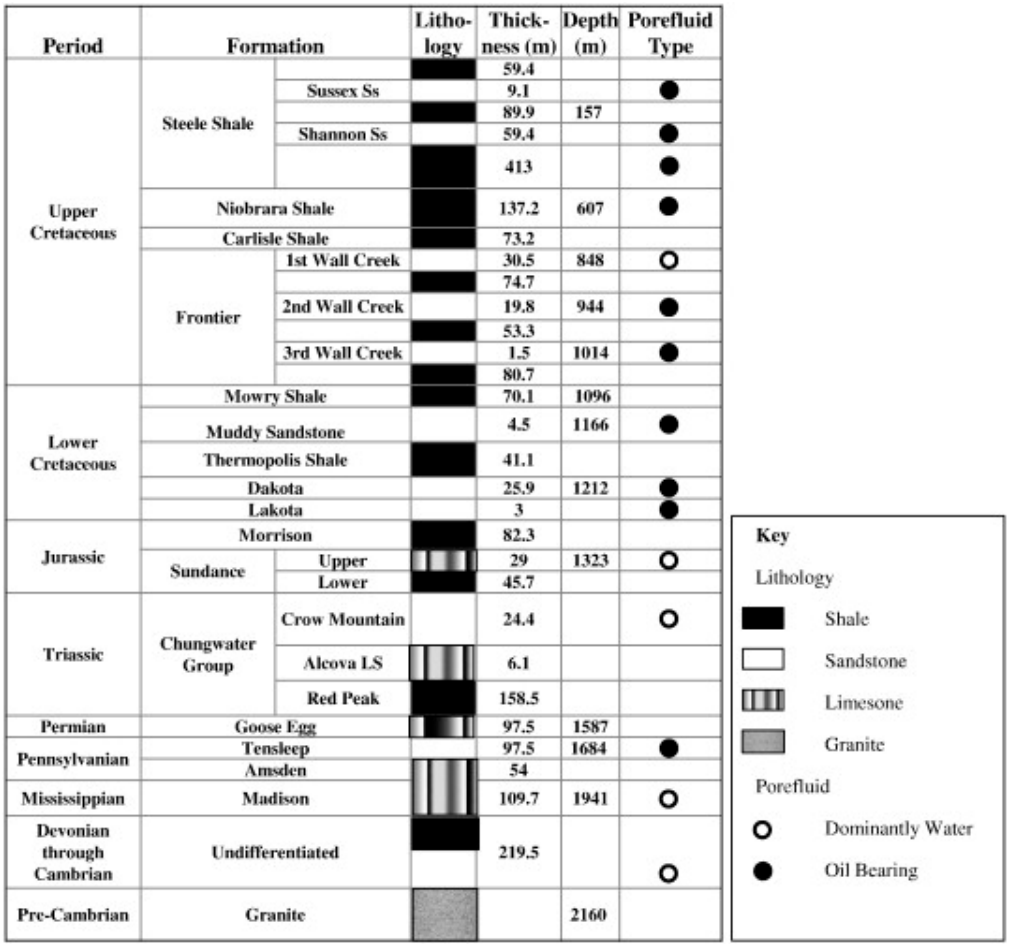

Figure 10. Geological column through the neighbouring Teapot Dome, showing lithology, thickness, depth, and fluid type (Mackintosh & Ballentine, 2012)

In 2002, Anadarko Petroleum purchased the Salt Creek field and, at the time, underwent water-alternating-gas EOR. The specific injection wells pattern is illustrated in Figure 8. Mackintosh (2009) reported a production rate of approximately 500 barrels per day in the neighbouring Teapot Dome (Mackintosh, 2009). The production rate is thought to be similar in the Salt Creek field.

Other physical properties of the reservoir are listed in Table 7. As shown in Figure 10, the geological column description of the neighbouring Teapot Dome shows that it is producing at a depth of approximately 944 metres, the 2nd Wall Creek. With a thickness of between 15-30 metres, operating pressure is strictly maintained to satisfy the minimum miscibility pressure (Mackintosh, 2009).

Table 7. Some physical properties of the site.

Criteria	Value
Temperature	150 F
Permeability	52 md
Porosity	19%
Injection pattern	Five spot
Bottom hole depth	~3,100 ft
CO_2 injection rate	1,000 – 3,000 MCF/day
Oil gravity	33.3 – 37.4 Baumè degrees

There is still a large amount of reservoir information missing before a complete study for Salt Creek can be performed. The *PVT* data from the reservoir fluid analysis is the most critical. These missing *PVT* data provide the physical properties of the gas and oil which are utilized in predicting the behaviour and fluid interactions in the reservoir for both black oil and compositional reservoir models.

As a result, the current report will employ a complete data set from the Good Oil reservoir, an existing reservoir with a complete data set, to illustrate the ability of the program and its options. These will later be combined with the actual complete field data from Salt Creek when available.

1.4. Objectives

The objectives of this study are as follow:

- to investigate the solubility coefficients of noble gases in *n*-decane at infinite dilution and reservoir conditions using atomistic simulation software
- to investigate the vapour-liquid equilibrium curves of the noble gases and *n*-decane binary mixtures with compositions representative of that at infinite dilution and reservoir conditions using atomistic simulation software
- to investigate the diffusion coefficients of noble gases in *n*-decane solution at reservoir conditions using atomistic simulation software
- from the diffusion coefficients obtained, investigate the extent of the tracers diffusion in a reservoir using reservoir simulation software

This thesis is organised into three parts. Following the introduction to noble gases and hydrocarbons, the first part describes the theoretical background required for the study of the solubility coefficients, vapour-liquid equilibrium, and diffusion coefficient via atomistic simulations and reservoir simulation. These include the Monte Carlo and molecular dynamics simulation approaches. In addition, the reservoir model used in this study will also be discussed. The second part deals with the computer simulations and parameterizations of the models utilized in this study. A number of key parameters were investigated and compared with the values from literature where available. The third and final part provides the findings, discussions, as well as conclusions and avenue for future work.

Part I. Theoretical Background

Chapter Two

Monte Carlo simulation

In statistical mechanics, the partition function encompasses the thermodynamic descriptions of the system in thermodynamic equilibrium. These descriptions include, but are not limited to, entropy, heat capacity, as well as internal energy. A canonical form of the partition function is given by:

$$Q = \frac{1}{N!\,h^{3N}} \int d\boldsymbol{p}^N d\boldsymbol{r}^N \exp[-\mathcal{H}(\boldsymbol{p}^N \boldsymbol{r}^N)/k_B T] \qquad (1)$$

Where

$\boldsymbol{r}^N$ = coordinates of all N particles

$\boldsymbol{p}^N$ = corresponding momenta for all N particles

k_B = Boltzmann's constant

h = Planck's constant

$\mathcal{H}(\boldsymbol{r}^N \boldsymbol{p}^N)$= Hamiltonian of the system which is a combination of Kinetic and Potential energy.

And subsequently, the statistical average of a property A is given as:

$$\langle A \rangle = \frac{\int d\boldsymbol{r}^N A(\boldsymbol{r}^N) \exp[-\beta \mathcal{U}(\boldsymbol{r}^N)]}{\int d\boldsymbol{r}^N \exp[-\beta \mathcal{U}(\boldsymbol{r}^N)]} \qquad (2)$$

Where

$\beta = 1/k_B T$

$\mathcal{U}$ = potential energy of the system

And the angle parentheses represent an average quantity.

Amongst the variations of Monte Carlo, the Metropolis importance sampling approach is of particular interest (Metropolis et al., 1953). Depicted by the infamous visualisation depth measurement, Figure 11 compares the conventional and Metropolis importance sampling methods.

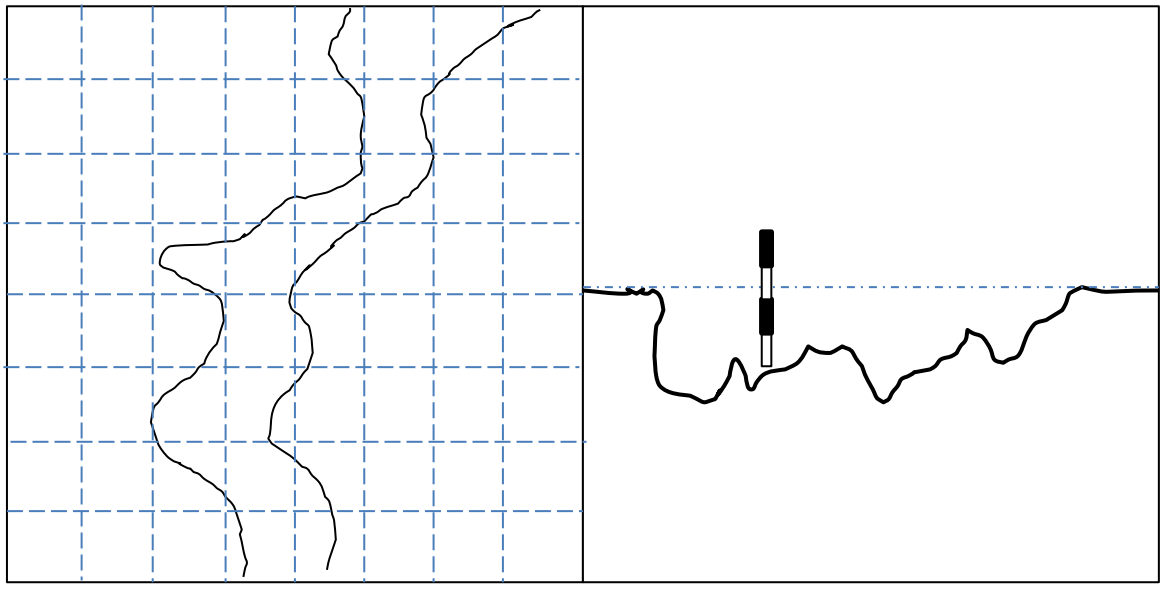

Figure 11. Comparison between conventional (left) and Metropolis importance sampling (right)

The left side of Figure 11 represents the conventional integration approach which considers the integration at predetermined values on the abscissa. On the right side of Figure 11, the Metropolis importance sampling considers only the relevant points through the weighted distribution. In this case, the average depth of the river represents the quantity we want to measure and not the entire grid. The measurement is promptly rejected if it is not within the body of water, thus saving time and improve the accuracy of the overall average (Frenkel & Smit, 2002).

One important quantity that is provided by the conventional quadrature evaluation is the total area of the river. This is the equivalent of the configurational part of the observable A, the denominator in equation (2), which cannot be calculated

directly via Monte Carlo approach. This is precisely what the Metropolis' approach addresses.

For further discussion, the denominator in equation (2) will now be defined as Z.

$$Z \equiv \int d\boldsymbol{r}^N exp[-\beta \mathcal{U}(\boldsymbol{r}^N)] \qquad (3)$$

Although *Z*, the absolute probability of visiting different sampling points, cannot be calculated directly, Metropolis had proposed a way around this by instead calculating the probability density of finding the system in the configuration $\boldsymbol{r}^N$ which can be written as (Frenkel & Smit, 2002)

$$\mathcal{N}(\boldsymbol{r}^N) \equiv \frac{exp[-\beta \mathcal{U}(\boldsymbol{r}^N)]}{Z} \qquad (4)$$

Such system with the configuration $\boldsymbol{r}^N$ henceforth will be that with a non-zero Boltzmann factor. The Metropolis importance sampling approach is carried out as follow (Frenkel & Smit, 2002):

1. A system of a configuration $\boldsymbol{r}^N$ is defined, denoted by 'o' for old, in relative to the other configurations to come. The Boltzmann factor for this system is given by $exp[-\beta \mathcal{U}(o)]$.
2. A new system of configuration $\boldsymbol{r}'^N$ is defined, denoted by 'n'. These two systems differ by a random displacement, Δ. The Boltzmann factor for this system is given by $exp[-\beta \mathcal{U}(n)]$.
3. The transition probability is given by $\pi(o \rightarrow n)$. Following the acceptance criteria imposed, the system now can either take on the new or keep the old configuration, becoming the next link in the Markov chain.

The steps are repeated for the desired number of cycles in the Markov chain. The underlying transition matrix of Markov chain, $\alpha(o \rightarrow n)$, can be expressed as:

$$\pi(o \to n) = \alpha(o \to n) \times acc(o \to n) \quad (5)$$

Where

$$acc(o \to n) = \begin{cases} 1 & if \quad \mathcal{N}(n) \geq \mathcal{N}(o) \\ \dfrac{\mathcal{N}(n)}{\mathcal{N}(o)} & if \quad \mathcal{N}(n) < \mathcal{N}(o) \end{cases} \quad (6)$$

And the transition probability of going from $o \to n$ must satisfy the detailed balance condition where the probability of accepting the transition is equal in either direction:

$$\mathcal{N}(o) \times \pi(o \to n) = \mathcal{N}(n) \times \pi(n \to o) \quad (7)$$

Where

$\pi(i \to j)$ = Transition probability of going from state *i* to *j*

2.1. Ensembles

A quantum system can be found in any state which is an energy eigenstate of the Hamiltonian of the system. These many body-system energy eigenstates are not equally likely to be occupied and obey the Boltzmann distribution. The average of all these quantum states is called *"ensembles"*. These microscopic system configurations are a snapshot representing the macroscopic thermodynamics of the system. In turn, the ensemble is a considerably large collection of configurations for which the partition function is shaped. There are several ensembles available within the Monte Carlo scheme. The one utilised in this study is the Gibbs Ensemble, proposed by Panagiotopoulos in 1987. Three types of perturbations are performed within this ensemble, ensuring regional, mechanical, and chemical potential equilibration. The following illustrations are of a typical Monte Carlo simulation of a system with two regions of different densities and the

interface between the two regions does not represent a conventional interaction between the two phases.

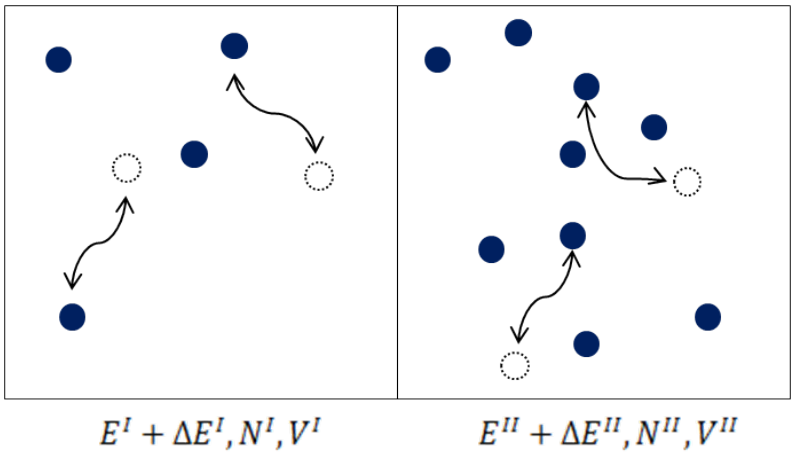

Figure 12. Random displacement within each region

The first type of perturbation considers a system under the *NVT* conditions, where the total number of particles (*N*) and the volume (*V*) are constant and are surrounded by a large bath of constant temperature (*T*). As depicted in Figure 12, this perturbation considers an intra-regional random displacement where a particle may be displaced without any modifications to the volume or the number of particles within the region. The energy in each region is represented by E^I and E^{II} where the energy change ΔE_{min} is the minimum reversible work required for the change, and is given by

$$\Delta E_{min} = \Delta E^I + \Delta E^{II} \qquad (8)$$

Additionally, the probability of accepting the new configuration, otherwise known as acceptance criterion, is given by

$$\mathcal{P} = \min(1, \exp[\Delta E_{min}/k_B T]) \qquad (9)$$

The second perturbation considers a system under the *NPT* conditions, where the total number of particles (*N*) under pressure (*P*) are constant. And similar to the previous perturbation, the system is surrounded by a large bath of constant temperature (*T*). As depicted in Figure 13, this perturbation considers the volume change between the two regions in such a way that the total system volume is constant, where the change in one region is reflected in the equal and opposite change in the other region, and the position of the particles are scaled up to the new volume (Panagiotopoulos, 1987).

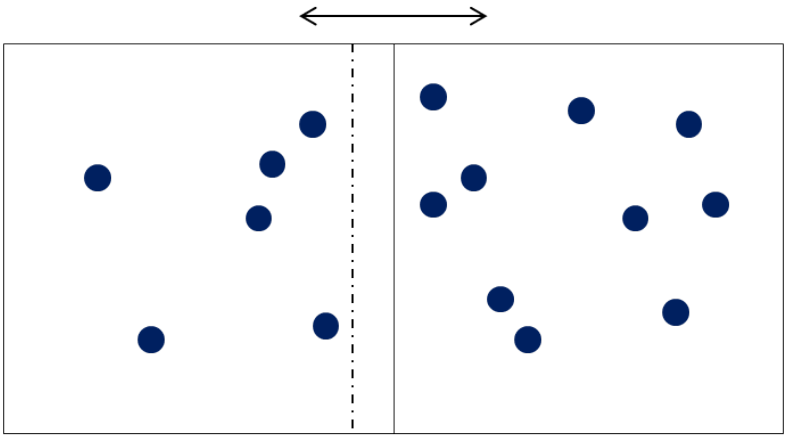

Figure 13. Change in volume of region I is reflected in equal and opposite change in region II

Similarly, the minimum reversible work required to perturb the system is given by:

$$\Delta E_{min} = \Delta E^I + \Delta E^{II} - N^I k_B T \ln \frac{V^I + \Delta V}{V^I} - N^{II} k_B T \ln \frac{V^{II} - \Delta V}{V^{II}} \quad (10)$$

And finally, as shown in Figure 14, the third and final perturbation in this ensemble considers the system under the grand canonical ensemble, μVT. The inter-regional particle insertions are carried out where a particle from one region is

removed and inserted in the other region. This ensures identical chemical potential of all components in both regions. The difference in the system configurational energy is given as:

$$\Delta E_{min} = \Delta E^{I} + \Delta E^{II} + N^{I} k_B T \ln \frac{N^{I}+1}{N^{I}} + N^{II} k_B T \ln \frac{N^{II}-1}{N^{II}} + k_B T \ln \frac{V^{II}}{N^{II}-1} - k_B T \ln \frac{V^{I}}{N^{I}+1} \quad (11)$$

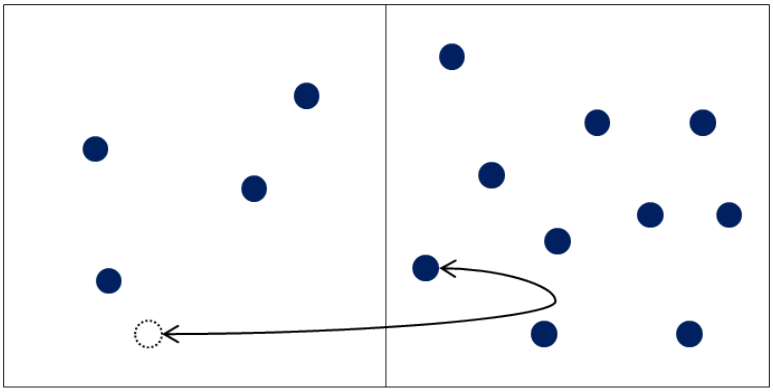

Figure 14. Inter-regional particle insertion

The move is rejected, prior to any calculations, if the minimum displacement is lower than r_{cutoff}, thus improving efficiency of the simulation.

Panagiotopoulos (1987) recommended that the choice of initial number of particles should be chosen in such a way that ensures an adequate number of molecules in each region after equilibrium is reached. The initial densities should not be similar to equilibrium conditions, if it is known. This is to ensure that the results are not affected by the initial conditions (Panagiotopoulos, 1987). Additionally, the acceptance rate for all moves should be 50%, although some authors may use a lower number.

It was observed that the lower the reduced temperature (T_r), the longer the simulation time is needed before equilibration is achieved. Additionally, this is further exaggerated when the system is close to the critical region. The system size dependent is particularly reflected in the results where small systems may not adequately represent the bulk phase. Panagiotopoulos (1987) recommended a minimum of 500 particles in the critical region simulation. Away from the critical region however, it was noted that the systems where each region contained 300 or 500 particles produced nearly identical results. This is formally known as the finite size effect which will be discussed later in this chapter.

2.2. Configurational Bias

Typically the chemical potential in molecular simulation is determined by the Widom insertion approach, applicable to both molecular dynamics and Monte Carlo schemes. Widom insertion method considers a system with N-1 particles with test particles insertion attempted at random. The test particle however does not remain in the system and thus remains unchanged.

Many Widom insertion attempts are required to attain a statistically sound chemical potential average. The Widom insertion approach is adequate for small particles and small systems (Leach, 2001). However, for a system with relative long chain molecules, the Widom insertion approach becomes increasingly inadequate as the density and the size of the molecules and system increases. A successfully inserted molecule must be of both the right shape and sizes, not overlapping itself nor other molecules within the system (Siepmann, 1990).

In 1990, Siepmann proposed a modified Widom insertion technique, configurational bias, to calculate the chemical potential for dense systems with chain molecules.

This novel approach followed the fundamental in equation (12) below where the excess chemical potential is the difference between the ideal gas and that of the actual system. The insertion probability is at the core of the excess chemical potential. By attempting to insert the test particle in the system, where the particle does not remain in the system and thus leaving the it unperturbed, the excess chemical potential of the system can be evaluated (Siepmann, 1990).

$$\mu_{ex} = -k_B T \ln \langle \exp\left(-\frac{V_{test}}{k_B T}\right) \rangle \qquad (12)$$

Where

V_{test}= the change in internal potential energy caused by the insertion attempt

μ_{ex}= excess chemical potential

k_B= Boltzmann constant

T= Temperature

The change in the internal potential energy is given as:

$$V_N = V_{N-1} + V_{test} \qquad (13)$$

Where

V_{test} = internal potential energy change by the attempted insertion

V_N = internal potential energy of N particles system

Following the work of Rosenbluth (Rosenbluth & Rosenbluth, 1955), Siepmann (1990) had devised the insertion evaluation for lattice box as follows:

1. The available space throughout the system under consideration is evaluated, providing it is not occupied by part of the previously inserted test particle.

2. One of these available positions is then chosen at random and the insertion attempt is calculated by the *Rosenbluth weight* as follows:

$$W_m = \frac{n'}{n} W_{m-1} \qquad (14)$$

Where

- n = total number of neighbouring sites
- n' = number of available sites
- W_{m-1} = weight from the previous step where $W_0 = 1$
- The weight, W_m, is zero if there is no site available, thus terminating the insertion evaluation.

Step 1 and 2 are then repeated as required. It should be noted that although this was demonstrated using lattice, application to our system will be modified slightly as the bond angles and other parameters will have to be taken into account.

Siepmann (1990) visualized these steps using Figure 15, where a three-segment molecule is being inserted and grown in a two dimensional lattice configuration. First, we consider the conventional Monte Carlo where the available site is chosen at random, S. From this position, there are four possible sites but only two are available (50%). If B were to be chosen, the procedure will be terminated as the molecule cannot be grown any further. However, if A were to be chosen, the molecule could be grown to its complete segment, ending at C. The overall probability of the successful insertion is 1/12 in this case.

The conventional Monte Carlo approach thus has an acceptance rate of 1/12. The configurational bias approach however favours the complete insertion, hence the 'bias'. This numerical preferential treatment is then removed by the acceptance rule modifications. While the conventional Monte Carlo considers all four possible

sites surrounding S as a valid option, the configurational bias Monte Carlo preferentially considers the two possible sites, A and B.

Following equation (14), the *Rosenbluth weight* is $W_1 = 1/2$. Next, if B were to be chosen, the trial will then be terminated. If A were chosen however, the neighbouring sites will then be considered further, giving the weight of $W_2=1/3 \times ½ = 1/6$. The overall weight is given by the results of all the successful trials, which is $1/2 \times 1/6 = 1/12$. The trial using the configurational bias Monte Carlo favours the successful insertion, favouring site A and C, with a probability of 1/2 in this case. This is a great improvement over the conventional Monte Carlo rate of 1/12.

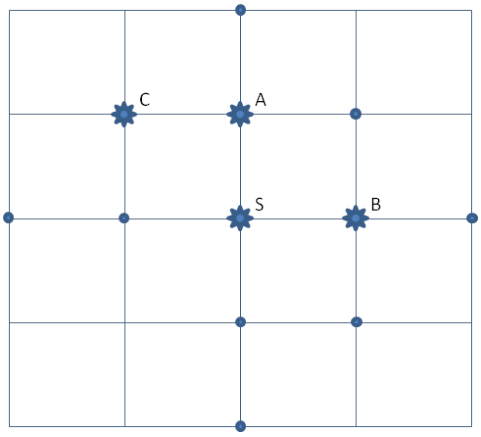

Figure 15. Configurational Biased insertion, the dot represent an occupied site and the star is the available insertion site, redrawn from (Siepmann, 1990)

The efficiency of the configuration bias Monte Carlo is reported to attain as much as 60 times more accepted insertions than the conventional counterpart, in the highest density investigated (Siepmann, 1990). Additionally, the modified Widom insertion also takes less time as many trials with lower probability of success will have been terminated earlier on in the procedure.

Depending on the ensemble and the type of moves utilized in the simulation, the acceptance rule must be modified to remove the aforementioned bias imposed on the system. This is simply to even to odds of particle removal from either box, satisfying the detailed balance, and can be given by

$$\mathcal{N}(o) \times \pi(o \to n) = \mathcal{N}(n) \times \pi(n \to o) \qquad (15)$$

Where

$\mathcal{N}(o)$= Statistical weight of the initial configuration in region *i* with volume V^i

$\pi(i \to j)$ = Transition probability of going from state *i* to *j*

The modified acceptance rule is thus given as (Mooji et al., 1992)

$$acc(o \to n) = min\left(1, \frac{V_I(N - N^I)}{(V - V_I)(N^I + 1)} \frac{W(n)}{W(o)}\right) \qquad (16)$$

where

$acc(o \to n)$= Acceptance probability of the configuration change.

2.3. Force fields

Two distinct approaches are noted when it comes to the potential describing alkanes, Explicit-hydrogen and United-atom. As the name suggests, the Explicit-hydrogen approach considers each C and H atom as an interaction site with individual accompanying parameters. Alternatively, the United-atom model considers a cluster of bonded C and H atoms as a single interaction site, introducing CH_3 and CH_4. The Explicit-Hydrogen model such as the Transferable Potentials for Phase Equilibria – Explicit-hydrogen (TraPPE-EH) is better suited for simulations of solid or higher density liquid phases (Chen & Siepmann, 1999;

Moller et al., 1991; Ryckaert et al., 1989). With a higher computational overhead requirement, a more accurate molecular representation of the alkanes by the Explicit-hydrogen force field gives a better agreement with the experimental results.

While the explicit approach represents a more realistic shape of the alkanes (Rai & Siepmann, 2007), the United-atom approach reduces the number of interaction sites to a third, reducing the required computational overhead by an order of magnitude (Martin & Siepmann, 1998) while maintaining a satisfactory alkanes descriptions.

The investigative results from the study by Martin & Siepmann (1999) of the Optimized Potentials for Liquid Simulation (OPLS), the Siepmann, Karaborni and Smit (SKS), and the Transferable Potential for Phase Equilibria (TraPPE) are compared over a wide range of alkanes and conditions including the descriptions of vapour-liquid equilibrium curves, specific densities and high-pressure equation of state, as well as second virial coefficients (Martin & Siepmann, 1999).

The OPLS was proposed by (Jorgensen et al., 1984). 12 pseudoatoms were proposed from the simulation of 15 liquid alkanes. The force field utilizes a different set of potential parameters for the methyl groups in ethane than that for other *n*-alkanes, ultimately predicting an accurate heat of vapourisation and liquid density profiles for short alkanes at ambient condition (Martin & Siepmann, 1998; Siepmann et al., 1993).

The Transferable Potential for Phase Equilibria (TraPPE) force field is similar to the OPLS in that the potential parameters for the methyl groups were acquired from ethane, however, it is also applied for all other *n*-alkanes (Martin & Siepmann, 1999). TraPPE-UA was developed with a focus on vapour-liquid

equilibrium curves, utilizing four types of pseudo-atoms, which are independent of the neighbouring pseudo-atom (Martin & Siepmann, 1999). All bonds between the pseudo-atoms within the TraPPE-UA are fixed to 1.54Å. Bond bending is described by a harmonic potential given as

$$u_{bend} = \frac{1}{2} k_\theta (\theta - \theta_0)^2 \qquad (17)$$

The SKS force field was parameterized in the Gibbs ensemble particularly designed for the prediction of vapour-liquid equilibrium profile for long *n*-alkanes, C_5 – C_{48} (Smit et al., 1995). Following the Continuum-configurational-bias model proposed by de Pablo (de Pablo et al., 1993) and the observation of Rodriguez where large difference in potential parameters $\epsilon_{CH3} \gg \epsilon_{CH2}$ (Rodriguez et al., 1991, 1993) was proposed. Similarly to the OPLS and the TraPPE, the SKS force field uses different well depth parameter for the methyl and the methylene groups. However, the well width parameter remains the same (Siepmann et al., 1993; Siepmann, 1993). Such large differences in the non-bonded potential parameter are observed in many models including that of (Almarza et al., 1992; de Pablo et al., 1993; Laso et al., 1992; Rodriguez et al., 1993; Siepmann et al., 1993).

The results from Martin & Siepmann (1998) comparison are tabulated in Table 8.

Table 8. United Atom force fields comparison tabulated from (Martin & Siepmann, 1998)

	OPLS	TraPPE	SKS
Vapour-liquid equilibrium curve, T_c, and T_b	Accurate for shorter alkanes. Errors increase with alkane length.	Relatively accurate for the entire range of alkanes tested. Considerably better than both OPLS and SKS.	Overestimates T_c, and T_b. Errors decrease with alkane length.
Specific densities and high-pressure equation of state	N/A	Within 1% of experiment for *n*-octane and *n*-dodecane at STP.	N/A
Second virial coefficients and compressibility factors	Relatively accurate for shorter alkane. Errors increase with alkane length.	Underestimate second virial coefficient for all alkanes.	Relatively accurate for the entire range of alkanes tested.

N/A: Not Available

The comparison between different united atom models for *n*-decane will also be carried out in this study to identify the most suitable force field and ensure accuracy of the study.

2.4. Lennard-Jones potential

This study utilizes the 12-6 Lennard-Jones potential to describe the non-bonded interactions of groups more than three bonds apart. The expression of the 12-6 potential can be written as

$$u(r_{ij}) = 4\epsilon_{ij}\left[\left(\frac{\sigma_{ij}}{r_{ij}}\right)^{12} - \left(\frac{\sigma_{ij}}{r_{ij}}\right)^{6}\right] \qquad (18)$$

Where

r_{ij} = separation between atom *i* and *j*

ϵ_{ij} = potential well depth

σ_{ij} = potential well width where $u(r) = 0$

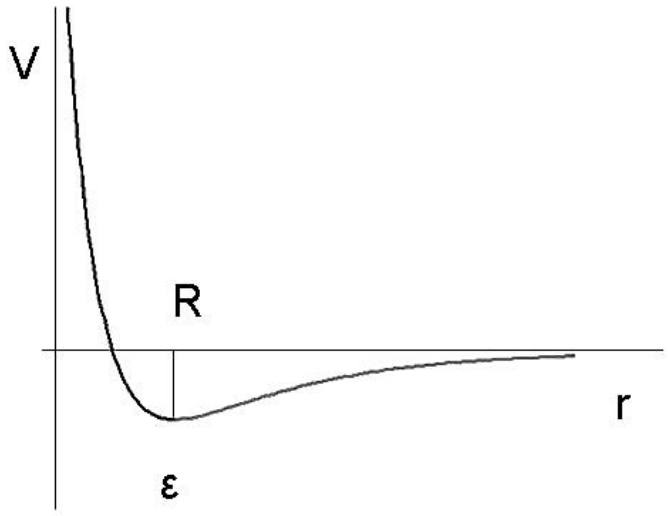

Figure 16. Lennard-Jones interaction potential

The graphical representation of a typical Lennard-Jones interaction potential is as shown in Figure 16.

Although the attractive term is modeled according to the London's Theory (London, 1930), where it varies radially as $\frac{1}{r^6}$, the power of 12 for the repulsive term historically has no theoretical significant. The twelfth power simplifies the calculation by squaring the attractive term. A better description of the interaction can be achieved by varying the exponent of the repulsive term. This is the generalized Lennard-Jones potential known as the Mie potential. However these Mie potentials were not investigated as it was beyond the scope of the objectives of this study. Readers are referred to the 'Truncation of interaction potential' in the Molecular Dynamics chapter for further discussion on the various truncation treatments and applications for the Lennard-Jones potential.

Additionally, Lorentz-Berthelot mixing rules are used to described the unlike interactions. This can be written as:

$$\sigma_{ij} = \frac{1}{2}(\sigma_{ii} + \sigma_{jj}) \qquad (19)$$

$$\epsilon_{ij} = \sqrt{\epsilon_{ii}\epsilon_{jj}} \quad (20)$$

2.5. Henry Coefficient

Amongst other factors, chemical potential increases with the partial pressure of a gas, and thus the more chemically active species in the mixture. Atkins & De Paula (2001) compared this to the loading up of the potential energy in a spring analogy to the increase of the partial pressure of the system, and thus chemical potential, to drive the reactions (Atkins & De Paula, 2001). Following this argument, equilibrium can then be described by the equalization of the chemical potential in all phases.

Raoult's law was observed through the measurement of partial vapour pressure of mixtures which state (Atkins & De Paula, 2001): "*The partial pressure vapour pressure of a substance in a mixture is proportional to its mole fraction in the solution and its vapour pressure when pure.*"

$$p_j = x_j p_j^* \quad (21)$$

Where

p_j^* = vapour pressure of the pure component *j*

x_j = mole fraction of component *j*

This simply means that the vapour pressure of the solvent is lower in a mixture than when it is pure. Additionally, the chemical potential of solvent can be written of the form

$$\mu_j = \mu_j^* + RT \ln x_j \quad (22)$$

Where

μ_j^* = standard chemical potential which is a constant and can be written as

$$\mu_j^* = \mu_j^*(g) + RT \ln p_j^* \quad (23)$$

Where

$\mu_j^*(g)$ = standard chemical potential of gas *j*

Coincidentally, through experimental observation, William Henry found that similar to Raoult's law, partial pressure can be written in terms of mole fraction for solute at infinite dilution. *The vapour pressure of a volatile solute B is proportional to its mole fraction in a solution*

$$p_i = x_i K_i \quad (24)$$

Where

K_i = Henry coefficient chosen so that the slope is tangential to the experimental curve at $x_i = 0$

Virtually identical to the chemical potential of solvent, the chemical potential of solute takes the same form as equation (22) and Henry coefficient replaces the vapour pressure in the standard chemical potential constant in equation (23).

The correlation used to calculate the Henry's coefficient is given as follow (Smith & Van Ness, 1987)

$$K_{1,2}(T,p) = \lim_{x_2 \to 0} \left[\frac{f_2(p,T,x_2)}{x_2} \right] \quad (25)$$

Where

x_2 = Molar fraction in the liquid solution

f_2 = fugacity of the solute (component 2) which is given by

$$f_2(p,T,x_2) = \varphi_2(p,T)y_2 p \quad (26)$$

And

$$\varphi_2(p,T) = \exp\left[\frac{p(B_{22} + y_1^2\delta_{12})}{RT}\right] \quad (27)$$

and

$$\delta_{12} = 2B_{12} - B_{11} - B_{22} \quad (28)$$

Where

φ_2 = fugacity coefficient of component 2

p = the vapor pressure of the saturated solution

y_2 = solute mole fraction in the vapor phase

B_{11} = second virial coefficient of the solvent

B_{12} = solute – solvent crossed second virial coefficient

B_{22} = second virial coefficient of the solute

These virial coefficients are obtained from various sources in the literature (Dymond et al., 1986) (Dymond & Smith, 1980). The author estimated the crossed virial coefficient using the Tsonopolous correlation (Poling et al., 2001).

The partial molar volumes were estimated using the correlation given in Tiepel and Gubbins publications (Tiepel & Gubbins, 1972a, 1972b). Tiepel and Gubbins correlation was proven to be accurate to within 3% for a number of gases in water (Bonifácio et al., 2010).

The Henry's constant at various temperatures can be represented by the equation of the form (Crovetto et al., 1982):

$$K_{1,2}(T, p_1^{sat}) = \sum_{i=0}^{n} \frac{A_i}{T^i} \quad (29)$$

Where

A_i = mixture specific coefficient

Alternatively, an expression of Valentiner type can also be used, which contains logarithmic temperature terms. For instance, (Clarke & Glew, 1966) gave such expression as (Crovetto et al., 1982):

$$K_{2,1}(T, p_1^{sat}) = A_0 + \frac{A_1}{10^{-2}T/K} + A_2 \ln\left(\frac{10^{-2}T}{K}\right) + A_3 \ln\left(\frac{10^{-2}T}{K}\right) + A_4 \ln\left(\frac{10^{-2}T}{K}\right)^2 \quad (30)$$

The fit provided by both equation (29) and (30) are not appreciably different (Crovetto et al., 1982).

From the Monte Carlo simulation, Bonifácio et al. (2010) calculated the Henry's constant using the following correlation:

$$K_{1,2}(T, p) = \lim_{x_2 \to 0}\left[RP\rho_1 \exp\left(\frac{\mu_2^{exc,\infty}}{x_2}\right)\right] \quad (31)$$

where

ρ_1 = density of pure solvent

$\mu_2^{exc,\infty}$ is the excess chemical potential between that of the solute 2 in solvent 1 at infinite dilution and the chemical potential of pure species 2 at the ideal gas state, which is given by:

$$\mu_2^{exc,\infty} = -RT\frac{\left[V \exp\left(\frac{u_{TP}}{k_B T}\right)\right]_{NpT}}{[V]_{NpT}} \quad (32)$$

where

V = volume of solvent in a given configuration

u_{TP} = the interaction energy of the test particle with a configuration of solvent molecules

2.6. Periodic Boundary Conditions

Considering the number of particles applied to a typical molecular simulation in the order of hundreds to a few thousands at most, they alone are hardly sufficient in representing the bulk phases for which they were intended. Particularly, the interactions between a particle and its neighbours may not be captured using only a few hundreds or thousands of particles. This problem can be overcome by the use of *"periodic boundary conditions"* where each particle in the box is duplicated as a ghost particle in the boxes surrounding it, representing a system of infinite size. A simple depiction of the simulated box omnidirectionally surrounded by its ghost image is shown in Figure 17. The position of the particles in the simulated box is duplicated in all other boxes. In the case where a particle leaves the primary simulated box, another in the neighboring box will replace its position.

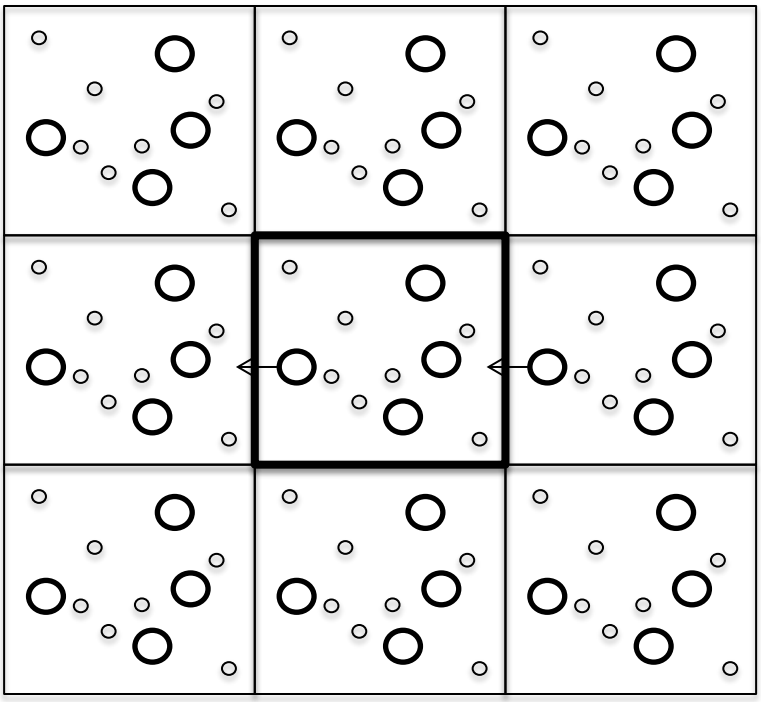

Figure 17. Ghost particles surrounding the system.

2.7. Finite Size Effect

In addition to the periodic boundary conditions, the finite size effect concerns the fact that a system of a finite size may not be adequate in representing bulk phase. While the bulk phases can be simulated by a small number of particles in a typical molecular simulation, with the aid of periodic boundary conditions, the size of these representative systems has been a cause for concerns.

In 1976, Mandell utilized the Born-Green equation to predict the size dependence of pressure and the anisotropy of radial distribution. It was found that the anisotropy of a system of 108 particles is considerably large, exhibiting a strong system size dependence. Although the size dependency of bulk pressure is also observed, they are exceeded by the uncertainty in potential (Mandell, 1976). Mandell noted that in systems much larger than 108 particles are quite adequate to

properly simulate the bulk phase. However, care should be taken where a system with relatively soft cores and long attractive tails are considered. Pratt & Haan (1981) also agree with findings by Mandell, although less system size dependency was observed at higher densities (Pratt & Haan, 1981). Regardless of the liquid under consideration, the bulk pressure is sensitive to the system size when it is small; $L_x < 8\sigma$ (Gonzalez-Melchor et al., 2005). Gonzalez-Melchor et al. recommended a minimum of $L_x = 10\sigma$ where the finite size effect is negligible.

Many other authors also investigated such effects on their systems. (Chen & Siepmann, 1999) briefly investigated the system size effect on their study. While their force field study utilized among the smallest configurations, 120 *n*-pentane molecules, a similar system with 512 *n*-pentane molecules also produced satisfactory comparable results.
(Martin & Siepmann, 1998) also compared the results from two systems of 200 and 1600 *n*-octane molecules to explore the finite size effects in their United Atom force field study. The simulation was carried out over a range of temperatures. Reportedly, the results from the two different system sizes are in agreement and their respective uncertainties. The system sizes implemented in their study for various *n*-alkanes ranged from 128 to 512 particles where the initial density of the liquid phase was doubled that of the gaseous counterpart.

The finite size effect verification has become a staple for atomistic modelling. This verification will also be carried out in this study which will be discussed in later chapter.

2.8. MCCCS TOWHEE

Throughout this study, the Monte Carlo for Complex Chemical Systems (MCCCS) Towhee was used as a Monte Carlo software package. The model was developed by the Siepmann Group at the University of Minnesota in 1994. More information about the simulation software package can be found through (Siepmann et al., 1994).

Chapter Three

Molecular Dynamics Simulation

An alternative to the Monte Carlo simulation is the time evolution study of the system - Molecular Dynamics. The idea behind Molecular Dynamics is that we can study the average behaviour of a many-body system by computing the natural trajectory of the particles. The given quantity of interest is thus a time-averaged result. In evaluating the Boltzmann distribution of the system, Molecular Dynamics utilizes Newton's law of motion which can be written in three dimensions as

$$F_{tot} = m_i \left[\frac{d^2 x_i}{dt^2}, \frac{d^2 y_i}{dt^2}, \frac{d^2 z_i}{dt^2} \right] \tag{5}$$

Where

F_{tot} = Total force acting on the particle

m_i = mass of particle

$\frac{d^2 x_i}{dt^2}, \frac{d^2 y_i}{dt^2}, \frac{d^2 z_i}{dt^2}$ = acceleration in x, y, z direction

The probability that particle i has a given momentum and temperature can be written as (Leach, 2001):

$$p(v_{ix}) = \left(\frac{m_i}{2\pi k_B T} \right)^{\frac{1}{2}} exp\left(-\frac{\frac{1}{2} m_i v_{ix}^2}{k_B T} \right) \tag{6}$$

Where

m_i = mass

v_{ix} = velocity in the x direction

The position, velocity, and force of a given particle is a function of all other particles within the system. Such a complex problem can be solved by breaking it down into smaller manageable sections separated by time steps known as the finite difference approach.

3.1. Finite Difference Approach

By breaking down the motion of particles into small time steps, Δt, we can predict the position and the velocity of each particle in the system by integrating the equation of motion where acceleration, $a(t)$, is the second derivative, and velocity, $v(t)$, is the first derivative of position, $r(t)$, as a function of time. A number of authors have proposed different approaches to integrate the equation of motion including the Verlet algorithm (Verlet, 1967), the Beeman algorithm (Beeman, 1976), and the Leap-frog algorithm (Hockney, 1970). Among many proposals of integration techniques Verlet velocity integration algorithm is one of the most popular, in some ways analogous to the Metropolis importance sampling to Monte Carlo simulation.

Verlet proposed the velocity integration algorithm in 1967 where velocity is not explicitly considered (Verlet, 1967). Rather, the algorithm considers the forward and backward Taylor expansion of the position of particles which can be written as

$$r(t+\Delta t) = r(t) + v(t)\cdot\Delta t + \frac{1}{2!}a(t)\cdot\Delta t^2 + \frac{1}{3!}b(t)\cdot\Delta t^3 + \cdots \tag{7}$$

and

$$r(t-\Delta t) = r(t) - v(t)\cdot\Delta t + \frac{1}{2!}a(t)\cdot\Delta t^2 - \frac{1}{3!}b(t)\cdot\Delta t^3 + \cdots \quad (8)$$

Where

$r(t)$ = position of particle as a function of time

$v(t)$ = velocity, the first derivative of position as a function of time

$a(t)$ = acceleration, the second derivative of position as a function of time

$b(t)$ = the fourth derivative of position as a function of time

The new position of the particle can be determined by adding equation (7) and (8):

$$r(t+\Delta t) = 2r(t) - r(t-\Delta t) + a(t)\cdot\Delta t^2 \quad (9)$$

Additionally, we can also obtain velocity by subtracting equation (7) and (8):

$$v(t) = \frac{r(t+\Delta t) - r(t-\Delta t)}{2\Delta t} + a(t)\cdot\Delta t^2 \quad (10)$$

Once the velocity is obtained, other quantities such as kinetic energy and instantaneous temperature can also be obtained. In particular, the instantaneous temperature at a given time can be written as (Frenkel & Smit, 1996)

$$k_B T(t) = \sum_{i=1}^{N} \frac{m\cdot v_i^2(t)}{N_f} \quad (11)$$

Where

N_f = Degree of freedom = $3N-3$ for system of N spherical particles

It should be pointed out that as velocity is not explicitly considered in the original Verlet approach, the velocity at time t may not be obtained until the position at time $t+\Delta t$ is obtained, as written in equation (10). What is more, it is not self-

starting - the new position of the particle is a function of the two previous time steps. While one can be obtained from the initial condition, the other will have to be obtained by other methods such as the truncation of the Taylor series.

Other modifications such as the Hockney's Leap-frog approach were proposed to circumvent these problems (Hockney, 1970). Proposed in 1970, Hockney used the half time step $\frac{\Delta t}{2}$ between t and Δt where velocity can be explicitly addressed. The position and velocity at this half time step can then be used to calculate that of the next time step which can be written as follow:

$$r(t + \Delta t) = r(t) + v\left(t + \frac{\Delta t}{2}\right)\Delta t \tag{12}$$

And

$$v\left(t + \frac{\Delta t}{2}\right) = v\left(t - \frac{\Delta t}{2}\right) + a(t)\Delta t \tag{13}$$

The velocity and the position expressions are overlapping each other by a half time step, hence Leap-frogging each other, and thus can be used to calculate the respective values for the next time step. It should be noted that the velocities obtained are at the half time step, should the velocities at the full time steps are required, one has to average the values of two half time steps, one full time step apart, as follows:

$$v(t) = \frac{1}{2}\left[v\left(t - \frac{\Delta t}{2}\right) + v\left(t + \frac{\Delta t}{2}\right)\right] \tag{14}$$

Although the Leap-frog algorithm evaluates the velocity explicitly, it still is not self-starting. Other algorithms like the Taylor expansion or the Euler method are

still required to initialize the calculation where the leapfrog algorithm or the original Verlet algorithm can then be used.

3.2. Periodic Boundary Conditions

It is computationally impossible for to model a bulk phase with a very large number of particles in the system. Instead, the representation of the bulk phase is achievable by using the ghost images of the primary box. These ghost images are the exact replica of the primary system under investigation, surrounding it in such a way that if any of the particles leaves the primary box, it is replaced by another from a adjacent box. For further discussions on this topic, readers are referred to the same topic under Monte Carlo simulation.

3.3. Truncation of interaction potential

Truncation is the process of assigning the distance at which the short-range interaction will be considered according to the potential model chosen, in this case, Lennard-Jones potential. Any interaction beyond the assigned cut-off distance (r_c) will be excluded, and thus it is very important to choose this cut-off distance in such a way that the intermolecular interaction beyond r_c is arbitrarily small, otherwise there will be a systematic error in the energy calculation (Frenkel & Smit, 2002). This is of great importance, especially in Molecular Dynamics where energy conservation is required. It is recommended that $r_c \leq \frac{L}{2}$ or $r_c = 2.5\sigma$ for Lennard-Jones fluid (Potoff & Panagiotopoulos, 1998; Smit, 1992), where L is the length of the simulation box. There are a number of truncation techniques available including *Truncation and Shift*, *Simple Truncation* without shift, *Switching Cut-*

off, and *Minimum Image Convention*. Some of these techniques are applicable to one molecular simulation approach but not the other.

The simplest form of truncation is the *Simple Truncation* without shift technique where the potential can be written as

$$\mathcal{U}(r) = \begin{cases} \mathcal{U}(r) & r \leq r_c \\ 0 & r > r_c \end{cases} \tag{15}$$

This truncation technique is not applicable to Molecular Dynamics due to the discontinuity of the potential at $r > r_c$ and energy conservation is of great importance in this molecular simulation approach. However, it can be used in Monte Carlo simulation where the correction to the potential energy is implicative in the tail correction term which is given by (Frenkel & Smit, 2002)

$$\mathcal{U}^{tail}(r) = \frac{8}{2} 4\pi\rho\varepsilon\sigma^3 \left[\frac{1}{3}\left(\frac{\sigma}{r_c}\right)^9 - \left(\frac{\sigma}{r_c}\right)^3\right] \tag{16}$$

On the other hand, *Truncation and Shift* technique is the potential which is predominantly applied to the Molecular Dynamics simulations. The potential in this case can be written as

$$\mathcal{U}^{TS}(r) = \begin{cases} \mathcal{U}(r) - \mathcal{U}(r_c) & r \leq r_c \\ 0 & r > r_c \end{cases} \tag{17}$$

The entire potential is shifted so that the potential at the cut-off distance is zero, thus no discontinuity is observed when compared to the *Simple Truncation* without shift technique. The equilibrium distances however can be decreased slightly when this truncation technique is used (Allen & Tildesley, 1989).

In addition, *Switching Cut-off* is also a valid truncation technique for Molecular Dynamics simulation for large coarsed-grain representation where larger cut-off radius is required. Similar to *Simple Truncation* without shift, the potential is modified at the cut-off radius; the potential is converged to zero within a given interval instead of abruptly cut off.

3.4. Ensembles

The averages of the microscopic system configurations, a snapshot of the macroscopic of the system, are called "ensembles". As in Monte Carlo simulation, there are many ensembles available for Molecular Dynamics simulation. As the canonical ensemble (NVT) is the natural ensemble for Monte Carlo simulation, the microcanonical ensemble (NVE) is the natural ensemble for Molecular Dynamics simulation. This naturally follows as Newton's law of motion conserves energy.
As previously discussed, in the Monte Carlo simulation the observable can be described by the partition function in terms of position of all particles in the system, $\boldsymbol{r}^N$, and their corresponding momenta, $\boldsymbol{p}^N$ as follows:

$$Q = c \int d\boldsymbol{p}^N d\boldsymbol{r}^N exp[-\mathcal{H}(\boldsymbol{p}^N \boldsymbol{r}^N)/k_B T] \tag{18}$$

Where

$\boldsymbol{r}^N$= coordinates of all N particles

$\boldsymbol{p}^N$=corresponding momenta for all N particles

k_B= Boltzmann's constant

$\mathcal{H}(\boldsymbol{r}^N \boldsymbol{p}^N)$= Hamiltonian of the system which is a combination of Kinetic and Potential energy.

c = proportionality constant

Regardless of the ensembles, the Ergodic hypothesis is the fundamental correlation between time-average properties of the ensembles and a physical system, validating the system properties of interest which represent that of the actual physical system. Ergodic hypothesis describes this equality as

$$\langle A \rangle_{time} = \langle A \rangle_{ensemble} \tag{19}$$

Where

$\langle A \rangle$ = average of observable A

Thus, to satisfy this equality, the simulation must generate an adequate number of system manifestations in configurational space.

The time-average of A can be written as

$$\langle A \rangle_{time} = \lim_{\tau \to \infty} \frac{1}{\tau} \int_{t=0}^{\tau} A\,(\boldsymbol{p}^N, \boldsymbol{r}^N) dt = \frac{1}{M} \sum_{t=1}^{M} A(\boldsymbol{p}^N, \boldsymbol{r}^N) \tag{20}$$

Where

$A(\boldsymbol{p}^N, \boldsymbol{r}^N)$ = instantaneous value of A

τ = length of simulation

M = number of time steps of the simulation

And the discrete time step within the simulation $\Delta t = \frac{t}{\tau}$

Similar to the Monte Carlo approach, there are several ensembles available to Molecular Dynamics. These include, but are not limited to, the Grand canonical ensemble, μVT, where chemical potential, volume and temperature bath are kept constant; Microcanonical ensemble, NVE, where the particle number, volume, and total energy are kept constant; and Isothermal-Isobaric ensemble, NPT, where the particle number, pressure, and temperature bath are kept constant. In particular,

the NPT ensemble will be used in this study as the desired pressure and temperature conditions can be specified in this ensemble.
The imposition of temperature and pressure onto the Molecular Dynamics simulation will now be discussed.

3.5. Barostat

As NPT is the primary ensemble used in this study, the pressure must be kept at a desired target. The target pressure can be adjusted by varying the volume. These volume changes can be isotropic, where the overall shape of the simulation box remains constant, or anisotropic, where the shape of the simulation box changes. In turns, the volume fluctuations can be written in terms of isothermal compressibility. Larger isothermal compressibility indicates a more easily compressed system and thus larger volume fluctuations, and vice versa for a slightly compressible substance like liquid H_2O.
There are several approaches available to maintain the pressure at the desirable target including Berendsen (Berendsen et al., 1984), Nosè-Hoover (Hoover, 1985; Nose & Klein, 1983), and Parrinello-Rahman (Parrinello & Rahman, 1981).

The Berendsen barostat is a weak pressure bath coupling, analogous to the temperature bath coupling for thermostat which will later be discussed (Berendsen et al., 1984). A specified length of the simulation box is scaled by a scaling factor λ which is given by the following equation:

$$\lambda = \left[1 - \frac{\kappa \Delta t}{\tau}(P_0 - P)\right]^{\frac{1}{3}} \tag{21}$$

Where

τ = relaxation constant

The scaling factor gives the new coordinates of the system by

$$\boldsymbol{r_i'} = \lambda^{\frac{1}{3}}\boldsymbol{r'} \tag{22}$$

This study utilizes the Berendsen barostat and thermostat which gives realistic temperature and pressure fluctuations (Berendsen et al., 1984).

3.6. Thermostat

The probability distribution of velocity is given in terms of Boltzmann distribution in Equation (6). The average kinetic energy per degree of freedom can be written as

$$\langle \frac{m_i v_{ij}^2}{2} \rangle = \frac{1}{2} k_B T \tag{23}$$

Where

v_{ij} = velocity of particle i, in $j = (x, y, z)$ direction

This is the same distribution used to assign the initial conditions to the system. The instantaneous can then be calculated by Equation (11). $T(t) = \langle T \rangle$ as $t \to \infty$ or for a sufficient long time.

Once the system is initiated, the temperature fluctuates as a result of round-off error and potential truncations during the integration. To obtain the desire temperature, we must apply some mathematical manipulations to the system. The simplest form of temperature control is the velocity scaling where all velocities are rescaled as follows

$$v_{ij}' = \sqrt{\frac{T}{T(t)}} \cdot v_{ij} \tag{24}$$

While its implementation is straightforward, it is not time reversible and thus only suitable for earlier in the simulation period.
Other widely use temperature control mechanisms include, but are not limited to, Nosè-Hoover, Langevin, and Berendsen.

Berendsen temperature control was designed as a weak temperature coupling similar to external bath in a physical experiment (Berendsen et al., 1984). The energy is added or removed from the system to maintain temperature as exponential decay function where the desired temperature is finally reached as follows

$$\frac{dT(t)}{dt} = \frac{1}{\tau}(T_0 - T(t)) \tag{25}$$

Where

τ = coupling parameter determining the strength of the coupling

T_0= target temperature

If $T_0 > T(t)$, energy will be added to increase the temperature and vice versa. The change in the kinetic energy can be written as

$$\Delta E = \frac{1}{2}\left(\sum_{i,j}(m_i v_{ij}'^2 - m_i v_{ij}^2)\right) = (\lambda^2 - 1)\frac{3Nk_BT}{2} \tag{26}$$

Subsequently, the velocities are scaled using the scaling factor where (Leach, 2001)

$$\lambda^2 = 1 + \frac{\Delta t}{\tau}\left(\frac{T_0}{T} - 1\right) \tag{27}$$

The Berendsen heat bath coupling approach can be viewed as a friction term which is added to the Newton equation, $-\gamma mv$, where γ is conveniently given by

$$\gamma = \frac{1}{\tau}\left(\frac{T_0}{T} - 1\right) \tag{28}$$

Berendsen weak heat bath coupling was the temperature control used in this study. The temperature response of various thermostats applied to a Lennard-Jones fluid can be observed in Figure 18. The Nosè-Hoover algorithm introduces wild fluctuation in temperature prior to equilibration, and thus is not suitable for early time in a simulation.

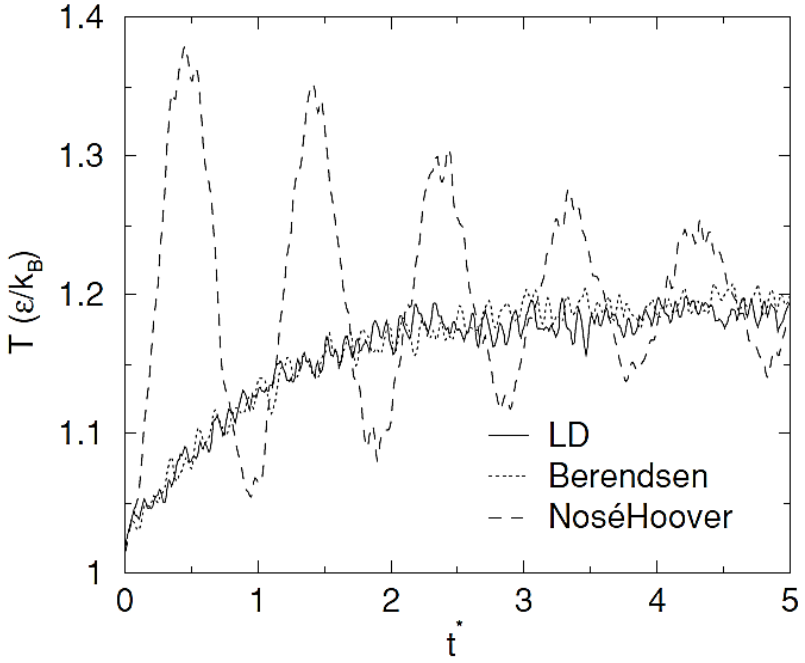

Figure 18. Temperature response of various thermostat of a Lennard-Jones fluid (Van Der Spoel et al., 2005)

3.7. Force fields

For continuity of the research, force fields used in the Monte Carlo simulation were converted and used in the Molecular Dynamics simulation. The intermolecular potential in both simulation approaches are described in the force fields discussions of Monte Carlo simulation. Furthermore, to ensure the reproducibility and accuracy of the results from both simulation approaches, the density profiles from various components in this study were also compared and discussed which will be exhibited in later chapters.

3.8. Diffusion coefficient

The diffusion coefficient is represented by the proportionality constant in Fick's law where a non-uniform solute concentration is smoothed out in absence of flow and can be written as (Frenkel & Smit, 2002)

$$\bar{J} = -D\nabla c \tag{29}$$

Where

$\bar{J}$ = flux of the diffusing species

D = diffusion coefficient

∇c = concentration gradient of diffusing species

Combining the Fick's law with the conservation of particles, we can obtain the

$$\frac{\partial}{\partial t} c\,(r,t) = D\nabla^2 c\,(r,t) \tag{30}$$

Where

$c\,(r,t)$ = distribution of probability of finding solute in the vicinity r at time t.

Equation (30) is a linear equation which can be solved with boundary and initial conditions via Green's function techniques

$$c\,(r,t) = \frac{\exp(-\frac{r^2}{4Dt})}{(4\,\pi Dt)^{\frac{d}{2}}} \tag{31}$$

Where

d = dimensionality of the system

Rewriting equation (30) in terms of time dependence element $\langle r^2(t)\rangle$ and multiplied by r^2, we have

$$\frac{\partial}{\partial t}\int d\boldsymbol{r}\, r^2 c(r,t) = D\int d\boldsymbol{r}\, r^2\, \nabla^2 c(r,t) \tag{32}$$

Where

$$\langle r^2(t)\rangle \equiv \int d\boldsymbol{r}\, c(r,t)\, r^2 \tag{33}$$

And

$$\int d\boldsymbol{r}\, c(r,t) = 1 \tag{34}$$

We have

$$\frac{\partial}{\partial t}\langle r^2(t)\rangle = D\int d\boldsymbol{r} r^2\nabla^2 c(r,t) = 2dD \tag{35}$$

For d = 3, as per usual molecular dynamics simulation, we have

$$\lim_{t\to\infty}\langle\left|\left|r_i(t) - r_i(0)\right|\right|^2\rangle_{i\in A} = 6Dt \tag{36}$$

Where

r_i = position of particle

Equation (36) implies that the diffusion coefficient can be calculated by the mean squared displacement, MSD, of the diffusing particle during time, t. As $t \to \infty$, D can be accurately determined as it approaches the asymptotic behavior where, for a three dimension system, it is 1/6 of the slope of the MSD and time step, generally achievable within 3-5 nanoseconds time frame. This calculation is known as the *Einstein relation*.

Additionally, D can also be calculated by the velocity autocorrelation function $[v_i(t) \cdot v_i(0)]_{i \in A}$ via the *Green-Kubo relation* as follow

$$D = \frac{1}{3}\int_0^\infty [v_i(t) \cdot v_i(0)]_{i \in A}\, dt \tag{37}$$

Where

v_i = velocity of particle

The Green-Kubo relation evaluates the velocity autocorrelation function, an equilibrium property, at two different reference time steps. Although the auto correlation function is believed to be faster than the mean square displacement approach, it is further complicated by the contribution of the long-time tails which do not decay exponentially as $t \to \infty$ (Allen & Tildesley, 1989; Spoel et al., 2013).

The diffusion coefficient can also be written in terms of friction coefficient, ξ, in the Einstein-Smoluchowski equation.

$$D = \frac{kT}{\xi} \tag{38}$$

Where

ξ = friction coefficient which is described by the sizes and shapes of the particles in the system

Other approaches for the evaluation of diffusion coefficient are also proposed by a number of authors (Krynicki et al., 1978; Rah et al., 2002; Yoshida et al., 2007).

3.9. Hydrodynamic model

Another well-known hydrodynamic relationship has also been used to calculate diffusion coefficient. A number of authors proposed different correlations in terms of friction coefficient, ξ (Krynicki et al., 1978; Rah et al., 2002; Yoshida et al., 2007). These modified Stoke-Einstein relation can be described by a general form as

$$D = \frac{kT}{\xi} = \frac{kT}{f\pi\eta R} \tag{39}$$

Where

η = Viscosity

R = Hydrodynamic radius

k = Boltzmann constant

ξ = Friction coefficient which is described by the sizes and shapes of the particles in the system

f = Numerical constant of the boundary condition depending on relative size of solute and solvent

The special case of this relation is notably when the relative size of the solute and solvent are similar, *slipping boundary limit*, the proportionality constant $f = 4$. Additionally when the relative size of the solvent is much smaller than that of the solute, *sticking boundary limit*, $f = 6$, and equation (39) reduces to the Stoke-Einstein equation.

Many accurate correlations are based on the free-volume model (Wang & Hou, 2011). The free-volume model considers the friction coefficient in terms of the minimum volume, free volume, and intermolecular potential, where diffusion only occurs when minimum volume is satisfied. Other similar semi-empirical approaches with integration of transition state theory have also been explored by (Adams et al., 1989; Frank et al., 1996).

Chapter Four

ECLIPSE Equation of State integration

This section will explain the theory and technical calculation procedure as well as various input parameters used in reservoir modelling, ECLIPSE 100 black oil model, a part of the Schlumberger software package (Schlumberger, 2008.2).

4.1. Darcy's Law

One of the fundamental laws for reservoir engineering is Darcy's Law which predicts the Newtonian fluid flow in porous media up to a certain range of flow rates; deviations are observed at high flow rates (Chen et al., 2006). Darcy noted the volumetric flow rate as a function of dimension of porous medium and the difference in hydraulic head. A simple form of Darcy's Law may be written as:

$$Q = KA\left[\frac{dh}{dl}\right] \quad (40)$$

where

$Q =$ Volumetric flow [m^3/s]

K = Hydraulic conductivity (dependent of size, arrangement of pores, fluid dynamics such as viscosity, density and gravitational effects)

$A =$ Cross sectional area [m^2]

l = Length of the porous medium [m]

$dh/_{dl} =$ Hydraulic gradient

This equation is later modified to describe reservoir fluid, oil, and gas (Satter et al., 2008b)

$$v = \frac{q}{A} = -\frac{k}{\mu}\left[\frac{\partial P}{\partial L} - 0.433\,\gamma\,cos\,\alpha\right] \quad (41)$$

where

ν = apparent fluid velocity

q = Darcy's flux where $q = \frac{Q}{A}$

A = cross sectional area of flow [m^2]

k = permeability of a porous medium [md]

μ = fluid viscosity [Pa.s]

$\frac{\partial P}{\partial L}$ = pressure gradient

α = angle of dip measured counter-clockwise between the vertical direction downward and the inclined place of the fluid flow

γ = fluid specific gravity [API]

From the Darcy's Law and its modification, Equation (40) and (41), the following implications can be drawn (Satter et al., 2008a)

1. In porous medium, the fluid is driven in the direction of the least pressure, i.e. the producing well.
2. Better volumetric flow rate, and thus the recovery can be observed in a reservoir with higher permeability.
3. As the flow rate is a function of inverse of viscosity, the fluid with higher viscosity will exhibit a lower volumetric flow rate. e.g. oil has higher viscosity, therefore will exhibit a lower flow rate than that of water.
4. As materials: oil, gas, and water, are removed from a given reservoir, pressure gradient decreases to uphold equilibrium within the reservoir (Satter et al., 2008a). The consequences may include liberation of dissolved gas and many other series of desire and undesired effects.

4.2. Permeability: K

Permeability is a measurement of the ability, through its entire saturated medium, to transmit fluid (Donnez, 2007). It is effectively the proportionality constant in Darcy's Law. It has a typical unit of millidarcy (md), as 1 Darcy is a relatively high permeability.

4.3. Porosity: ∅

Rock porosity is a storage capacity. Mathematically, it is the unitless ratio of pore volume to the total bulk volume.

$$\emptyset = \frac{\text{pore volume}}{\text{bulk volume}} \quad (42)$$

Different pore spaces are formed during the geological time of the rock. Some pores are interconnected and others are isolated. This essentially produces two different types porosity: absolute porosity and effective porosity.

Absolute porosity is the ratio of total pore volume to the total bulk volume. Absolute porosity can be determined by comparing the volume difference when the rock sample is crushed.

$$\emptyset_a = \frac{\text{total pore volume}}{\text{bulk volume}} \quad (43)$$

Effective porosity is the ratio of the accessible pore volume to the total bulk volume.

$$\emptyset = \frac{\text{interconnected pore volume}}{\text{bulk volume}} \quad (44)$$

Effective porosity can be determined by weighting the saturated rock sample and note the difference from the dry sample. The density of the fluid used must be known, in order to make an accurate estimation.

4.4. Formation volume factors, B

B is the ratio of the volume of the considered phase (usually oil or gas) at a given temperature and pressure, often at reservoirs conditions, to that at standard conditions. The standard conditions are usually at 100kPa and 289K. The unit of B is reservoir barrels/stock tank barrels (rb/stb) for oil and reservoir barrels/standard cubic feet (rb/scf) for gas. B_o is used to denote oil formation volume factor which is given by

$$B_o = \frac{V_o(p,t)}{V_o(std)} \quad (45)$$

Where

$V_o(p,t)$ = volume of oil at given pressure and temperature

$V_o(std)$ = volume of oil at standard conditions

Similarly, B_g is used to denote gas formation volume factor which is given by

$$B_g = \frac{V_g(p,t)}{V_g(std)} \quad (46)$$

Where

$V_g(p,t)$ = volume of oil at given pressure and temperature

$V_g(std)$ = volume of oil at standard conditions

B_g is often small and is thus often reported in units of reservoir barrels/thousand standard cubic feet (rb/Mscf). For a single phase system, the formation volume factor can be written in terms of density as (Donnez, 2007).

$$B_n = \frac{\rho_s}{\rho} \quad (47)$$

Where

n = denotes the phase consider

ρ_s = density at standard conditions

ρ = density at the given conditions

4.5. Solution Gas-Oil Ratio, Rs

Slightly different from the formation volume factor (B) the solution gas oil ratio describes the ratio of the volume of gas dissolved in a given volume of oil at standard condition at 100 kPa and 273.15 K. This is written as

$$R_s = \frac{V_g(std)}{V_o(std)} \quad (48)$$

Where

$V_g(std)$ = volume of gas at standard conditions

$V_o(std)$ = volume of oil at standard conditions

R_s is given in the field unit of scf/bbl (standard cubic feet/barrel)

However, there is a pressure limit where gas could not be further dissolved called the 'bubble-point pressure' or 'saturation pressure'. Figure 19 shows the typical plots of bubble-point pressure relative to formation volume factor, viscosity, and solution gas-oil ratio.

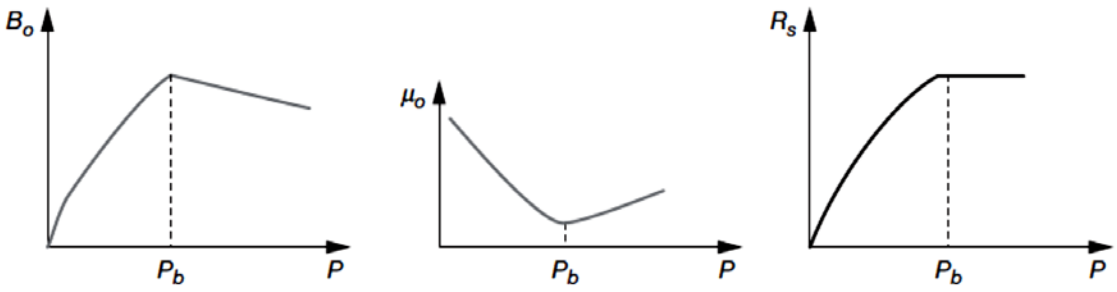

Figure 19. typical plots of formation volume factor, B_o, viscosity, μ_o, and solution gas-oil ratio, R_s (Donnez, 2007).

4.6. Bubble-point pressure, Pb, and Dew-point pressure, Pd

Bubble-point pressure (P_b) is the pressure where the first bubble appears as dissolved gas is liberated from the fluid. It is a strong function of gas-oil ratio (R_s), oil gravity (API), gas gravity (γ_g), and temperature (Ahmed, 2006). On the other hand, the Dew-point pressure (P_d) is the pressure where the liberated gas condenses and forms droplets. This is best illustrated in Figure 20. Point 4 represents the reservoir pressure which can reduce quickly during a production process, reaching the bubble-point and dew-point pressure. In a pure-component system, the bubble-point and dew-point pressure are the same (Ahmed, 2006).

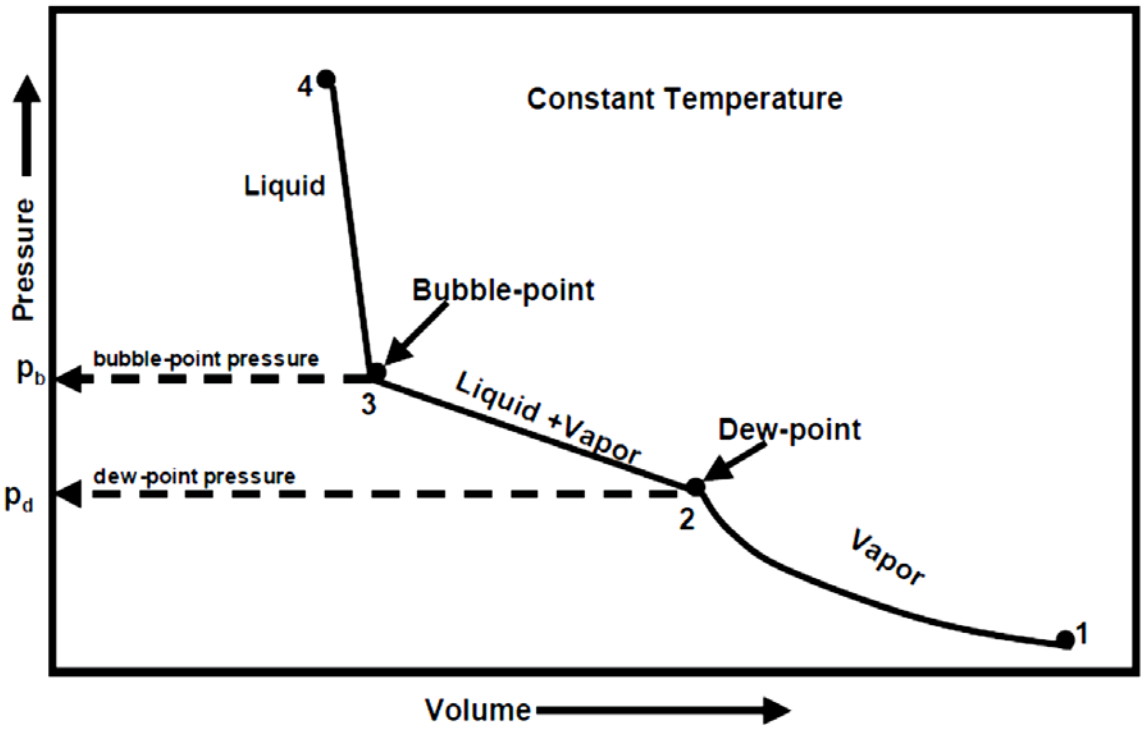

Figure 20. bubble-point and dew-point of a two component system in terms of volume (Ahmed, 2006)

4.7. Transmissibility

Transmissibility is a quantitative quality made up of viscosity, permeability, and thickness. It is an expression derived from Darcy's Law. Transmissibility of phase l is given by (Donnez, 2007):

$$T_l = \frac{k \times k_{rl}}{\mu_l \times B_l} \qquad (49)$$

Where

$k =$ Absolute permeability [md]

k_{rl} = Relative permeability of fluid [md]

μ_l = Fluid viscosity [Pa.s]

B_l = Fluid formation volume factor

To solve the partial differential equations describing the fluid flow, a reservoir simulation discretizes a large reservoir into cubic blocks of manageable sizes. The transmissibility is then measured between two neighbouring blocks by applying Darcy's law between the two centroids.

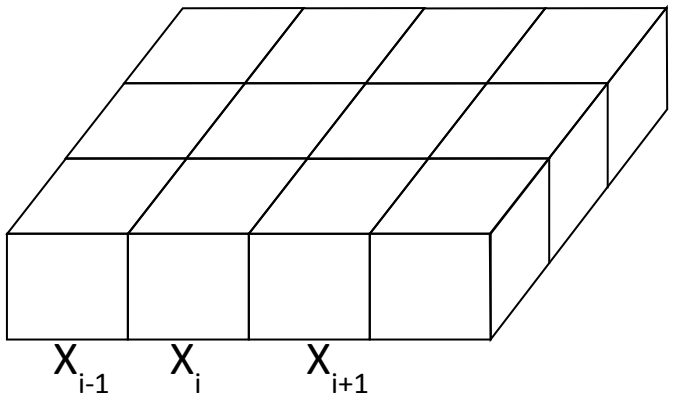

Figure 21. Reservoir representation

The distance fluid has to travel is reduced to two instances, from one centroid of one block to the interface, and from this interface to the centroid of the neighbouring block. This can be written as (Donnez, 2007):

$$T_i = k_i + \frac{\Delta y \times \Delta z}{\frac{\Delta x_i}{2}} \quad (50)$$

Where

T_i = transmissibility for block i

For the distance from the centroid to the shared interface, and

$$T_{i+1} = k_i + \frac{\Delta y \times \Delta z}{\frac{\Delta x_{i+1}}{2}} \quad (51)$$

For the distance from the shared interface to the centroid of the neighbouring block, absolute permeability is used in the calculation to circumvent the transmissibility dependency on the fluids. Similar to the parallel resistors in a circuit, the resistance to flow, $\frac{1}{T_{i,i+1}}$, is given by (Donnez, 2007)

$$\frac{1}{T_{i,i+1}} = \frac{1}{T_i} + \frac{1}{T_{i+1}} = \frac{T_i \times T_{i+1}}{T_i + T_{i+1}} \quad (52)$$

Where

T_i: Transmissibility from the centroid to the block interface

T_{i+1}: Transmissibility from the interface to the neighbouring block centroid

$T_{i,i+1}$: Transmissibility at block interface connection

4.8. Diffusive flow calculation

The gas-in-oil diffusive flow correlation is given by

$$F_{go} = \frac{MW_g \cdot J_g \cdot A \cdot \phi}{\rho_g} \quad (53)$$

Where

MW_g = molecular weight of gas

J_g = molar flux of gas per unit area

A = area of flow

ϕ = porosity

ρ_g = surface density of gas

And the diffusion coefficient correlation is given by

$$J_g = -c_0 \cdot D_{go} \cdot \frac{dx_g}{dl} \quad (54)$$

Where

c_0 = total molar concentration of the gas phase

$\frac{dx_g}{dl}$ = mole fraction gradient of gas

D_{go} = gas-in-oil diffusion coefficient

4.9. Finite difference method

Similar to the concept of Molecular Dynamics, only a few simple partial differential equations can be solved analytically. Larger more complex differential problems can be solved by utilizing an adequate approximation method. To obtain a solution, the partial differential equation is replaced by its approximate finite-

difference counterpart and then Taylor expanded and solved. A simple first order partial differential function can be written as

$$\frac{\partial f}{\partial x} = \lim_{h \to 0} \frac{f(x+h) - f(x)}{h} \qquad (55)$$

Taylor expansion gives

$$\mathrm{f(x+h)} = f(x) + h\frac{df}{dx} + \frac{h^2}{2!}\frac{d^2f}{dx^2} + \frac{h^3}{3!}\frac{d^3f}{dx^3} + \cdots \qquad (56)$$

Rearranging for $\frac{df}{dx}$

$$\frac{df}{dx} = \frac{f(x+h) - f(x)}{h} - \frac{h}{2!}\frac{d^2f}{dx^2} \qquad (57)$$

And

$$\mathrm{f(x-h)} = f(x) - h\frac{df}{dx} + \frac{h^2}{2!}\frac{d^2f}{dx^2} - \frac{h^3}{3!}\frac{d^3f}{dx^3} + \cdots \qquad (58)$$

Therefore

$$f(x+h) - f(x-h) = 2h\frac{df}{dx} + 2\frac{h^3}{3!}\frac{d^3f}{dx^3} + \cdots \qquad (59)$$

Neglecting the second term and the truncation in the order of h is introduced as follows

$\Delta f = f(x+h) - f(x)$ ---------- Forward difference

$\Delta f = f(x) - f(x-h)$ ---------- Backward difference

$\Delta f = f\left(x + \frac{h}{2}\right) - f(x - \frac{h}{2})$ ---------- Central difference

The second derivative for the Taylor expansion can be obtained from

$$f(x+h) - f(x-h) = 2f(x) + h^2 \frac{d^2f}{dx^2} + 2\frac{h^4}{4!}\frac{d^4f}{dx^4} + \cdots \quad (60)$$

Therefore

$$\frac{d^2f}{dx^2} = \frac{f(x+h) - 2f(x) + f(x-h)}{h^2} - 2\frac{h^4}{4!}\frac{d^4f}{dx^4} \quad (61)$$

4.10. Single-Phase and Multiphase Fluid Flow Equations

The more simple single-phase flow through a porous media equation can be derived by employing:

1. The conservation of mass
2. Darcy's rate equation to relates velocity to pressure gradient
3. Equation of state to express the density in pressure terms

The fundamental step in the derivation is the conservation of mass which is given by

$$Mass\ rate\ in - Mass\ rate\ out = Mass\ rate\ of\ accumulation$$

$$(v_x\ \rho_x\ \Delta y\ \Delta z) - (v_{x+\Delta x}\ \rho_{x+\Delta x}\ \Delta y\ \Delta z) = (\Delta x\ \Delta y\ \Delta z)\emptyset\frac{(\rho_{t+\Delta t} - \rho_t)}{\Delta t} \quad (62)$$

Dividing by $\Delta x\ \Delta y\ \Delta z$

$$\frac{(v_{x+\Delta x}\ \rho_{x+\Delta x}) - (v_x\ \rho_x)}{\Delta x} = \frac{\emptyset(\rho_{t+\Delta t} - \rho_t)}{\Delta t} \quad (63)$$

Where

ρ = density

v = velocity

$\emptyset$ = porosity

Taking the limit as $\begin{Bmatrix}\Delta x\\ \Delta t\end{Bmatrix}$ approach zero simultaneously

$$\frac{\partial(v\rho)}{\partial x} = -\emptyset\frac{\partial\rho}{\partial t} \quad (64)$$

Then for three-dimensional flow, this can be written as

$$\frac{\partial(v\rho)}{\partial x} + \frac{\partial(v\rho)}{\partial y} + \frac{\partial(v\rho)}{\partial z} = -\emptyset\frac{\partial\rho}{\partial t} \quad (65)$$

This is the continuity equation for the linear system and can also be written as:

$$-\nabla\cdot(\rho_n\boldsymbol{\nu_n}) = \frac{\partial}{\partial \mathrm{t}}(\phi\rho_n S_n) \quad (66)$$

Where

Subscript n denote the fluid phase of oil, water, or gas

S_n = Fluid saturation

ρ_n = Density of the n phase

$\emptyset$ = Porosity

The Darcy's rate equation is now introduced to relate the velocity to the pressure gradient

$$v = -\frac{k}{\mu}\frac{\partial \mathrm{P}}{\partial x} \quad (67)$$

Also, the Darcy's equation for each phase flow can be written as

$$\boldsymbol{v_n} = -\nabla \cdot P_n \frac{k k_{rn}}{\mu_n} \quad (68)$$

Where

subscript n denotes the fluid phase of oil, water, or gas

k = Absolute permeability (md)

k_{rn} = Relative permeability of fluid (md)

μ_n = Fluid viscosity (Pa.s)

L = Length of the porous medium

The equation of state is required here to express density in terms of pressure (Kutasov, 1989)

$$\rho = \rho_0 e^{c(P-P_0)} \quad (69)$$

Where

ρ = Density at P

ρ_0 = Density at P_0

C is the isothermal compressibility which can be defined as

$$C \equiv -\frac{1}{V}\left(\frac{dV}{dP}\right)_T \quad (70)$$

Via simple substitution and chain rule

$$\left(\frac{k}{\mu}\frac{\partial^2 \mathrm{P}}{\partial x^2}\rho + \frac{k}{\mu}\frac{\partial \rho}{\partial \mathrm{P}}\left(\frac{\partial \mathrm{P}}{\partial x}\right)^2\right) = \emptyset \frac{\partial \rho}{\partial \mathrm{P}}\frac{\partial \mathrm{P}}{\partial \mathrm{t}} \quad (71)$$

Assuming small pressure gradient, $\left(\frac{\partial \mathrm{P}}{\partial x}\right)^2$ is neglected

And the compressibility in terms of pressure and density can be written as

$$C = \frac{1}{\rho}\frac{\partial \rho}{\partial P} \quad (72)$$

Thus

$$\frac{k}{\mu}\frac{\partial^2 \mathrm{P}}{\partial x^2} = \emptyset \mathrm{C}\frac{\partial \mathrm{P}}{\partial \mathrm{t}} \quad (73)$$

If $\frac{k}{\mu}$ is considered independent of spatial dimension (Crichlow, 1977)

$$\frac{\partial^2 \mathrm{P}}{\partial x^2} = \frac{\emptyset \mathrm{C} k}{\mu}\frac{\partial \mathrm{P}}{\partial \mathrm{t}} \quad (74)$$

This equation is generally known as the diffusivity equation due to its resemblance to the heat transfer diffusivity (Crichlow, 1977).

If $\frac{k}{\mu}$ is a function of the spatial dimension (Crichlow, 1977)

$$\frac{\partial\left(\frac{k}{\mu}\frac{\partial \mathrm{P}}{\partial \mathrm{t}}\right)}{\partial x} = \emptyset \mathrm{C}\frac{\partial \mathrm{P}}{\partial \mathrm{t}} \quad (75)$$

Similarly to the single-phase flow equation, the multiphase flow equation can also be derived and written as follows.

Flow equation for oil can then be written as

$$\frac{\partial}{\partial \mathrm{L}}\left[\frac{k k_{ro}}{\mathrm{B}_o \mu_o}\frac{\partial P_o}{\partial \mathrm{L}}\right] - \mathrm{q}'_{\mathrm{o}} = \frac{\partial}{\partial \mathrm{t}}\left[\frac{\phi S_o}{\mathrm{B}_o}\right] \quad (76)$$

Transport of oil – well potential = accumulation of oil

Flow equation for water can then be written as

$$\frac{\partial}{\partial \mathrm{L}}\left[\frac{k k_{rw}}{\mathrm{B}_w \mu_w}\frac{\partial P_w}{\partial \mathrm{L}}\right] - \mathrm{q}'_{\mathrm{w}} = \frac{\partial}{\partial \mathrm{t}}\left[\frac{\phi S_w}{\mathrm{B}_w}\right] \quad (77)$$

Transport of water – well potential = accumulation of water

Flow equation for gas is slightly more complicated due to the terms describing free gas as well as dissolved gas. It can be written as

$$\frac{\partial}{\partial \mathrm{L}}\left[\frac{kk_{rg}}{\mathrm{B}_g\mu_g}\frac{\partial P_g}{\partial \mathrm{L}}+\mathrm{R_{so}}\frac{kk_{ro}}{\mathrm{B}_o\mu_o}\frac{\partial P_o}{\partial \mathrm{L}}\right]-\mathrm{q'_g}-\mathrm{R_{so}q'_o} = \frac{\partial}{\partial \mathrm{t}}\left[\frac{\phi S_g}{\mathrm{B}_g}+\mathrm{R_{so}}\frac{\phi S_o}{\mathrm{B}_o}\right] \quad (78)$$

[Transport of free gas + Transport of dissolved gas] – Free gas well potential – Dissolved gas well potential = accumulation of free gas + accumulation of dissolved gas

Where

o, g, w= oil, gas, and water respectively

k = Absolute permeability (md)

k_{rn} = Relative permeability of fluid (md)

μ_n = Fluid viscosity (Pa.s)

L = Length of the porous medium

B = Formation volume factor

q' = flow rate

4.11. Black Oil Model

The black oil system is made up of two major components: pseudo surface gas and pseudo surface dead oil, both of which possess a fixed composition. Gas reservoirs with fixed fluid composition, independent of pressure, can also be treated as dead oil systems.

It is the discretization of the space and time into grid block and time step, allowing the partial differential equation to be solved as discussed above. The discretization can be achieved by performing a mass balance on the system as follow (Donnez, 2007)

Mass accumulation rate = Mass exchange between block + Production and/or Injection

$$\sum_{e} T_{i,e}\left[\frac{k_{rn}}{\mu_n}\rho_n\right](\phi_{ne}-\phi_{ni})+\delta(i)q_n=\frac{\Delta m_n}{\Delta t} \quad (79)$$

Where

$T_{i,e}$ = Connection value for block i with its neighbours

$k_{rn}, \mu_n =$ Relative permeability and viscosity of the respective phase

$\phi_{ne}-\phi_{ni}$ = Potential different between exterior block e and i

Δm_n = Mass exchange during the time step in cell i

ρ_n = Density of the n phase

$\delta(i)$ = Dirac delta function. Set equal to 0 for production and 1 for injection rate from well perforation

Subscript n denotes the 3 phases considered: water, dead oil, and pseudo gas.

With pseudo gas however the potential difference from the solution gas and free gas has to be taken into account as follow (Donnez, 2007)

$$\sum_{e} T_{i,e}\left[\frac{k_{rL}}{\mu_L}\rho_{DG}\right](\phi_{Le}-\phi_{Li})+\frac{k_{rG}}{\mu_G}\rho_G(\phi_{Ge}-\phi_{Gi})+\delta(i)(q_{DG}+q_G)=\frac{\Delta m_{DG}+\Delta m_G}{\Delta t} \quad (80)$$

Where

subscript G and DG denote free gas and dissolved gas.

$\phi_{Le} - \phi_{Li}$ = Potential difference between exterior block e and i for liquid phase

$\phi_{Ge} - \phi_{Gi}$ = Potential difference between exterior block e and i for gas phase

In a black oil system modelling, three phases are considered: water, gas, and oil. There are several approaches to tackle the reservoir modelling problem. Listed below are the methods used in ECLIPSE and these will be subsequently discussed.

- Fully Implicit Algorithm
- Implicit Pressure Explicit Saturation (IMPES)

Each of these algorithms offers different advantages and disadvantages.

4.12. Fully Implicit Algorithm

All primary terms are evaluated simultaneously at the end of the time step. This fully implicit procedure offers a highly stable algorithm, allowing a longer time step to be evaluated. However, it requires large computing power compared to other algorithms, as will be subsequently discussed in the appendix, and thus more suitable for smaller problems.

For each block in the model, there is one error R_i associated with each phase, water, gas, and oil, forming a vector $\begin{bmatrix} R_w \\ R_g \\ R_o \end{bmatrix}_i$ (Donnez, 2007).

$$R_n = \frac{\Delta m_n}{\Delta t} - \delta(i) q_n - \sum_e T_{i,e} \left[\frac{k_{rn}}{\mu_n} \rho_n \right] (\phi_{ne} - \phi_{ni}) \quad (81)$$

The solution is obtained when

$$R(X) = 0$$

This is achieved using the Newton iteration.

4.13. Implicit Pressure Explicit Saturation (IMPES)

An alternative to the fully implicit algorithm is, as the name implies, Implicit Pressure Explicit Saturation algorithm. It is the preferred method in the industry, especially for slightly compressible and incompressible fluids (Chen, 2007). It was originally proposed by Sheldon et al. (1959) where the pressure terms are separated from the saturation terms in the calculation (Sheldon et al., 1959). Only the pressure terms are evaluated implicitly; saturation and bubble point pressure terms are evaluated explicitly. All calculations are carried out using pressure and saturation dependant terms which are passed on from the previous time step. In doing so, the flow term where each term was a 3×3 sub matrix is now a scalar quantity. This reduces the storage and the computational overhead required when compared to the fully implicit method.

According to fluid mechanics in porous medium, saturation changes more rapidly in time than pressure. Thus, the time step restriction is more stringent on the saturation terms. The improvement to the IMPES exploits this fact and reduces the size of the time step for saturation calculations when compared to that for the pressure terms. For each time step, the saturation is assumed to be constant during the time step. The calculations are carried out at the end of the time step where the

saturation values of the previous Newton iteration are used. The work flow for the IMPES algorithm is depicted in Figure 22.

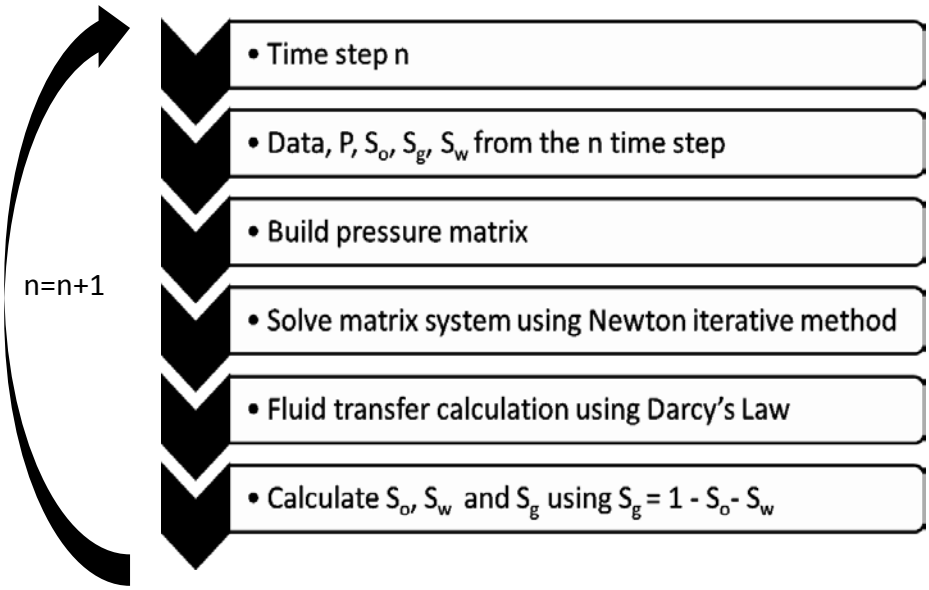

Figure 22. Work flow of Implicit Pressure Explicit Saturation algorithm

4.14. Equation of State

PVT properties of hydrocarbon fluid are the essential input used to predict phase behaviour and performance of the reservoir and post processing of the extracted fluids. In 1873, van der Waals proposed an equation of state, a modification to the ideal gas equation, in an attempt to predict the behaviour of real gases. Van der Waals argued that, at high pressure, gas molecules occupy a significant portion of the container volume and therefore, the co-volume, *b*, should be subtracted from the molar volume V_M (Ahmed, 2006). Furthermore, a pressure correction term for the molecular attractive forces $\frac{a}{V_M^2}$ was proposed, where real gases exert less

pressure on the walls of the container than ideal gas by $\frac{a}{V_M^2}$ (McCain, 1990). Van der Waals equation is of the form

$$\left(P + \frac{a}{V_M^2}\right)(V_M - b) = RT \qquad (82)$$

Where

$V_M =$ molar volume

P = pressure

T = temperature

R = universal gas constant

a, b = attractive and repulsive parameters respectively

The additional a and b terms are the proposed correction for attractive and repulsive interactions between molecules which can be obtained from the fluid critical properties. It is often referred to as cubic equation of state simply because it can be arranged into a form where V_M is of the 3rd power as follows

$$V_M^3 - \left(b + \frac{RT}{p}\right)V_M^2 + \left(\frac{a}{p}\right)V_M - \frac{ab}{p} = 0 \qquad (83)$$

While it was a very useful equation at the time, the ability to correctly predict the behaviour of real gas dramatically reduces as the temperature and pressure approaches the critical point (McCain, 1990). Since van der Waals, there have been countless modifications proposed, both empirical and theoretical, over the past century in an attempt to improve the accuracy and applicable range of temperatures and pressures. Early modified equations of state applications were for nonpolar mixtures (Peng & Robinson, 1976; Soave, 1972). Later (Graboski &

Daubert, 1978), among other authors, applied the equation of state to a slightly polar systems.

In 1949, concentrating on the vapour phase properties, Redlich and Kwong proposed an additional temperature dependent term $T^{-0.5}$ to the equation of state as follows

$$P = \frac{RT}{V-b} - \frac{aT^{-0.5}}{V(V+b)} \qquad (84)$$

The Redlich-Kwong equation of state offers an improvement in both density and temperature dependence over the original van der Waals' (Tsonopoulos & Heidman, 1985). It was later realized that constant a, and perhaps b, with temperature dependence term will significantly improve the Redlich-Kwong equation of state (Tsonopoulos & Heidman, 1985). In 1970, Joffe and Zudkevitch proposed that both constant a and b be temperature dependence by simultaneously matching liquid density and, at pure component's vapour pressure, force the fugacities to be equal (Tsonopoulos & Heidman, 1985; Zudkevitch & Joffe, 1970).

Peng and Robinson also proposed another widely accepted modification in 1976. An additional term, $b(v-b)$, was introduced to the attractive term. This improved the liquid density prediction without requiring any temperature dependence of the constant b (Tsonopoulos & Heidman, 1985).

Another well-known and widely used equation of state is the modification by Soave to the Redlich-Kwong equation of state. The Soave-Redlich-Kwong (SRK) equation of state can accurately predict the vapour-liquid equilibrium of hydrocarbon mixtures (Graboski & Daubert, 1978). The SRK equation of state takes a form as follow (Redlich & Kwong, 1949)

$$P = \frac{RT}{V - b} - \frac{a(T)}{V(V + b)} \quad (85)$$

Tsonopoulos and Heidman suggested that, although very similar to Soave's when it comes to VLE, the Peng-Robinson equation of state is more suitable for liquid density (Tsonopoulos & Heidman, 1985).

Many authors have utilized these equations of state and its constituents to investigate various thermodynamic models of both homogeneous and heterogeneous systems (Diamond & Akinfiev, 2003; Duan et al., 1996; Duan & Sun, 2003; Kiselev & Fly, 2000; Lu et al., 2009; Spycher & Pruess, 2005; Spycher et al., 2003; Valtz et al., 2004; Wu et al., 2009).

In ECLIPSE, four different two-parameter equations of state are used to determine compressibility factors and phase fugacity for each component, and ultimately the mole fraction and fluid composition for each grid block at each iteration. These equations of state include:

- Peng-Robinson
- Redlich-Kwong
- Soave-Redlich-Kwong
- Zudkevitch-Joffe-Redlich-Kwong

Their generalized form can be described in terms of compressibility as follows (Martin, 1979)

$$Z^3 + E_2 Z^2 + E_1 Z + E_0 = 0 \quad (86)$$

Where

$E_2 = (m_1 + m_2 - 1)B - 1$

$E_1 = A - (m_1 + m_2 - m_1 m_2)B^2 - (m_1 + m_2)B$

$E_0 = -[AB + m_1 m_2 B^2(B + 1)]$

m_1 & m_2 for each equation of state are given in Table 9 below.

The largest of the three roots is the compressibility factor of the vapor phase while the smallest is that of the liquid phase.

Table 9. m_1 & m_2 for each equation of state, redrawn from (Schlumberger, 2008.2).

Equation of State	m_1	m_2
Peng-Robinson	0	1
Redlich-Kwong	0	1
Soave-Redlich-Kwong	0	1
Zudkevitch-Joffe-Redlich-Kwong	$1+\sqrt{2}$	$1-\sqrt{2}$

The fugacity coefficient can then be calculated by (Schlumberger, 2008.2)

$$\ln\left(\frac{f_i}{px_i}\right) = -\ln(Z-B) + \frac{A}{(m_1-m_2)B}\left(\frac{2\Sigma_i}{A}-\frac{B_i}{B}\right)\ln\left(\frac{Z+m_2B}{Z+m_1B}\right)+\frac{B_i}{B}(Z_i-1) \quad (87)$$

Where

$$\Sigma_i = \sum_j A_{ij}x_j$$

$$A = \sum_{i=1}^{n}\sum_{j=1}^{n} x_j x_k A_{jk}$$

$$B = \sum_{j=1}^{n} x_j B_j$$

$$A_{jk} = \left(1-\delta_{jk}\right)\left(A_j A_k\right)^{0.5}$$

δ_{jk} = binary interaction coefficient amongst the components.

Although actually made up of thousands of components, reservoir fluids are characterized by pseudo components, analogous to the use of united atom or coarse-grain model, to represent a rather complex composition. Typically, 4-8 pseudo components, along with a host of species specific parameters, are used in reservoir model to represent a given reservoir fluid (Schlumberger, 2008.2). The species specific parameters include

- Critical pressure, P_c
- Critical temperature T_c
- Critical volume, V_c
- Critical compressibility factor, Z_c
- Accentric factor, ω

Noting the ability, or lack thereof, of the two-parameter equations of state in predicting the liquid properties, it is also possible to employ three-parameter equation of state in ECLIPSE. Utilizing the Péneloux *et al.* volume shift as a third parameter, a molar volume correction term, which can be written as follows (Péneloux et al., 1982)

$$V_{mol,p} = V_{mol,p}^{EoS} - \sum_{i=1}^{N} z_i c_i \qquad (88)$$

Where

$V_{mol,p}^{EoS}$ = molar volume of the phase predicted by two-parameter equation of state

$z_i = (x_i, y_i)$ = liquid and vapor mole compositions

c_i = set of volume corrections

$subscript\ p$ = phase of the system

4.15. Initialization of the simulation model

The petrophysical and reservoir properties lists discussed previously are then put together in the ECLIPSE 100 context. The model employs a five spot pattern similar to the Salt Creek field but other chemical and physical properties will be that of the Good Oil reservoir as follows:

For further details on the data and parameters utilized in the current model, please refer to the appendix section. The current model employs the size of $50i \times 50j \times$

$50k$, a total of 125,000 grid blocks. The *PVT* properties along with the petrophysical properties such as bubble point pressure, gas and oil formation volume factor as well as viscosities are then specified utilizing those given by the Good Oil Company.

Table 10. Chemical and physical properties used in the illustrative model

Depth	4000 ft
Horizontal permeability	700 md
Vertical Permeability	700 x 0.2 md
Mean reservoir thickness	85 ft
Sand porosity	0.2
Initial oil saturation	80%
Injection wells	1
Producing wells	4
Bottom hole depth	4000 ft
Bottom hole pressure targets	200 PSIA

The injection rates of the supercritical CO_2 varied between 1,000-3,000 Mscf/day depending on the well response. As a result, a mean of 2,000 Mscf/day were used. Among other constraints, the bottom hole target pressure for each well was set at 200 PSIA. Only a small number of physical parameters from the actual Salt Creek field were used in the Good Oil model, where appropriate. It was then fine-tuned with the adjustable parameter such as bottom hole pressure, densities, and discretization of time and space into small time step and grid blocks. Other fine tuning methods (such as history matching) were also possible but is not utilised for the current Good Oil model since we do not have the data on such production history and this is only for illustration purposes.

Part II. Parameterisation

Chapter Five

Monte Carlo and Molecular Dynamics Parameterisation

The parameters used in this study were first verified against the literature data before they are applied to the simulation software. These comparisons included the verification of force fields from a number of sources for all components within this study, comparison between the two simulation approaches, and reproduction of the results in literature with similar compositions.

5.1. Visual aid of conditional formatting

To ensure the system's equilibration, the author used the visual aid of conditional formatting in the spreadsheet where a given quantity, for example densities, were compared against each other within the set and displayed graphically. An example of the graphical display is shown in the Figure 23. An increasing or decreasing pattern can be observed in Figure 23a, indicative of an unequilibrated system. On the other hand, Figure 23b exhibits no observable pattern but a random distribution which fluctuates about a point, indicative of an equilibrated system.

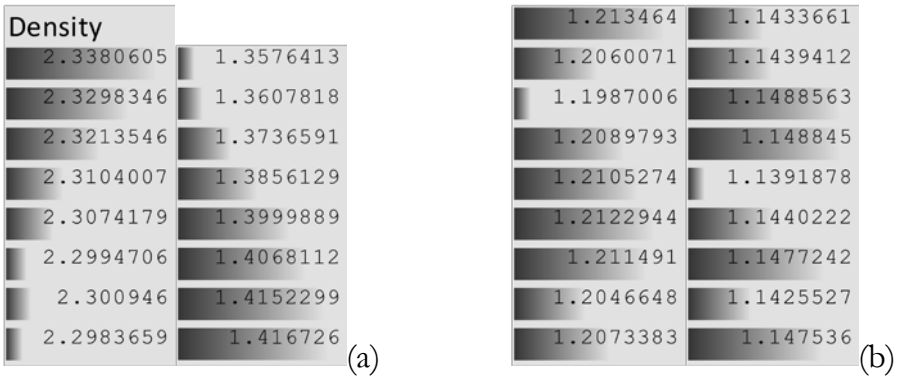

Figure 23. An example of visual aid of conditional formatting: (a) unequilibrated system and (b) equilibrated system.

5.2. *n*-Decane Potential

As previously discussed, three different United Atom force fields namely, SKS (Siepmann, 1993; Smit et al., 1995), OPLS (Jorgensen et al., 1984), and TraPPE (Martin & Siepmann, 1998, 1999) were evaluated at a pressure of 10MPa, 100MPa, and 200MPa and temperatures between 340K - 460K. The values of Lennard-Jones potential parameters are tabulated in Table 11.

Table 11. Lennard-Jones potential parameters

Pseudo-atom	SKS[1]		OPLS[2]		TraPPE[3]	
	ε (K)	σ (Å)	ε (K)	σ (Å)	ε (K)	σ (Å)
CH_2	47	3.93	59.37956	3.905	46	3.75
CH_3	114	3.93	88.06297	3.905	98	3.95

[1](Siepmann, 1993; Smit et al., 1995), [2] (Jorgensen et al., 1984), [3](Martin & Siepmann, 1998, 1999)

A system of 500 *n*-decane molecules was used for the potential comparison via Molecular Dynamics simulations. With the exception of the potential parameters, the systems were otherwise virtually identical in all cases. Plots of density vs. temperature at various pressures for all three interaction potentials are shown in Figure 24. The systems were allowed to equilibrate for 5ns before the time average densities were taken from the next 5ns. It should be noted that the simulation uncertainty in all cases are smaller than the markers on the plots.

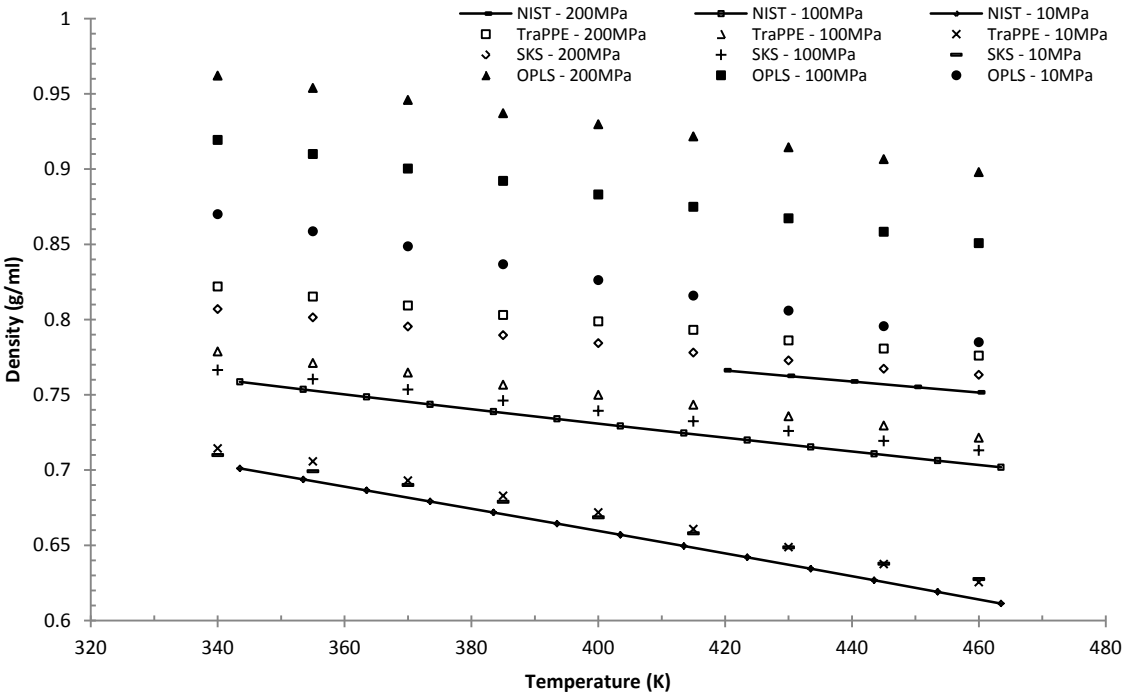

Figure 24. Comparison of the three United Atom force fields for pure *n*-decane with NIST data

The results were then compared with that of the National Institute of Standards and Technology (NIST) where available (Linstrom & Mallard). In all cases, the simulation trial systematically overestimated the density of *n*-decane, where deviation increases with pressure and temperature. The SKS and TraPPE force fields predictions were virtually identical at 10MPa, this is to be expected as SKS is the predecessor of the TraPPE interaction potential. However, as the pressure increases, the SKS interaction potential gives a much better agreement than TraPPE. The OPLS, on the other hand, consistently overestimated the density by a large margin. The SKS predicted density of decane with average absolute deviations of 1.44%, 1.18%, and 1.40% at 10MPa, 50MPa, and 200MPa when compared to the NIST values respectively. The density profile comparisons at the three pressures are shown in Figure 25.

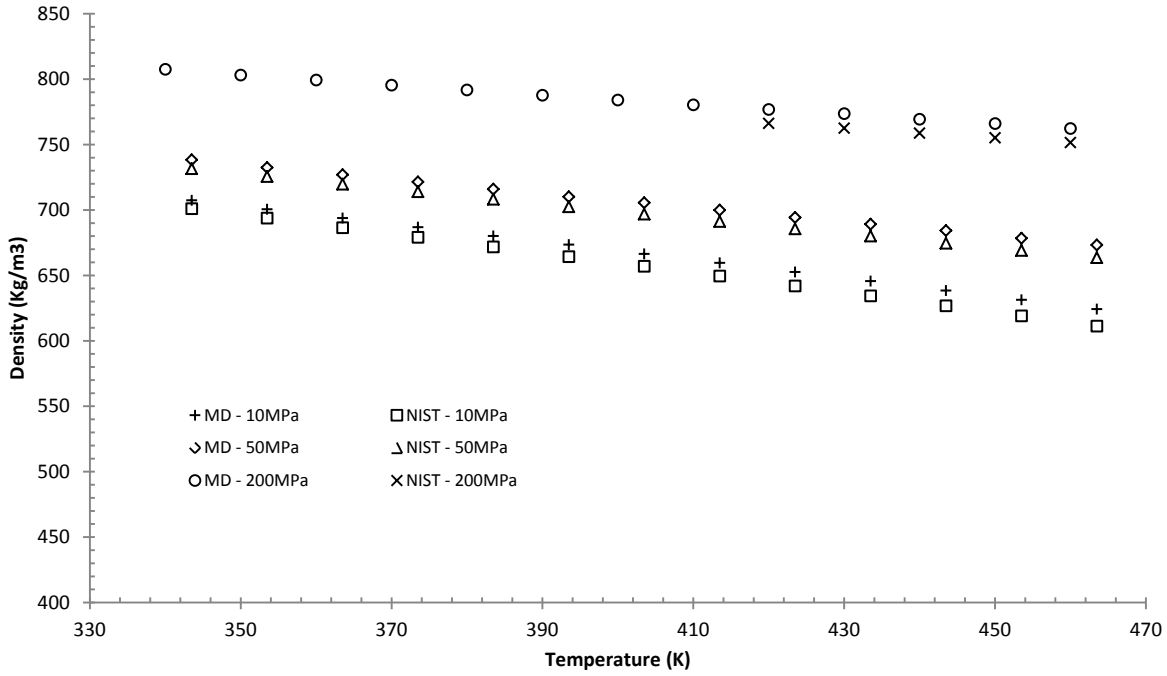

Figure 25. Density vs. temperature comparison for *n*-decane at 10MPa, 50MPa, and 200MPa. MD denotes SKS potential

These systematic overestimations reflect the specific set of values of ∈ and σ, representing the effective potentials and not the true potential. In fact, similar systematic misalignment is also observed in the estimation of the second virial coefficient where the effective pair potential accounts for 10-20% of the discrepancy between the simulation and experimental results (Martin & Siepmann, 1998). The simulation results for pure decane are thus satisfactory as it is well within this error margin.

5.3. Simulation Approaches Verification

In addition to the comparison of the United Atom interaction potential parameters from different authors, the comparison between Monte Carlo and Molecular Dynamics simulations were also carried out. Fundamentally, there should be no difference when identical parameters were used in either simulation. This was

confirmed in both simulation approaches, where there were less than 0.4% difference in all cases, as shown in Figure 26. Thus, it will be assumed henceforth that the results from both methodologies with the same parameters are identical.

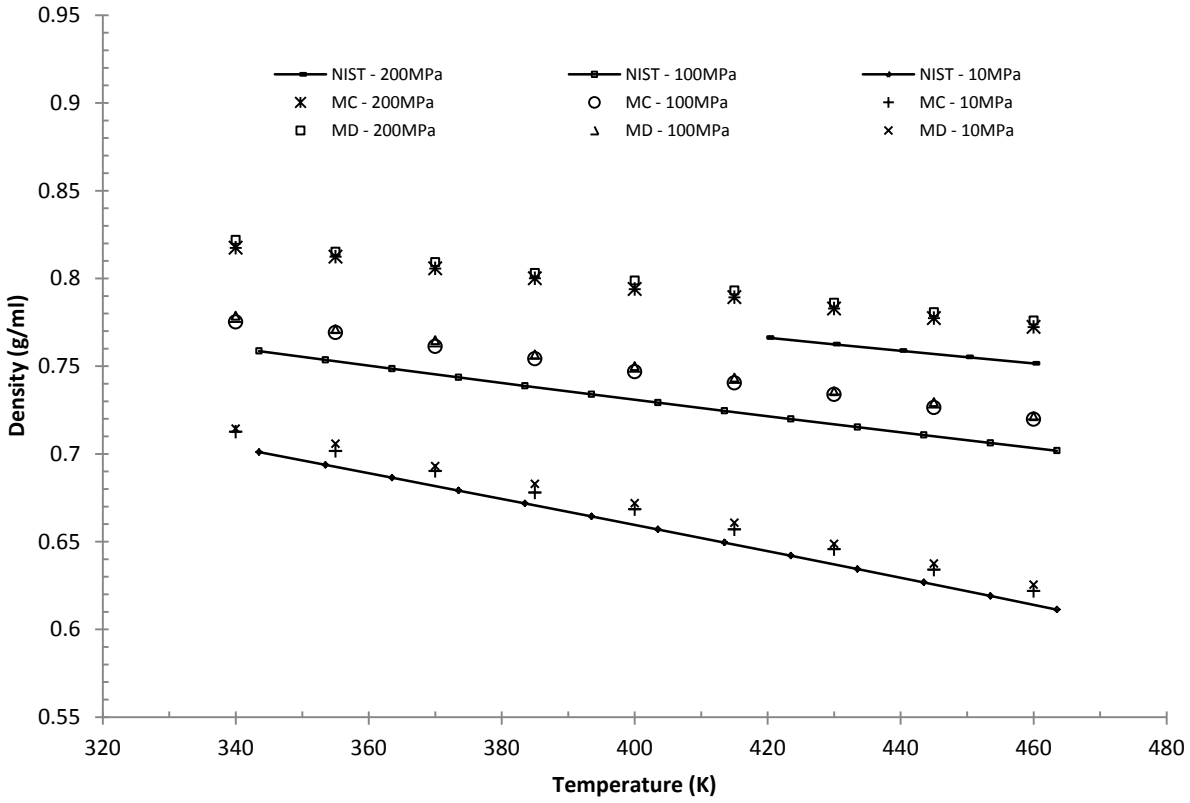

Figure 26. Density vs. temperature plots for n-decane comparing the Monte Carlo (MC), Molecular Dynamic (MD) simulations, and data from National Institute of Standards and Technology (NIST)

5.4. Noble Gases

The Lennard-Jones potential parameters for the noble gases were taken from several sources, particularly when the density predictions had a greater than 2% difference when compared to the NIST data. The final Lennard-Jones potential parameters utilized in this study are given in Table 12.

Table 12. Lennard-Jones potential parameters for noble gases used in this study.

Noble Gas	ε (K)	σ (Å)	Reference
He	10.22	2.556	(Kell et al., 1978)
Ne	35.7	2.789	(Skoulidas & Sholl, 2002)
Ar	124.07	3.42	(Skoulidas & Sholl, 2002)
Kr	164.7	3.635	(Potter & Clynne, 1978)
Xe	227.856	3.9478	(Bonifácio et al., 2002)

All the pure component trials for all noble gases were carried out in NPT Monte Carlo Gibbs Ensemble with 500 particles at 10MPa, 50MPa, and 200MPa, and temperature between 340K and 460K. The trials were allowed to equilibrate for 5,000 cycles before the results were taken from the following 10,000 cycles. Additionally, an equivalent systems were also evaluated in molecular dynamics simulation where systems of 500 particles are allow to equilibrated for 5ns before the results were taken from the next 5ns. To ensure the accuracy of the force field parameters and the results in both simulation approaches, they are then compared with NIST data. It should be noted that the simulation uncertainty in all cases are smaller than the markers on the plots.

5.4.1. Helium

Three different intermolecular potentials by Kell et al. (1978), DeBoer & Michels (1938), and Chakravarty (1997) were investigated. As depicted in Figure 27 and Figure 28, Kell and Deboer's density profiles are very similar where Kell's potential gives the average absolute deviation of 0.37% and 0.12% at 10MPa and 50MPa respectively.

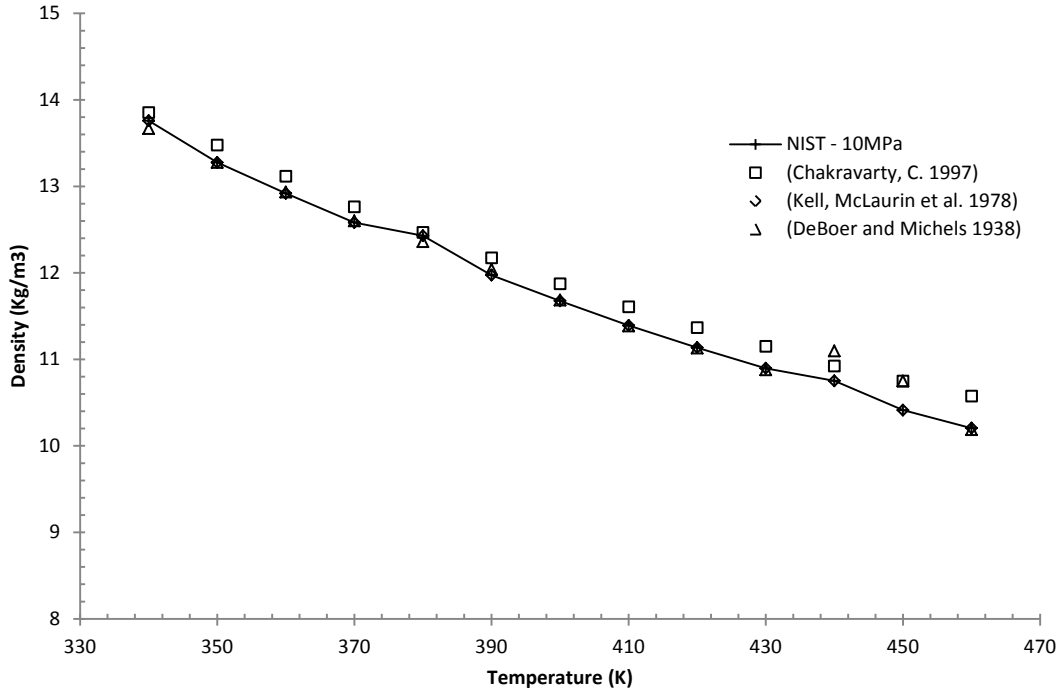

Figure 27. Helium density profiles comparison between three different authors and NIST data at 10MPa

On the other hand, DeBoer's potential gives the average absolute deviation of 0.94% and 0.10% at 10MPa and 50MPa respectively. While the average absolute deviations percentage at 10MPa are similar in both cases, and tend to increase with pressure, Kell's potential offers a much lower average absolute deviation at 50MPa. There is no NIST data available for comparison purpose at 200MPa.

The interaction potential parameters provided by Chakravarty gave relatively poor helium density predictions in both 10MPa and 50MPa cases with average absolute deviation of 2.2% and 3.6% respectively.

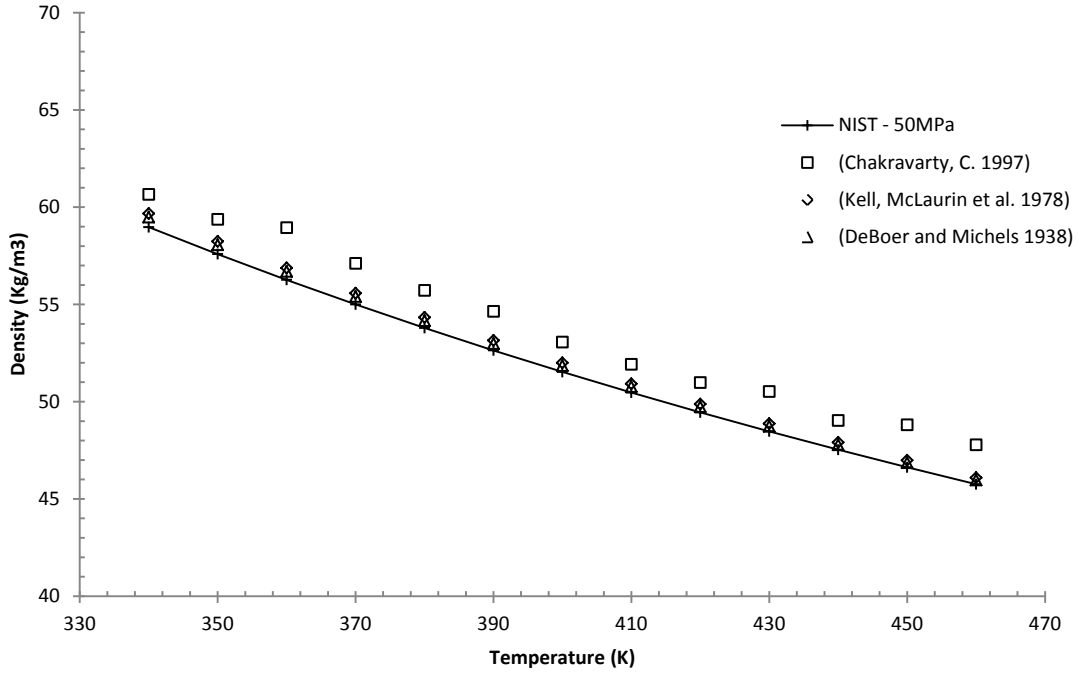

Figure 28. Helium density profiles comparison between three different authors and NIST data at 50MPa

5.4.2. Neon

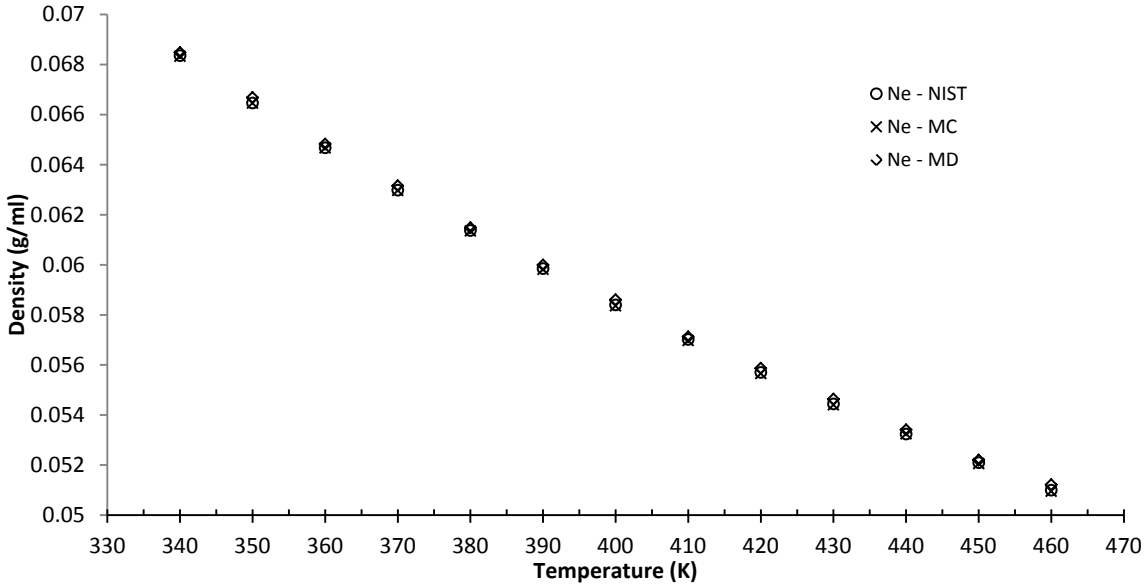

Figure 29. Neon density comparison between Monte Carlo simulation, Molecular Dynamics simulation, and NIST data at 10MPa

The token comparison between the Monte Carlo simulation, the Molecular Dynamics simulation, and the data from NIST was carried out to ensure the accuracy. As depicted in Figure 29, all simulation results are in good agreement with NIST data. In all cases, the differences between the simulation results and the NIST data are less than 0.9%. The difference between Monte Carlo and Molecular Dynamics simulation results are well under 0.03%.

Figure 30 shows the density comparison between Molecular Dynamics simulation and NIST data at 10MPa, 50MPa, and 200NMPa. The average absolute deviations are 0.27%, 0.28%, and 0.53% at 10MPa, 50MPa, and 200MPa respectively.

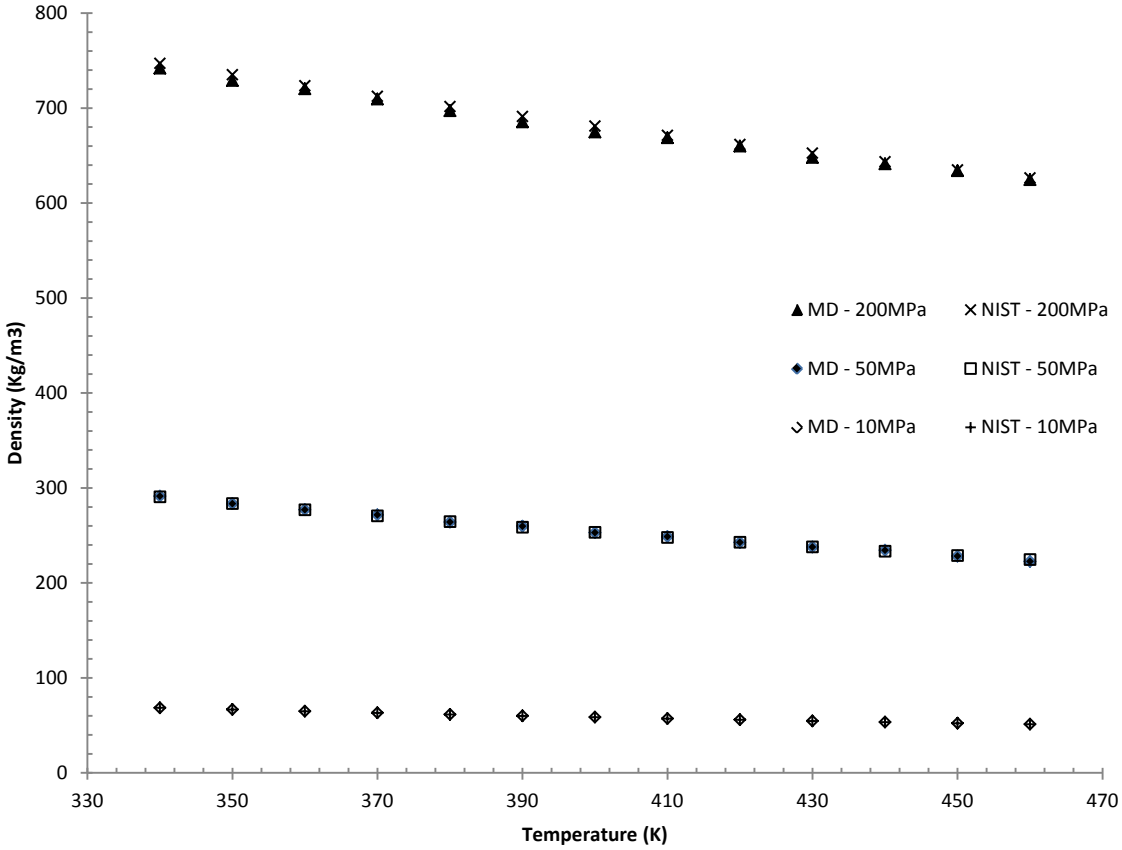

Figure 30. Neon density comparison between Molecular Dynamics simulations and NIST data at 10MPa, 50MPa, and 200MPa

5.4.3. Argon

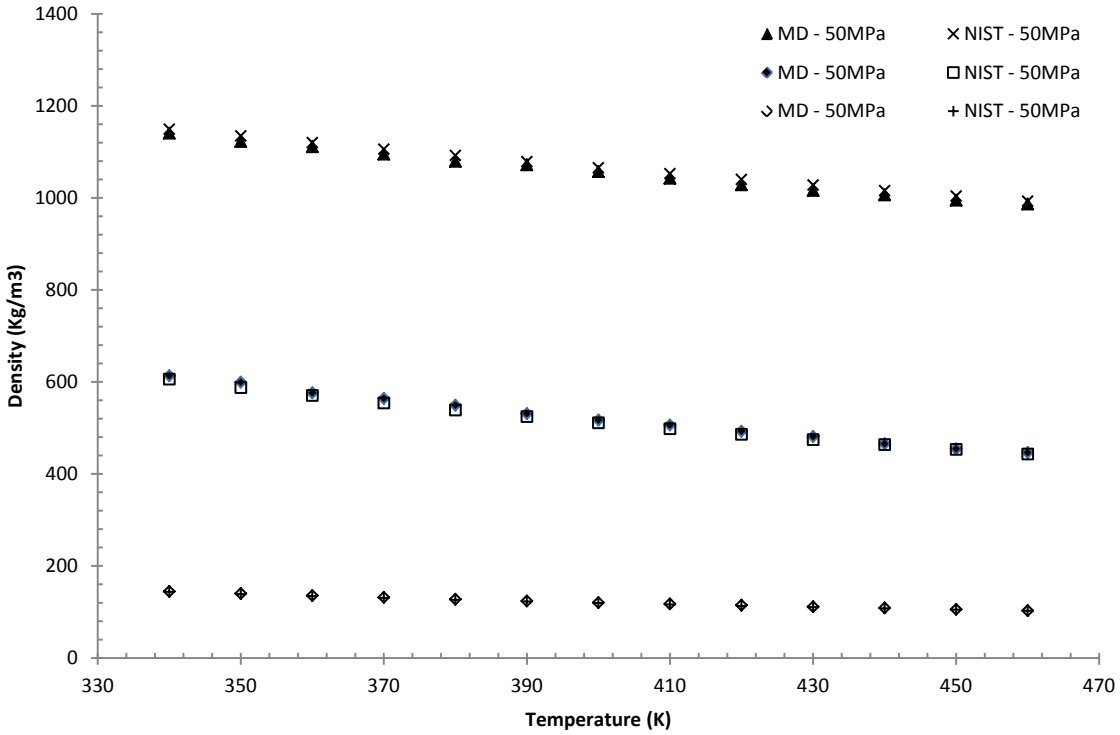

Figure 31. Argon density comparison between Molecular Dynamics simulations and NIST data at 10MPa, 50MPa, and 200MPa

The difference between Monte Carlo simulation and NIST results were all under 2%. Similar to other noble gas force fields tested, the average absolute deviations were 0.9%, 1.2%, and 0.93% at 10MPa, 50MPa, and 200MPa respectively.

5.4.4. Krypton

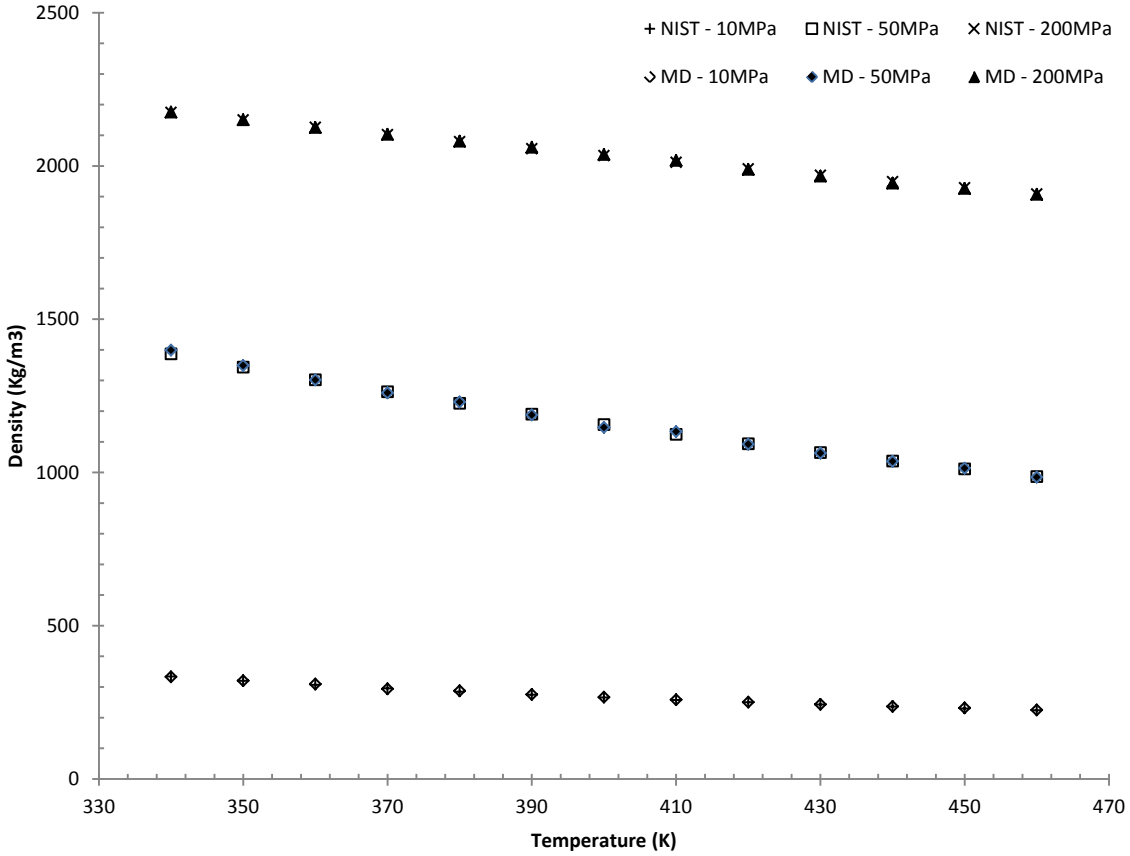

Figure 32. Krypton density comparison between Molecular Dynamics simulations and NIST data at 10MPa, 50MPa, and 200MPa

For krypton, the average absolute deviations when compared to the NIST data were 0.45%, 0.37%, and 0.12% at 10MPa, 50MPa, and 200MPa respectively.

5.4.5. Xenon

Interaction potential parameters for xenon were taken from three authors including Bonifácio et al. (2002), Rowley (1994), and Skoulidas & Sholl (2002). The density profiles were then compared at 50MPa and 200MPa as depicted in Figure 33.

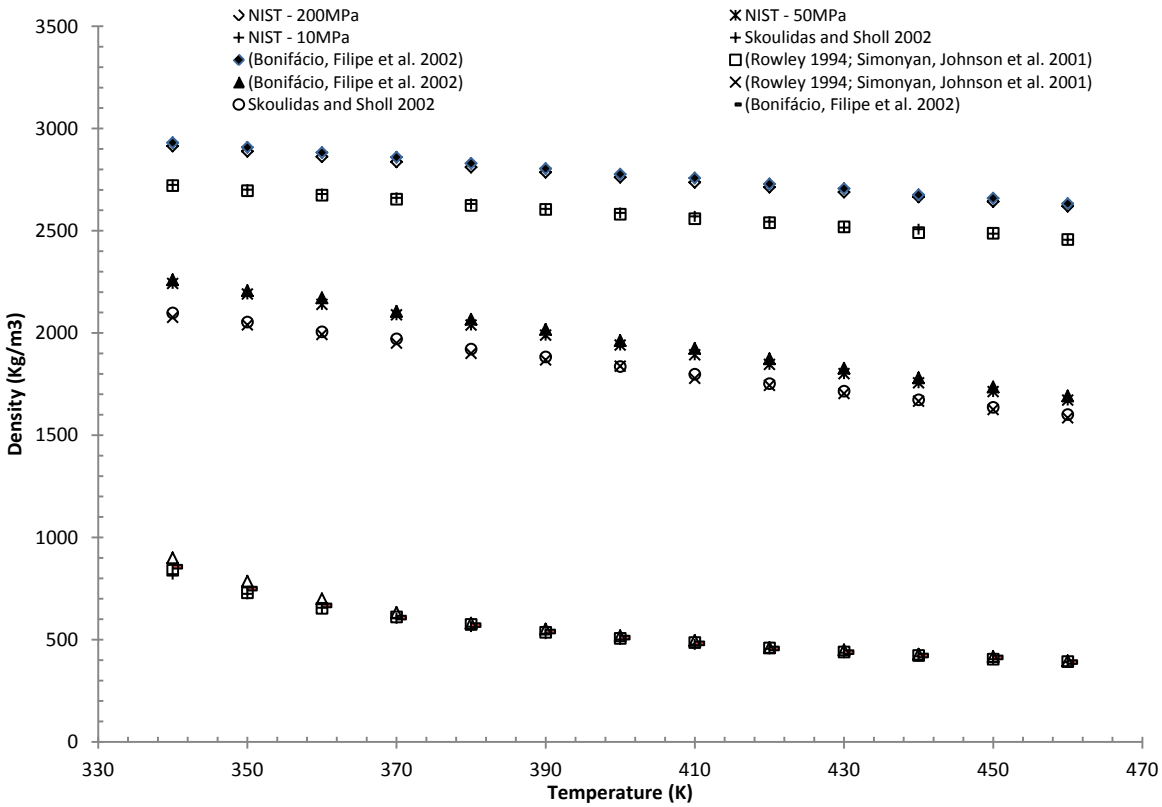

Figure 33. Xenon density comparisons between three authors at 50MPa and 200MPa

The interaction potential provided by (Bonifácio et al., 2002) has consistently accurately reproduced the density profiles for Xenon with average absolute deviations of 1.5%, 1.2%, and 0.61% at 10MPa, 50MPa, and 200MPa respectively. The error increased with decreasing temperature at 10MPa, however, no systematic errors were observed at higher pressures.

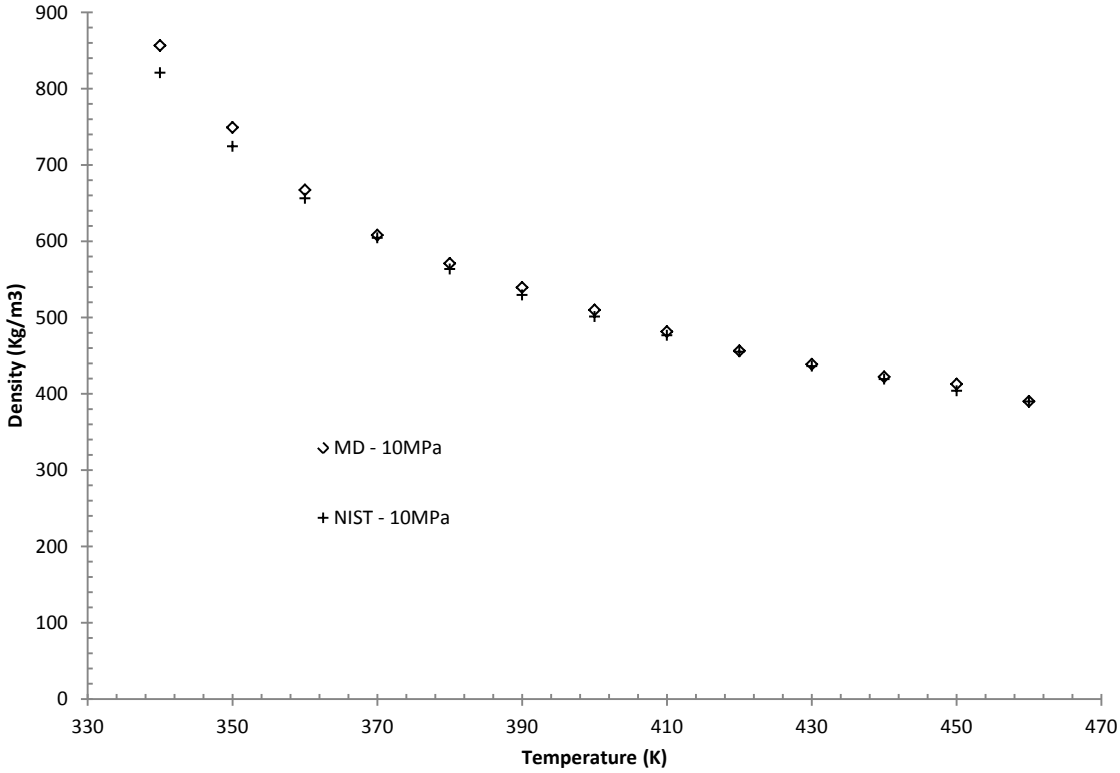

Figure 34. Xenon density profile comparison between MD simulation and NIST at 10MPa

The potential provided by (Rowley, 1994) gives a far less accurate density profile at 10MPa, 50MPa, and 200MPa with average absolute deviations of 1.2%, 6.4%, and 6.9% respectively. Additionally, the potential used in (Skoulidas & Sholl, 2002) study produced the least accurate density profiles overall at these pressure with average absolute deviations of 4.2%, 5.6%, and 6.7% at corresponding pressure of 10MPa, 50MPa,s and 200MPa respectively. It should also be noted that the potential provided by (Rowley, 1994) and (Skoulidas & Sholl, 2002) both consistently underestimated the density at higher pressures.

5.5. Henry coefficient reproduction trial

The Henry coefficient trial was first compared to that of Bonifácio et al. (2010) where a system of *n*-hexane + Xe was investigated (Bonifácio et al., 2010). The Monte Carlo simulation was used in this reproduction trial with a system of 500 *n*-hexanes and 1000 Widom's insertion attempts per cycle. The systems were first equilibrated for 30,000 cycles before the measurements were taken from the next 30,000 cycles.

While Bonifácio et al. (2010) simulation results can remarkably accurately predict the experimental results at lower temperature region, Figure 35, the deviations seem to increase with temperature with a maximum of 9% at the highest temperature tested. In turn, our average absolute deviation was found to be 8.16% from their simulation results. This can be contributed mainly to the different interaction potential parameters applied between the two studies. The force field used in this study has shown to adequately represent *n*-decane very well, to within 2%. However, it was not verified for *n*-hexane. The overall trend is however satisfactorily reproduced, which is the intended purpose.

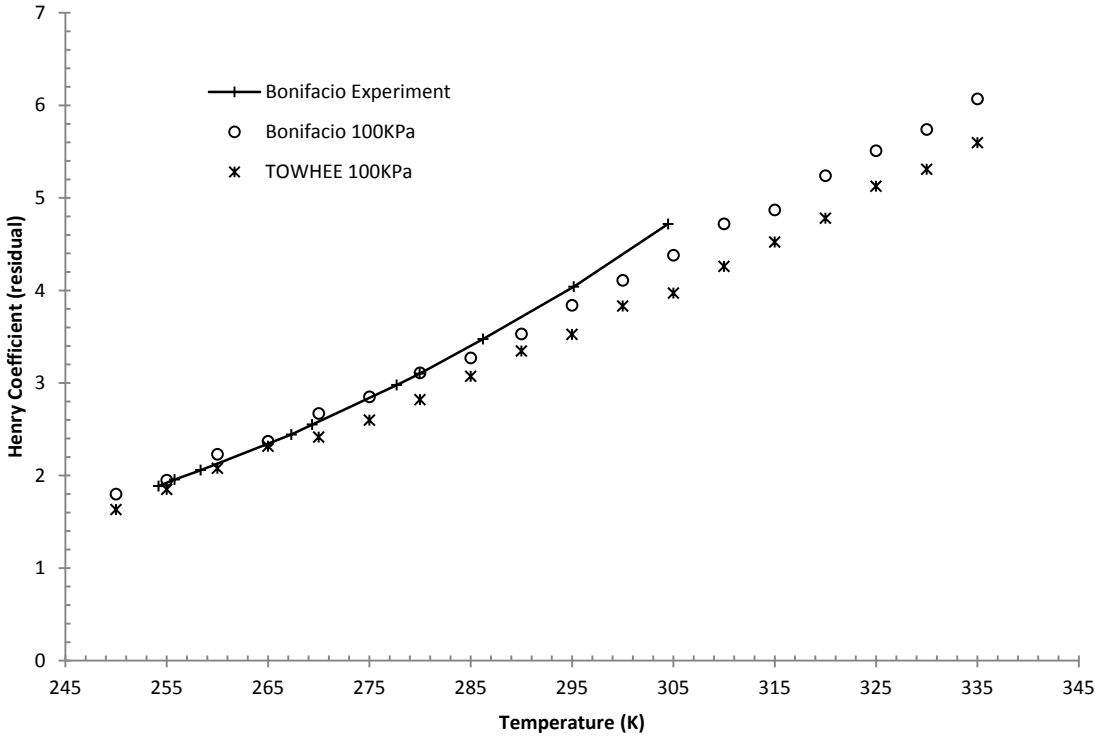

Figure 35. Comparison of Henry coefficient for Xe in *n*-decane as a function of temperature between (Bonifácio et al., 2010) and the Monte Carlo simulation from the current study denoted by TOWHEE.

5.6. Diffusion coefficient reproduction trial

The experimental diffusion coefficient data provided by (Chen et al., 1982) for a number of noble gas + *n*-decane binary mixtures was used to verify the accuracy of the model. The reproduction trials for each noble gas diffusion coefficient were completed in Molecular Dynamics with 500 *n*-decanes. At least eight separate trials of 5ns were completed to increase the statistical accuracy, an approach recommended by (Wang & Hou, 2011).

The diffusion coefficient for the noble gas + *n*-decane systems were taken from (Chen et al., 1982) as shown in Table 13. These measurements were completed by way of Taylor Dispersion Technique where solute is injected into a linear flow of

solvent, the diffusion coefficient is then measured in terms of Gaussian distribution.

Table 13. Diffusion coefficients (10^5 cm^2/sec) of noble gases in *n*-decane at various temperatures as reported by (Chen et al., 1982)

Temperature (K)	Ar	Kr	Xe
298	4.87±0.007	3.51±0.006	2.86±0.003
333	7.72±0.007	5.75±0.003	4.60±0.003
373	-	-	7.13±0.005
433	19.3±0.002	14.6±0.001	12.2±0.001

The diffusion coefficient comparisons are shown in Table 14 and Figure 36, with average absolute deviation of 15.87%, 19.43%, and 18.63% for Ar, Kr, and Xe + *n*-decane binary mixture respectively. While there is no consistent trend, the overall accuracy tends to increase with increasing temperature, in line with the observation of Dysthe et al. in their fluid transport study of various united atom force fields (Dysthe et al., 2000).

Table 14. Diffusion coefficient (10^5 cm^2/sec) comparison between simulation results and that of (Chen et al., 1982) where MD denotes the results of 8 separate trials of Molecular Dynamics simulation.

Temperature (K)	Xe		Kr		Ar	
	Chen	MD	Chen	MD	Chen	MD
298	2.86	3.9741	3.51	4.6726	4.87	5.98397
333	4.6	5.65974	5.75	7.659	7.72	9.84489
373	7.13	8.43313	-	9.07519	-	14.193
433	12.2	13.9098	14.6	15.9512	19.3	20.8509

The average absolute deviations for each binary mixture were within an expected range - a deviation in density by 2% can reflect a 30% deviation in transport coefficients (Dysthe et al., 2000). What is more, unlike other bulk properties such as density, great statistical inaccuracies of diffusion coefficients were observed even among experimental measurements where they can be as large as 40% (Wang & Hou, 2011). This is particularly true in the region where pressure is high and temperature is low (Clarke & Brown, 1987).

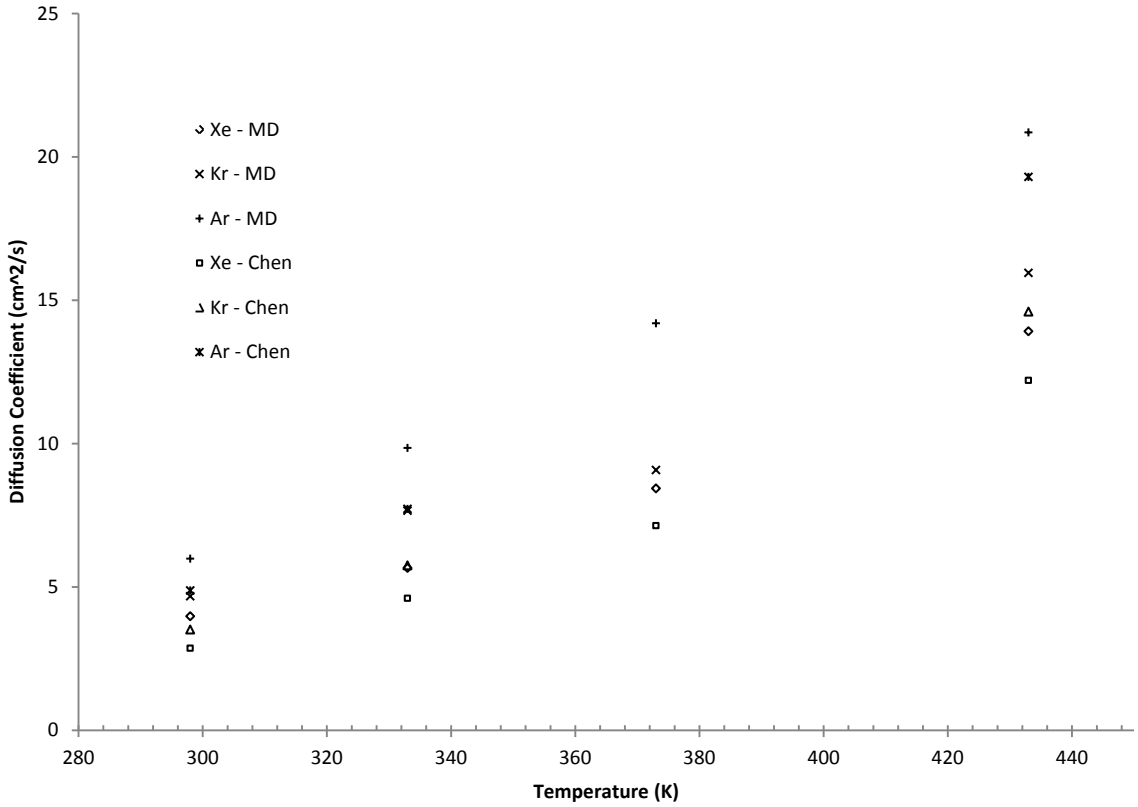

Figure 36. Diffusion coefficient comparison between (Chen et al., 1982) and Molecular Dynamics simulation

In light of the statistical significance, the diffusion coefficient reproduction is considered to be relatively accurate and within the expected range, where the largest error is contributed by the density prediction in *n*-decane as previously discussed.

The verification of the pure components as well as reasonable reproduction of binary mixtures and their properties has been reproduced within a relatively stringent guideline. While all simulation results were well within the expected ranges, explanations have been provided where larger deviations were observed. These thus give a higher level of confidence in the parameters which will be employed throughout the study.

Part III. Results and Discussions

Chapter Six

Henry Coefficients of noble gases in n-decane

The Henry coefficient calculations were conducted using Monte Carlo simulation. The trials were completed at reservoir conditions with temperatures between 340 K- 460 K and pressures between 10 MPa and 200 MPa. The Widom insertion technique was utilized in a system of 500 *n*-decane molecules attempting 1,000 insertions per cycle for each noble gas. The system of *n*-decane was first allowed to equilibrate for 20,000 cycles and the measurements were taken from the next 40,000 cycles. The conditional formatting visual aid was used to help verify the equilibration as previously discussed. Figure 37 to Figure 41 depicts the Henry coefficients for each noble gas in *n*-decane while Figure 42 to Figure 51 depicts the Henry coefficient for all noble gases at different pressures. The standard errors for each measurement are given in Table 15 to Table 19.

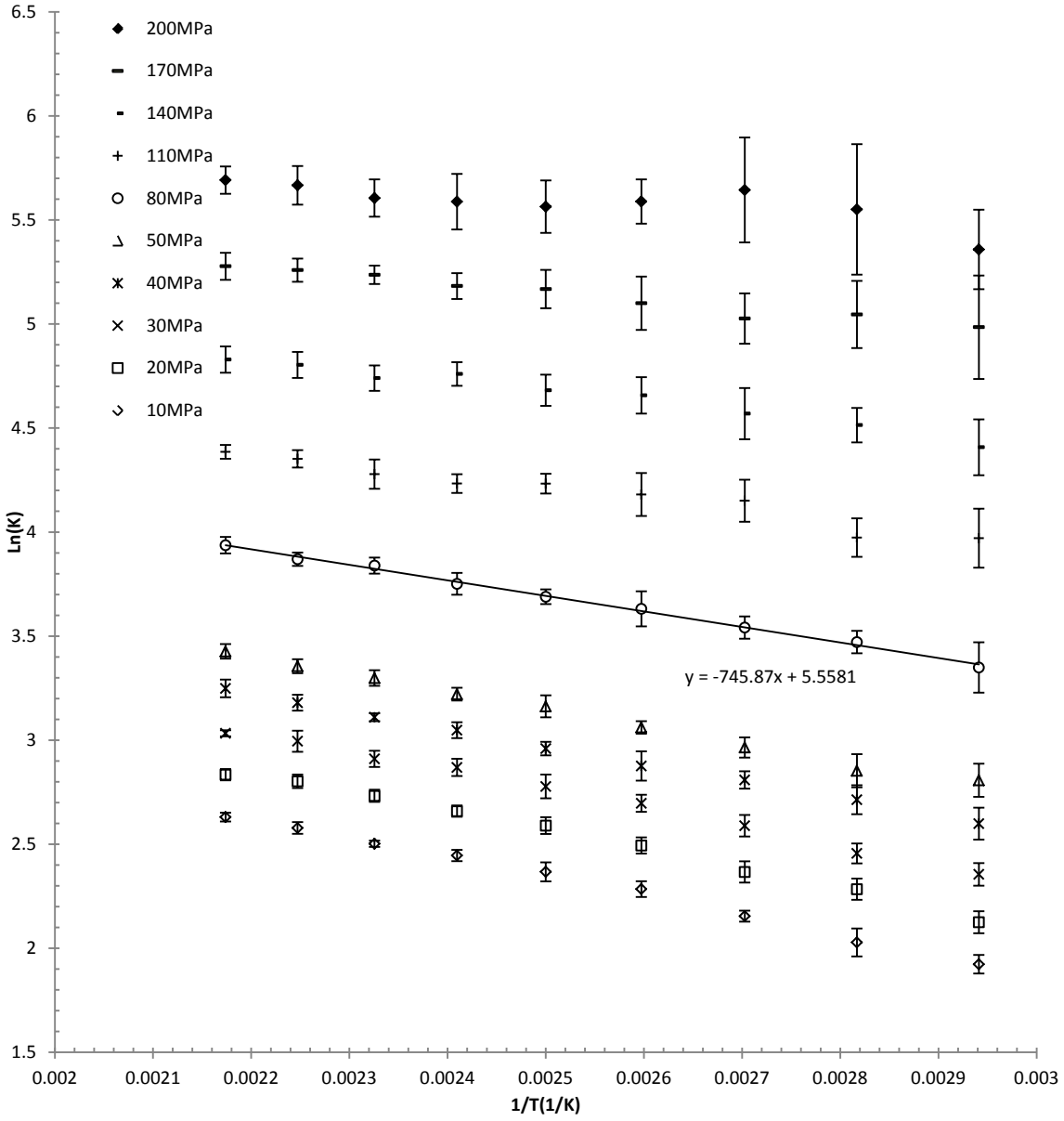

Figure 37. Henry coefficients for Xe in *n*-decane

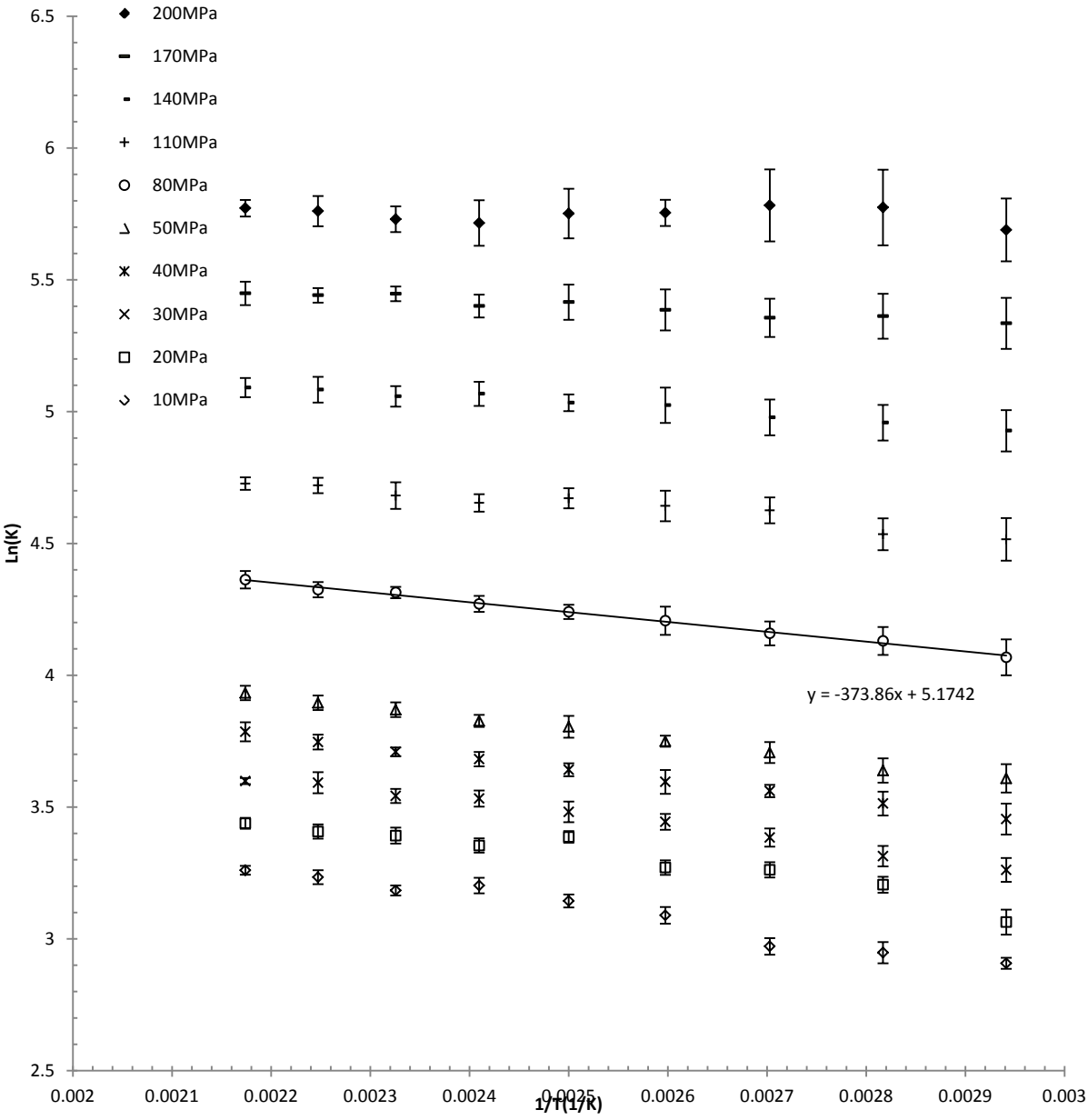

Figure 38. Henry coefficients for Kr in *n*-decane

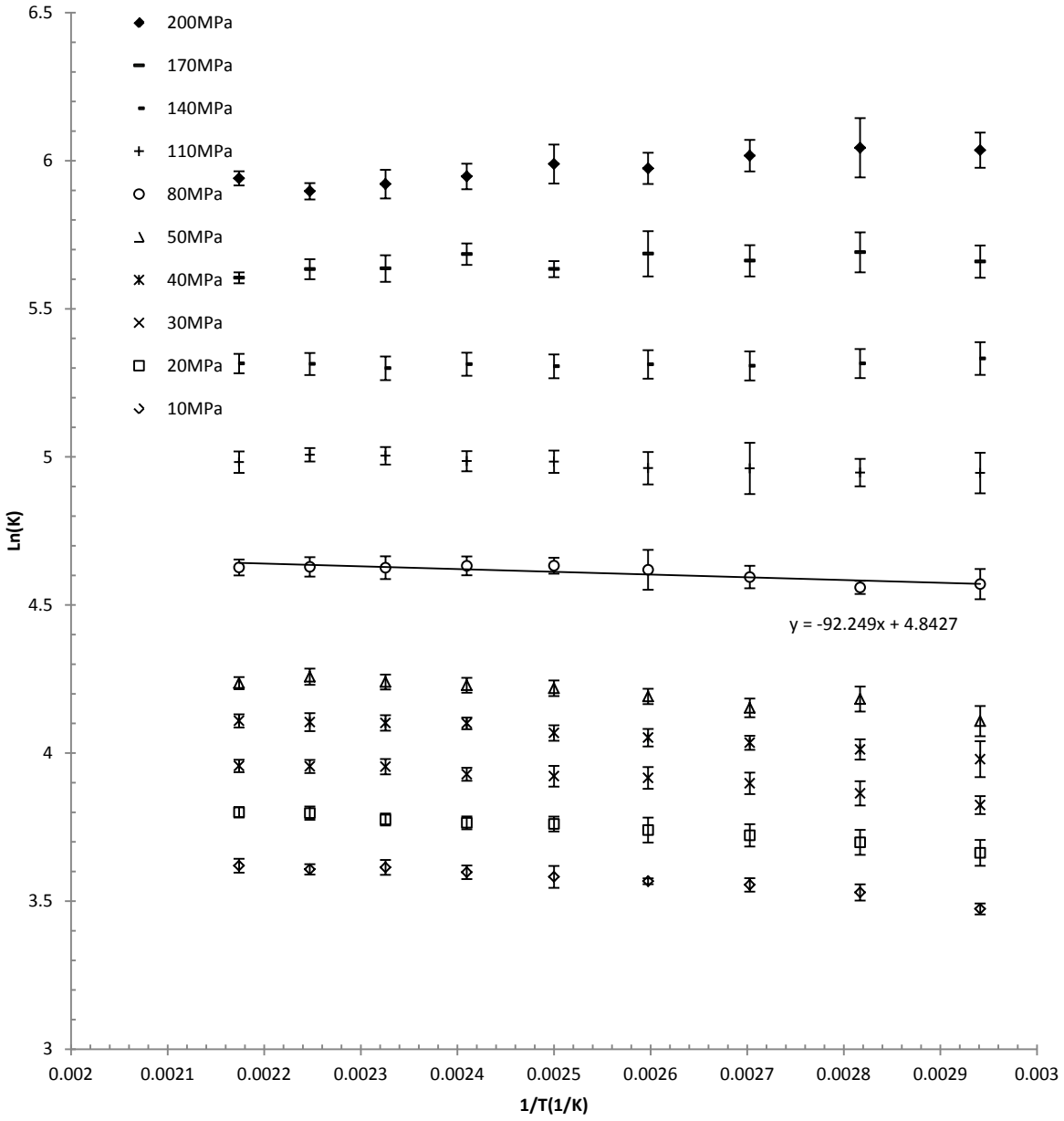

Figure 39. Henry coefficient for Ar in *n*-decane

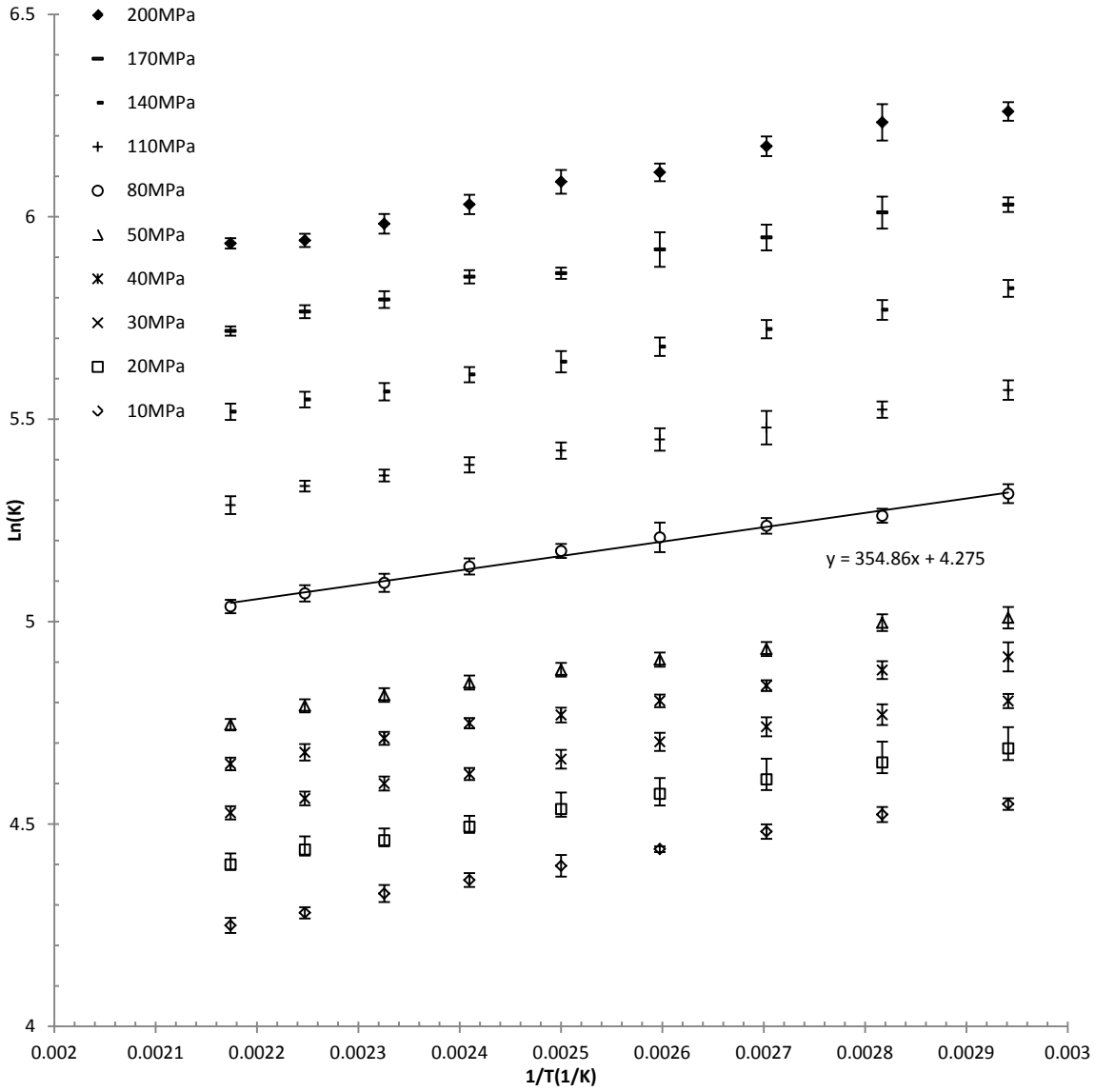

Figure 40. Henry coefficient for Ne in *n*-decane

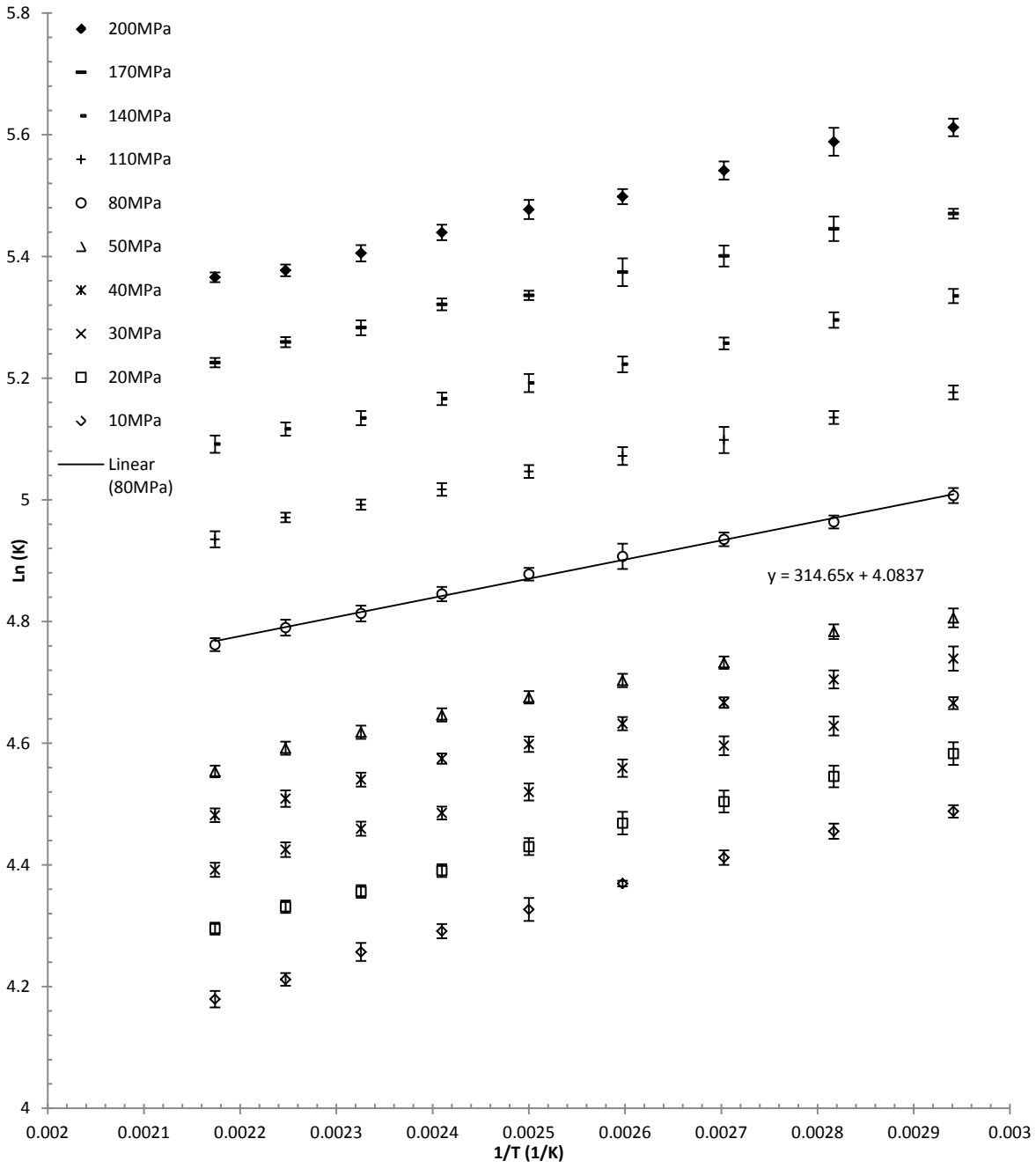

Figure 41. Henry coefficient for He in *n*-decane

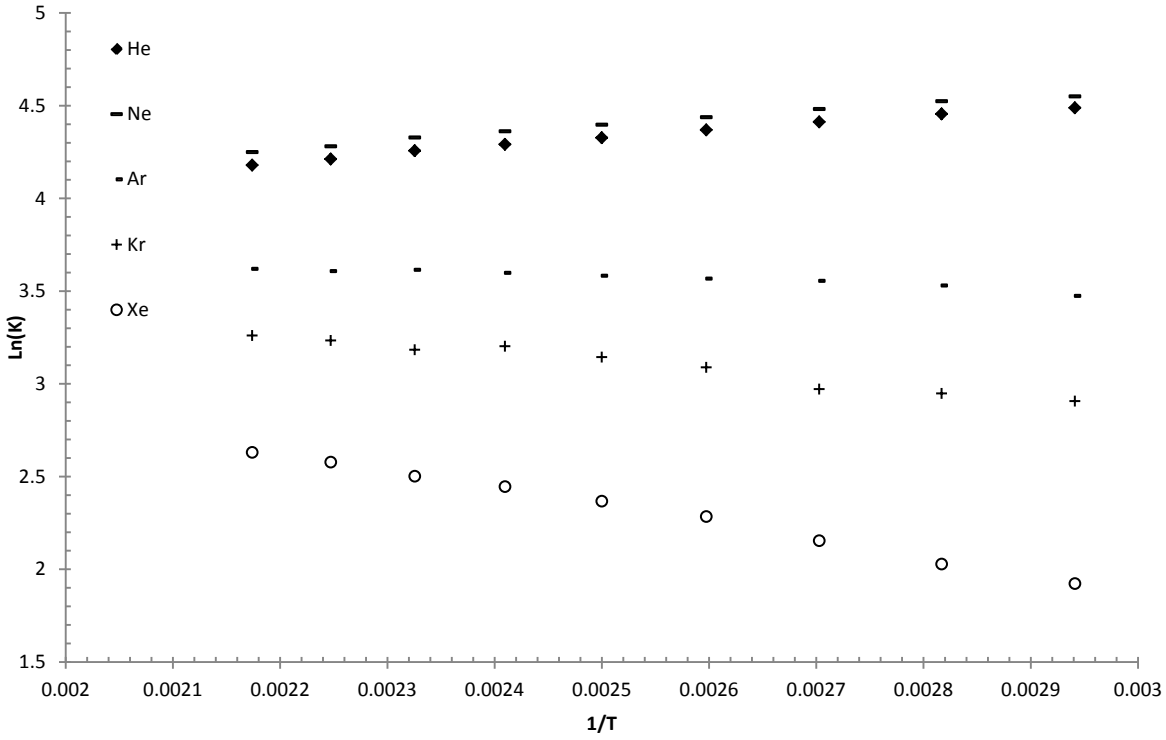

Figure 42. Henry coefficient of each noble gas in *n*-decane at 10 MPa

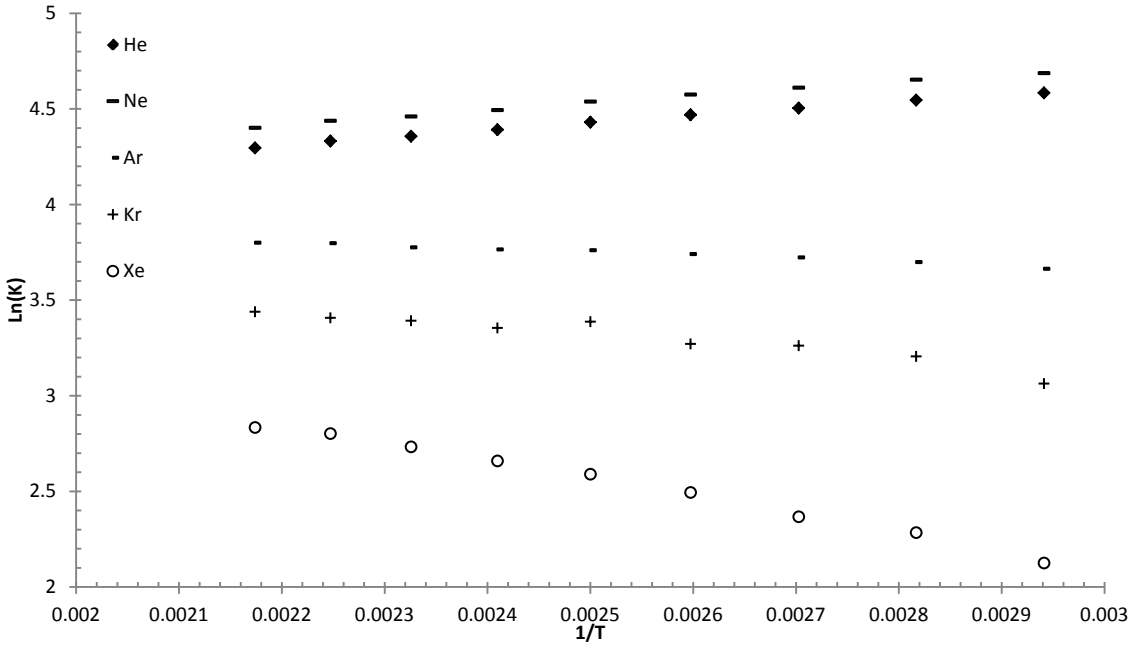

Figure 43. Henry coefficient of each noble gas in *n*-decane at 20 MPa

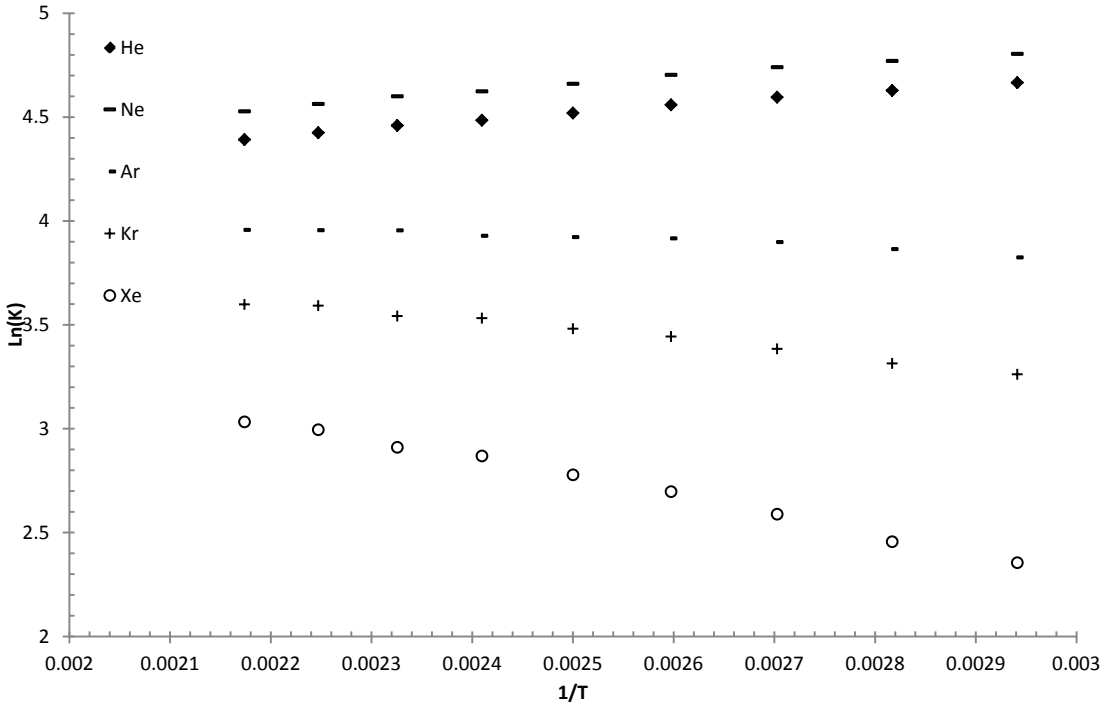

Figure 44. Henry coefficient of each noble gas in *n*-decane at 30 MPa

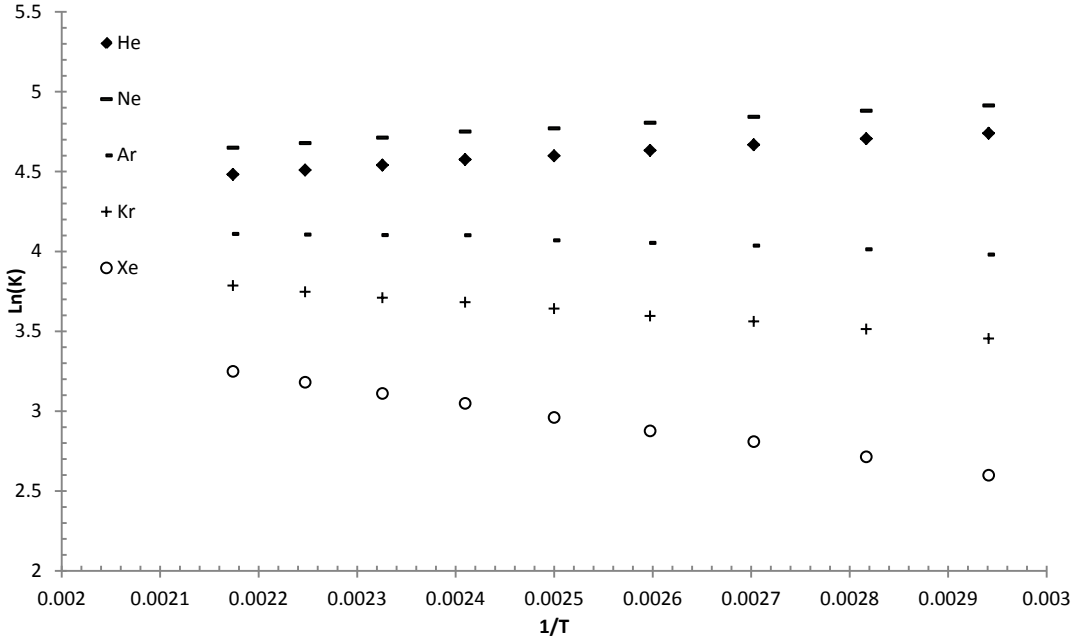

Figure 45. Henry coefficient of each noble gas in *n*-decane at 40 MPa

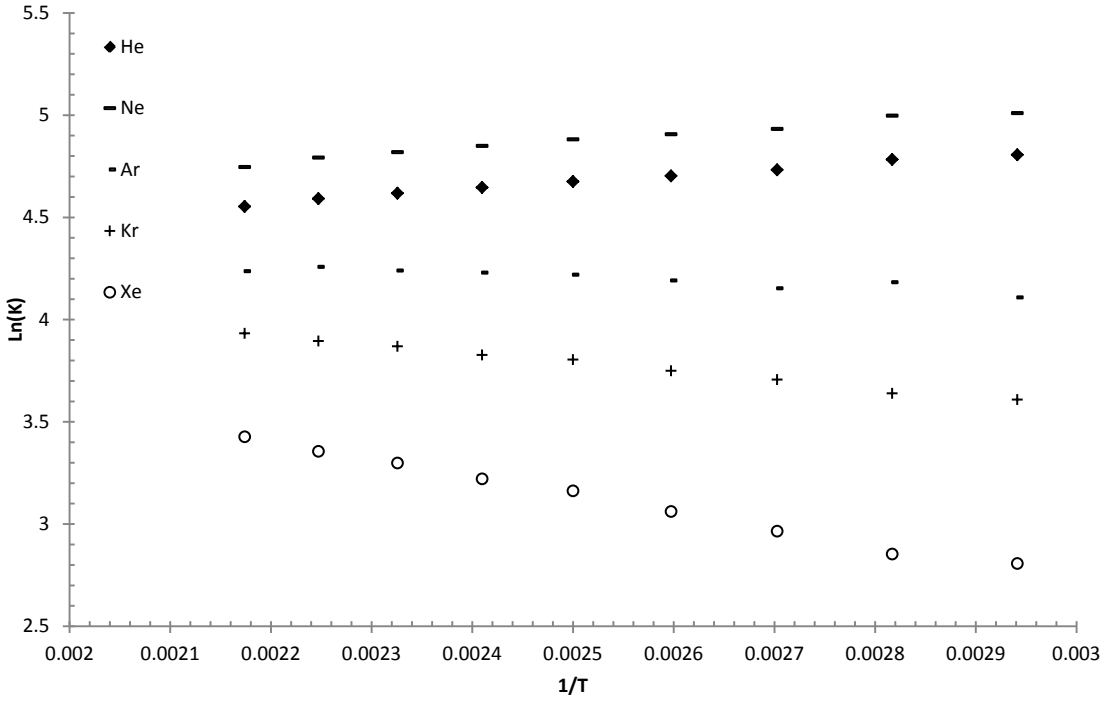

Figure 46. Henry coefficient of each noble gas in *n*-decane at 50 MPa

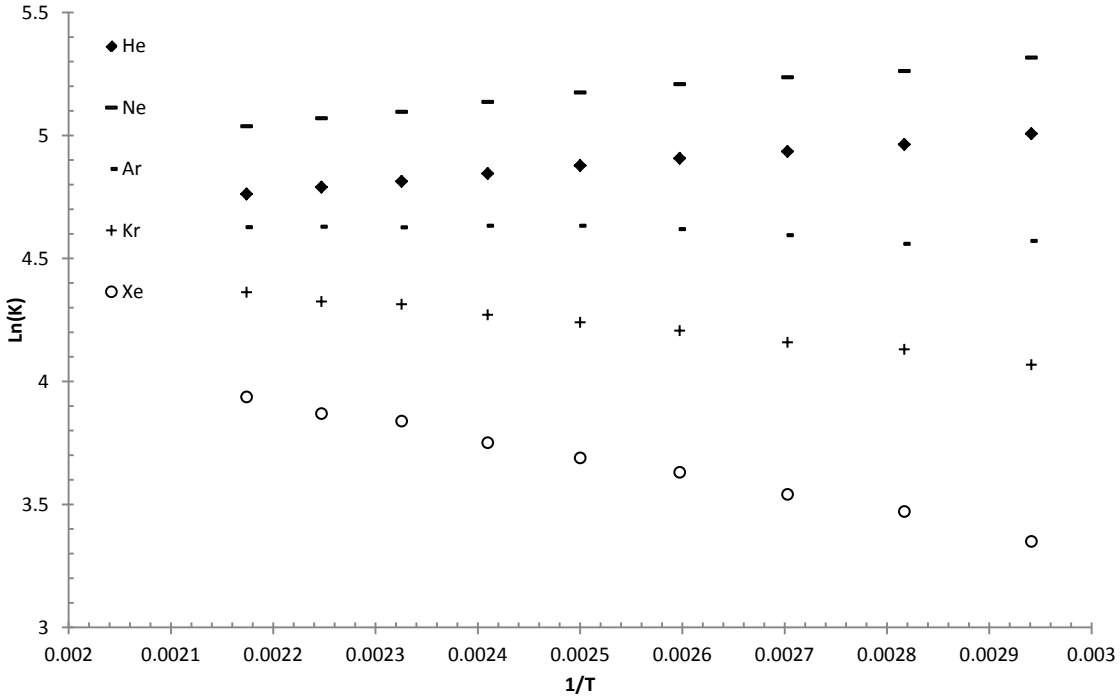

Figure 47. Henry coefficient of each noble gas in *n*-decane at 80 MPa

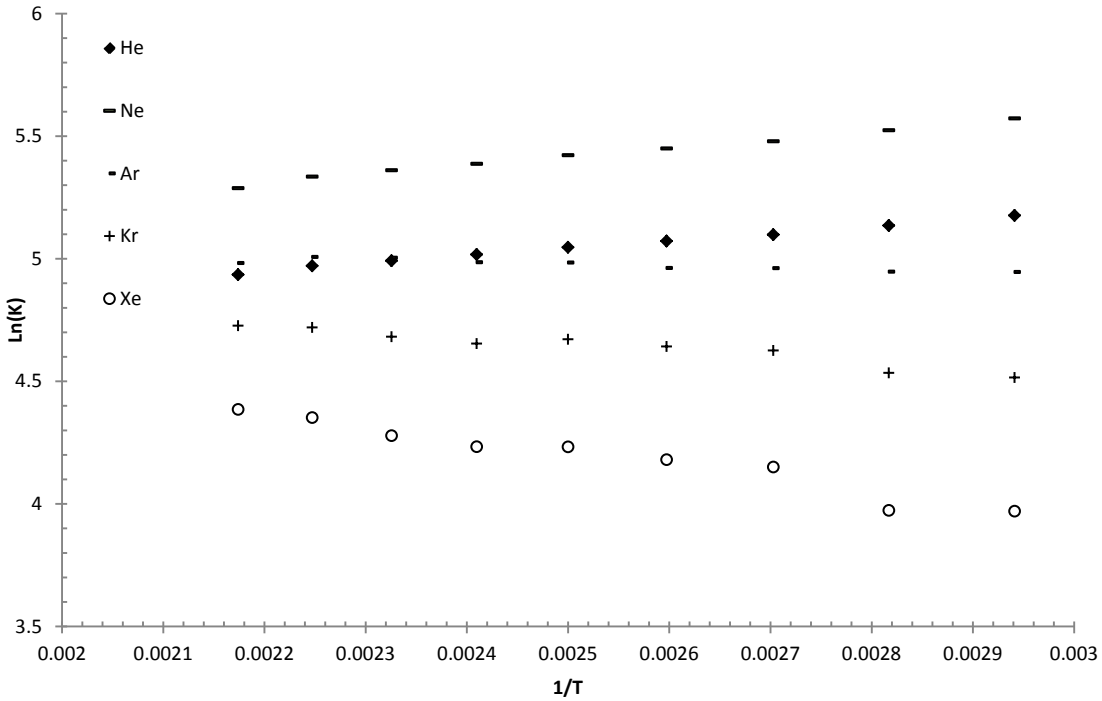

Figure 48. Henry coefficient of each noble gas in *n*-decane at 110 MPa

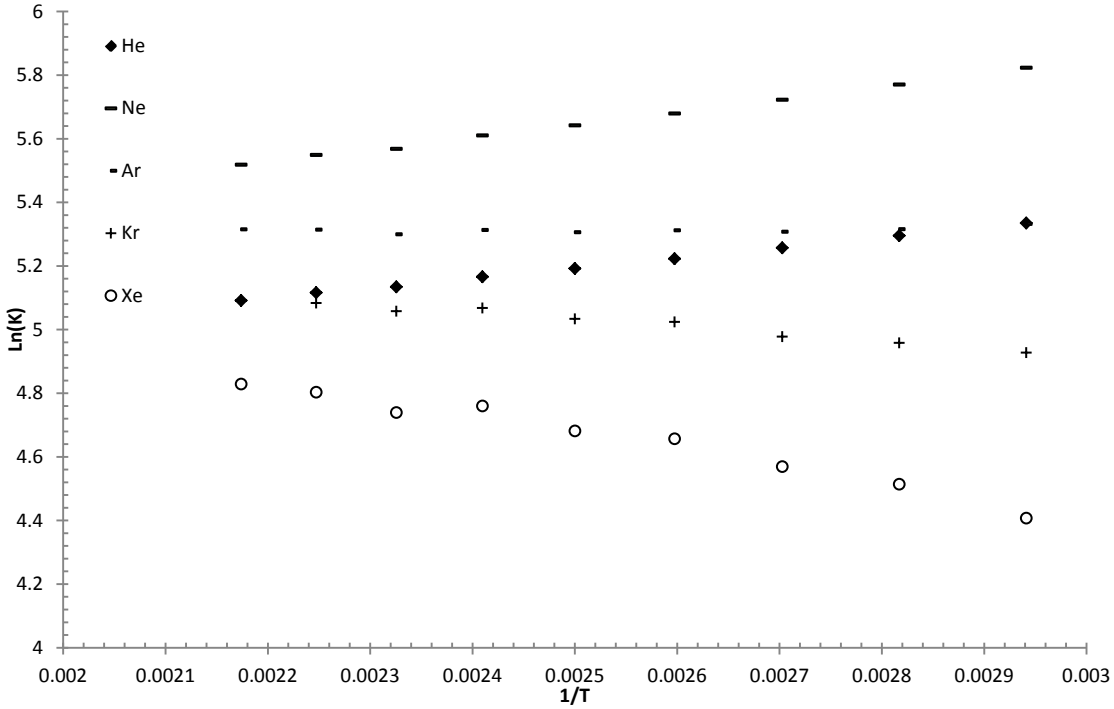

Figure 49. Henry coefficient of each noble gas in *n*-decane at 140 MPa

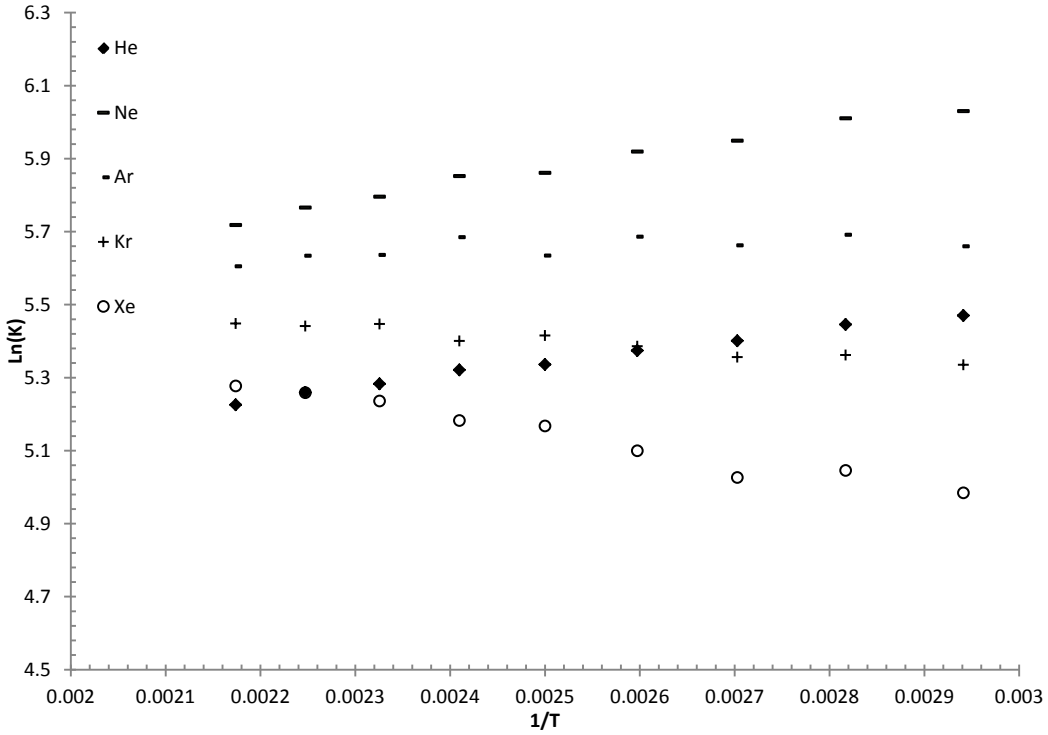

Figure 50. Henry coefficient of each noble gas in *n*-decane at 170 MPa

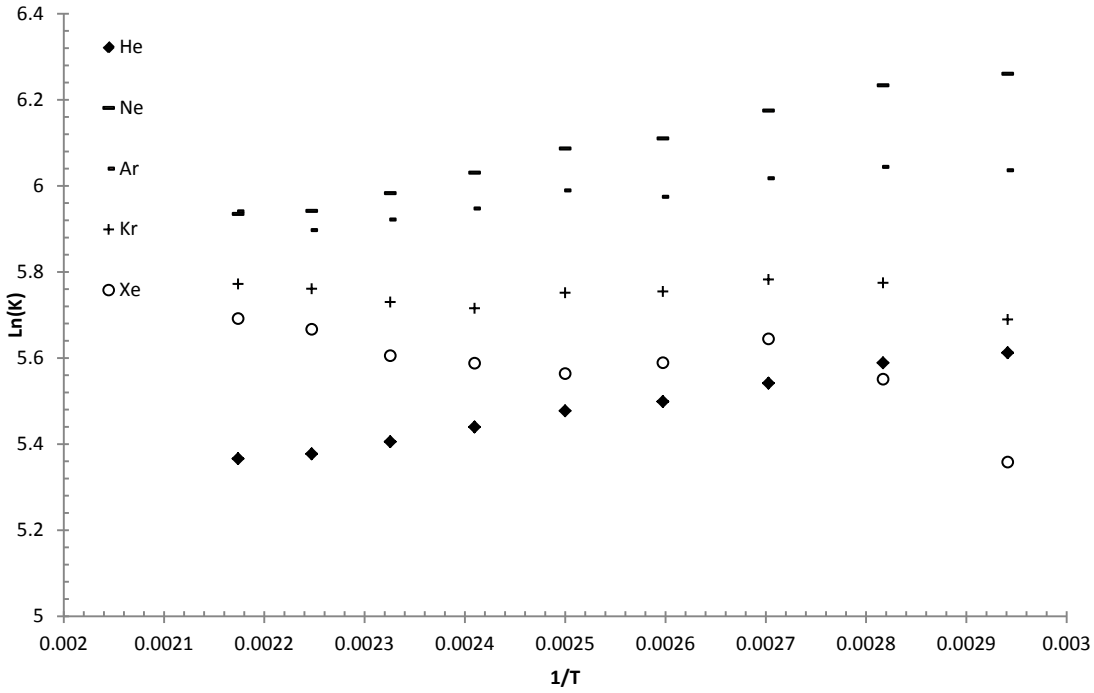

Figure 51. Henry coefficient of each noble gas in *n*-decane at 200 MPa

Table 15. Henry coefficient of Xe in *n*-decane

Pressure (MPa)	Temperature (K)								
	340	355	370	385	400	415	430	445	460
10	6.84	7.60	8.62	9.82	10.67	11.54	12.21	13.17	13.88
20	8.38	9.82	10.67	12.11	13.32	14.29	15.37	16.49	17.02
30	10.54	11.66	13.31	14.83	16.08	17.62	18.36	19.99	20.76
40	114.33	110.48	106.36	102.73	99.32	96.99	93.70	90.83	88.38
50	16.57	17.35	19.40	21.36	23.63	25.06	27.08	28.66	30.78
80	28.49	32.20	34.51	37.76	40.02	42.58	46.48	47.93	51.29
110	53.01	53.18	63.46	65.42	68.91	68.94	72.13	77.64	80.29
140	82.08	91.28	96.47	105.33	107.94	116.73	114.38	121.89	125.11
170	146.12	155.36	152.38	163.95	175.54	178.11	187.96	192.24	195.83
200	212.34	257.43	282.64	267.40	260.79	267.17	271.84	289.01	296.32
Standard Deviation									
10	0.30	0.51	0.23	0.37	0.49	0.31	0.18	0.37	0.30
20	0.44	0.50	0.54	0.47	0.54	0.39	0.45	0.53	0.47
30	0.57	0.56	0.69	0.60	0.92	0.73	0.71	1.01	0.31
40	1.03	1.05	0.69	1.25	0.62	0.80	0.43	0.92	1.09
50	1.32	1.38	0.94	0.64	1.25	0.77	1.02	0.97	1.07
80	3.45	1.74	1.84	3.17	1.41	2.23	1.80	1.54	2.03
110	7.52	4.92	6.42	6.75	3.27	3.12	5.08	3.24	2.66
140	11.02	7.58	11.89	9.21	8.12	6.63	6.98	7.62	7.89
170	36.35	25.05	18.45	21.02	16.17	11.09	8.34	10.73	12.77
200	40.58	80.74	71.21	28.45	32.85	35.68	24.42	26.87	19.46

Table 16. Henry coefficient of Kr in *n*-decane

Pressure (MPa)	Temperature (K)								
	340	355	370	385	400	415	430	445	460
10	18.30	19.07	19.52	21.96	23.19	24.59	24.13	25.38	26.06
20	21.40	24.66	26.09	26.32	29.57	28.62	29.72	30.18	31.14
30	26.09	27.49	29.50	31.31	32.51	34.20	34.54	36.33	36.55
40	13.45	15.09	16.59	17.74	19.29	21.07	22.42	24.06	25.76
50	36.92	38.05	40.72	42.51	44.91	45.92	47.90	49.17	51.04
80	58.43	62.19	64.00	67.14	69.45	71.57	74.73	75.54	78.45
110	91.44	93.19	102.05	103.78	106.84	104.98	107.95	112.17	112.96
140	138.03	142.32	145.18	152.05	153.47	158.80	157.23	161.34	162.57
170	207.45	213.14	211.87	218.30	224.80	221.54	232.01	230.73	232.38
200	295.69	321.95	324.52	315.51	314.65	303.51	307.93	317.61	321.10
Standard Deviation									
10	0.38	0.77	0.61	0.70	0.57	0.73	0.46	0.67	0.44
20	1.02	0.75	0.76	0.73	0.65	0.77	0.90	0.81	0.65
30	1.18	1.07	1.02	0.95	1.27	1.05	0.93	1.45	0.43
40	1.86	1.52	0.83	1.64	0.94	1.08	0.69	1.19	1.60
50	1.98	1.76	1.62	0.89	1.86	1.05	1.33	1.36	1.39
80	3.98	3.30	2.90	3.58	1.88	2.17	1.62	2.20	2.59
110	7.40	5.63	5.01	6.00	4.07	3.48	5.45	3.28	2.66
140	10.81	9.65	9.86	10.19	4.87	7.28	6.12	7.88	5.92
170	20.10	18.16	15.36	17.02	15.00	9.61	6.48	6.35	10.32
200	35.28	46.23	44.28	15.68	29.62	26.21	14.99	18.22	10.13

Table 17. Henry coefficient of Ar in *n*-decane

Pressure (MPa)	Temperature (K)								
	340	355	370	385	400	415	430	445	460
10	32.26	34.11	34.99	35.42	35.94	36.50	37.11	36.87	37.32
20	38.98	40.39	41.35	42.10	42.97	43.14	43.62	44.58	44.70
30	45.80	47.65	49.29	50.19	50.49	50.83	52.15	52.19	52.27
40	53.48	55.26	56.52	57.51	58.43	60.36	60.44	60.61	60.86
50	60.82	65.53	63.59	66.10	67.96	68.65	69.39	70.66	69.13
80	96.60	95.51	98.92	101.39	102.79	102.75	102.09	102.37	102.17
110	140.57	140.72	142.73	142.85	146.04	146.29	148.98	149.47	145.81
140	206.87	203.40	201.81	202.76	201.51	202.94	200.19	203.09	203.36
170	286.97	296.16	287.80	294.65	279.82	294.27	280.34	279.71	271.74
200	418.14	421.45	410.37	393.12	398.99	382.60	372.84	363.89	380.05
Standard Deviation									
10	0.60	0.93	0.79	0.35	1.32	0.84	0.93	0.64	0.87
20	1.71	1.69	1.56	1.78	1.08	0.94	0.88	1.00	0.78
30	1.39	1.95	1.79	1.84	1.78	1.11	1.35	1.16	1.10
40	3.25	1.89	1.34	1.70	1.52	1.18	1.58	1.84	1.35
50	3.11	2.76	2.01	1.70	1.79	1.73	1.74	1.95	1.40
80	4.92	2.12	3.76	6.83	2.78	3.27	3.93	3.35	2.75
110	9.63	6.52	12.34	7.82	5.52	4.97	4.40	3.41	5.30
140	11.45	9.97	9.88	9.73	8.13	7.87	8.00	7.57	6.67
170	15.57	20.02	15.17	22.51	7.59	10.72	12.62	9.46	5.03
200	24.87	42.16	21.87	20.73	26.22	16.52	17.98	10.05	9.08

Table 18. Henry coefficient of Ne in *n*-decane

Pressure (MPa)	Temperature (K)								
	340	355	370	385	400	415	430	445	460
10	94.55	92.16	88.35	84.59	81.18	78.37	75.81	72.28	70.08
20	108.48	104.81	100.52	96.98	93.42	89.42	86.47	84.50	81.45
30	121.96	117.92	114.46	110.26	105.63	101.84	99.47	95.87	92.53
40	136.02	131.62	126.67	122.01	117.82	115.48	111.22	107.45	104.39
50	149.85	148.00	138.70	135.11	131.76	127.66	123.77	120.53	115.06
80	203.54	192.76	187.97	182.72	176.71	170.06	163.34	159.13	154.06
110	262.92	250.52	239.62	232.70	226.39	218.55	212.88	207.38	197.89
140	337.96	320.50	305.60	292.65	281.98	273.13	261.87	256.85	249.20
170	415.62	407.63	383.27	371.99	350.90	347.86	328.76	319.11	304.22
200	523.23	509.38	480.24	450.21	439.81	415.85	396.48	380.51	377.74
Standard Deviation									
10	1.37	1.72	1.58	0.60	2.16	1.34	1.60	1.01	1.31
20	3.09	2.79	2.67	2.80	1.80	1.35	1.30	1.25	1.09
30	2.12	3.01	2.70	2.47	2.45	1.53	1.72	1.62	1.51
40	4.88	2.90	1.70	1.92	2.16	1.47	1.79	2.20	1.63
50	3.96	3.07	2.41	2.38	2.24	2.19	2.10	1.94	1.62
80	4.74	3.37	3.64	6.67	3.03	3.36	3.66	3.21	2.55
110	6.31	5.09	9.92	6.43	4.54	4.11	3.14	2.78	4.36
140	7.07	7.86	6.90	6.70	7.41	5.12	5.62	4.98	5.03
170	7.49	16.11	12.25	15.89	4.83	5.70	6.84	5.06	3.48
200	12.01	22.86	11.64	9.80	12.93	9.91	9.56	6.20	4.88

Table 19. Henry coefficient of He in *n*-decane

Pressure (MPa)	Temperature (K)								
	340	355	370	385	400	415	430	445	460
10	88.94	86.08	82.43	78.99	75.70	73.05	70.59	67.48	65.32
20	97.81	94.20	90.39	87.24	83.94	80.69	77.97	76.04	73.36
30	106.25	102.34	99.08	95.49	91.82	88.70	86.44	83.52	80.79
40	114.33	110.48	106.36	102.73	99.32	96.99	93.70	90.83	88.38
50	122.24	119.51	113.56	110.28	107.28	104.22	101.30	98.66	94.96
80	149.46	143.11	139.07	135.25	131.34	127.12	123.13	120.28	116.98
110	177.08	169.92	163.75	159.50	155.49	150.97	147.24	144.16	139.08
140	207.46	199.43	191.93	185.42	179.82	175.21	169.75	166.73	162.63
170	237.53	231.71	221.57	215.75	207.67	204.63	196.92	192.33	185.95
200	273.72	267.34	254.99	244.30	239.17	230.31	222.58	216.38	213.95
Standard Deviation									
10	0.90	1.07	0.98	0.37	1.43	0.86	1.05	0.70	0.89
20	1.82	1.69	1.64	1.62	1.16	0.85	0.81	0.77	0.72
30	1.04	1.60	1.54	1.36	1.29	0.94	0.99	1.01	0.94
40	2.28	1.64	0.92	1.12	1.26	0.81	1.07	1.23	0.98
50	1.90	1.44	1.15	1.21	1.09	1.14	1.10	1.06	0.91
80	1.86	1.52	1.57	2.82	1.37	1.50	1.59	1.58	1.23
110	2.00	1.81	3.53	2.34	1.65	1.57	1.24	1.13	1.83
140	2.42	2.53	1.87	2.39	2.69	1.81	1.97	1.83	2.32
170	1.92	4.65	3.83	4.93	1.60	1.99	2.41	1.59	1.43
200	3.96	6.14	3.82	3.02	3.78	2.93	2.99	2.08	1.69

As the solubility coefficient is an equilibrium constant, the gradient of the $\ln K \; vs. \left(\frac{1}{T}\right)$ represents the excess enthalpy of solvation at infinite dilution and its intercept represents the excess entropy of solvation. The plots of all the solubility coefficients were adequately fitted with linear trend where the gradient and interception are reported in Figure 52 to Figure 56. The entropy and enthalpy of solvation are reported in Table 20. It should be noted that in the cases of Xe and Kr at 200 MPa where a maximum was observed, linear trends were not fitted.

Table 20. Excess enthalpy (kJ/mol) and entropy (J/mol K) of solvation at infinite dilution

	Pressure (MPa)									
	10	20	30	40	50	80	110	140	170	200
					Xe					
ΔH	-7.98	-7.73	-7.52	-6.93	-6.98	-6.20	-4.53	-4.40	-3.35	N/A
ΔS	-38.99	-40.66	-41.78	-42.02	-43.62	-46.21	-46.32	-49.88	-51.21	N/A
					Kr					
ΔH	-4.11	-3.63	-3.79	-3.49	-3.59	-3.11	-2.25	-1.81	-1.29	N/A
ΔS	-36.18	-36.68	-38.35	-39.02	-40.49	-43.02	-44.26	-46.35	-48.15	N/A
					Ar					
ΔH	-1.43	-1.43	-1.37	-1.75	-1.41	-0.77	-0.64	0.14	0.61	1.52
ΔS	-33.32	-34.77	-36.00	-37.41	-38.49	-40.26	-42.99	-43.81	-45.48	-45.84
					Ne					
ΔH	3.33	3.15	3.01	2.87	2.83	2.95	2.90	3.29	3.40	3.83
ΔS	-28.18	-29.79	-31.19	-32.48	-33.45	-35.54	-37.77	-38.69	-40.28	-40.91
					He					
ΔH	3.40	3.14	2.97	2.79	2.71	2.62	2.51	2.64	2.64	2.83
ΔS	-27.44	-28.95	-30.14	-31.24	-32.07	-33.95	-35.66	-36.58	-37.78	-38.92

The data from Table 20 are plotted in Figure 57 and Figure 58. The overall trends of entropies of these systems are similar amongst the different noble gases. While the values are varying with the sizes of solutes, there were neither maximum nor minimum observed. The reduction in entropy implies that the solvent helps structure the solution, particularly in the case of Xe and Kr mixture.

A minimum in enthalpy was observed at pressure of 110 MPa for He and 50 MPa for Ne. These minima were not observed in other systems. Positive enthalpies, indicating endothermic reactions, were observed in the He and Ne systems. On the other hand, exothermic reactions are observed in Xe and Kr systems with negative enthalpies. Enthalpies of solvation for Ar are slightly negative at lower pressure region (between 10 MPa and 110 MPa) and slightly positive at higher pressures for Ar system.

The behaviour of the solubility coefficients of Xe and Kr in *n*-decane at infinite dilution, except for the maxima at 200 MPa, are as expected. In fact, the Lennard-Jones ε values for Xe and Kr are much larger than for the CH_3 group as is shown in Table 12. The dissolution process may be broken down into two processes – the formation of cavity to accommodate the solute and the interaction between the solute and solvent molecules. For Xe and Kr, the energy required for cavity formation for larger gases is compensated by the favoured induced dipole-induced dipole dispersion forces. These dispersion forces are larger for bigger gases as their valence electrons are further apart from the nuclei and thus easier to form temporary dipole-induced dipole – easier to polarize.

On the other hand, the energy required to form the cavity during the dissolution for smaller and less polarizable gases such as He and Ne are not compensated by intermolecular interactions between solvents and solutes. And thus the endothermic interactions are observed, consistent with the solvation enthalpy calculations. It is interesting to note the change in enthalpies of Ar system as it is neither the largest nor the smallest gas in the noble gas group. The ε value for Ar is nearly identical to that of the CH_3 group as noted in Table 12. The results seem to indicate that Ar is at the region where the energy required for cavity formation and that resulting from the interaction between solvent and solute molecules are nearly identical.

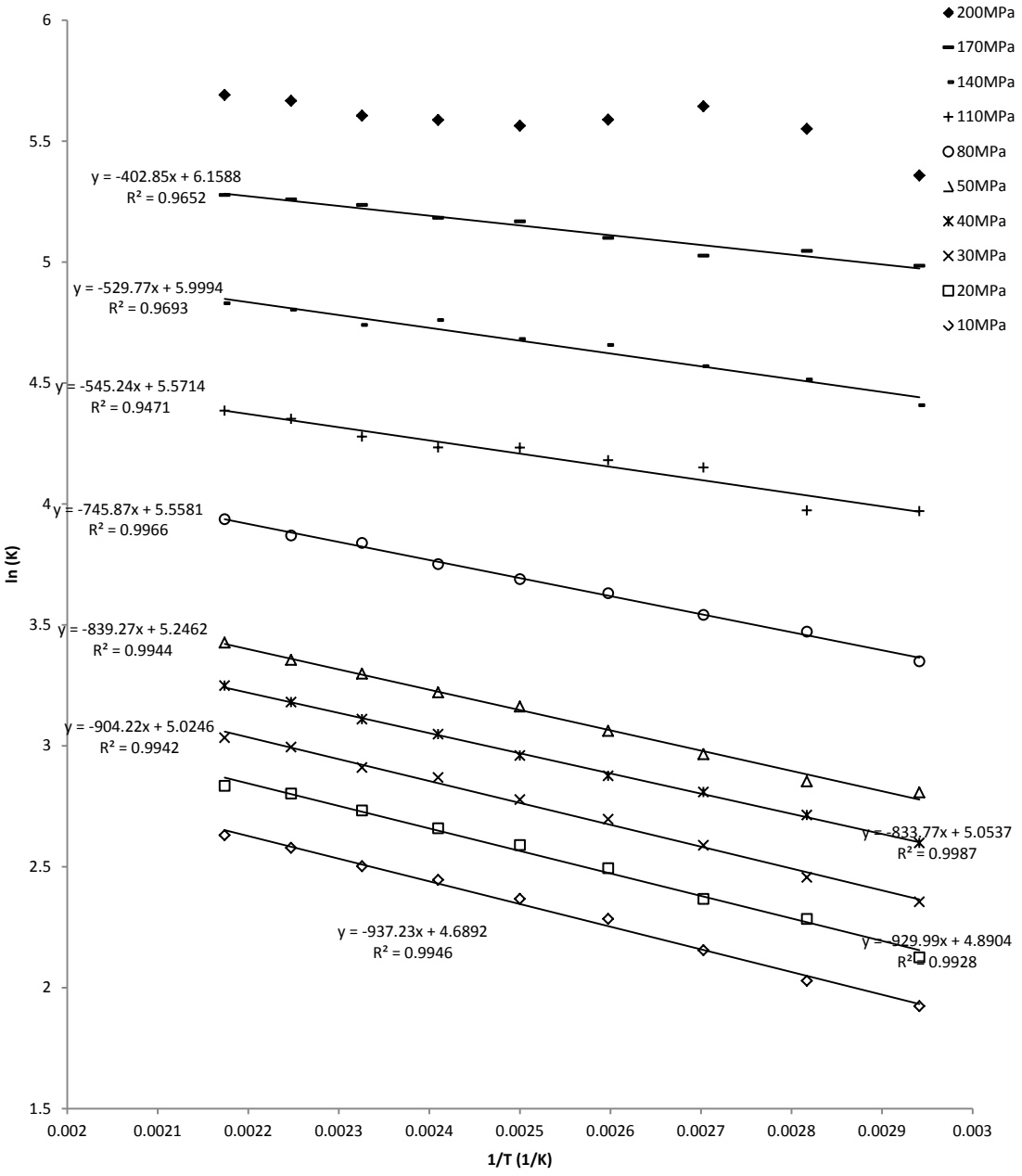

Figure 52. ln(K) vs. 1/T for Xe in *n*-decane fitted with linear trend at various temperatures

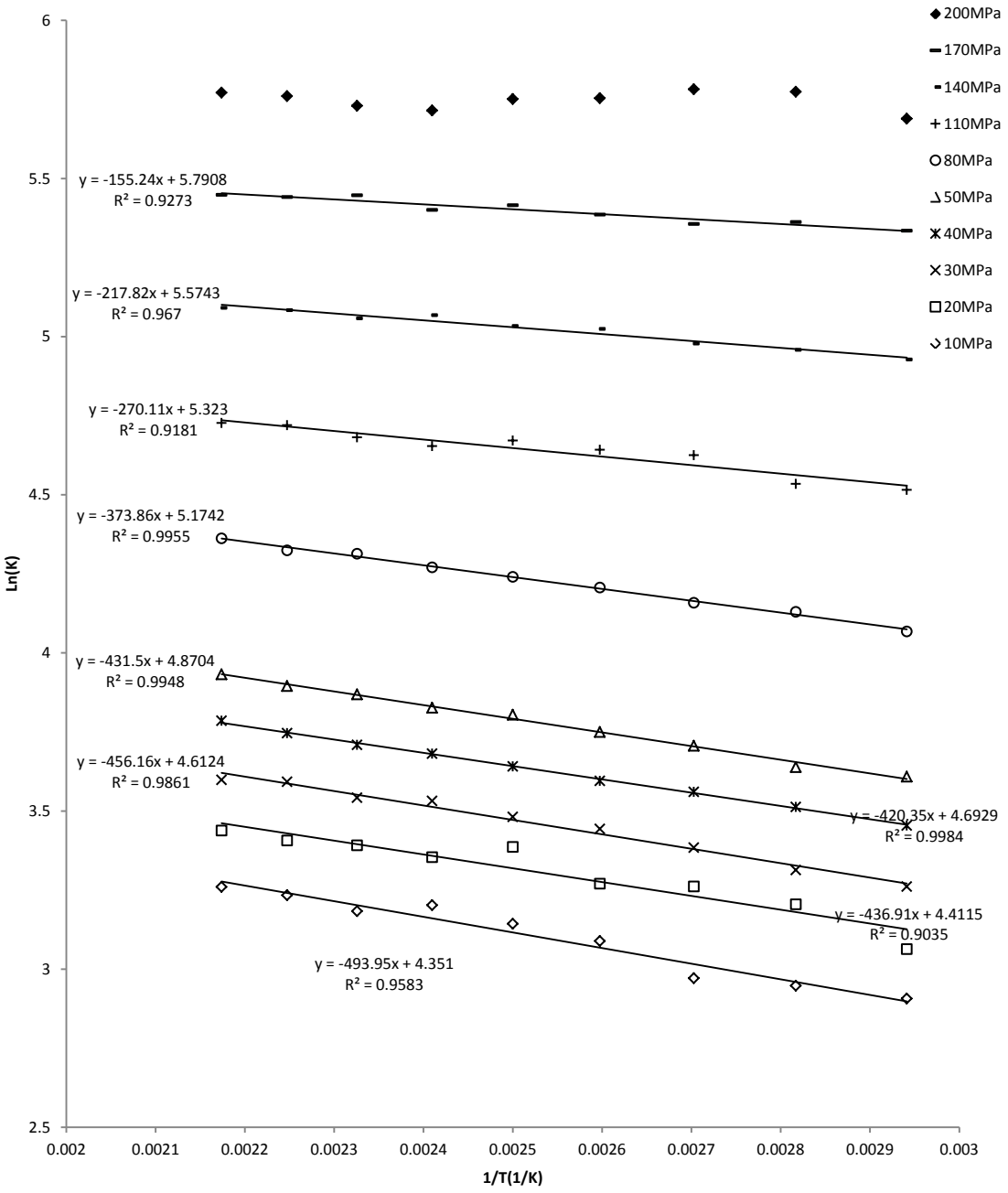

Figure 53. ln(K) vs. 1/T for Kr in *n*-decane fitted with linear trend at various temperatures

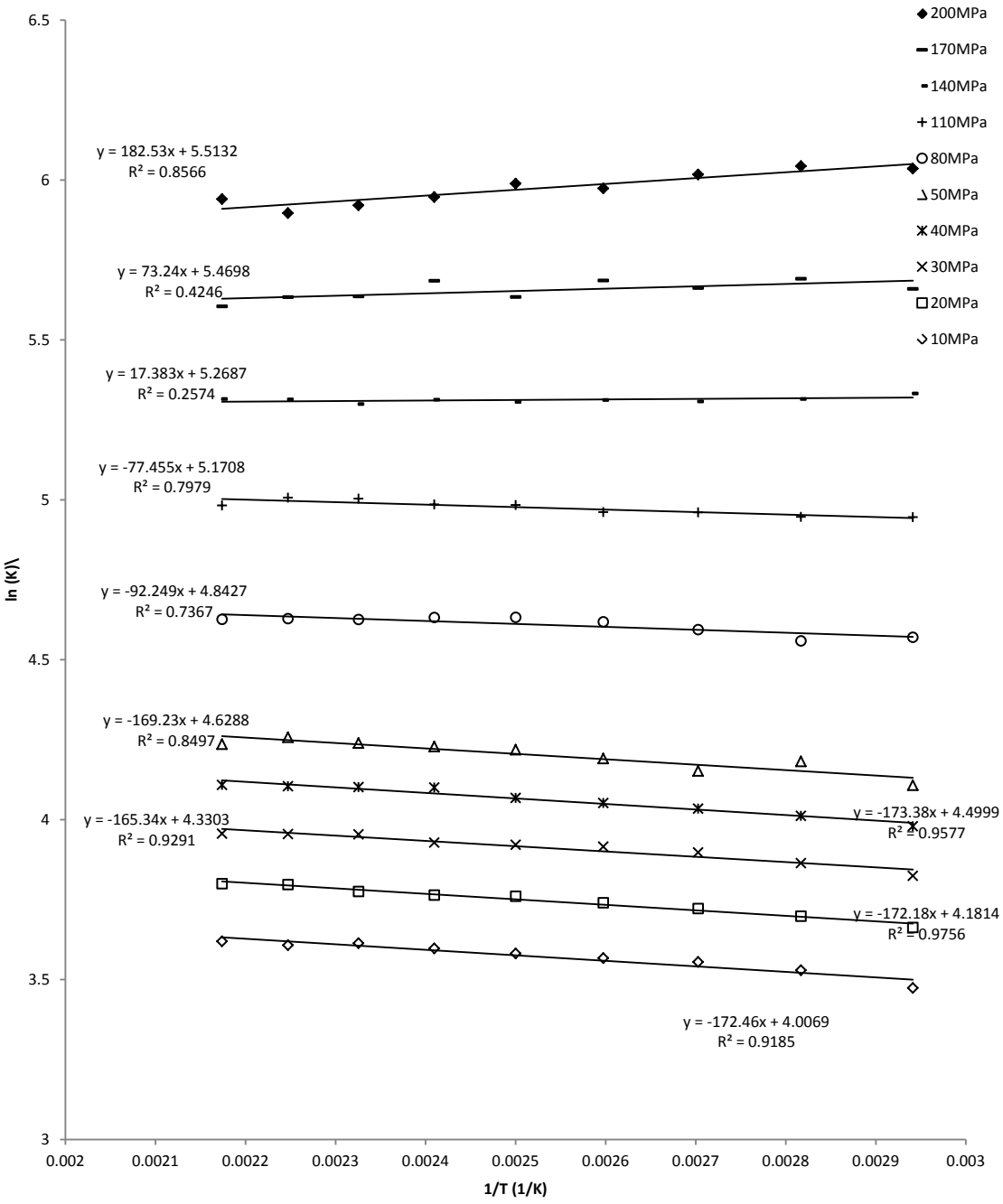

Figure 54. ln(K) vs. 1/T for Ar in *n*-decane fitted with linear trend at various temperatures

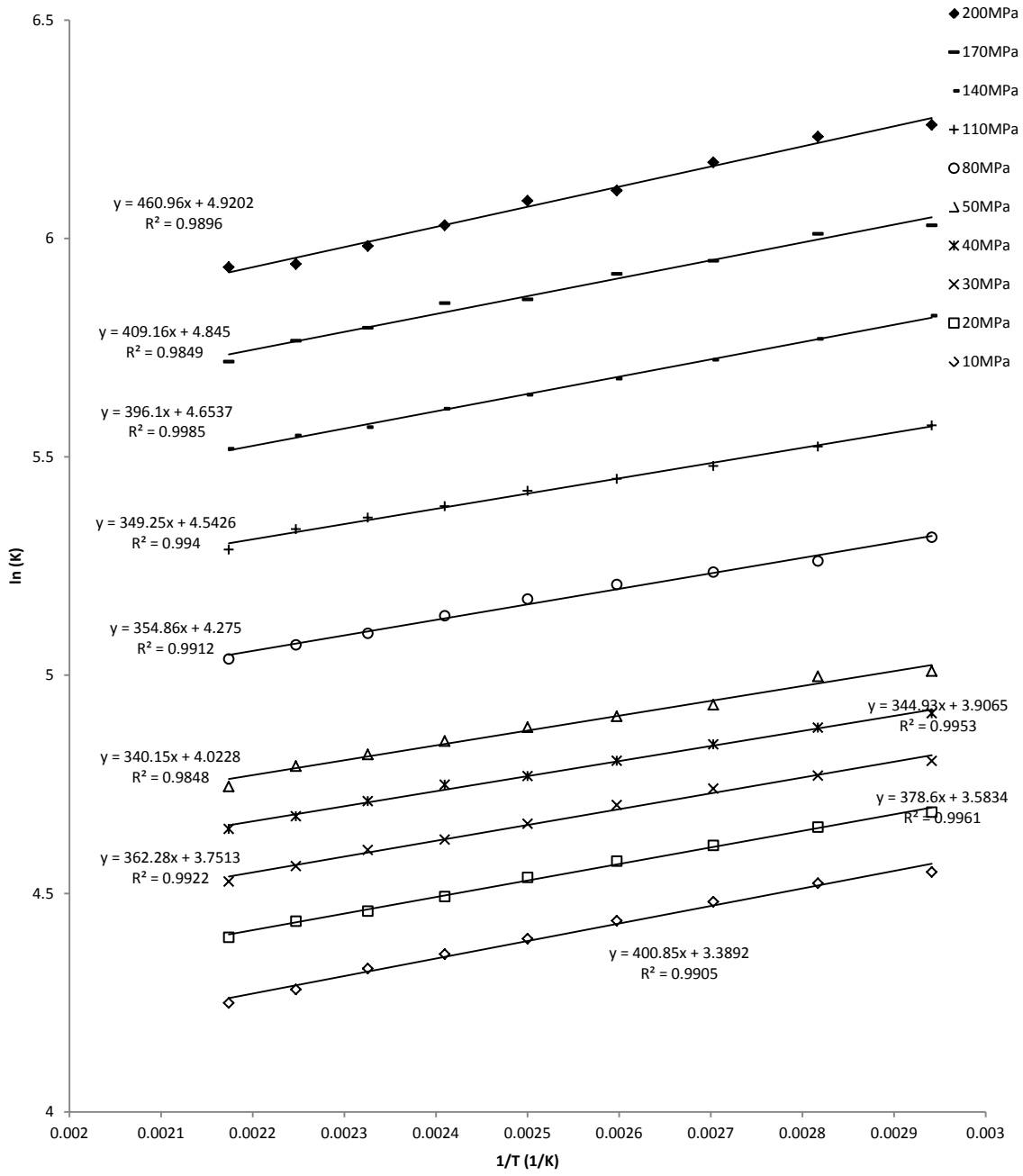

Figure 55. ln(K) vs. 1/T for Ne in *n*-decane fitted with linear trend at various temperatures

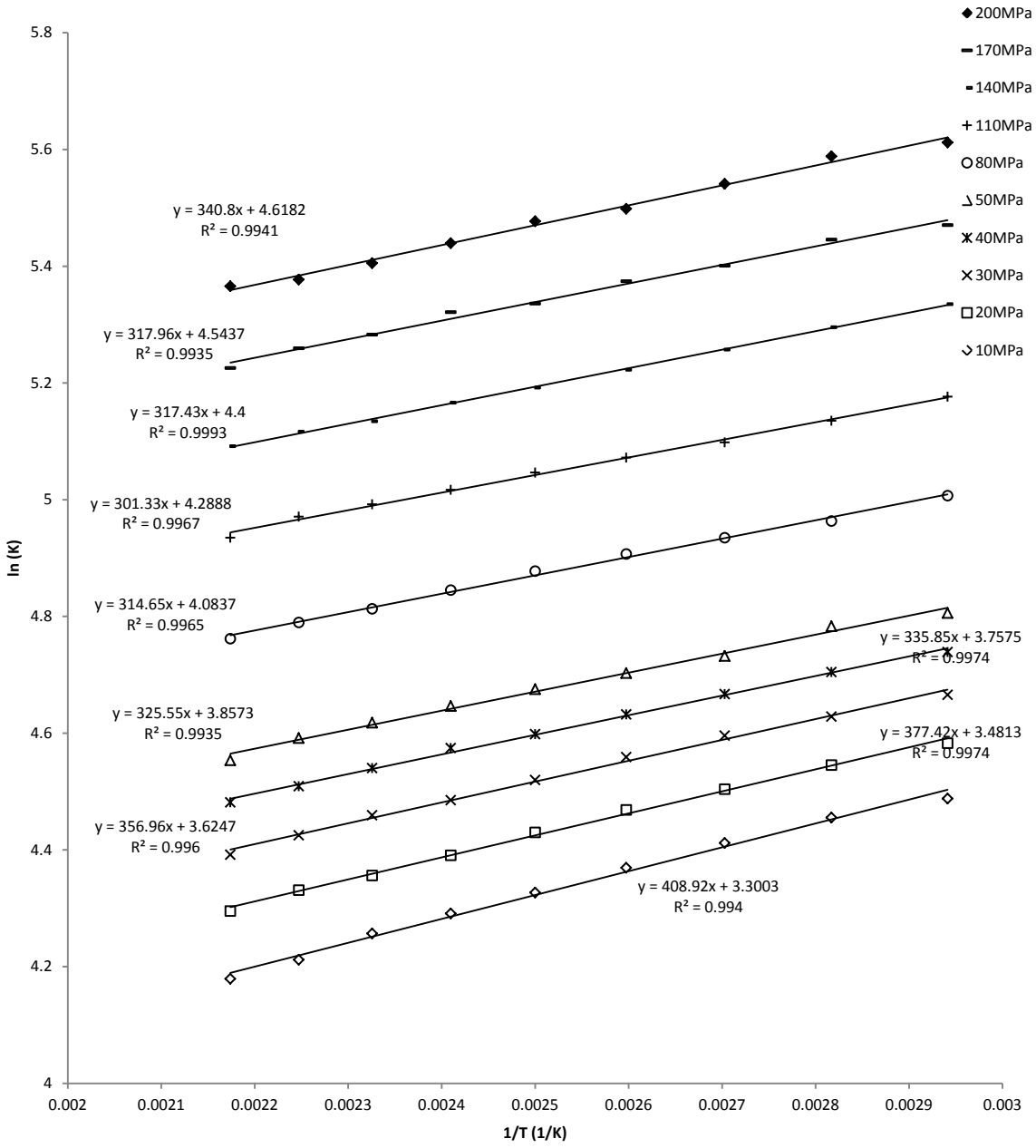

Figure 56. ln(K) vs. 1/T for He in *n*-decane fitted with linear trend at various temperatures

Table 21. Lennard-Jones potential parameters used in this study.

Noble Gas	ε (K)	σ (Å)	Reference
He	10.22	2.556	(Kell et al., 1978)
Ne	35.7	2.789	(Skoulidas & Sholl, 2002)
Ar	124.07	3.42	(Skoulidas & Sholl, 2002)
Kr	164.7	3.635	(Potter & Clynne, 1978)
Xe	227.856	3.9478	(Bonifácio et al., 2002)
CH_3	114	3.93	(Siepmann, 1993; Smit et al., 1995)
CH_2	47	3.93	(Siepmann, 1993; Smit et al., 1995)

The interesting feature is the maximum observed in the plots of $\ln K \ vs. 1/\mathrm{T}$ for Xe and Kr at infinite dilution. While the errors are larger in the maximum region between 340 K – 385 K than other area, they are of the same number of cycles as other points reported here. What is interesting here is that a similar maximum on the Xe plot was also reproduced, although smaller, on the Kr plot as well. There is no immediate explanation as to what causes these irregularities for heavier gases. No other literature for similar system and in similar conditions has been found. Further investigation including additional points and longer simulation cycles to reduce the errors in these regions, if at all possible, will have to be completed.

Interestingly, Bonifácio et al. observed a maximum of entropy of solvation at infinite dilution for Xe + *n*-pentane and Xe + *n*-hexane binary mixtures at 101kPa which correspond to the solvent reduced temperature, T_r, of 0.54 (Bonifácio et al., 2010). What is more, this value of T_r is in the region where excess enthalpies of several equimolar *n*-alkanes binary mixtures approach zero. However, our solvents' reduced temperatures, given in Table 22, are well beyond $T_r = 0.54$.

Table 22. Reduced temperature of *n*-decane between 340 K – 460 K

Temperature (K)	340	355	370	385	400	415	430	445	460
n-decane	0.55	0.57	0.60	0.62	0.65	0.67	0.70	0.72	0.74

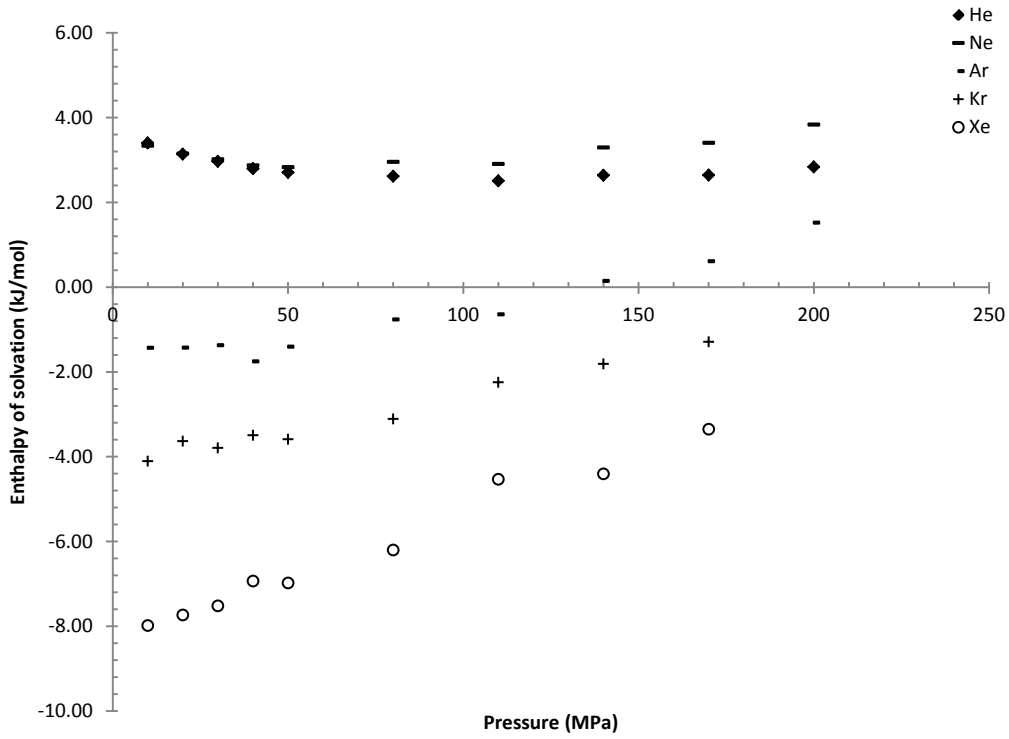

Figure 57. Enthalpy of solvation for all noble gases in *n*-decane

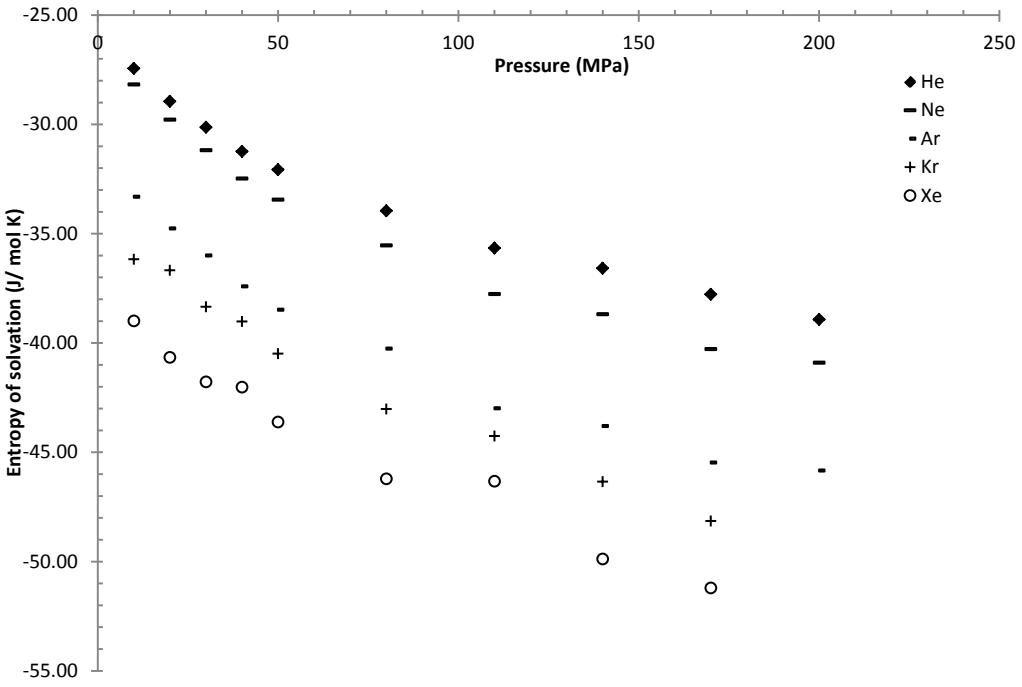

Figure 58. Entropy of solvation for all noble gases in *n*-decane

6.1. Critical temperature correlation

Overall, our solubility coefficient results are remarkably similar to that of (Makrodimitri et al., 2007) where solubility coefficients at infinite dilution for the noble gases in PDMS polymer was measured. Their measurements were completed at pressures between 0.1 MPa - 40 MPa and temperatures between 300 K – 450 K as depicted in Figure 59.

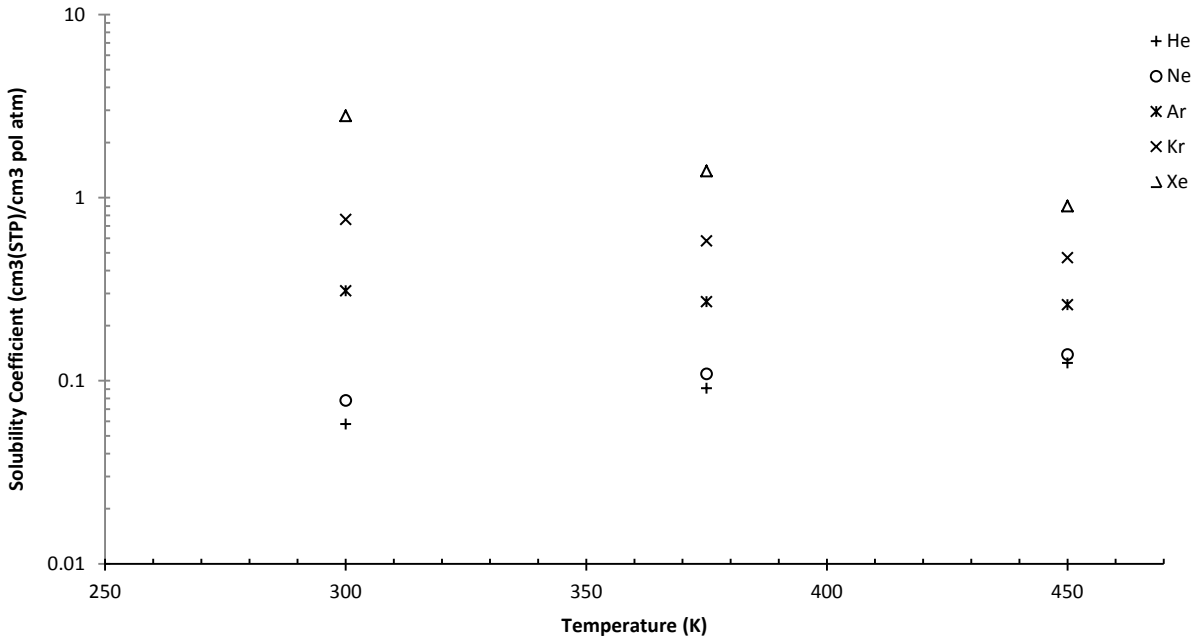

Figure 59. Infinite dilution solubility coefficients of noble gases in PDMS at 0.1 MPa redrawn from (Makrodimitri et al., 2007).

The two systems are similar in that the PDMS polymer is a long nonpolar molecule, analogous to *n*-decane in our binary mixtures. Makrodimitri et al. (2007) also noted the relation between critical temperature, T_c, of solute and the solubility of noble gases in polymer. Kamiya et al. (2000) and Makridimitri et al (2007) reported slope of $\frac{d(\log S_0)}{dT_c}$ equal to 0.0076 and 0.007 respectively for noble gases in PDMS (Kamiya et al., 2000; Makrodimitri et al., 2007). Surprisingly similar, Can Amerongen reported the slope of 0.0071 for H_2, O_2, N_2, CO_2, CH_4, C_2H_6, and

C_3H_8 in rubber (Van Amerongen, 1946). Additionally, Merkel et al. (2000) also reported the slope of 0.0062 for H_2, O_2, N_2, CO_2, CH_4, C_2H_6, and C_3H_8 in PDMS (Merkel et al., 2000). The solubility coefficient (S_0) at infinite dilution can be expressed as

$$S_0 = \frac{22400 \frac{cm^3(STP)}{mol}}{RT} \lim_{x_{solute} \to 0} \exp(-\beta \mu^{ex}_{solute}) \quad (89)$$

.

Where

STP = standard conditions which is taken as 101.325 kPa and 273.15 K

S_0 is reported in the units of $cm^3(STP)/(cm^3\ pol\ atm)$

Although critical temperature is a derivative of the size of the gas where a larger gas has a higher critical temperature and lower solubility than a smaller gas, it is interesting to note these correlations. $\ln(K)\ vs.\ T_c$ was plotted in Figure 60 where linear trends were fitted to the 340 K trials at pressure of 10, 50, and 200 MPa. It is clear that we do not have a linear correlation between $\ln(K)$ and T_c, particularly at lower critical temperature region. However, the slope of the linear trends are similar in magnitude to that reported by (Kamiya et al., 2000; Van Amerongen, 1946; Makrodimitri et al., 2007).

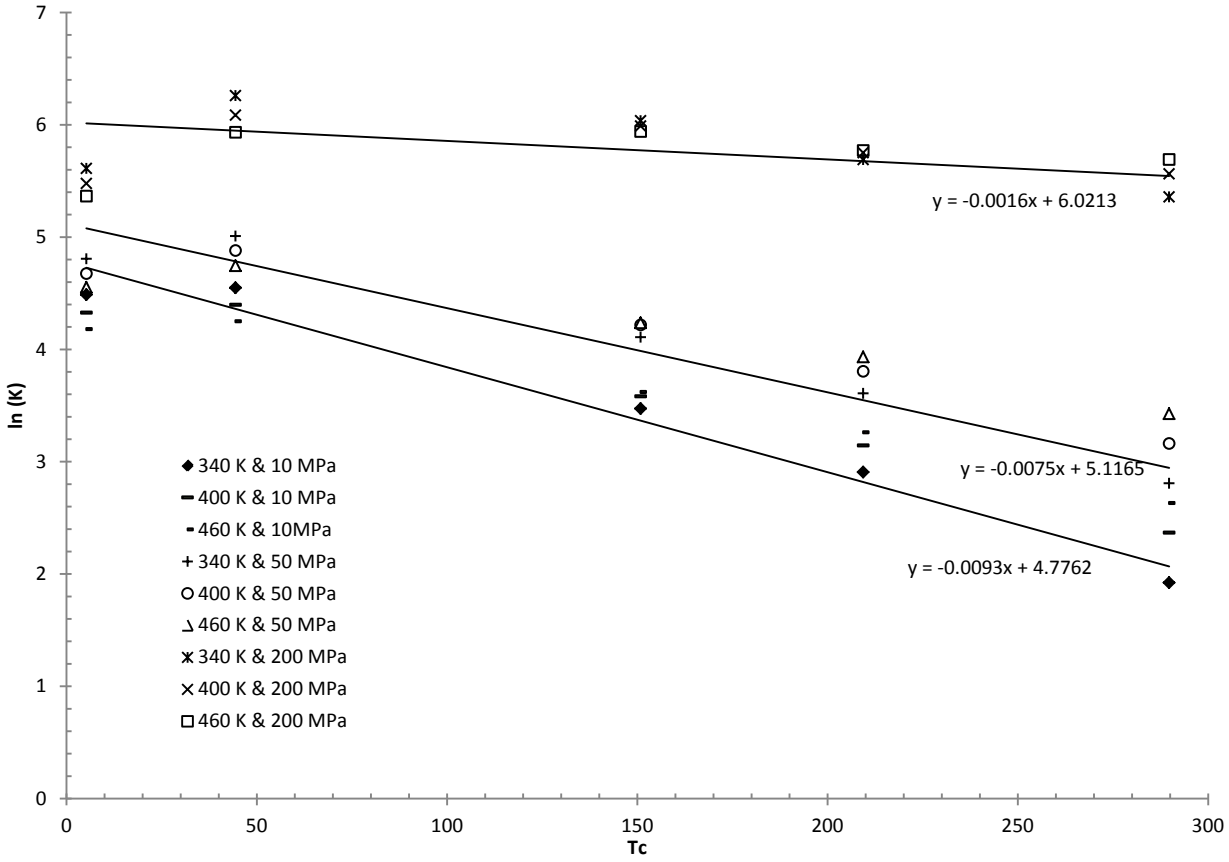

Figure 60. $\ln(K)$ $vs.$ T_c for all noble gases at 10, 50, and 200 MPa (linear trends were fitted to the 340 K cases)

Following the work of Chandler & Andersen (1972) Schweizer & Curro (1994) proposed the Polymer reference interaction site (PRISM) theory (Chandler & Andersen, 1972; Schweizer & Curro, 1994). PRISM theory makes a number of predictions about the solubilities of noble gases in polyethylene (Curro et al., 1997). These include

- increase of solubility as the size of solute increases
- monotonicity increase of solubility as a function of critical temperature (T_c) of solute.
- direct correlation between temperature and solubility for solutes with $T_c \sim$ 65 K and vice versa as depicted in Figure 61.

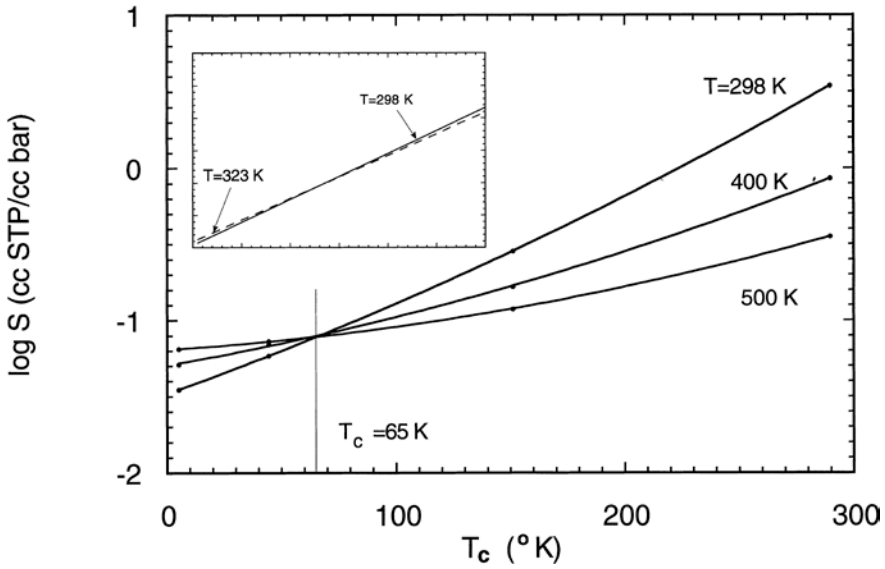

Figure 61. Solubility as a function of critical temperature and the crossover at approximately 65 K, adopted from (Curro et al., 1997)

Positive temperature and solubility correlation was observed amongst the solute gases having $T_c < 65$ K and vice versa (Curro et al., 1997). However, it was noted that the dependency on T_c reduces as temperature increases.

The critical temperatures of the noble gases are given Table 23 below. Only He and Ne have $T_c < 65$ K, where, according to PRISM theory, positive correlation between temperature and solubility would be predicted in polyethylene. And indeed, He and Ne are the only two noble gases which show the positive correlation. Additionally, the trend is reversed for Kr and Xe where $T_c > 65$ K. What is interesting is that a switching correlation between temperature and solubility is observed in Ar – a slightly negative correlation was observed at lower pressure and this slowly switched to a slightly positive correlation as the pressure increases.

Table 23. Critical temperature of noble gases

Molecular formula	Molecular weight	T_c (K)
Xe	131.29	289.74
Kr	83.8	209.35
Ar	39.948	150.86
Ne	20.1797	44.4
He	4.0026	5.2

Several authors including (Clarke & Glew, 1966; Krause & Benson, 1989) have proposed a smoothing function, describing the temperature dependence of Henry coefficients within a small temperature region. Clarke & Glew described Henry coefficients was given as (Clarke & Glew, 1966)

$$\ln\left[K_{2,1}(T, p_1^{sat})\right] = A_0 + \frac{A_1 \times 10^2}{T} + A_2 \ln\left(\frac{T}{100}\right) + A_3 \left(\frac{T}{100}\right) + \cdots \tag{90}$$

The simulated Henry coefficients were fitted to Equation (90) and the parameters are given in Table 24. Only two parameters are used as the fit between two and three parameters are nearly identical and the gradients are linear as previously discussed and adequately fitted with linear trends. The accuracy tends to increase as the size of the solute decreases.

Another smoothing function was given by (Krause & Benson, 1989) as referenced in (Costa Gomes & Grolier, 2001) as

$$\ln\left[K_{2,1}(T, p_1^{sat})\right] = \sum_i^n \frac{B_i}{T} \tag{91}$$

This smoothing function however is far less accurate for our mixtures.

Table 24. Fitted coefficients and average absolute deviation percentage for equation (90) as given by (Clarke & Glew, 1966)

	Pressure (MPa)									
	10	**20**	**30**	**40**	**50**	**80**	**110**	**140**	**170**	**200**
					Xe					
A0	4.689	4.890	5.025	5.054	5.246	5.558	5.571	5.999	6.159	6.307
A1	-9.371	-9.300	-9.042	-8.338	-8.393	-7.458	-5.452	-5.297	-4.028	-2.865
AAD%	0.335	0.373	0.242	0.114	0.301	0.134	0.365	0.270	0.161	0.552
					Kr					
A0	4.351	4.411	4.612	4.693	4.870	5.174	5.323	5.574	5.790	5.815
A1	-4.938	-4.369	-4.562	-4.203	-4.315	-3.738	-2.700	-2.177	-1.550	-0.267
AAD%	0.345	0.553	0.141	0.050	0.120	0.069	0.159	0.088	0.110	0.242
					Ar					
A0	4.007	4.181	4.330	4.500	4.629	4.842	5.170	5.268	5.469	5.513
A1	-1.723	-1.721	-1.653	-1.733	-1.692	-0.921	-0.773	0.175	0.735	1.827
AAD%	0.125	0.068	0.148	0.124	0.202	0.159	0.093	0.055	0.178	0.095
					Ne					
A0	3.389	3.583	3.751	3.906	4.023	4.275	4.543	4.654	4.845	4.920
A1	4.010	3.786	3.623	3.449	3.402	3.549	3.493	3.961	4.092	4.610
AAD%	0.067	0.053	0.088	0.065	0.092	0.074	0.058	0.027	0.110	0.061
					He					
A0	3.300	3.481	3.625	3.758	3.857	4.084	4.289	4.400	4.544	4.618
A1	4.090	3.774	3.570	3.358	3.255	3.147	3.013	3.174	3.180	3.408
AAD%	0.055	0.056	0.060	0.047	0.060	0.046	0.040	0.015	0.062	0.043

6.2. Partial molar volume

In addition to $\ln(K)\ vs.\ 1/T$, $\ln(K)\ \ vs.P$ are also plotted as shown in Figure 62 to Figure 66. The trends are adequately fitted by quadratic equations as displayed on the plots. The gradients of these plots represent the volume change with the compressibility correction factor which can be written as

$$\left(\frac{\partial \ln(K)}{\partial \mathrm{P}}\right)_T = \frac{V^{m,\infty}}{RT} \tag{92}$$

Where

$$V^{m,\infty} = V_0^{m,\infty} + V_1^{m,\infty}(P - P^0)$$

These coefficients for the fitted quadratic equation of the form $A_0x^2 + A_1x + A_2$ are shown in Table 25. For simplicity and ease of observation, only the trial at 340 K and 460 K are fitted.

Table 25. Fitted quadratic function for the $\ln(K)$ $vs.$ $1/T$ plots

	Temperature (K)				
	340	460		340	460
	Xe			Ne	
A0	-0.00002	-0.00002	A0	-0.00001	-0.00002
A1	0.0196	0.0229	A1	0.0118	0.0122
A2	2.4614	1.6947	A2	4.4532	4.1634
	Kr			He	
A0	-0.00002	-0.00002	A0	-0.00001	-0.00002
A1	0.0168	0.0181	A1	0.0081	0.0092
A2	3.1166	2.7307	A2	4.4246	4.119
	Ar				
A0	-0.00001	-0.00002			
A1	0.0163	0.0153			
A2	3.3359	3.5006			

From the gradients, it is clear that Xe + *n*-decane at infinite dilution experience greater volume changes then the He + *n*-decane throughout the temperature range. This is directly proportional to the size of the gas solutes, the bigger the gas the larger the change in volume.

Once again, a crossing of gradients is observed in the Ar system at approximately 135 MPa. This may be the results of the similar size between Ar and CH_3 group.

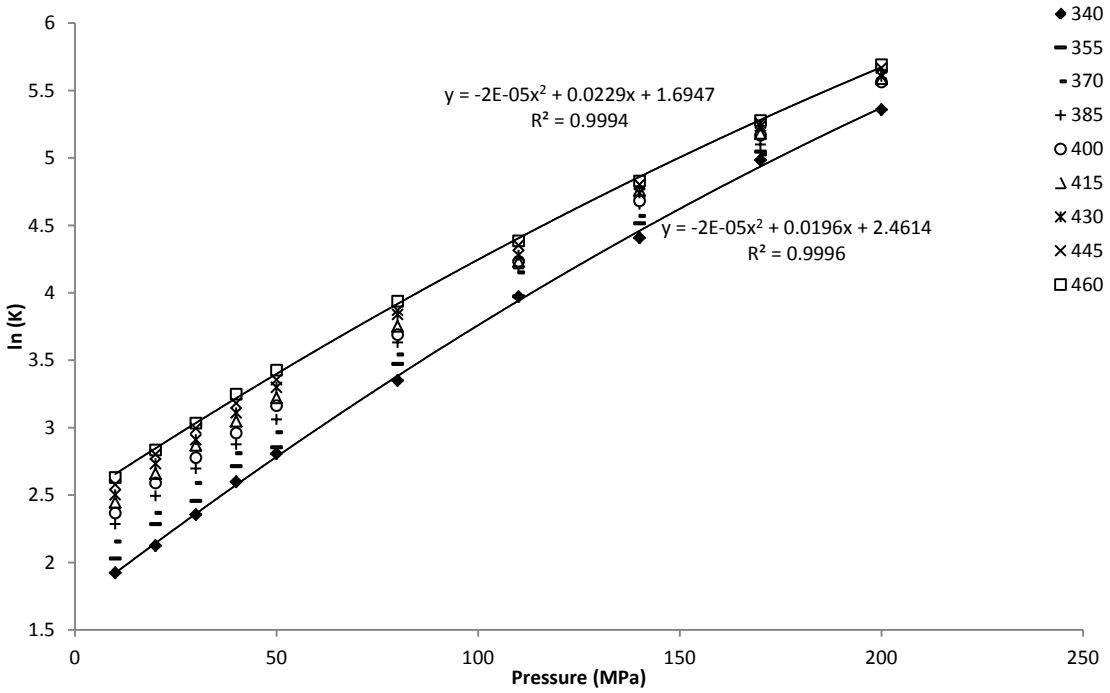

Figure 62. Fitted $\ln(K)$ $vs.$ P for Xe at constant temperature

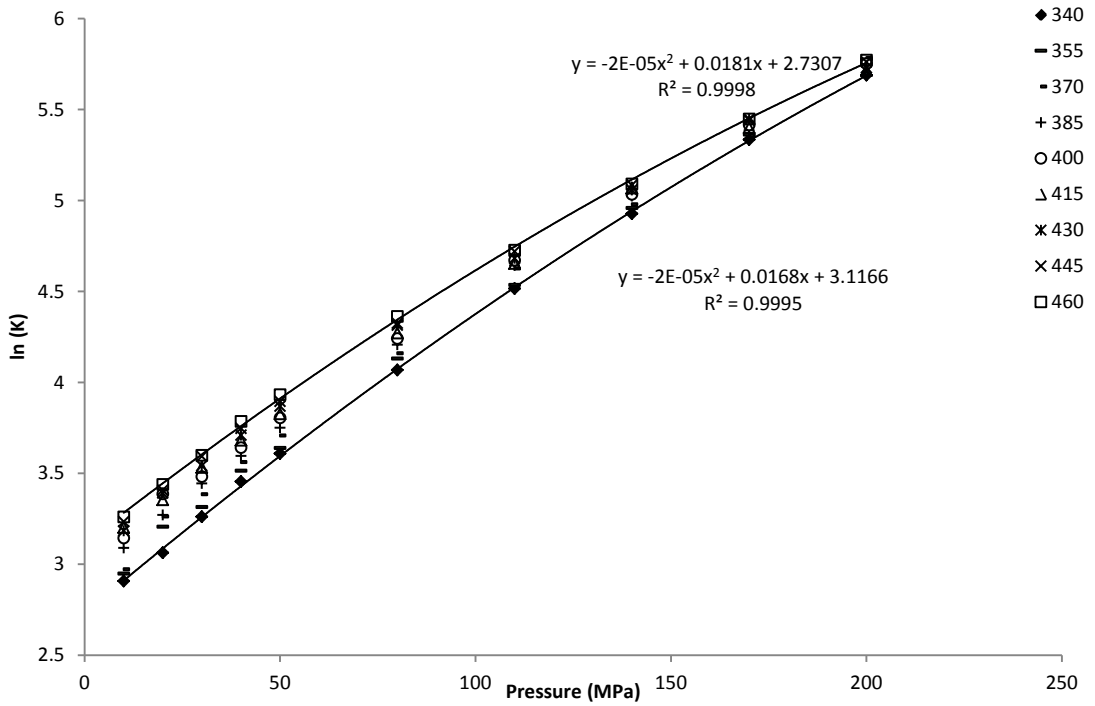

Figure 63. Fitted $\ln(K)$ $vs.$ P for Kr at constant temperature

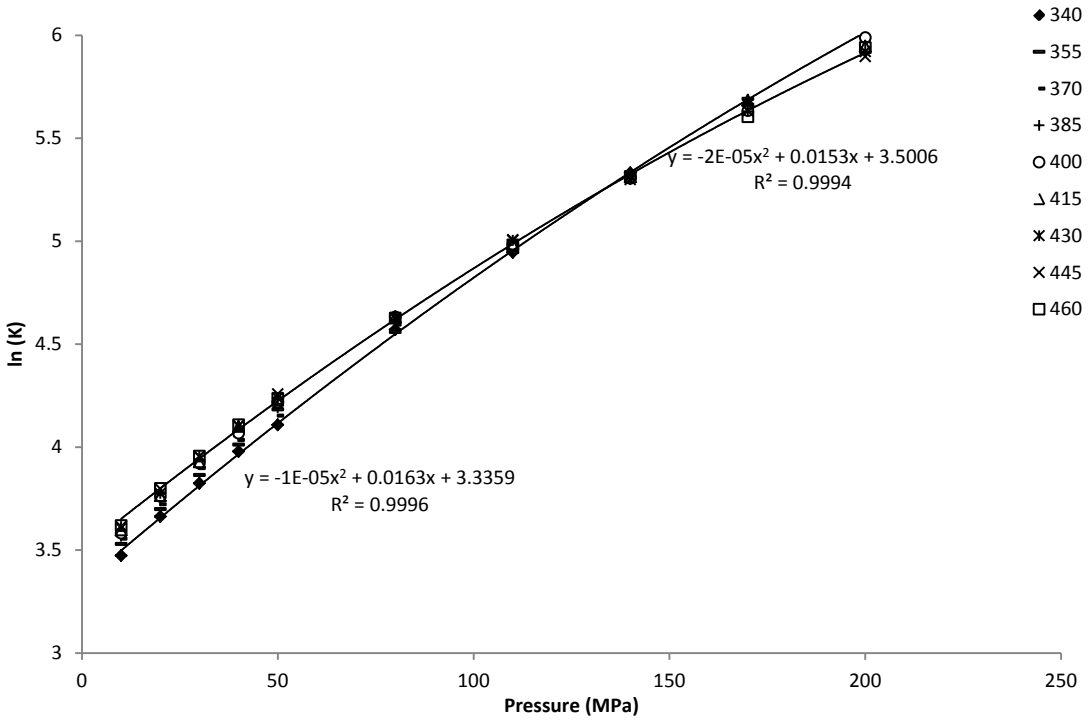

Figure 64. Fitted $\ln(K)$ $vs.$ P for Ar at constant temperature

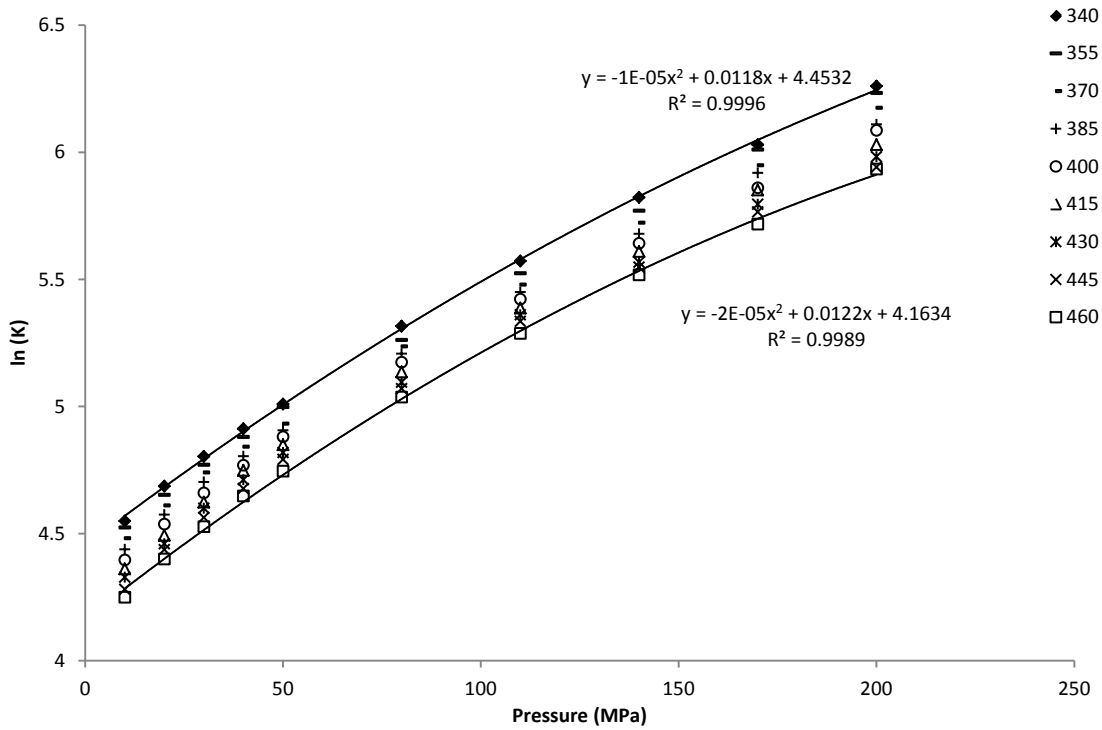

Figure 65. Fitted $\ln(K)$ $vs.$ P for Ne at constant temperature

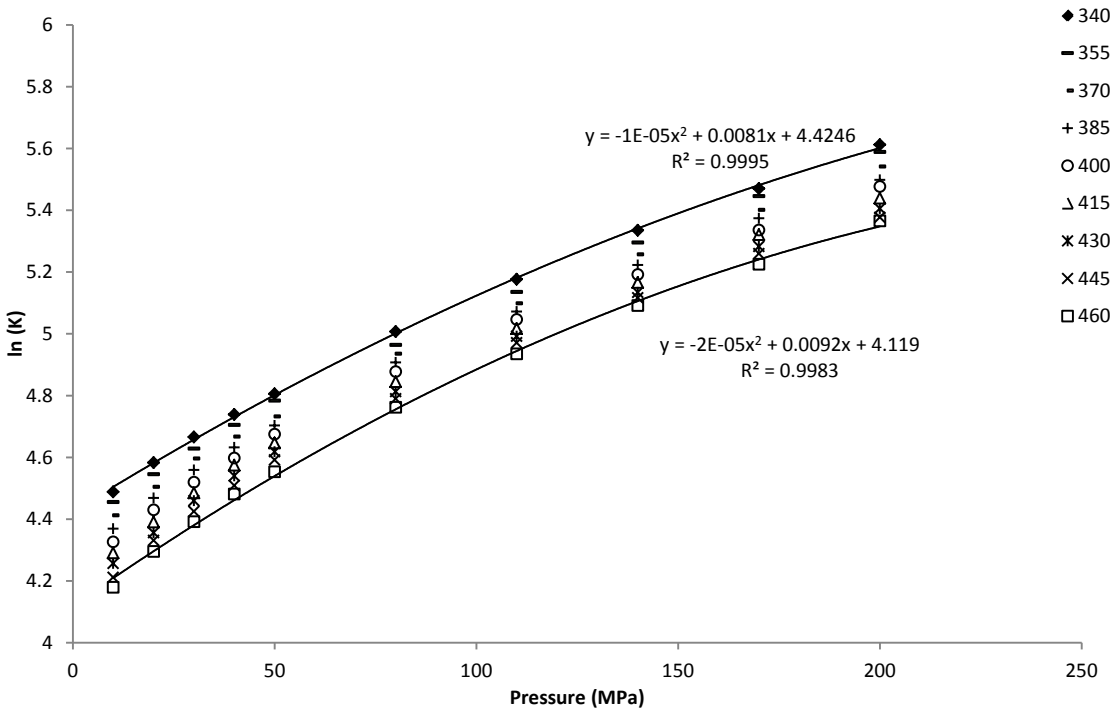

Figure 66. Fitted $\ln(K)$ *vs.* P for He at constant temperature

Chapter Seven

Vapor-Liquid Equilibrium of Noble Gas + n-decane

Binary Mixtures

Considering the high pressure within the reservoir conditions, a large portion of these pressures and temperatures will have surpassed the critical region where phase separations are no longer observable. Table 26 summarizes the conditions for all noble gas + *n*-decane binary mixtures where phase separation was observed prior to the critical region.

Table 26. Conditions where phase separation was observed within the region considered (340 K – 460 K and 10 MPa – 200 MPa)

Noble Gas	Conditions	
	Temperature (K)	Pressure (MPa)
Xe	385 - 460	10
Kr	340 - 460	10 - 20
Ar	340 - 460	10 - 40
Ne	340 - 460	10 - 200
He	340 - 460	10 - 200*

* denotes the range of pressure where not all cases exhibit phase separation.

Although our original intention was to model the phase equilibria with the composition representative of that at infinite dilution, in line with the solubility coefficient, the system cannot be set up in such a way due to the high pressure in the region considered in this study. Such large pressure compresses the box size beyond the minimum cut-off length $(\frac{L}{2})$ if the number of particles in the noble gas phase is not sufficiently large. For example, at 10 MPa, at least 600 particles are required so that the gas phase at equilibrium is not compressed beyond the cut-off length; the number of particles required for the gas phase also increases with pressure. To allow for positive and negative box size adjustment during a Monte Carlo trial, a noble gas phase of 900 particles is used at the region from 10 MPa to 80 MPa and 1200 particles for the remaining pressure, up to 200 MPa. With this

minimum gas phase particle requirement, an even larger number of *n*-decane particles are required to achieve an infinite dilution composition. With 300 *n*-decane and 900 noble gas molecules, roughly 2-3 weeks are required to complete the equilibration and production trials and at least a week extra is required for larger systems in higher pressure regions. Any larger system may require a coarse-grain model rather than atomistic simulation, which is beyond the scope of this study. It should also be noted that for a given simulation, the overall composition is kept constant – i.e. the composition of the vapour and liquid combined is fixed.

Smaller systems were allowed to equilibrate for at least 10,000 cycles before the measurements were taken from the next 20,000 cycles with the assistance of the conditional formatting visual aid as previously discussed. For larger systems, 20,000 cycles were applied before the measurements were taken. However, phase separation was not observed at all pressure within the reservoir conditions considered, as listed in Table 26.

Although the pressure ranges from 10 MPa to 200 MPa, the pressure intervals of the trials are completed at 10, 20, 30, 40, 50, 80, 110, 140, 170, and 200 MPa. The pressure ranges given in Table 26 are thus the nearest pressure interval to the critical region.

As a result of two different system sizes at two pressure regions, the mole fractions were changed slightly from 1:3 to 1:4 between the two pressure regions, slightly increasing the bubble point pressure. Through a simple Peng-Robinson equation of state (PR EoS) model, where the binary interaction coefficient is set to zero, the bubble point pressure were determined for the mole fraction of 1:3 *n*-decane:noble gas as indicated in Table 27 and Figure 67 to Figure 70.

Table 27. Bubble point pressure for ratio *n*-decane:noble gas of 1:3 mole fraction as calculated via Peng-Robinson EoS (Elliott & Lira, 2012)

Temperature (K)	Bubble Point Pressure (MPa)				
	Xe	Kr	Ar	Ne	He
340	7.514	21.6	45.35	427	427.4
355	8.611	22.53	45.32	391.5	312.1
370	9.627	23.22	45.01	359.9	243.2
385	10.53	23.68	44.42	331.4	197.1
400	11.31	23.9	43.56	305.3	164.1
415	11.93	23.9	42.47	281.3	139.1
430	12.4	23.68	41.13	258.8	119.5
445	12.69	23.23	39.55	237.8	103.5
460	12.79	22.56	37.74	217.9	90.09

Phase separations from the simulation were observed to be in accordance with the bubble point pressure predicted by the Peng-Robinson EoS calculation. This is not surprising since the *n*-decane + noble gas binary mixtures, although has a large size disparity, are nonpolar and intermolecular interactions are weak and short-ranged in nature.

A maximum is observed in the *n*-decane + Krypton binary mixture, Figure 68, while a plateau is observed in all other binary mixtures at temperature between 340 K and 460 K.

All five noble gases under the reservoir conditions are well within the supercritical region, while *n*-decane is essentially involatile and maintains a liquid phase with density ranging from approximately 0.6 – 0.75 g/ml throughout the reservoir conditions. From Table 27, the binary mixture of Xenon + *n*-decane has the lowest bubble point pressure and is the only mixture with lower bubble pressure than the minimum pressure considered, 10 MPa. Phase separations in *n*-decane + Xenon system are observed only between 385 K-460 K and 10 MPa, precisely what is predicted by PR EoS. Similarly, phase separations are also observed in *n*-decane + Krypton and *n*-decane + Argon within the predicted region. The *n*-decane + Neon binary mixture has the highest bubble pressure, well above the

highest pressure considered in this study, 200 MPa. Similar to this mixture, *n*-decane + Helium system also has high bubble pressures, spanning the largest pressure range of all *n*-decane + noble gas binary mixtures' bubble pressure. Unfortunately, due to the system size and time restriction, phase equilibria studies for *n*-decane + Neon and *n*-decane + Helium were not completed beyond 80 MPa. The available results are nevertheless as predicted by the Peng-Robinson Equation of State (PR EoS).

Table 28 Critical properties of decane and noble gases (Design Institute for Physical Properties)

IUPAC name	Molecular formula	Molecular weight	T_c (K)	P_c (Pa)	V_c (m3/kmol)	Z_c
DECANE	$C_{10}H_{22}$	142.2817	617.7	2110000	0.617	0.254
XENON	Xe	131.29	289.74	5840370	0.118	0.286
KRYPTON	Kr	83.8	209.35	5501950	0.0912	0.288
ARGON	Ar	39.948	150.86	4898000	0.07459	0.291
NEON	Ne	20.1797	44.4	2653000	0.0417	0.3
HELIUM	He	4.0026	5.2	227500	0.0573	0.302

Due to the involatility of *n*-decane, the conventional plot of compositions in both phases cannot be effectively applied to the data. Instead, the plots of density vs. temperature for both phases are presented here. The density gap between the two phases reduces as they approach the bubble pressure. They are not immediately apparent on the plots of Xe and Kr + n-decane binary mixtures as the bubble pressure are much lower than other binary mixtures, resulting in a few numbers of data points available. However, for the binary mixtures of Ar, Ne, and He with *n*-decane, the reduction in density gaps can be easily identified. Interestingly, the gas phase densities are relatively insensitive to the increase in pressure for smaller gases such as He and Ne. The sensitivity of the density response to the increase in pressure can be clearly observed in Figure 73 - Figure 75. This behaviour is quite counter-intuitive as the critical temperature and critical pressure of the noble gases are positively and monotonically correspond to their sizes while the critical compressibility factors are larger as the size decreases. These critical properties are given in Table 28.

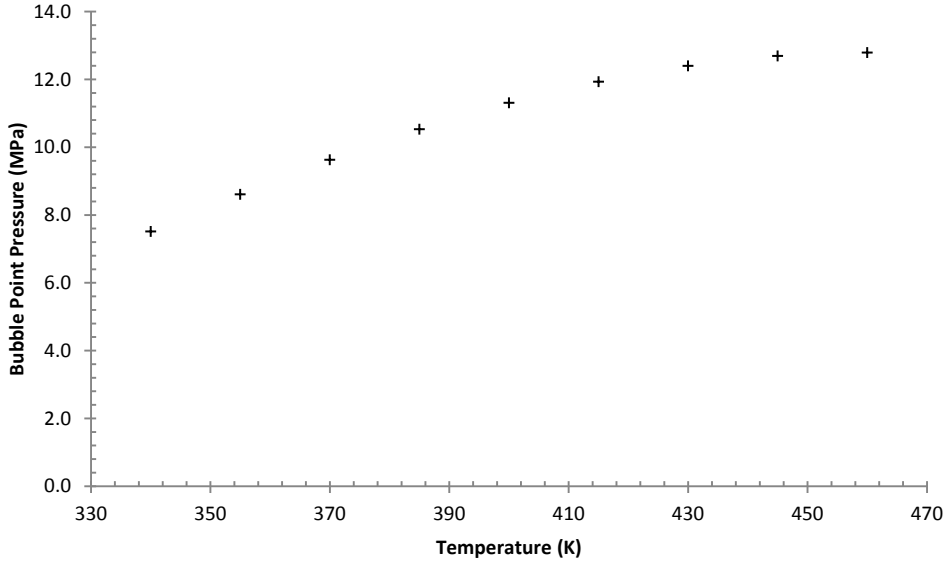

Figure 67. Bubble point pressure of *n*-decane + Xenon binary mixture s predicted by PR EoS

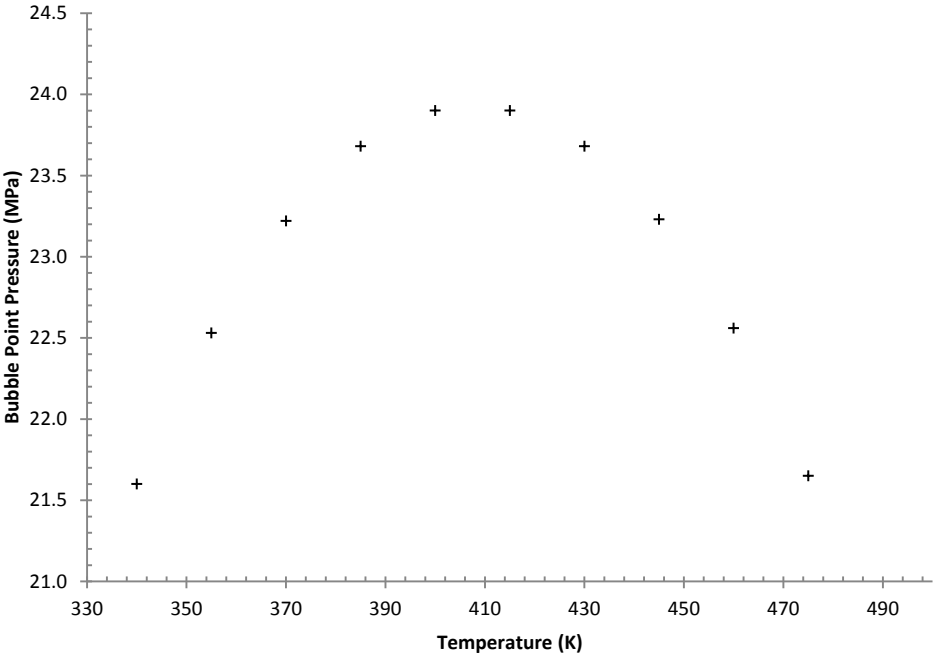

Figure 68. Bubble point pressure of *n*-decane + Krypton binary mixture as predicted by PR EoS

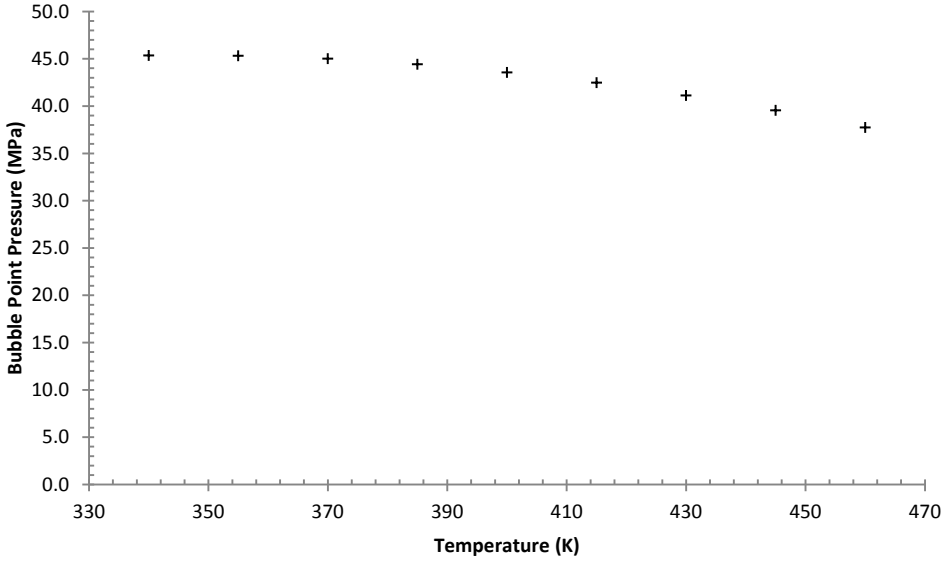

Figure 69. Bubble point pressure of *n*-decane + Argon binary mixture as predicted by PR EoS

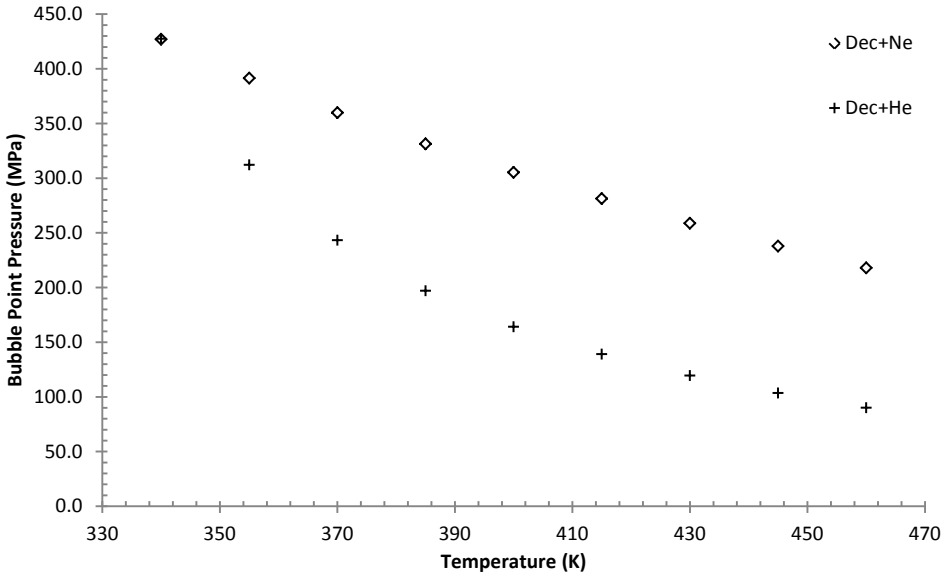

Figure 70. Bubble point pressure of *n*-decane + Neon and *n*-decane + Helium binary mixture as predicted by PR EoS

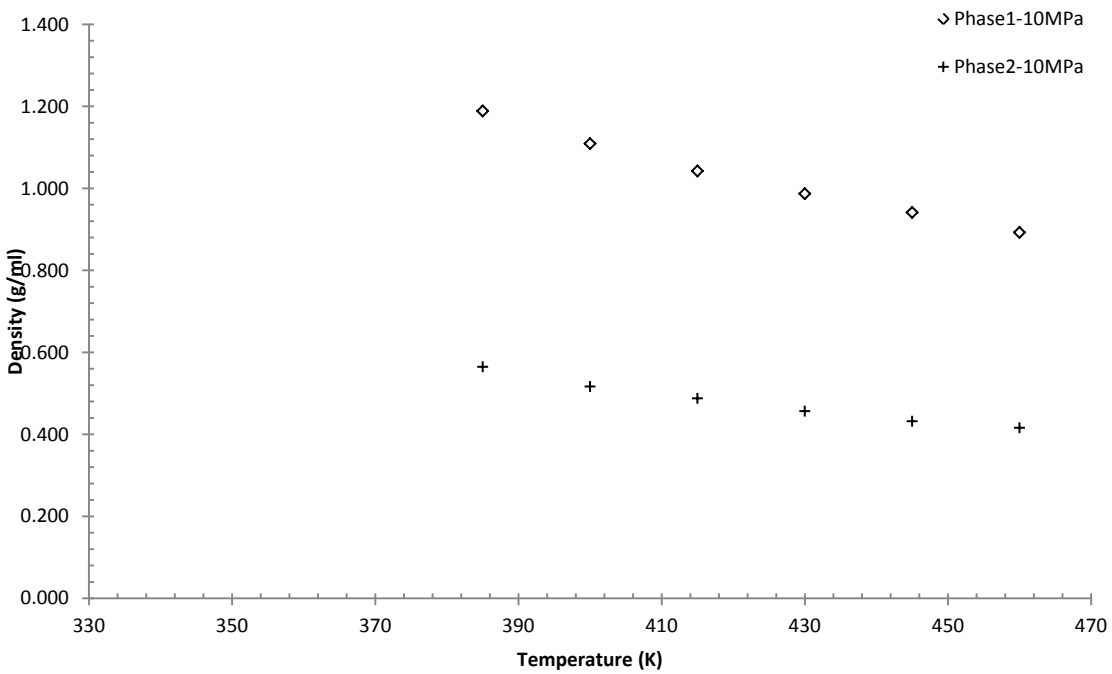

Figure 71. Density of *n*-decane + Xe binary mixture at 10 MPa

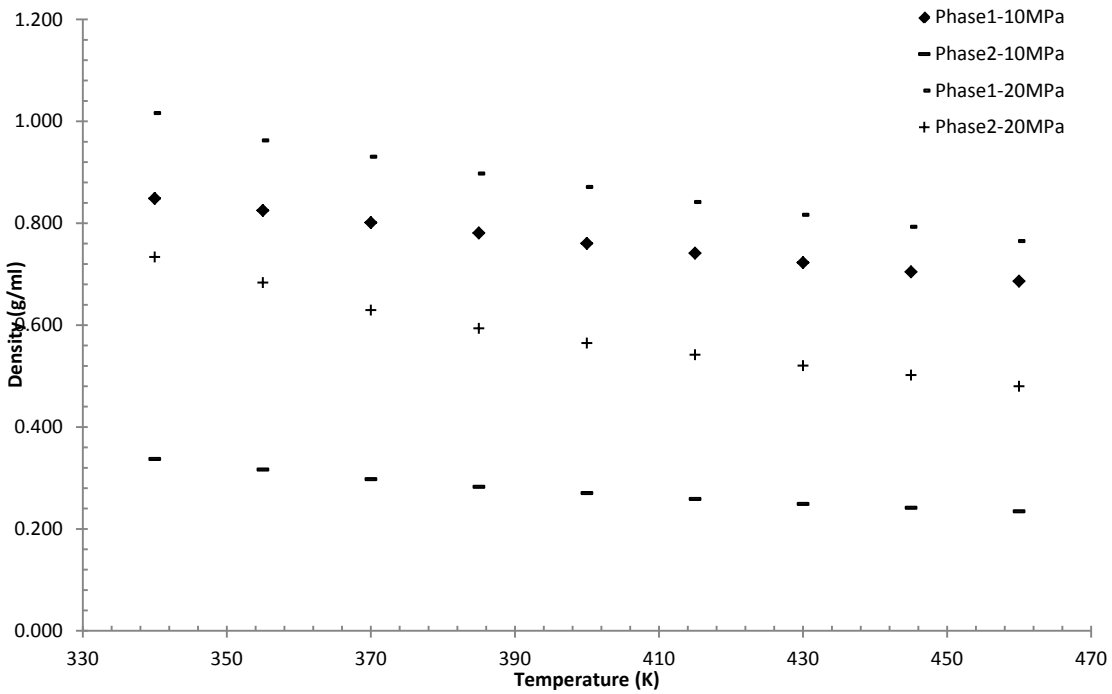

Figure 72. Density of *n*-decane + Kr binary mixture at 10 and 20 MPa

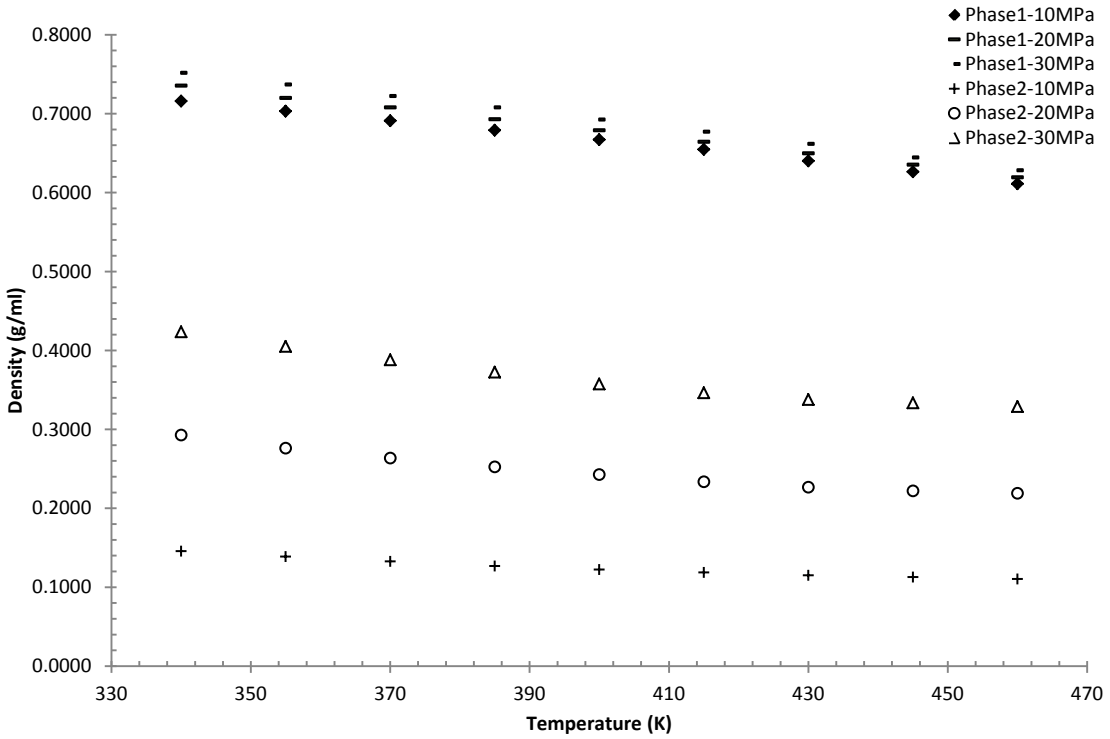

Figure 73. Density of *n*-decane + Ar binary mixture at 10, 20, and 30 MPa

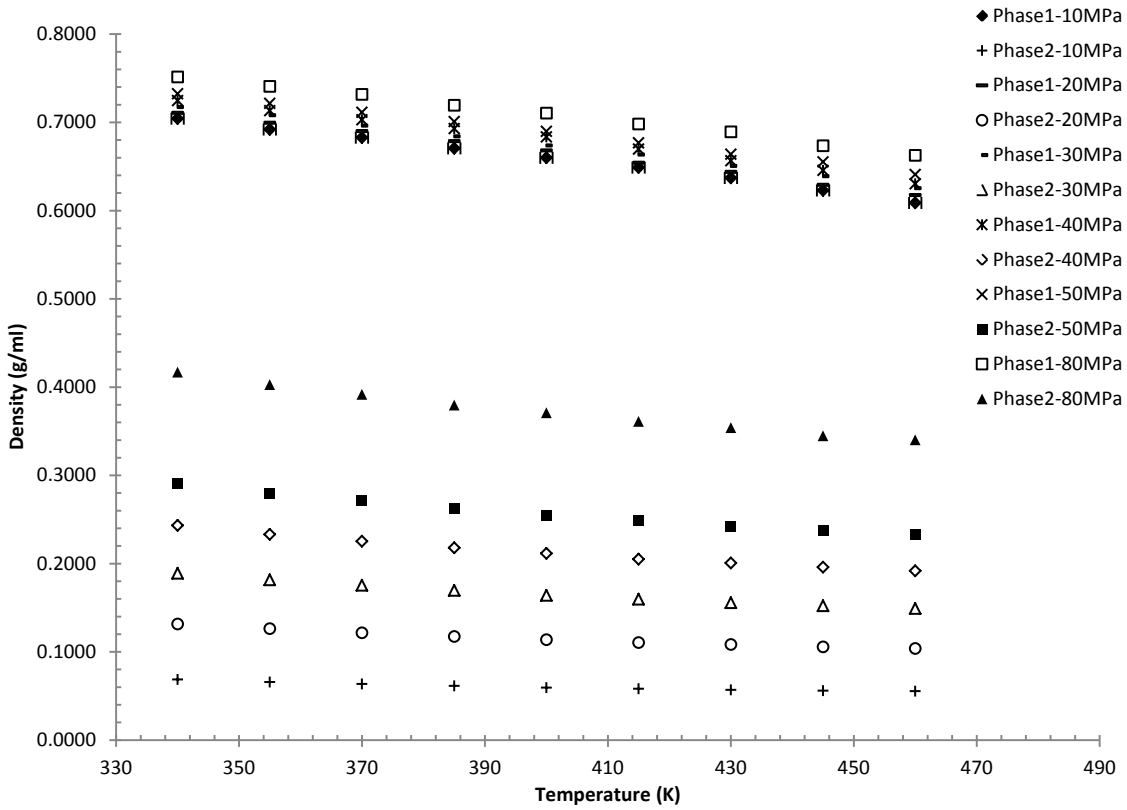

Figure 74. Density of *n*-decane + Ne binary mixture between 10 - 80 MPa

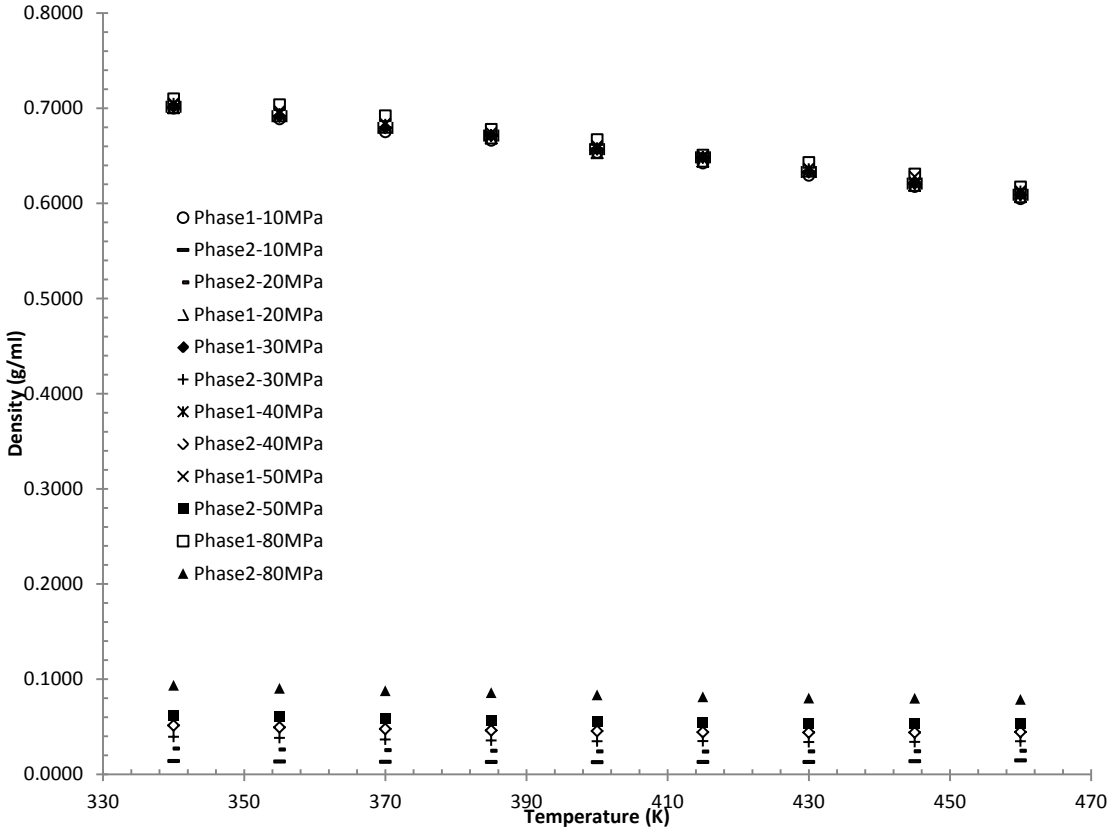

Figure 75. Density of *n*-decane + He binary mixture between 10 - 80 MPa

Table 29. Density and composition of Xe + *n*-decane binary mixture at 10 MPa from Monte Carlo simulations, C10 denotes *n*-decane

Temperature (K)	Phase 1				Phase 2			
	ρ (g/ml)	±	Mole fraction		ρ (g/ml)	±	Mole fraction	
			C10	Xe			C10	Xe
385	1.189	0.003	0.2843	0.7157	0.565	0.006	0.0098	0.9902
400	1.109	0.004	0.3329	0.6671	0.517	0.002	0.0135	0.9865
415	1.042	0.002	0.3720	0.6280	0.488	0.002	0.0189	0.9811
430	0.987	0.002	0.3987	0.6013	0.457	0.001	0.0239	0.9761
445	0.941	0.001	0.4096	0.5904	0.432	0.001	0.0296	0.9704
460	0.892	0.001	0.4516	0.5484	0.416	0.001	0.0433	0.9567

Table 30. Density and composition of Kr + *n*-decane binary mixture at 10 MPa from Monte Carlo simulations, C10 denotes *n*-decane

Temperature (K)	Phase 1				Phase 2			
	ρ (g/ml)	±	Mole fraction		ρ (g/ml)	±	Mole fraction	
			C10	Kr			C10	Kr
340	0.849	0.002	0.5693	0.4307	0.3368	0.0006	0.0020	0.9980
355	0.825	0.001	0.5899	0.4101	0.3161	0.0007	0.0029	0.9971
370	0.8012	0.0009	0.6055	0.3945	0.2974	0.0006	0.0036	0.9964
385	0.7808	0.0007	0.6145	0.3855	0.2824	0.0006	0.0055	0.9945
400	0.7604	0.0005	0.6334	0.3666	0.2701	0.0006	0.0086	0.9914
415	0.7410	0.0003	0.6433	0.3567	0.2583	0.0003	0.0124	0.9876
430	0.7227	0.0004	0.6492	0.3508	0.2487	0.0005	0.0166	0.9834
445	0.7044	0.0005	0.6507	0.3493	0.2411	0.0005	0.0227	0.9773
460	0.6860	0.0007	0.6598	0.3402	0.2341	0.0006	0.0327	0.9673

Table 31. Density and composition of Kr + *n*-decane binary mixture at 20 MPa from Monte Carlo simulations, C10 denotes *n*-decane

Temperature (K)	Phase 1				Phase 2			
	ρ (g/ml)	±	Mole fraction		ρ (g/ml)	±	Mole fraction	
			C10	Kr			C10	Kr
340	1.016	0.003	0.3098	0.6902	0.734	0.004	0.0069	0.9931
355	0.962	0.002	0.3602	0.6398	0.683	0.002	0.0101	0.9899
370	0.930	0.002	0.3710	0.6290	0.629	0.002	0.0102	0.9898
385	0.897	0.002	0.3924	0.6076	0.593	0.002	0.0138	0.9862
400	0.871	0.001	0.3968	0.6032	0.565	0.003	0.0170	0.9830
415	0.841	0.001	0.4198	0.5802	0.542	0.002	0.0253	0.9747
430	0.8162	0.0008	0.4307	0.5693	0.520	0.003	0.0320	0.9680
445	0.7925	0.0006	0.4305	0.5695	0.502	0.003	0.0378	0.9622
460	0.765	0.001	0.3995	0.6005	0.480	0.002	0.0416	0.9584

Table 32. Density and composition of Ar + *n*-decane binary mixture at 10 MPa from Monte Carlo simulations, C10 denotes *n*-decane

Temperature (K)	Phase 1				Phase 2			
	ρ (g/ml)	±	Mole fraction		ρ (g/ml)	±	Mole fraction	
			C10	Ar			C10	Ar
340	0.7158	0.0008	0.7373	0.2627	0.1456	0.0004	0.0010	0.9990
355	0.7032	0.0008	0.7417	0.2583	0.1387	0.0002	0.0018	0.9982
370	0.6909	0.0007	0.7440	0.2560	0.1326	0.0002	0.0027	0.9973
385	0.6790	0.0008	0.7513	0.2487	0.1268	0.0002	0.0042	0.9958
400	0.6671	0.0009	0.7536	0.2464	0.1223	0.0002	0.0062	0.9938
415	0.655	0.001	0.7562	0.2438	0.1186	0.0002	0.0099	0.9901
430	0.6402	0.0008	0.7522	0.2478	0.1152	0.0003	0.0128	0.9872
445	0.626	0.002	0.7506	0.2494	0.1128	0.0003	0.0183	0.9817
460	0.6111	0.0008	0.7469	0.2531	0.1104	0.0001	0.0238	0.9762

Table 33. Density and composition of Ar + *n*-decane binary mixture at 20 MPa from Monte Carlo simulations, C10 denotes *n*-decane

Temperature (K)	Phase 1				Phase 2			
	ρ (g/ml)	±	Mole fraction		ρ (g/ml)	±	Mole fraction	
			C10	Ar			C10	Ar
340	0.7353	0.0004	0.5699	0.4301	0.293	0.001	0.0031	0.9969
355	0.7197	0.0004	0.5598	0.4402	0.2763	0.0007	0.0029	0.9971
370	0.7077	0.0006	0.5779	0.4221	0.2637	0.0005	0.0047	0.9953
385	0.6927	0.0008	0.5733	0.4267	0.2526	0.0007	0.0064	0.9936
400	0.6788	0.0006	0.5720	0.4280	0.2427	0.0006	0.0087	0.9913
415	0.6642	0.0007	0.5719	0.4281	0.2337	0.0004	0.0109	0.9891
430	0.650	0.001	0.5715	0.4285	0.2267	0.0007	0.0151	0.9849
445	0.6352	0.0007	0.5691	0.4309	0.2220	0.0003	0.0200	0.9800
460	0.619	0.001	0.5636	0.4364	0.2191	0.0006	0.0275	0.9725

Table 34. Density and composition of Ar + *n*-decane binary mixture at 30 MPa from Monte Carlo simulations, C10 denotes *n*-decane

Temperature (K)	Phase 1				Phase 2			
	ρ (g/ml)	±	Mole fraction		ρ (g/ml)	±	Mole fraction	
			C10	Ar			C10	Ar
340	0.7517	0.0009	0.4367	0.5633	0.424	0.002	0.0043	0.9957
355	0.7367	0.0006	0.4352	0.5648	0.405	0.003	0.0068	0.9932
370	0.7223	0.0008	0.4457	0.5543	0.388	0.003	0.0097	0.9903
385	0.7079	0.0006	0.4477	0.5523	0.372	0.002	0.0116	0.9884
400	0.692	0.001	0.4439	0.5561	0.358	0.002	0.0136	0.9864
415	0.6771	0.0009	0.4458	0.5542	0.346	0.001	0.0185	0.9815
430	0.662	0.001	0.4450	0.5550	0.338	0.001	0.0237	0.9763
445	0.644	0.002	0.4344	0.5656	0.334	0.002	0.0321	0.9679
460	0.628	0.002	0.4314	0.5686	0.329	0.003	0.0415	0.9585

Table 35. Density and composition of Ar + *n*-decane binary mixture at 40 MPa from Monte Carlo simulations, C10 denotes *n*-decane

Temperature (K)	Phase 1				Phase 2			
	ρ (g/ml)	±	Mole fraction		ρ (g/ml)	±	Mole fraction	
			C10	Ar			C10	Ar
340	0.7689	0.0007	0.3347	0.6653	0.540	0.003	0.0089	0.9911
355	0.7507	0.0006	0.3160	0.6840	0.518	0.006	0.0126	0.9874
370	0.7385	0.0005	0.3408	0.6592	0.505	0.005	0.0176	0.9824
385	0.717	0.001	0.3178	0.6822	0.484	0.003	0.0196	0.9804
400	0.700	0.002	0.3217	0.6783	0.465	0.001	0.0218	0.9782
415	0.683	0.001	0.3204	0.6796	0.452	0.002	0.0280	0.9720
430	0.658	0.002	0.2989	0.7011	0.442	0.002	0.0350	0.9650
445	0.648	0.002	0.3133	0.6867	0.445	0.004	0.0522	0.9478
460	0.613	0.005	0.2750	0.7250	0.52	0.03	0.1573	0.8427

Table 36. Density and composition of Ne + *n*-decane binary mixture at 10 MPa from Monte Carlo simulations, C10 denotes *n*-decane

Temperature (K)	Phase 1				Phase 2			
	ρ (g/ml)	±	Mole fraction		ρ (g/ml)	±	Mole fraction	
			C10	Ne			C10	Ne
340	0.7043	0.0009	0.9016	0.0984	0.0686	0.0001	0.0004	0.9996
355	0.692	0.001	0.8952	0.1048	0.0657	0.0001	0.0004	0.9996
370	0.6826	0.0008	0.8945	0.1055	0.06341	0.00004	0.0012	0.9988
385	0.671	0.001	0.8884	0.1116	0.0613	0.0001	0.0020	0.9980
400	0.6598	0.0008	0.8846	0.1154	0.0594	0.0001	0.0031	0.9969
415	0.6488	0.0009	0.8810	0.1190	0.0580	0.0001	0.0050	0.9950
430	0.6369	0.0007	0.8767	0.1233	0.0568	0.0001	0.0075	0.9925
445	0.623	0.001	0.8695	0.1305	0.0558	0.0002	0.0104	0.9896
460	0.609	0.001	0.8626	0.1374	0.0553	0.0002	0.0143	0.9857

Table 37. Density and composition of Ne + *n*-decane binary mixture at 20 MPa from Monte Carlo simulations, C10 denotes *n*-decane

Temperature (K)	Phase 1				Phase 2			
	ρ (g/ml)	±	Mole fraction		ρ (g/ml)	±	Mole fraction	
			C10	Ne			C10	Ne
340	0.7106	0.0007	0.8199	0.1801	0.1315	0.0001	0.0004	0.9996
355	0.6994	0.0004	0.8113	0.1887	0.1262	0.0001	0.0005	0.9995
370	0.6899	0.0006	0.8078	0.1922	0.1215	0.0001	0.0008	0.9992
385	0.6785	0.0008	0.8002	0.1998	0.1173	0.0001	0.0012	0.9988
400	0.668	0.001	0.7940	0.2060	0.1138	0.0001	0.0021	0.9979
415	0.654	0.001	0.7822	0.2178	0.1105	0.0001	0.0031	0.9969
430	0.6438	0.0006	0.7785	0.2215	0.1083	0.0002	0.0055	0.9945
445	0.629	0.001	0.7644	0.2356	0.1055	0.0003	0.0065	0.9935
460	0.6174	0.0008	0.7586	0.2414	0.1037	0.0002	0.0094	0.9906

Table 38. Density and composition of Ne + *n*-decane binary mixture at 30 MPa from Monte Carlo simulations, C10 denotes *n*-decane

Temperature (K)	Phase 1				Phase 2			
	ρ (g/ml)	±	Mole fraction		ρ (g/ml)	±	Mole fraction	
			C10	Ne			C10	Ne
340	0.7171	0.0006	0.7485	0.2515	0.1890	0.0002	0.0002	0.9998
355	0.7079	0.0009	0.7460	0.2540	0.1816	0.0001	0.0003	0.9997
370	0.6960	0.0007	0.7341	0.2659	0.1754	0.0002	0.0008	0.9992
385	0.684	0.001	0.7225	0.2775	0.1696	0.0002	0.0013	0.9987
400	0.6736	0.0008	0.7151	0.2849	0.1639	0.0002	0.0017	0.9983
415	0.663	0.001	0.7098	0.2902	0.1595	0.0002	0.0028	0.9972
430	0.650	0.001	0.6968	0.3032	0.1556	0.0003	0.0042	0.9958
445	0.639	0.001	0.6874	0.3126	0.1521	0.0002	0.0058	0.9942
460	0.6251	0.0009	0.6742	0.3258	0.1490	0.0002	0.0076	0.9924

Table 39. Density and composition of Ne + *n*-decane binary mixture at 40 MPa from Monte Carlo simulations, C10 denotes *n*-decane

Temperature (K)	Phase 1				Phase 2			
	ρ (g/ml)	±	Mole fraction		ρ (g/ml)	±	Mole fraction	
			C10	Ne			C10	Ne
340	0.725	0.001	0.6920	0.3080	0.2432	0.0008	0.0013	0.9987
355	0.7131	0.0008	0.6808	0.3192	0.2330	0.0004	0.0005	0.9995
370	0.703	0.001	0.6702	0.3298	0.2252	0.0004	0.0004	0.9996
385	0.6928	0.0008	0.6637	0.3363	0.2178	0.0003	0.0012	0.9988
400	0.683	0.001	0.6606	0.3394	0.2114	0.0003	0.0021	0.9979
415	0.670	0.002	0.6433	0.3567	0.2050	0.0004	0.0028	0.9972
430	0.656	0.002	0.6257	0.3743	0.2005	0.0003	0.0040	0.9960
445	0.646	0.002	0.6203	0.3797	0.1958	0.0005	0.0057	0.9943
460	0.630	0.001	0.5996	0.4004	0.1917	0.0003	0.0071	0.9929

Table 40. Density and composition of Ne + *n*-decane binary mixture at 50 MPa from Monte Carlo simulations, C10 denotes *n*-decane

Temperature (K)	Phase 1				Phase 2			
	ρ (g/ml)	±	Mole fraction		ρ (g/ml)	±	Mole fraction	
			C10	Ne			C10	Ne
340	0.7324	0.0008	0.6482	0.3518	0.2912	0.0005	0.0002	0.9998
355	0.7214	0.0008	0.6334	0.3666	0.2798	0.0005	0.0004	0.9996
370	0.7113	0.0009	0.6272	0.3728	0.2719	0.0005	0.0016	0.9984
385	0.701	0.002	0.6155	0.3845	0.2618	0.0003	0.0011	0.9989
400	0.690	0.002	0.6053	0.3947	0.2541	0.0002	0.0020	0.9980
415	0.6766	0.0006	0.5846	0.4154	0.2483	0.0003	0.0027	0.9973
430	0.6638	0.0008	0.5721	0.4279	0.2417	0.0001	0.0037	0.9963
445	0.655	0.002	0.5693	0.4307	0.237	0.001	0.0057	0.9943
460	0.641	0.002	0.5510	0.4490	0.233	0.001	0.0084	0.9916

Table 41. Density and composition of Ne + *n*-decane binary mixture at 80 MPa from Monte Carlo simulations, C10 denotes *n*-decane

Temperature (K)	Phase 1				Phase 2			
	ρ (g/ml)	±	Mole fraction		ρ (g/ml)	±	Mole fraction	
			C10	Ne			C10	Ne
340	0.751	0.002	0.5265	0.4735	0.4168	0.0008	0.0007	0.9993
355	0.741	0.001	0.5103	0.4897	0.4026	0.0005	0.0002	0.9998
370	0.732	0.001	0.5075	0.4925	0.3916	0.0004	0.0012	0.9988
385	0.7192	0.0006	0.4865	0.5135	0.3796	0.0008	0.0011	0.9989
400	0.710	0.002	0.4804	0.5196	0.371	0.001	0.0031	0.9969
415	0.698	0.002	0.4638	0.5362	0.3610	0.0009	0.0034	0.9966
430	0.689	0.001	0.4622	0.5378	0.3539	0.0006	0.0057	0.9943
445	0.673	0.002	0.4332	0.5668	0.345	0.000	0.0054	0.9946
460	0.663	0.001	0.4228	0.5772	0.340	0.001	0.0086	0.9914

Table 42. Density and composition of He + *n*-decane binary mixture at 10 MPa from Monte Carlo simulations, C10 denotes *n*-decane

Temperature (K)	Phase 1				Phase 2			
	ρ (g/ml)	±	Mole fraction		ρ (g/ml)	±	Mole fraction	
			C10	He			C10	He
340	0.7001	0.0009	0.8983	0.1017	0.01389	0.00003	0.0002	0.9998
355	0.6888	0.001	0.8941	0.1059	0.01335	0.00003	0.0003	0.9997
370	0.6751	0.0004	0.8871	0.1129	0.01302	0.00005	0.0007	0.9993
385	0.666	0.001	0.8854	0.1146	0.01282	0.00005	0.0015	0.9985
400	0.653	0.002	0.8802	0.1198	0.01264	0.00007	0.0022	0.9978
415	0.642	0.001	0.8755	0.1245	0.0128	0.0001	0.0037	0.9963
430	0.6293	0.0009	0.8701	0.1299	0.01289	0.00008	0.0052	0.9948
445	0.618	0.001	0.8660	0.1340	0.0137	0.0002	0.0085	0.9915
460	0.605	0.001	0.8612	0.1388	0.0146	0.0001	0.0123	0.9877

Table 43. Density and composition of He + *n*-decane binary mixture at 20 MPa from Monte Carlo simulations, C10 denotes *n*-decane

Temperature (K)	Phase 1				Phase 2			
	ρ (g/ml)	±	Mole fraction		ρ (g/ml)	±	Mole fraction	
			C10	He			C10	He
340	0.7003	0.0007	0.8141	0.1859	0.0270	0.0001	0.0002	0.9998
355	0.6918	0.0006	0.8114	0.1886	0.02592	0.00006	0.0002	0.9998
370	0.6799	0.0009	0.8028	0.1972	0.02524	0.00006	0.0005	0.9995
385	0.6686	0.0007	0.7956	0.2044	0.0245	0.0001	0.0009	0.9991
400	0.653	0.001	0.7833	0.2167	0.02394	0.00003	0.0012	0.9988
415	0.644	0.001	0.7796	0.2204	0.02372	0.00009	0.0020	0.9980
430	0.6338	0.0009	0.7741	0.2259	0.0239	0.0001	0.0034	0.9966
445	0.619	0.001	0.7623	0.2377	0.0241	0.0003	0.0047	0.9953
460	0.607	0.001	0.7559	0.2441	0.0247	0.0003	0.0067	0.9933

Table 44. Density and composition of He + *n*-decane binary mixture at 30 MPa from Monte Carlo simulations, C10 denotes *n*-decane

Temperature (K)	Phase 1				Phase 2			
	ρ (g/ml)	±	Mole fraction		ρ (g/ml)	±	Mole fraction	
			C10	He			C10	He
340	0.701	0.001	0.7443	0.2557	0.03933	0.00006	0.0001	0.9999
355	0.6917	0.0005	0.7368	0.2632	0.0381	0.0001	0.0003	0.9997
370	0.679	0.001	0.7269	0.2731	0.0366	0.0001	0.0003	0.9997
385	0.671	0.002	0.7249	0.2751	0.03552	0.00005	0.0005	0.9995
400	0.657	0.001	0.7105	0.2895	0.03465	0.00005	0.0008	0.9992
415	0.648	0.001	0.7062	0.2938	0.0348	0.0004	0.0020	0.9980
430	0.633	0.001	0.6925	0.3075	0.0339	0.0001	0.0022	0.9978
445	0.621	0.001	0.6831	0.3169	0.0340	0.0003	0.0033	0.9967
460	0.609	0.001	0.6751	0.3249	0.0347	0.0003	0.0051	0.9949

Table 45. Density and composition of He + *n*-decane binary mixture at 40 MPa from Monte Carlo simulations, C10 denotes *n*-decane

Temperature (K)	Phase 1				Phase 2			
	ρ (g/ml)	±	Mole fraction		ρ (g/ml)	±	Mole fraction	
			C10	He			C10	He
340	0.705	0.001	0.6900	0.3100	0.0513	0.0001	0.0001	0.9999
355	0.694	0.001	0.6806	0.3194	0.0493	0.0001	0.0001	0.9999
370	0.683	0.001	0.6708	0.3292	0.0477	0.0001	0.0002	0.9998
385	0.671	0.001	0.6593	0.3407	0.0461	0.0001	0.0003	0.9997
400	0.658	0.002	0.6477	0.3523	0.0454	0.0002	0.0009	0.9991
415	0.648	0.001	0.6409	0.3591	0.0443	0.0001	0.0012	0.9988
430	0.636	0.002	0.6310	0.3690	0.0440	0.0002	0.0019	0.9981
445	0.622	0.002	0.6184	0.3816	0.0439	0.0006	0.0030	0.9970
460	0.6129	0.0004	0.6119	0.3881	0.0444	0.0001	0.0043	0.9957

Table 46. Density and composition of He + *n*-decane binary mixture at 50 MPa from Monte Carlo simulations, C10 denotes *n*-decane

Temperature (K)	Phase 1				Phase 2			
	ρ (g/ml)	±	Mole fraction		ρ (g/ml)	±	Mole fraction	
			C10	He			C10	He
340	0.704	0.001	0.6354	0.3646	0.0623	0.0001	0.0000	1.0000
355	0.697	0.001	0.6334	0.3666	0.0605	0.0003	0.0002	0.9998
370	0.684	0.001	0.6184	0.3816	0.0585	0.0002	0.0003	0.9997
385	0.674	0.002	0.6123	0.3877	0.0566	0.0002	0.0004	0.9996
400	0.660	0.001	0.5963	0.4037	0.0551	0.0001	0.0006	0.9994
415	0.650	0.001	0.5888	0.4112	0.0541	0.0002	0.0010	0.9990
430	0.636	0.002	0.5759	0.4241	0.0531	0.0002	0.0015	0.9985
445	0.628	0.001	0.5715	0.4285	0.0538	0.0004	0.0029	0.9971
460	0.611	0.001	0.5523	0.4477	0.0532	0.0003	0.0035	0.9965

Table 47. Density and composition of He + *n*-decane binary mixture at 80 MPa from Monte Carlo simulations, C10 denotes *n*-decane

Temperature (K)	Phase 1				Phase 2			
	ρ (g/ml)	±	Mole fraction		ρ (g/ml)	±	Mole fraction	
			C10	He			C10	He
340	0.710	0.001	0.5265	0.4735	0.0935	0.0001	0.0000	1.0000
355	0.704	0.0004	0.5267	0.4733	0.0903	0.0002	0.0000	1.0000
370	0.692	0.002	0.5148	0.4852	0.0878	0.0005	0.0002	0.9998
385	0.678	0.002	0.4965	0.5035	0.0858	0.0005	0.0005	0.9995
400	0.667	0.002	0.4858	0.5142	0.0835	0.0001	0.0006	0.9994
415	0.651	0.002	0.4670	0.5330	0.0815	0.0003	0.0009	0.9991
430	0.643	0.002	0.4655	0.5345	0.080	0.001	0.0014	0.9986
445	0.631	0.002	0.4541	0.5459	0.0799	0.0009	0.0022	0.9978
460	0.617	0.001	0.4414	0.5586	0.0788	0.0005	0.0027	0.9973

Chapter Eight

Diffusion Coefficients of noble gases in n-decane

The errors in the diffusion coefficient for all noble gases from ten separate simulations are approximately 10%. The overall trend of the diffusion coefficients for each noble gas in *n*-decane at reservoir conditions, pressure between 10 MPa – 200 MPa and temperature between 340 K – 460 K, are arguably linear with respect to temperature. The diffusion coefficients for each noble gas in *n*-decane solution are shown in Table 48.

Table 48. Diffusion coefficient for Xe in *n*-decane solution

Temperature (K)	Xe	Kr	Ar	Ne	He
340	5 ± 1	6.4 ± 0.9	8.7 ± 0.8	17 ± 2	31 ± 2
355	6.6 ± 0.6	7.9 ± 0.8	9.4 ± 0.9	20 ± 2	36 ± 4
370	6.7 ± 0.8	10 ± 1	11 ± 1	20 ± 3	40 ± 3
385	8.1 ± 0.8	10.0 ± 0.8	12 ± 2	23 ± 2	41 ± 5
400	10 ± 1	12 ± 1	13 ± 1	25 ± 2	47 ± 6
415	10.6 ± 0.8	12 ± 2	15 ± 2	26 ± 3	51 ± 6
430	11 ± 2	14 ± 1	16 ± 2	29 ± 3	51 ± 3
445	12 ± 1	14 ± 2	17 ± 2	30 ± 4	58 ± 7
460	13 ± 1	16 ± 2	18 ± 2	33 ± 3	61 ± 9

The linear trend was fitted with the results. Additionally, the slope of the fitted linear trend is increasing with decreasing σ. To further investigate this trend, comparisons were made with the Stoke-Einstein's relation and the hard-sphere Enskog's relation. In both approaches, diffusion coefficients are expressed in terms of σ. However, this radius of interaction is not explicitly clear whether it is the $\frac{\sigma_{solute}+\sigma_{solute}}{2}$, $\frac{\sigma_{solute}+\sigma_{solvent}}{2}$, or $\sigma_{solute} + R_{gyration}$. Thus, the comparison with the Stoke-Einstein's relation and the hard-sphere Enskog's relation in three cases as follow

- $R_1 = \frac{\sigma_{solute}+\sigma_{solute}}{2}$
- $R_2 = \frac{\sigma_{solute}+\sigma_{solvent}}{2}$
- $R_3 = \sigma_{solute} + R_{gyration}$

Where $R^2_{gyration} = 11.27 \pm 0.05$ for *n*-decane (Cui et al., 1996)

8.1. Stoke-Einstein's Relation

As previously discussed, the Brownian based diffusion coefficient given by the Stoke-Einstein's relation can be written as

$$D = \frac{kT}{f\pi\eta\sigma} \tag{93}$$

where f is a constant depending on the boundary condition for fluid flow on the sphere's surface. Slip or stick boundary conditions correspond to $f = 4$ and $f = 6$ respectively. This relation was dismissed by a number of authors (Chen et al., 1981; de Pablo et al., 1992; Pollack et al., 1990), particularly when the difference between solute and solvent radii is large. However, when we consider the diffusion coefficient ratio between noble gases, the dependency on temperature, viscosity, and boundary condition are removed, and only the relative radii are compared. For example, the diffusion coefficient ratio of Xe and Kr can be written as

$$\frac{D_i}{D_j} = \frac{\sigma_j}{\sigma_i} \tag{94}$$

The radii for noble gases used in this study are shown in Table 49, these are the same potential parameters used in the simulation and have proven to adequately represent the pure components.

Table 49. Lennard-Jones potential parameters for noble gases used in this study.

Noble Gas	ε (K)	σ (Å)	Reference
He	10.22	2.556	(Kell et al., 1978)
Ne	35.7	2.789	(Skoulidas & Sholl, 2002)
Ar	124.07	3.42	(Skoulidas & Sholl, 2002)
Kr	164.7	3.635	(Potter & Clynne, 1978)
Xe	227.856	3.9478	(Bonifácio et al., 2002)
CH_3	114	3.93	(Siepmann, 1993; Smit et al., 1995)

The results are then plotted to show the ratio among the diffusion coefficient in *n*-decane as shown in Figure 76 to Figure 79. The trend are linear and virtually a constant with small slopes ranging from -0.00009 to 0.0009. Additionally, the three cases of radius ratios between the five noble gases are listed in Table 50 to Table 52.

Table 50. The radius ratios between the five noble gases where $R_1 = \frac{\sigma_{solute}+\sigma_{solute}}{2}$

	σ_{Xe}	σ_{Kr}	σ_{Ar}	σ_{Ne}	σ_{He}
σ_{Xe}	1	1.09	1.15	1.42	1.54
σ_{Kr}	0.92	1	1.06	1.30	1.42
σ_{Ar}	0.87	0.94	1	1.23	1.34
σ_{Ne}	0.71	0.77	0.82	1	1.09
σ_{He}	0.65	0.70	0.75	0.92	1

Table 51. The radius ratios between the five noble gases where $R_2 = \frac{\sigma_{solute}+\sigma_{CH_3}}{2}$

	σ_{Xe}	σ_{Kr}	σ_{Ar}	σ_{Ne}	σ_{He}
σ_{Xe}	1	1.06	1.10	1.24	1.31
σ_{Kr}	0.95	1	1.04	1.18	1.24
σ_{Ar}	0.91	0.96	1	1.13	1.19
σ_{Ne}	0.80	0.85	0.88	1	1.05
σ_{He}	0.76	0.81	0.84	0.95	1

Table 52. The radius ratios between the five noble gases where $R_3 = \sigma_{solute} + R_g$

	σ_{Xe}	σ_{Kr}	σ_{Ar}	σ_{Ne}	σ_{He}
σ_{Xe}	1	1.04	1.08	1.19	1.24
σ_{Kr}	0.96	1	1.03	1.14	1.18
σ_{Ar}	0.93	0.97	1	1.10	1.15
σ_{Ne}	0.84	0.88	0.91	1	1.04
σ_{He}	0.81	0.85	0.87	0.96	1

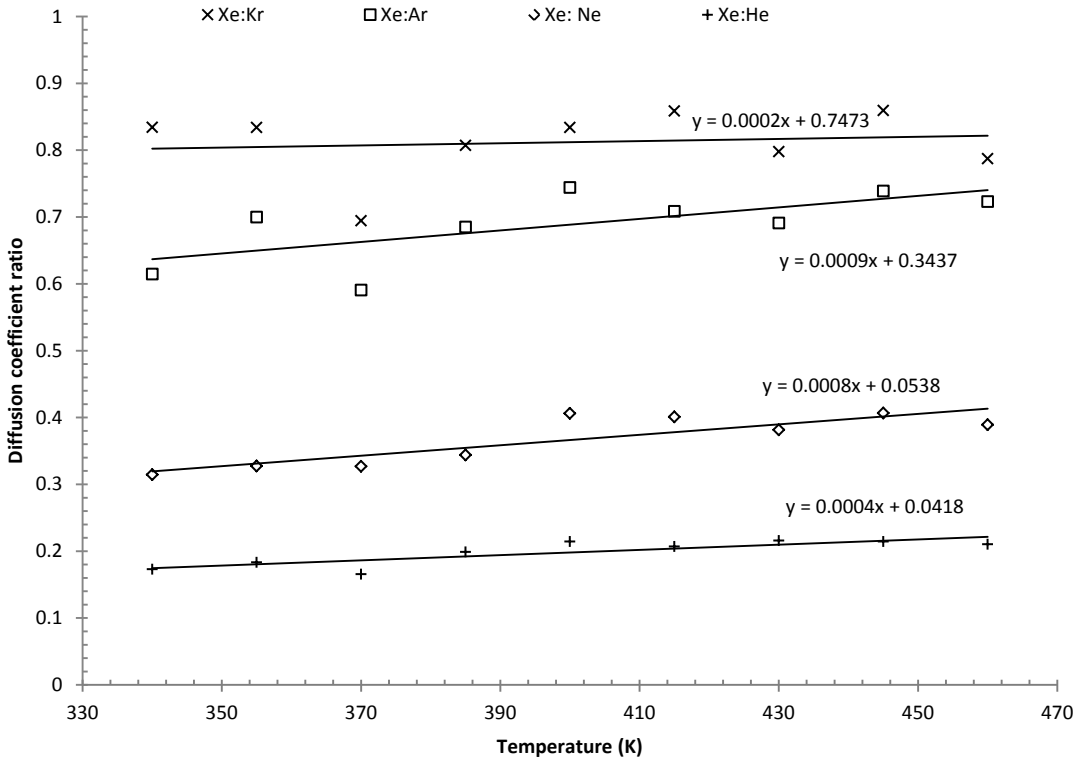

Figure 76. Ratio of diffusion coefficient of Xe and other noble gases at 30 MPa

From the plots of the ratio of diffusion coefficients, while the ratio is a constant, they do not show a monotonically increasing or decreasing trend amongst all the mixtures. While very small slopes of diffusion coefficient ratio can be observed in all plots, the inherent error of 10% makes it hard to draw a definitive conclusion.

Additionally, the radius ratio from the case where $R_3 = \sigma_{solute} + R_g$ is the closest to the expected ratio of 1. In the rheology study of *n*-decane, Cui et al. (1996) noted in the comparison with tetracosane and hexadecane that *n*-decane is considerably stiff for the hydrocarbon of this length. This indicates that, for a given configuration, it is very rigid and best describe the level of interaction between the solute and solvent for binary the mixtures in this study.

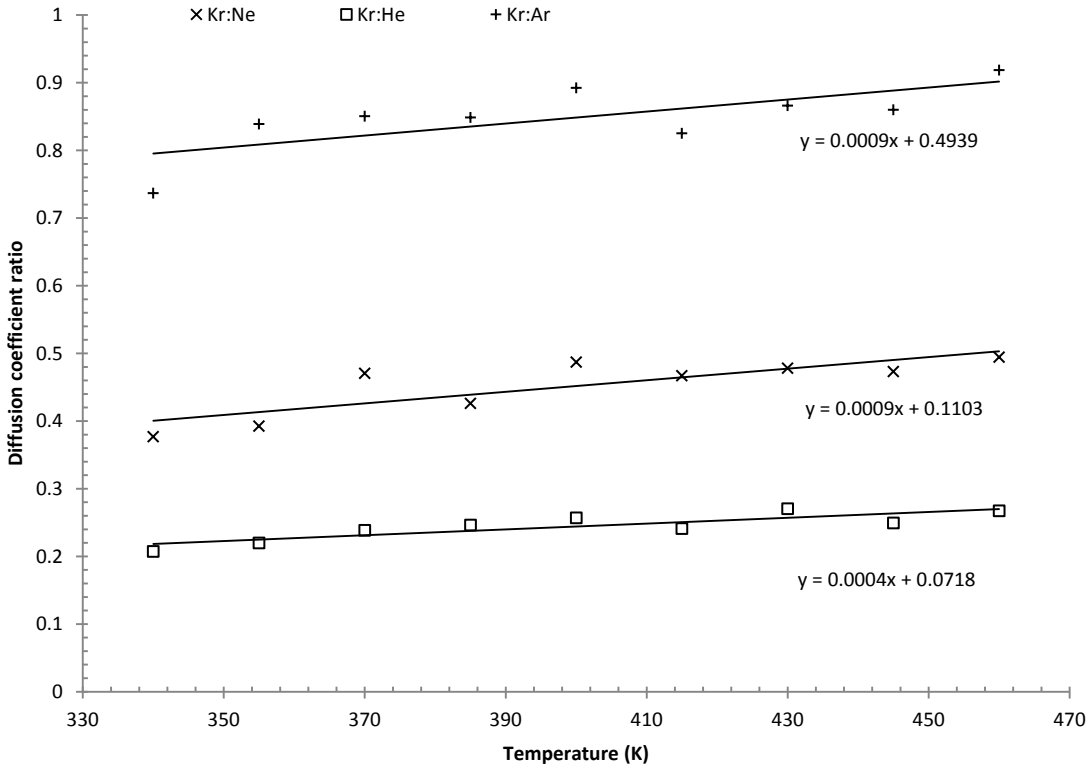

Figure 77. Ratio of diffusion coefficient of Kr and other noble gases at 30 MPa

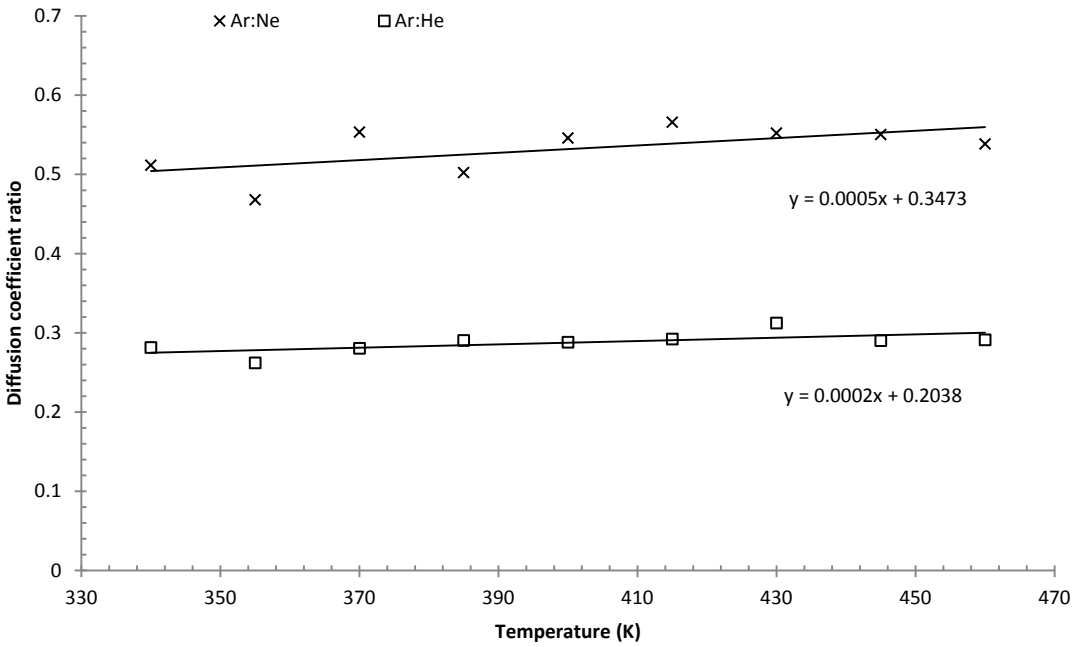

Figure 78. Ratio of diffusion coefficient of Ar and other noble gases at 30 MPa

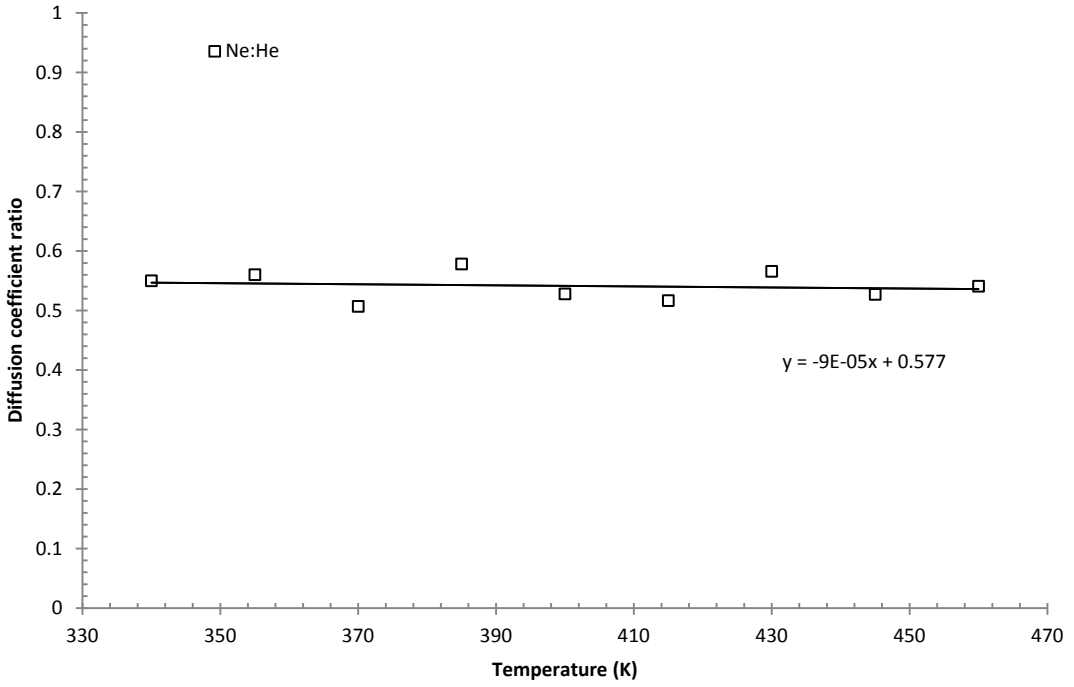

Figure 79. Ratio of diffusion coefficient of Ne:He at 30 MPa

Further to the Stoke-Einstein's relation evaluation, the σ prediction by the relation was calculated as shown in Table 53 to Table 55. The radii of interaction were calculated for 10, 50, and 200 MPa where viscosity data are available. These radii are much smaller than the effective radii used in the force field by an order of magnitude. And thus, the Stoke-Einstein's relation cannot be used to adequately explain the mechanics of diffusion as has been pointed out by several authors.

Table 53. σ prediction (Å) by Stoke-Einstein's relation for noble gas + *n*-decane binary mixture at 10 MPa

Temperature (K)	σ_{Xe}	σ_{Kr}	σ_{Ar}	σ_{Ne}	σ_{He}
340	0.82	0.68	0.50	0.26	0.14
355	0.81	0.68	0.57	0.27	0.15
370	0.96	0.67	0.57	0.31	0.16
385	0.94	0.76	0.65	0.32	0.19
400	0.89	0.74	0.66	0.36	0.19
415	0.98	0.84	0.69	0.39	0.20
430	1.09	0.87	0.75	0.41	0.23
445	1.10	0.94	0.81	0.45	0.24
460	1.21	0.95	0.88	0.47	0.26

Table 54. σ prediction (Å) by Stoke-Einstein's relation for noble gas + *n*-decane binary mixture at 50 MPa

Temperature (K)	σ_{Xe}	σ_{Kr}	σ_{Ar}	σ_{Ne}	σ_{He}
340	0.56	0.47	0.34	0.18	0.10
355	0.55	0.46	0.39	0.18	0.10
370	0.65	0.45	0.38	0.21	0.11
385	0.64	0.52	0.44	0.22	0.13
400	0.60	0.50	0.45	0.24	0.13
415	0.66	0.56	0.46	0.26	0.14
430	0.73	0.58	0.50	0.28	0.16
445	0.73	0.63	0.54	0.30	0.16
460	0.80	0.63	0.57	0.31	0.17

Table 55. σ prediction (Å) by Stoke-Einstein's relation for noble gas + *n*-decane binary mixture at 200 MPa

Temperature (K)	σ_{Xe}	σ_{Kr}	σ_{Ar}	σ_{Ne}	σ_{He}
415	0.27	0.23	0.19	0.11	0.06
430	0.31	0.24	0.21	0.12	0.07
445	0.31	0.27	0.23	0.13	0.07
460	0.34	0.27	0.25	0.13	0.07

Note: the viscosity data are only available from 415K at 200MPa from NIST

8.2. Enskog's hard-sphere relation

As investigated by various authors including (Chen et al., 1981; Evans et al., 1981; Maitland et al., 1985a, 1985b; Vesovic & Wakeham, 1989) the diffusion coefficient derived from the Enskog's hard-sphere theory can be written as

$$D_{ij}^{E} = \frac{3}{8n\sigma_{ij}^{2}g_{ij}(\sigma)} \cdot \left(\frac{k_B T}{2\pi m_{ij}}\right)^{\frac{1}{2}} \tag{95}$$

Where

$g_{ij}(\sigma)$ = radial distribution function between solute and solvent at contact

n = fluid density

m_{ij} = reduced mass of solute and solvent

Although our system is a soft-sphere model, it is interesting to relate this in terms of hard-sphere framework. Similarly to our comparison of the ratio between diffusion coefficients of noble gas in *n*-decane for the Stoke-Einstein's relation, for instance we can write

$$\frac{D_i^E}{D_j^E} = \frac{\sigma_j^2}{\sigma_i^2} \cdot \frac{g_j(\sigma)}{g_i(\sigma)} \tag{96}$$

It is clear that the for a hard-sphere mixture, the radius of interaction is that of the distance of the closest approach between solute and solvent. However, it is unclear when it comes to large molecules like *n*-decane. Instead of a function of σ as implicated by the Stoke-Einstein's relation, the diffusion coefficient ratio is now a function of σ^2 and a correction term from the radial distribution function ratio. The ratios of square radius are for different radius combinations are given in Table 56 to Table 58. At the moment, we do not have the radial distribution function values and thus cannot be certain of what number these values should be. With further analysis of the radial distribution function, they could very well be corrections to unity as indicated in previous figures of diffusion coefficient ratios.

Table 56. Ratios of square radius between the five noble gases where $R_1 = \frac{\sigma_{solute}+\sigma_{solute}}{2}$

	σ_{Xe}	σ_{Kr}	σ_{Ar}	σ_{Ne}	σ_{He}
σ_{Xe}	1	1.18	1.33	2.00	2.39
σ_{Kr}	0.85	1	1.13	1.70	2.02
σ_{Ar}	0.75	0.89	1	1.50	1.79
σ_{Ne}	0.50	0.59	0.67	1	1.19
σ_{He}	0.42	0.49	0.56	0.84	1

Table 57. The radius ratios between the five noble gases where $R_2 = \frac{\sigma_{solute}+\sigma_{CH_3}}{2}$

	σ_{Xe}	σ_{Kr}	σ_{Ar}	σ_{Ne}	σ_{He}
σ_{Xe}	1	1.11	1.21	1.55	1.71
σ_{Kr}	0.90	1	1.08	1.39	1.53
σ_{Ar}	0.83	0.92	1	1.28	1.42
σ_{Ne}	0.65	0.72	0.78	1	1.11
σ_{He}	0.58	0.65	0.70	0.90	1

Table 58. The radius ratios between the five noble gases where $R_3 = \sigma_{solute} + R_g$

	σ_{Xe}	σ_{Kr}	σ_{Ar}	σ_{Ne}	σ_{He}
σ_{Xe}	1	1.09	1.16	1.41	1.53
σ_{Kr}	0.92	1	1.06	1.29	1.40
σ_{Ar}	0.86	0.94	1	1.22	1.31
σ_{Ne}	0.71	0.77	0.82	1	1.08
σ_{He}	0.66	0.72	0.76	0.93	1

8.3. Finite Size Effect Verification

To verify the finite size effect, additional systems twice as large of 1000 *n*-decane were also completed. Each point at a given temperature was an average of 10 separate trials. The comparison was carried out at 340 K and 30 MPa for all noble gases.

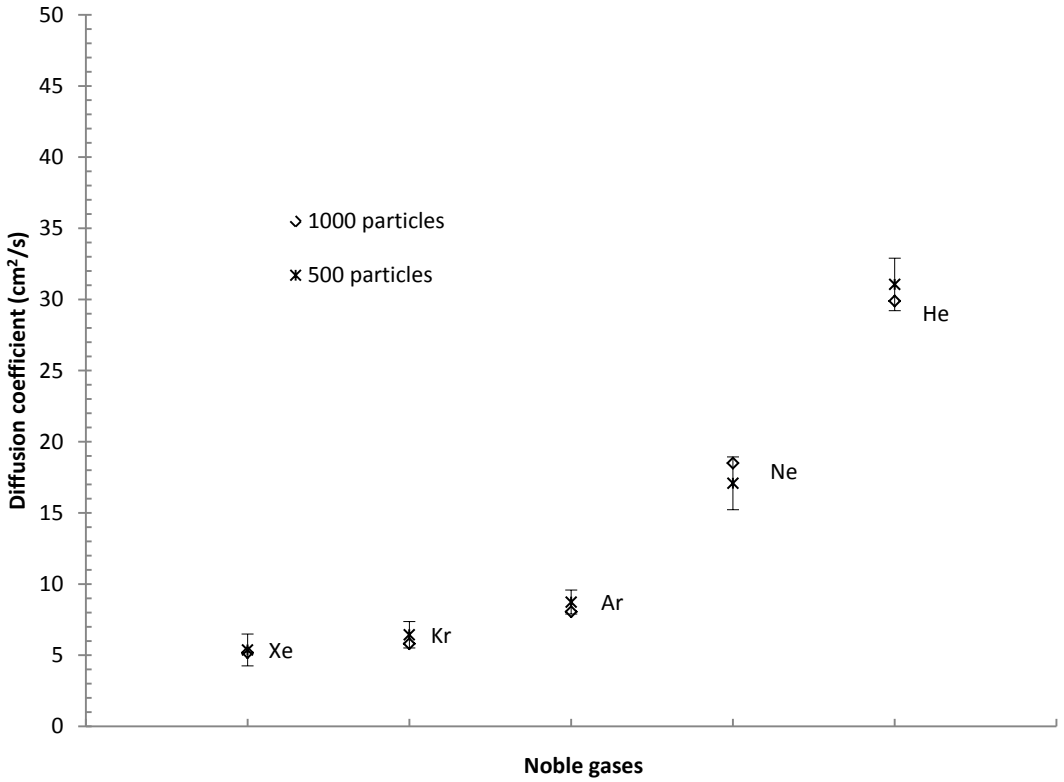

Figure 80. Finite size effect verification between 500 and 1000 *n*-decane systems at 340K and 30MPa

The results were within the respective error margins. There was no systematic error observed. It should also be noted that all the final equilibrated box length (L_x) in the simulations in this study are much greater than the $L_x > 10\sigma$ recommended by (Gonzalez-Melchor et al., 2005). It is thus reasonable to assume that the system sizes of 500 *n*-decane particles utilized in the diffusion coefficient study are not of any observable influences of the finite size effect.

8.4. Reservoir Model

With the five spot injection pattern and other parameters as described previously, the results of field oil production, gas oil ratio and tracer production rate are reported below. The noble gas tracer production rates are identical in all cases.

The diffusion coefficients at 340 K and 30 MPa for each noble gas in *n*-decane were used in the reservoir model. The simple black oil model was used due to the allotted time. The tracer injection field experiment at Salt Creek, in the state of Wyoming provides us with a guideline on the time scale of the tracer breakthrough as depicted in Figure 81. It should be noted that we are considering a very small area of a large field in the simulation which reflect in the relatively fast reduction of oil production.

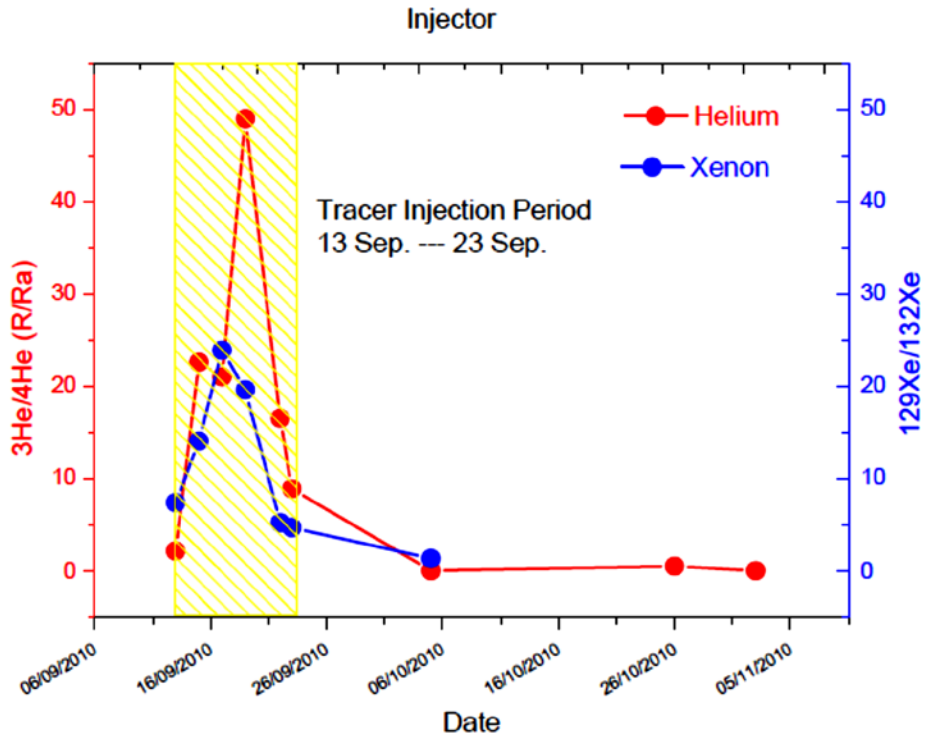

Figure 81. Tracer breakthrough from Salt Creek field samples

The results of simple calculations of the distance travelled by the noble gas tracers in *n*-decane from the diffusion coefficient at various temperatures are shown in Table 59. It is clear from this calculation that diffusion will not play a significant role within the reservoirs, where much larger fluid flow is observed.

Table 59. Rough calculation of the distance travel from diffusion coefficient data

Temperature (K)	Distance travelled (m)				
	Xe	Kr	Ar	Ne	He
340	0.09	0.10	0.12	0.16	0.22
355	0.10	0.11	0.12	0.18	0.24
370	0.10	0.12	0.13	0.18	0.25
385	0.11	0.12	0.14	0.19	0.25
400	0.12	0.14	0.14	0.20	0.27
415	0.13	0.14	0.15	0.20	0.28
430	0.13	0.15	0.16	0.21	0.28
445	0.14	0.15	0.16	0.22	0.30
460	0.14	0.16	0.17	0.23	0.31

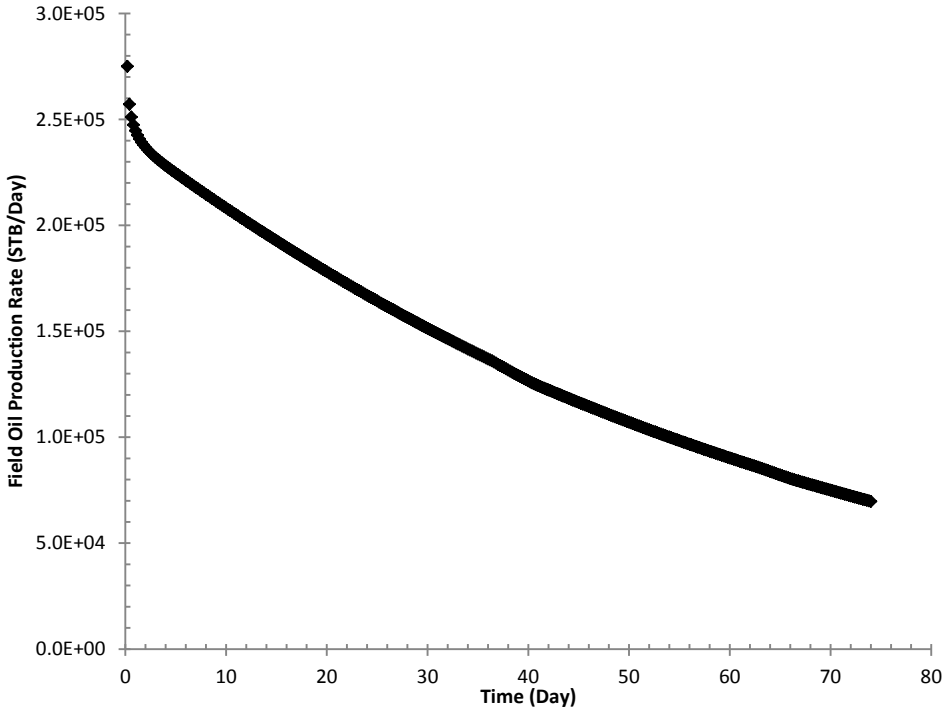

Figure 82. Field oil production rate (Stock tank barrel/Day)

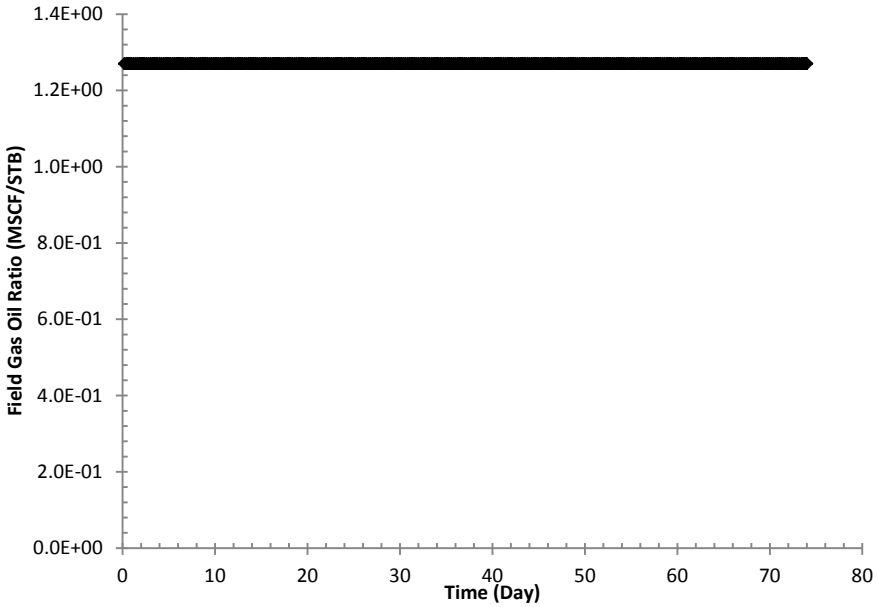

Figure 83. Gas oil ratio

In Figure 81 and Figure 84, the trends of the oil production and tracers breakthrough are identical and presence on the first day it was injected. This further emphasize that diffusion may not play an important role in a reservoir with large flow. As such noble gas tracers breakthrough cannot be a results of diffusion mechanism.

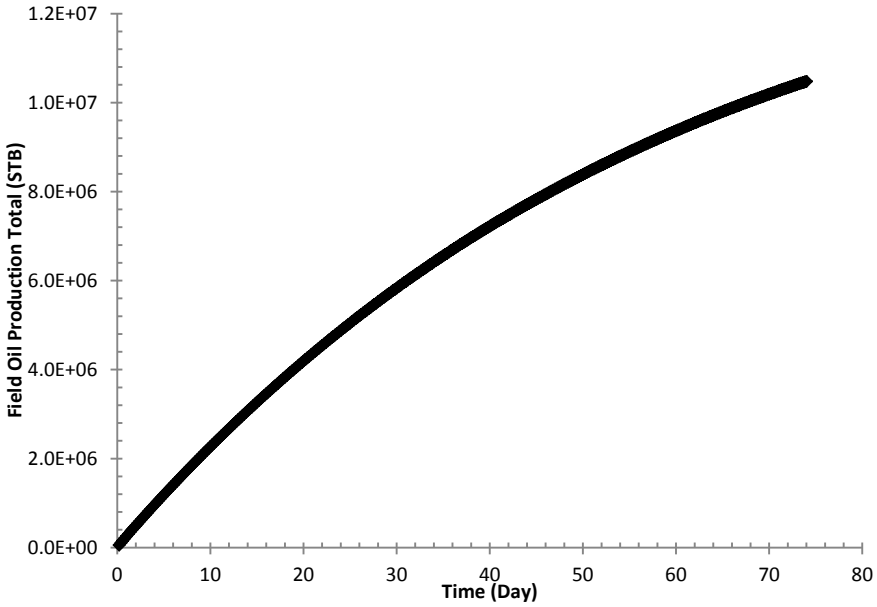

Figure 84. Field oil production total

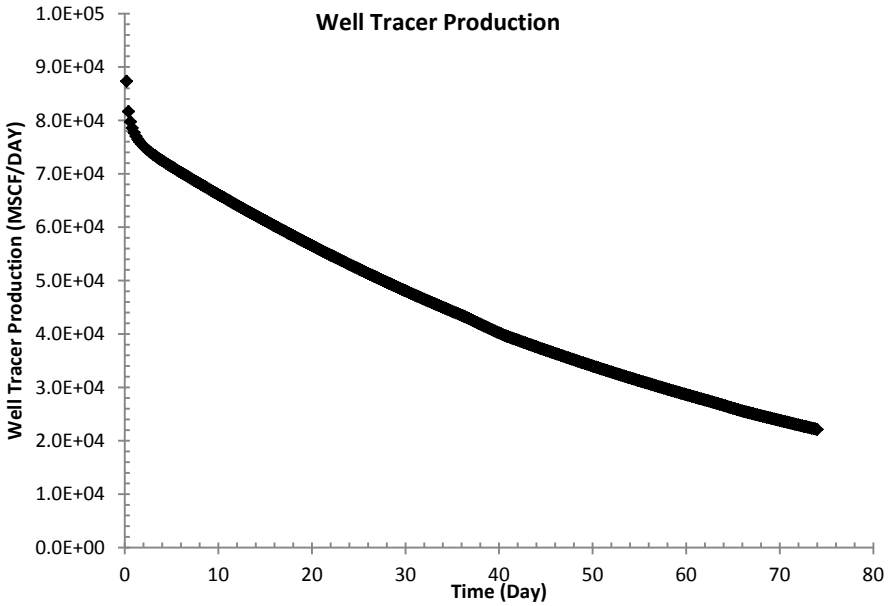

Figure 85. Tracer production rate for all 5 noble gas tracers

Chapter Nine

Conclusions and Future Work

Following the four objectives previously set out for this study, various aspects of the five noble gas + *n*-decane binary mixtures were investigated. Atomistic simulation were utilised for the study of Henry coefficients, vapour-liquid equilibrium, and diffusion coefficients. Reservoir simulation software package was also used to confirm the effect of diffusion coefficients within the reservoir.

9.1. Henry coefficients

Monte Carlo simulation and Widom insertion technique was utilised in the study of the solubility coefficient of noble gas + *n*-decane at infinite dilution and reservoir conditions. Size of the solutes plays a great role in the simulation where positive enthalpies of solvation were observed for He and Ne in *n*-decane, indicating an endothermic reaction. On the other end of the spectrum, negative enthalpies of solvation were observed for Kr and Xe in *n*-decane solution at reservoir conditions. The maxima in the gradient were observed on the $\ln K \ vs. 1/\mathrm{T}$ plots for Xe and Kr in *n*-decane solution at 200 MPa. While these maxima are reproduced on the two of the largest gases considered, they are accommodated by larger uncertainties and further investigation will have to be completed before they can be confirmed. Additionally, a change in enthalpies of solvation for Ar in *n*-decane from negative at lower pressure and positive at higher pressure were also observed. This are thought to be caused by the similarity in ε values between Ar and CH_3 group and the energy required for the cavity formation to accommodate the solute are nearly compensated by the favourable interaction between the solute and solvent molecules.

The results were also plotted in terms of critical temperature of the solutes where nonlinear correlations were observed. Additionally, the results were also linearly fitted with the smoothing function of Clarke & Glew using the first two coefficients. The partial molar volume was also investigated where larger gases experience greater volume changes upon insertion, as expected. What is more, the change in partial molar volume for Ar system is not consistent throughout the temperature and pressure ranges. This was thought to be a result of similarity in the ε values between Ar and CH_3 group.

9.2. Vapour-liquid equilibrium

By way of the Monte Carlo simulation, the vapour-liquid equilibrium curves of the noble gas + *n*-decane binary mixtures were investigated. Although the intentions were originally to use the composition representative to that at infinite dilution, such high pressure range for the reservoir conditions has prevented the simulations of practical system size and composition to be completed. The relatively large system sizes of 1200 particles for lower pressure range and 1500 particles for higher pressure range were utilised in the vapour-liquid equilibrium study. The results were great agreement with the predictions by the Peng-Robinson equation of state. He + *n*-decane and Ne + *n*-decane are the two systems with higher bubble pressure than the highest pressure considered in this study. The binary mixture of Xe + *n*-decane on the other hand has the lowest bubble pressure. Additionally, the density of the He + *n*-decane and Ne + *n*-decane mixtures are relatively insensitive to the pressure changes when compared to heavier gases.

9.3. Diffusion coefficients and reservoir simulation

The study of diffusion coefficients of noble gases in *n*-decane solution at reservoir conditions were completed in molecular dynamics simulations. The plots of the diffusion coefficient ratios were fitted with linear trend with negligibly small slope. The ratio of the diffusion coefficients were further investigated in light of the Stoke-Einstein's relation and the hard-sphere Enskog's relation. Once put in the form of ratio, both methodologies express diffusion coefficient ratios in terms of ratio of radii. These radii of the interaction between solute and solvent molecules are not clear when it comes to particles with large size disparity. Three different measures of interaction radii were investigated. Interestingly, the best fit was observed when $R = \sigma_{solute} + R_{gyration}$.

The diffusion coefficients were then utilised in the reservoir simulation. The results confirm the calculation where the diffusion does not play an important role when the breakthrough is expected in relatively small time scale (days). However, the combination of different noble gas tracers may be utilised to investigate reservoir characteristics as diffusion coefficient of Xe in *n*-decane are approximately six times lower than that of He.

9.4. Future work

Although large amount of data including the solubility, diffusivity, and phase equilibrium of noble gas + *n*-decane binary mixtures have been compiled throughout this study, there are still much more work to be done to fully understand the thermodynamics of noble gas tracers within the reservoir. Some interesting topics can be investigated immediately following this study through powerful molecular simulation software.

In terms of solubility coefficients, the maxima observed in both Xe and Kr plots are an interesting feature. Longer and additional number of simulations should be applied to reduce the unusually high uncertainty associated with the maximum region. Accompanying the solubility of noble gases in *n*-decane at infinite dilution, phase partitioning of noble gases should be further investigated. This perhaps can be completed by way of a coarsed-grain model to allow for larger number of particles and composition similar to that at infinite dilution. Such study will help verify the maxima observed in the solubility study.

The radial distribution function should be completed to better understand the diffusivity of noble gases in *n*-decane at reservoir conditions. Additionally, other binary or tertiary mixtures should also be investigated including CO_2 and other much heavier hydrocarbon components. A typical geological sequestration site is a complex subterranean structure where its fluid is comprised of a large number of components interacting at conditions far from ideal. A more detailed study of the reservoir can be carried out where compositional model could be used to further investigate the role of noble gases within the reservoir.

One thing to keep in mind is that this is a temporary fix. The consumption habits must be addressed to truly resolve the climate change issue, and perhaps many others in the process.

"What we do for ourselves dies with us.
What we do for others and the world, remains and is immortal."
Albert Pine

References

Adams, J. B., Foiles, S. M., & Wolfer, W. G. (1989). Self-diffusion and impurity diffusion of fee metals using the five-frequency model and the Embedded Atom Method. *Journal of Materials Research, 4*(01), 102-112.

Ahmed, T. (2006). *Reservoir Engineering Handbook (3rd Edition)*: Elsevier.

Alder, B., Alley, W., & Dymond, J. (1974). Studies in molecular dynamics. XIV. Mass and size dependence of the binary diffusion coefficient. *The Journal of Chemical Physics, 61*, 1415.

Allen, M. P., & Tildesley, D. J. (1989). *Computer simulation of liquids*: Oxford university press.

Almarza, N. G., Enciso, E., & Bermejo, F. J. (1992). Monte Carlo simulation of liquid n-alkanes. I. Intramolecular structure and thermodynamics. *The Journal of Chemical Physics, 96*(6), 4625-4632.

Aparicio-Martínez, S., & Hall, K. R. (2006). Use of PC-SAFT for Global Phase Diagrams in Binary Mixtures Relevant to Natural Gases. 1. n-Alkane + n-Alkane. *Industrial & Engineering Chemistry Research, 46*(1), 273-284.

Atkins, P. W., & De Paula, J. (2001). *The Elements of Physical Chemistry* (Vol. 8): Oxford University Press Oxford.

Bachu, S. (2008). CO2 storage in geological media: Role, means, status and barriers to deployment. *Progress in Energy and Combustion Science, 34*(2), 254-273.

Ballentine, C. J., Burgess, R., & Marty, B. (2002). Tracing fluid origin, transport and interaction in the crust. *Reviews in mineralogy and geochemistry, 47*(1), 539-614.

Bargas, C., Montgomery, H., Sharp, D., & Vosika, J. (1992). Immiscible CO2 Process for the Salt Creek Field. *SPE reservoir engineering, 7*(4), 397-402.

Beeman, D. (1976). Some multistep methods for use in molecular dynamics calculations. *Journal of Computational Physics, 20*(2), 130-139.

Berendsen, H. J., Postma, J. P. M., van Gunsteren, W. F., DiNola, A., & Haak, J. (1984). Molecular dynamics with coupling to an external bath. *The Journal of Chemical Physics, 81*, 3684.

Bonifácio, R. P., Filipe, E. J. M., McCabe, C., Costa Gomes, M. F., & PÁDua, A. A. H. (2002). Predicting the solubility of xenon in n-hexane and n-perfluorohexane: a simulation and theoretical study. *Molecular Physics, 100*(15), 2547-2553.

Bonifácio, R. P. M. F., Martins, L. s. F. G., McCabe, C., & Filipe, E. J. M. (2010). On the Behavior of Solutions of Xenon in Liquid n-Alkanes: Solubility of Xenon in n-Pentane and n-Hexane. *The Journal of Physical Chemistry B, 114*(48), 15897-15904.

Bruant, R. G., Jr, Jr., Celia, M. A., Guswa, A. J., & Peters, C. A. (2002). Peer Reviewed: Safe Storage of CO2 in Deep Saline Aquifiers. *Environmental Science & Technology, 36*(11), 240A-245A.

Chandler, D., & Andersen, H. C. (1972). Optimized Cluster Expansions for Classical Fluids. II. Theory of Molecular Liquids. *The Journal of Chemical Physics, 57*(5), 1930-1937.

Chen, B., & Siepmann, J. I. (1999). Transferable Potentials for Phase Equilibria. 3. Explicit-Hydrogen Description of Normal Alkanes. *The Journal of Physical Chemistry B, 103*(25), 5370-5379.

Chen, S. H., Davis, H. T., & Evans, D. F. (1981). Tracer diffusion in polyatomic liquids. II. *The Journal of Chemical Physics, 75*(3), 1422-1426.

Chen, S. H., Davis, H. T., & Evans, D. F. (1982). Tracer diffusion in polyatomic liquids. III. *The Journal of Chemical Physics, 77*(5), 2540-2544.

Chen, Z. (2007). Reservoir Simulation - Mathematical Techniques in Oil Recovery. *Society for Industrial and Applied Mathematics*, 83-129.

Chen, Z., Huan, G., & Ma, Y. (2006). *Computational methods for multiphase flows in porous media* (Vol. 2): Siam.

Clarke, E. C. W., & Glew, D. N. (1966). Evaluation of thermodynamic functions from equilibrium constants. *Transactions of the Faraday Society, 62*(0), 539-547.

Clarke, J., & Brown, D. (1987). The rheological properties of liquids composed of flexible chain molecules: A molecular dynamics computer simulation study. *The Journal of Chemical Physics, 86*, 1542.

Costa Gomes, M. F., & Grolier, J.-P. (2001). Determination of Henry's law constants for aqueous solutions of tetradeuteriomethane between 285 and 325 K and calculation of the H/D isotope effect. [10.1039/B008755F]. *Physical Chemistry Chemical Physics, 3*(6), 1047-1052.

Crichlow, H. B. (1977). *Modern Reservoir Engineering: a simulation approach*: Prentice-Hall Englewood Cliffs, NJ.

Crovetto, R., Fernandez-Prini, R., & Japas, M. L. (1982). Solubilities of inert gases and methane in H2O and in D2O in the temperature range of 300 to 600 K. *The Journal of Chemical Physics, 76*(2), 1077-1086.

Cui, S., Gupta, S., Cummings, P., & Cochran, H. (1996). Molecular dynamics simulations of the rheology of normal decane, hexadecane, and tetracosane. *The Journal of Chemical Physics, 105*, 1214.

Curro, J. G., Honnell, K. G., & McCoy, J. D. (1997). Theory for the Solubility of Gases in Polymers: Application to Monatomic Solutes. *Macromolecules, 30*(1), 145-152.

de Pablo, J. J., Bonnin, M., & Prausnitz, J. M. (1992). Vapor-liquid equilibria for polyatomic fluids from site-site computer simulations: pure hydrocarbons and binary mixtures containing methane. *Fluid Phase Equilibria, 73*(3), 187-210.

de Pablo, J. J., Laso, M., Siepmann, J. I., & Suter, U. W. (1993). Continuum-Configurational-Bias Monte-Carlo Simulations Of Long-Chain Alkanes. [Article]. *Molecular Physics, 80*(1), 55-63.

Design Institute for Physical Properties, S. b. A. DIPPR Project 801 - Full Version: Design Institute for Physical Property Research/AIChE.

Diamond, L. W., & Akinfiev, N. N. (2003). Solubility of CO2 in water from -1.5 to 100 degrees C and from 0.1 to 100 MPa: evaluation of literature data and thermodynamic modelling. *Fluid Phase Equilibria, 208*(1-2), 265-290.

Dias, L. M. B., Filipe, E. J. M., McCabe, C., & Calado, J. C. G. (2004). Thermodynamics of Liquid (Xenon + Methane) Mixtures. *The Journal of Physical Chemistry B, 108*(22), 7377-7381.

Donnez, P. (2007). *Essentials of reservoir engineering*: Editions OPHRYS.

Duan, Z. H., Moller, N., & Weare, J. H. (1996). A general equation of state for supercritical fluid mixtures and molecular dynamics simulation of mixture PVTX properties. *Geochimica Et Cosmochimica Acta, 60*(7), 1209-1216.

Duan, Z. H., & Sun, R. (2003). An improved model calculating CO2 solubility in pure water and aqueous NaCl solutions from 273 to 533 K and from 0 to 2000 bar. *Chemical Geology, 193*(3-4), 257-271.

Dymond, J. H., Cholinski, J. A., Sząfranski, A., & Wyrzykowska-Stankiewicz, D. (1986). Second virial coefficients for N-alkanes; recommendations and predictions. *Fluid Phase Equilibria, 27*(0), 1-13.

Dymond, J. H., & Smith, E. B. (1980). *The virial coefficients of pure gases and mixtures: a critical compilation*: Clarendon Press.

Dysthe, D., Fuchs, A., & Rousseau, B. (2000). Fluid transport properties by equilibrium molecular dynamics. III. Evaluation of united atom interaction potential models for pure alkanes. *The Journal of Chemical Physics, 112*, 7581.

Ekiner, O., & Thodos, G. (1966a). The Critical Temperature and Critical Pressures of the Ethane-n-Pentane-n-Heptane System. *Journal of Chemical and Engineering Data, 11*(4), 457-460.

Ekiner, O., & Thodos, G. (1966b). Critical Temperatures and Critical Pressures of the Ethane-n-Pentane System. *Journal of Chemical & Engineering Data, 11*(2), 154-155.

Elliott, J. R., & Lira, C. T. (2012). *Introductory Chemical Engineering Thermodynamics*: Prentice Hall.

Estabrook, E. L., & Rader, C. M. (1925). History of production of Salt Creek oil field, Wyoming. *Petroleum development and technology in*, 199-254.

Evans, D. F., Tominaga, T., & Davis, H. T. (1981). Tracer diffusion in polyatomic liquids. *The Journal of Chemical Physics, 74*(2), 1298-1305.

Filipe, E. J. M., Gomes de Azevedo, E. J. S., Martins, L. F. G., Soares, V. A. M., Calado, J. C. G., McCabe, C., & Jackson, G. (2000). Thermodynamics of Liquid Mixtures of Xenon with Alkanes: (Xenon + Ethane) and (Xenon + Propane). *The Journal of Physical Chemistry B, 104*(6), 1315-1321.

Filipe, E. J. M., Martins, L. F. G., Calado, J. C. G., McCabe, C., & Jackson, G. (2000). Thermodynamics of Liquid Mixtures of Xenon with Alkanes: (Xenon + n-Butane) and (Xenon + Isobutane). *The Journal of Physical Chemistry B, 104*(6), 1322-1325.

Frank, W., Breier, U., Elsässer, C., & Fähnle, M. (1996). First-Principles Calculations of Absolute Concentrations and Self-Diffusion Constants of Vacancies in Lithium. *Physical Review Letters, 77*(3), 518-521.

Frenkel, D., & Smit, B. (1996). *Understanding molecular simulation: from algorithms to applications*. San Diego: Academic Press.

Frenkel, D., & Smit, B. (2002). *Understanding molecular simulation: from algorithms to applications* (2nd ed. ed.): Academic.

Gonzalez-Melchor, M., Orea, P., Lopez-Lemus, J., Bresme, F., & Alejandre, J. (2005). Stress anisotropy induced by periodic boundary conditions. *The Journal of Chemical Physics, 122*(9), 094503.

Gough, C., Shacley, S., & Cannell, M. G. (2002). *Evaluating the options for carbon sequestration*: Tyndall Centre for Climate Change Research.

Graboski, M. S., & Daubert, T. E. (1978). A modified Soave equation of state for phase equilibrium calculations. 1. Hydrocarbon systems. *Industrial & Engineering Chemistry Process Design and Development, 17*(4), 443-448.

Hockney, R. W. (1970). Potential Calculation and Some Applications: Langley Research Center, Hampton, Va.

Hoover, W. G. (1985). Canonical dynamics: Equilibrium phase-space distributions. *Physical Review A, 31*(3), 1695.

Jorgensen, W. L., Madura, J. D., & Swenson, C. J. (1984). Optimized intermolecular potential functions for liquid hydrocarbons. *Journal of the American Chemical Society, 106*(22), 6638-6646.

Kamiya, Y., Naito, Y., Terada, K., Mizoguchi, K., & Tsuboi, A. (2000). Volumetric Properties and Interaction Parameters of Dissolved Gases in Poly(dimethylsiloxane) and Polyethylene. *Macromolecules, 33*(8), 3111-3119.

Kay, W. B. (1968). Critical locus curve and the phase behavior of mixtures. *Accounts of Chemical Research, 1*(11), 344-351.

Kell, G. S., McLaurin, G. E., & Whalley, E. (1978). Second virial coefficient of helium from 0 to 500[degree]C by the two-temperature gas-expansion method. *The Journal of Chemical Physics, 68*(5), 2199-2205.

Kharaka, Y. K., & Specht, D. J. (1988). The solubility of noble gases in crude oil at 25–100 C. *Applied geochemistry, 3*(2), 137-144.

Kiselev, S. B., & Fly, J. F. (2000). Simplified crossover SAFT equation of state for pure fluids and fluid mixtures. *Fluid Phase Equilibria, 174*(1-2), 93-113.

Konynenburg, P. H. V., & Scott, R. L. (1980). Critical Lines and Phase Equilibria in Binary Van Der Waals Mixtures. *Philosophical Transactions of the Royal Society of London. Series A, Mathematical and Physical Sciences, 298*(1442), 495-540.

Krause, D., Jr., & Benson, B. (1989). The solubility and isotopic fractionation of gases in dilute aqueous solution. IIa. solubilities of the noble gases. *Journal of Solution Chemistry, 18*(9), 823-873.

Krynicki, K., Green, C. D., & Sawyer, D. W. (1978). Pressure and temperature dependence of self-diffusion in water. [10.1039/DC9786600199]. *Faraday Discussions of the Chemical Society, 66*(0), 199-208.

Kutasov, I. M. (1989). Water FV Factors at Higher Pressure and Temperatures. *Oil & Gas J.*, 102-104.

Laso, M., de Pablo, J. J., & Suter, U. W. (1992). Simulation of phase equilibria for chain molecules. *The Journal of Chemical Physics, 97*(4), 2817-2819.

Leach, A. (2001). *Molecular modelling : principles and applications*: Pearson Prentice Hall.

Lindeberg, E. (2003). *The quality of a CO2 repository: What is the sufficient retention time of CO2 stored underground.* Paper presented at the IEA GHG Technology Conference.

Linstrom, E. P. J., & Mallard, W. G. NIST Standard Reference Database Number 69 Vol. National Institute of Standards and Technology, Gaithersburg MD, 20899.

London, F. (1930). Zur theorie und systematik der molekularkräfte. *Zeitschrift für Physik, 63*(3-4), 245-279.

Lu, C., Han, W. S., Lee, S. Y., McPherson, B. J., & Lichtner, P. C. (2009). Effects of density and mutual solubility of a CO2-brine system on CO2 storage in geological formations: "Warm" vs. "cold" formations. *Advances in Water Resources, 32*(12), 1685-1702.

Mackintosh, S. (2009). The use of noble gases as a tracer in CO2 sequestration. *Unpublished PhD Thesis, University of Manchester. 185*.

Mackintosh, S. J., & Ballentine, C. J. (2012). Using 3He/4He isotope ratios to identify the source of deep reservoir contributions to shallow fluids and soil gas. *Chemical Geology, 304–305*(0), 142-150.

Maitland, G. C., Vesovic, V., & Wakeham, W. A. (1985a). The inversion of thermophysical properties. *Molecular Physics, 54*(2), 301-319.

Maitland, G. C., Vesovic, V., & Wakeham, W. A. (1985b). The inversion of thermophysical properties. *Molecular Physics, 54*(2), 287-300.

Mandell, M. J. (1976). On the properties of a periodic fluid. *Journal of Statistical Physics, 15*(4), 299-305.

Marchetti, C. (1977). On geoengineering and the CO2 problem. *Climatic change, 1*(1), 59-68.

Martin, J. J. (1979). Cubic equations of state-which? *Industrial & Engineering Chemistry Fundamentals, 18*(2), 81-97.

Martin, M. G., & Siepmann, J. I. (1998). Transferable Potentials for Phase Equilibria. 1. United-Atom Description of n-Alkanes. *The Journal of Physical Chemistry B, 102*(14), 2569-2577.

Martin, M. G., & Siepmann, J. I. (1999). Novel Configurational-Bias Monte Carlo Method for Branched Molecules. Transferable Potentials for Phase Equilibria. 2. United-Atom Description of Branched Alkanes. *The Journal of Physical Chemistry B, 103*(21), 4508-4517.

McCain, W. (1990). *The properties of petroleum fluids*: PennWell Books.

Merkel, T. C., Bondar, V. I., Nagai, K., Freeman, B. D., & Pinnau, I. (2000). Gas sorption, diffusion, and permeation in poly(dimethylsiloxane). *Journal of Polymer Science Part B: Polymer Physics, 38*(3), 415-434.

Metropolis, N., Rosenbluth, A. W., Rosenbluth, M. N., Teller, A. H., & Teller, E. (1953). Equation of State Calculations by Fast Computing Machines. *The Journal of Chemical Physics, 21*(6), 1087-1092.

Mizerovsky, L. N., & Smirnova, K. P. (2010). Temperature dependence of the solubility of nitrogen in n-alkanes at atmospheric pressure. *Russian Chemical Bulletin, 59*(4), 673-676.

Moller, M. A., Tildesley, D. J., Kim, K. S., & Quirke, N. (1991). Molecular dynamics simulation of a Langmuir--Blodgett film. *The Journal of Chemical Physics, 94*(12), 8390-8401.

Mooji, G. C. A. M., Frenkel, D., & Smit, B. (1992). Direct simulation of phase equilibria of chain molecules. *J. Phys.: Condens. Matter, 4*, L255-L259.

Nose, S., & Klein, M. (1983). Constant pressure molecular dynamics for molecular systems. *Molecular Physics, 50*(5), 1055-1076.

Panagiotopoulos, A. Z. (1987). Direct determination of phase coexistence properties of fluids by Monte Carlo simulation in a new ensemble. *Molecular Physics, 61*(4), 813-826.

Parrinello, M., & Rahman, A. (1981). Polymorphic transitions in single crystals: A new molecular dynamics method. *Journal of Applied physics, 52*, 7182.

Péneloux, A., Rauzy, E., & Fréze, R. (1982). A consistent correction for Redlich-Kwong-Soave volumes. *Fluid Phase Equilibria, 8*(1), 7-23.

Peng, D.-Y., & Robinson, D. B. (1976). A new two-constant equation of state. *Industrial & Engineering Chemistry Fundamentals, 15*(1), 59-64.

Poling, B. E., Prausnitz, J. M., O'Connell, J. P., & Reid, R. C. (2001). *The properties of gases and liquids* (5th ed. ed.). New York, London: McGraw-Hill.

Pollack, G. L. (1981). Solubility of xenon in n-alkanes: n-pentane through n-hexadecane. *The Journal of Chemical Physics, 75*(12), 5875-5878.

Pollack, G. L., & Enyeart, J. J. (1985). Atomic test of the Stokes-Einstein law. II. Diffusion of Xe through liquid hydrocarbons. *Physical Review A, 31*(2), 980-984.

Pollack, G. L., & Himm, J. F. (1982). Solubility of xenon in liquid n-alkanes: Temperature dependence and thermodynamic functions. *The Journal of Chemical Physics, 77*(6), 3221-3229.

Pollack, G. L., Kennan, R. P., Himm, J. F., & Stump, D. R. (1990). Diffusion of xenon in liquid alkanes: Temperature dependence measurements with a new method. Stokes–Einstein and hard sphere theories. *The Journal of Chemical Physics, 92*(1), 625-630.

Potoff, J. J., & Panagiotopoulos, A. Z. (1998). Critical point and phase behavior of the pure fluid and a Lennard-Jones mixture. *The Journal of Chemical Physics, 109*(24), 10914-10920.

Potter, R., II, & Clynne, M. (1978). The solubility of the noble gases He, Ne, Ar, Kr, and Xe in water up to the critical point. *Journal of Solution Chemistry, 7*(11), 837-844.

Pratt, L. R., & Haan, S. W. (1981). Effects of periodic boundary conditions on equilibrium properties of computer simulated fluids. II. Application to simple liquids. *The Journal of Chemical Physics, 74*(3), 1873-1876.

Rah, K., Kwak, S., Eu, B. C., & Lafleur, M. (2002). Relation of Tracer Diffusion Coefficient and Solvent Self-Diffusion Coefficient. *The Journal of Physical Chemistry A, 106*(48), 11841-11845.

Rai, N., & Siepmann, J. I. (2007). Transferable Potentials for Phase Equilibria. 9. Explicit Hydrogen Description of Benzene and Five-Membered and Six-Membered Heterocyclic Aromatic Compounds. *The Journal of Physical Chemistry B, 111*(36), 10790-10799.

Reamer, H. H., Lower, J., & Sage, B. H. (1964). Duffusion Coefficients in Hydrocarbon Systems. Ethane in the Liquid Phase of the Ethane-n-Decane System. *Journal of Chemical & Engineering Data, 9*(1), 54-59.

Reamer, H. H., Sage, B. H., & Lacey, W. N. (1960). Phase Equilibria in Hydrocarbon Systems. Volumetric and Phase Behavior of the Ethane-n-Pentane System. *Journal of Chemical & Engineering Data, 5*(1), 44-50.

Redlich, O., & Kwong, J. (1949). On the Thermodynamics of Solutions. V. An Equation of State. Fugacities of Gaseous Solutions. *Chemical Reviews, 44*(1), 233-244.

Rodriguez, A. L., Vega, C., Freire, J. J., & Lago, S. (1991). Potential Parameters Of Methyl And Methylene Obtained From 2nd Virial-Coefficients Of N-Alkanes. [Article]. *Molecular Physics, 73*(3), 691-701.

Rodriguez, A. L., Vega, C., Freire, J. J., & Lago, S. (1993). Improved Results For The Potential Parameters Of Methyl And Methylene Obtained From 2nd Virial-Coefficients Of N-Alkanes. [Note]. *Molecular Physics, 80*(6), 1565-1567.

Rosenbluth, M. N., & Rosenbluth, A. W. (1955). Monte Carlo Calculation Of The Average Extension Of Molecular Chains. *Journal Name: Journal of Chemical Physics (U.S.); Journal Volume: Vol: 23; Other Information: Orig. Receipt Date: 31-DEC-55*, Medium: X; Size: Pages: 356-359.

Rowley, R. L. (1994). *Statistical mechanics for thermophysical property calculations*: Prentice Hall New Jersey:.

Rowlinson, J. S., & Swinton, F. L. (1982). *Liquids and liquid mixtures*: Butterworth Scientific.

Ryckaert, J.-P., McDonald, I. R., & Klein, M. L. (1989). Disorder in the pseudohexagonal rotator phase of n-alkanes: molecular-dynamics calculations for tricosane. *Molecular Physics, 67*(5), 957-979.

Satter, A., Iqbal, G. M., & Buchwalter, J. L. (2008a). *Practical Enhanced Reservoir Engineering - Assisted with Simulation Software*: PennWell.

Satter, A., Iqbal, G. M., & Buchwalter, J. L. (2008b). *Practical Enhanced Reservoir Engineering: Assisted With Simulated Software*: Pennwell Books.

Schlumberger. (2008.2). ECLIPSE Technical Description Manual.

Schweizer, K. S., & Curro, J. G. (1994). *Adv. Polym. Sci., 116*(321).

Shafeen, A., Croiset, E., Douglas, P., & Chatzis, I. (2004). CO2 sequestration in Ontario, Canada. Part I: storage evaluation of potential reservoirs. *Energy Conversion and Management, 45*(17), 2645-2659.

Sheldon, J., Zondek, B., & Cardwell, W. (1959). One-dimensional, incompressible, noncapillary, two-phase fluid flow in a porous medium. *Trans. SPE AIME, 216*, 290-296.

Siepmann, J. I. (1990). A method for the direct calculation of chemical potentials for dense chain systems. *Molecular Physics, 70*(6), 1145-1158.

Siepmann, J. I., Karaborni, S., & Smit, B. (1993). Vapor-liquid equilibria of model alkanes. *Journal of the American Chemical Society, 115*(14), 6454-6455.

Siepmann, J. I., Martin, M. G., Chen, B., Wick, C. D., & Potoff, J. J. (1994). MCCCS Towhee Retrieved July, 2012, from http://towhee.sourceforge.net/

Siepmann, J. I. K., Sami; Smit, Berend. (1993). Simulating the critical behaviour of complex fluids. *Nature, 365*(6444), 330-332.

Skoulidas, A. I., & Sholl, D. S. (2002). Transport Diffusivities of CH4, CF4, He, Ne, Ar, Xe, and SF6 in Silicalite from Atomistic Simulations. *The Journal of Physical Chemistry B, 106*(19), 5058-5067.

Smit, B. (1992). Phase diagrams of Lennard ‐ Jones fluids. *The Journal of Chemical Physics, 96*(11), 8639-8640.

Smit, B., Karaborni, S., & Siepmann, J. I. (1995). Computer simulations of vapor--liquid phase equilibria of n-alkanes. *The Journal of Chemical Physics, 102*(5), 2126-2140.

Smith, J. M., b. ., & Van Ness, H. C. (1987). *Introduction to chemical engineering thermodynamics* (4th ed. ed.). New York, London: McGraw-Hill.

Soave, G. (1972). Equilibrium constants from a modified Redlich-Kwong equation of state. *Chemical Engineering Science, 27*(6), 1197-1203.

Solomon, S., Qin, D., Manning, M., Chen, Z., Marquis, M., Averyt, K. B., . . . (eds.), H. L. M. IPCC, 2007. *Climate Change 2007: The Physical Science Basis. Contribution of Working Group I to the Fourth Assessment Report of the Intergovernmental Panel on Climate Change*(Cambridge University Press, Cambridge, United Kingdom and New York, NY, USA.).

Spoel, D. v. d., Lindahl, E., Hess, B., & team, a. t. G. d. (2013). GROMACS User Manual version 4.6.3. *www.gromacs.org*.

Spycher, N., & Pruess, K. (2005). CO2-H2O mixtures in the geological sequestration of CO2 center dot. II. Partitioning in chloride brines at 12-100 degrees C and up to 600 bar. *Geochimica Et Cosmochimica Acta, 69*(13), 3309-3320.

Spycher, N., Pruess, K., & Ennis-King, J. (2003). CO2-H2O mixtures in the geological sequestration of CO2. I. Assessment and calculation of mutual solubilities from 12 to 100 degrees C and up to 600 bar. *Geochimica Et Cosmochimica Acta, 67*(16), 3015-3031.

Tiepel, E. W., & Gubbins, K. E. (1972a). Partial molal volumes of gases dissolved in electrolyte solutions. *The Journal of Physical Chemistry, 76*(21), 3044-3049.

Tiepel, E. W., & Gubbins, K. E. (1972b). Theory of gas solubility in mixed solvent systems. *The Canadian Journal of Chemical Engineering, 50*(3), 361-365.

Tsonopoulos, C., & Heidman, J. (1985). From Redlich-Kwong to the present. *Fluid Phase Equilibria, 24*(1), 1-23.

Valtz, A., Chapoy, A., Coquelet, C., Paricaud, P., & Richon, D. (2004). Vapour-liquid equilibria in the carbon dioxide-water system, measurement and modelling from 278.2 to 318.2K. *Fluid Phase Equilibria, 226*, 333-344.

Van Amerongen, G. J. (1946). The Permeability of Different Rubbers to Gases and Its Relation to Diffusivity and Solubility. *Journal of Applied physics, 17*(11), 972-985.

Van Der Spoel, D., Lindahl, E., Hess, B., Groenhof, G., Mark, A. E., & Berendsen, H. J. C. (2005). GROMACS: Fast, flexible, and free. *Journal of Computational Chemistry, 26*(16), 1701-1718.

Verlet, L. (1967). Computer "Experiments" on Classical Fluids. I. Thermodynamical Properties of Lennard-Jones Molecules. *Physical Review, 159*(1), 98-103.

Vesovic, V., & Wakeham, W. A. (1989). Prediction of the viscosity of fluid mixtures over wide ranges of temperature and pressure. *Chemical Engineering Science, 44*(10), 2181-2189.

Wang, J., & Hou, T. (2011). Application of molecular dynamics simulations in molecular property prediction II: Diffusion coefficient. *Journal of Computational Chemistry, 32*(16), 3505-3519.

Weiskopf, R. B., Lynch III, C., Baum, J., & Tenbrinck, R. (2000). Xenon anesthesia. *Anesthesiology, 92*(3), 865-870.

Wo, S., Whitman, L., & Steidtmann, J. (2009). *Estimates of Potential CO2 Demand for CO2 EOR in Wyoming Basins*. Paper presented at the SPE Rocky Mountain Petroleum Technology Conference.

Wu, G. W., Ennis-King, J., & Paterson, L. (2009). An improved perturbed hard-sphere equation of state. *Fluid Phase Equilibria, 284*(2), 118-128.

Yang, H., Xu, Z., Fan, M., Gupta, R., Slimane, R. B., Bland, A. E., & Wright, I. (2008). Progress in carbon dioxide separation and capture: A review. *Journal of Environmental Sciences, 20*(1), 14-27.

Yoshida, K., Matubayasi, N., & Nakahara, M. (2007). Solvation shell dynamics studied by molecular dynamics simulation in relation to the translational and rotational dynamics of supercritical water and benzene. *The Journal of Chemical Physics, 127*(17), 174509.

Zudkevitch, D., & Joffe, J. (1970). Correlation and prediction of vapor - liquid equilibria with the redlich - kwong equation of state. *AIChE Journal, 16*(1), 112-119.

Makrodimitri, Z. A., Dohrn, R., & Economou, I. G. (2007). Atomistic Simulation of Poly(dimethylsiloxane): Force Field Development, Structure, and

Thermodynamic Properties of Polymer Melt and Solubility of n-Alkanes, n-Perfluoroalkanes, and Noble and Light Gases. *Macromolecules, 40*(5), 1720-1729.

Appendix A

Typical black oil reservoir fluid study (courtesy Core Laboratories, Inc.)

Page 1 of 15
File RFL 76000

Company Good Oil Company — Date Sampled
Well Oil Well No. 4 — County Samson
Field Productive — State Texas

FORMATION CHARACTERISTICS

Formation Name	Cretaceous
Date First Well Completed	, 19
Original Reservoir Pressure	4100 PSIG @ 8692 Ft.
Original Produced Gas-Oil Ratio	600 SCF/Bbl
Production Rate	300 Bbl/Day
Separator Pressure and Temperature	200 PSIG. 75 °F.
Oil Gravity at 60° F.	°API
Datum	8000 Ft. Subsea
Original Gas Cap	No

WELL CHARACTERISTICS

Elevation	610 Ft.
Total Depth	8943 Ft.
Producing Interval	8684-8700 Ft.
Tubing Size and Depth	2-7/8 In. to 8600 Ft.
Productivity Index	1.1 Bbl/D/PSI @ 300 Bbl/Day
Last Reservoir Pressure	3954* PSIG @ 8500 Ft.
Date	, 19
Reservoir Temperature	217* °F. @ 8500 Ft.
Status of Well	Shut in 72 hours
Pressure Gauge	Amerada
Normal Production Rate	300 Bbl/Day
Gas-Oil Ratio	600 SCF/Bbl
Separator Pressure and Temperature	200 PSIG, 75 °F.
Base Pressure	14.65 PSIA
Well Making Water	None % Cut

SAMPLING CONDITIONS

Sampled at	8500 Ft.
Status of Well	Shut in 72 hours
Gas-Oil Ratio	SCF/Bbl
Separator Pressure and Temperature	PSIG, °F.
Tubing Pressure	1400 PSIG
Casing Pressure	PSIG
Sampled by	
Type Sampler	Wofford

REMARKS:

* Pressure and temperature extrapolated to the mid-point of the producing interval = 4010 PSIG and 220°F.

Figure 86. Example of black oil reservoir fluid, adopted from (McCain, 1990)

Page 2 of 15

File RFL 76000

Company Good Oil Company Formation Cretaceous

Well Oil Well No. 4 County Samson

Field Productive State Texas

HYDROCARBON ANALYSIS OF Reservoir Fluid SAMPLE

COMPONENT	MOL PERCENT	WEIGHT PERCENT	DENSITY @ 60° F. GRAMS PER CUBIC CENTIMETER	° API @ 60° F.	MOLECULAR WEIGHT
Hydrogen Sulfide	Nil	Nil			
Carbon Dioxide	0.91	0.43			
Nitrogen	0.16	0.05			
Methane	36.47	6.24			
Ethane	9.67	3.10			
Propane	6.95	3.27			
iso-Butane	1.44	0.89			
n-Butane	3.93	2.44			
iso-Pentane	1.44	1.11			
n-Pentane	1.41	1.09			
Hexanes	4.33	3.97			
Heptanes plus	33.29	77.41	0.8515	34.5	218
	100.00	100.00			

Figure 87. Reservoir fluid analysis report, adopted from (McCain, 1990)

Wells representation

An injection or production well is defined as a point at the centroid of the block. It is the form of communication between the reservoir and the surface. The flow between the block and the well, perforation, is similar to the transmissibility between blocks. The flow rate between the block and the well is defined as follow:

Flow rate = dead oil rate + water rate + free gas rate + solution gas rate

$$q_i = W_k \left[\frac{k_{r0}}{\mu_0 B_0} + \frac{k_{rw}}{\mu_w B_w} + \frac{k_{rg}}{\mu_g B_g} + \frac{R_s k_{r0}}{\mu_0 B_0} \right] \Delta P \qquad (1)$$

Or in matrix form

$$q_i = W_k \cdot \Delta P \cdot \begin{bmatrix} \frac{k_{r0}}{\mu_0 B_0} + R_v \frac{k_{rg}}{\mu_g B_g} \\ \frac{k_{rw}}{\mu_w B_w} \\ \frac{k_{rg}}{\mu_g B_g} + \frac{R_s k_{r0}}{\mu_0 B_0} \end{bmatrix} \quad (2)$$

Where

W_k: perforation connection factor in block i, sometimes refer to as geometric factor

k_r: relative permeability of specified phase: oil, water and gas as denoted

μ: viscosity of the specified phase: oil, water, and gas as denoted

B: Formation volume factor of the specified phase: oil, water, and gas as denoted

ΔP: Pressure different between the wellblock i and the opposite wellblock

A perforation can be operating in different mode, shut-in well, open well with specific flow rate, pressure gradient, and bottom hole pressure. The operating mode can be specified in the model.

Newton-Ralphson iteration

This process is also known as non-linear iteration and outer-iteration. Since three errors $R = \begin{bmatrix} R_w \\ R_g \\ R_o \end{bmatrix}_i \rightarrow \begin{bmatrix} S_w \\ S_g \; or \; R_s \; or \; R_v \\ P_0 \end{bmatrix}$ are associated with each block in the building block, the iteration and the Jacobian $\frac{\partial R}{\partial X}$ can be written as follow

$$R(X + x) = R(X) + \frac{\partial R}{\partial X} x = 0 \quad (3)$$

$$\frac{\partial R_i}{\partial X_j} = \begin{bmatrix} \frac{\partial R_o}{\partial P_o} & \frac{\partial R_o}{\partial S_w} & \frac{\partial R_o}{\partial S_g} \\ \frac{\partial R_w}{\partial P_o} & \frac{\partial R_w}{\partial S_w} & \frac{\partial R_w}{\partial S_g} \\ \frac{\partial R_g}{\partial P_o} & \frac{\partial R_g}{\partial S_w} & \frac{\partial R_g}{\partial S_g} \end{bmatrix}_{ij} \quad (4)$$

And

$$J \times x = R(X) \rightarrow x = J^{-1}R(X) \quad (5)$$

The Jacobian is a matrix of partial derivatives of the blocks relative to R. And R(X) is the non-linear error of the previous iteration. The Newton-Ralphson iteration algorithm is as follow

Compute the Jacobian

1. Evaluate the new R(X) → R(X+x)
2. If the error is larger than the tolerance limit, repeat step 2
3. When the error is within the tolerance limit, update the Jacobian and proceed to the next time step and repeat the iteration.

After n iteration, the error becomes

$$r_n = b - A \times x_n \quad (6)$$

$$B \times q_n = r_n \quad (7)$$

B is the approximation matrix to A. This approximation matrix contributes greatly to the efficiency of the solution acquisition. The objective is to minimize the material balance error. ECLIPSE utilizes Nested Factorization preconditioning to obtain the approximation matrix B, as is widely accepted.

The mass balance during each time step can be written as a vector M per unit fluid surface density

$$M = V_p \begin{bmatrix} \frac{S_0}{B_0} + \frac{R_v S_g}{B_g} \\ \frac{S_w}{B_w} \\ \frac{S_g}{B_g} + \frac{R_s S_0}{B_0} \end{bmatrix} \quad (8)$$

$V_P =$ vaper volume

S = saturation in the specify phase: gas, oil, or water

B = formation volume factor in the specify phase: gas, oil, or water

R_v = gas condensate ratio

R_s = solution gas oil ratio